Terahertz Quantum Cascade Lasers: towards high performance operation

by

Saeed Fathololoumi

A thesis
presented to the University of Waterloo
in fulfillment of the
thesis requirement for the degree of
Doctor of Philosophy
in
Electrical and Computer Engineering

Waterloo, Ontario, Canada, 2010

I hereby declare that I am the sole author of this thesis. This is a true copy of the thesis, including any required final revisions, as accepted by my examiners.

I understand that my thesis may be made electronically available to the public.

Abstract

Terahertz (THz) frequency range (wavelength of $300 - 30\mu m$, frequency of $1 - 10\ THz$ and photon energy of $\sim 4 - 40\ meV$), the gap between infrared and microwave electromagnetic waves, have remained relatively unexplored for a long time, due to lack of a high power, coherent, and compact source, as well as the lack of an appropriate detector and the transmission devices. THz wave has recently received considerable attention for potential applications in non-invasive medical imaging, detecting trace of gases in the environment, sensing of organic and biological molecules, security controls, local oscillators for heterodyne receiver systems, free space communication, etc. THz quantum cascade laser (QCL), as the relatively high power and coherent THz radiation source, was demonstrated in 2002. After near a decade of intense research, THz QCLs operate only up to 186 K in pulse mode with maximum power of 250 mW at 10 K.

This thesis discusses many aspects of theoretical and experimental design considerations for THz QCLs. The objective is to obtain a laser device that emits high powers and works towards the temperatures achievable by thermoelectric coolers. This work includes designing the active gain medium, and the engineering of the waveguide and heat removal structures. A density matrix based model is developed to explain the charge transport and gain mechanism in the intersubband devices, particularly for three well resonant phonon based THz QCLs. The model allows for designing of the optimum and novel active gain mediums that work at higher temperatures. The designed active gain mediums are fabricated using discussed low loss waveguide and efficient heat removal structures. The maximum operating temperatures as high as $\sim 176\ K$ is achieved. Finally a promising lasing scheme based on phonon-photon-phonon emissions is proposed that improves the population inversion and offers high gain peak.

Acknowledgements

I would like to thank Professor Dayan Ban for his kind supervision and inspiration. Without his continuous support and invaluable guidance, accomplishment of this thesis would have been impossible. I want to express my gratitude to the members of my PhD committee: Prof. Gottfried Strasser, Prof. Safieddin Safavi-Naeini, Prof. Siva Sivoththaman, and Prof. Frank Wilhelm, for reading my thesis and helpful discussions. Also, I would like to express my deepest appreciation to my parents, my brother and his wife for their unconditional love and support.

This work would not have been possible without the support of my colleagues at institute for microstructural sciences at National Research Council of Canada (NRCC), where most of this research have been conducted. I am indebted to Dr. H.C. Liu, Dr. Emmanuel Dupont, Mr. Sylvain Laframboise, Dr. Marcel Graf, Dr. Hui Luo and Mr. Richard Dudek for patiently teaching me the details of device modeling, fabrication and characterization and also aiding me with the experiments. I would like to also thank Dr. Zbigniew Wasilewski, Dr. Bulent Aslan, Dr. Chun-Ying Song, Mr. Abderraouf Boucherif, Dr. Andrew Bezinger, Dr. Margaret Buchanan, and many other individuals at NRCC, who helped me through this project.

I also want to express my gratitude to Mr. Ghasem Razavipour, Mr. Jun Chen, Mr. Rudra Dhar, and Miss. Somayyeh Rahimi, the members of Dr. Ban's group at University of Waterloo.

I owe this thesis to all my friends who helped me throughout my PhD program. In particular I would like to thank my best friend, Dr. Majid Gharghi, who taught me the basics of semiconductor physics during my bachelor's degree as a TA and kindly continued supporting me during past seven years, as a friend. I hope I can sometimes make all of these up to him. I also want to express my gratitude to all my friends who supported me, including but not limited to Dr. Maryam Moradi, Dr. Shahrzad Naraghi, Dr. Mojgan

Daneshmand, Mr. Arash A. Fomani, Miss. Bahareh S. Makki, Dr. Shahab Ardalan, Dr. Pedram Mousavi, Mr. Danial Nikfal, Mr. John Q. Nguyen, Mr. Behzad Malek, Mr. Vinh Tieu, Dr Hossein Sarbishaei, Mr. Hassan Sarbishaei, Dr. M.R. Ahmadi, Dr. M.R. Esmaeilirad, Dr. Pedram K. Amiri, Mr. Ehsan Fathi, Mr. A. Goldan, and Mr. Salam R. Gabran. I really enjoyed their company and help during the time spent with them.

Finally I thank the University of Waterloo and National Research Council of Canada for their friendly environments and resourceful research facilities during my research.

Dedication

To my parents

Contents

List of Tables

List of Figures

List of Abbreviations

BTC	Bound to continuum
CCD	Charge coupled device
CSL	Chirped superlattice
CW	Continuous wave
DFG	Difference frequency generation
DI	Deionized
EOS-MLS	earth observing system microwave limb soundere
FP	Fabry Perot
FSR	Free spectral range
FTIR	Fourier transform infrared IR spectrometer
FWHM	Full width half maximum
HR	High reflective
IPA	Isopropanol
IR	Infrared

LI	Light - Current
LIV	Light - Current - Voltage
LO	Longitudinal optical
MBE	Molecular beam epitaxy
MM	Metal-metal
MQW	Multiple quantum well
NDR	Negative differential resistance
PDE	partial differential equation
PL	Photoluminescence
QCL	Quantum cascade laser
QWP	Quantum well photodetector
RP	Resonant phonon
RTA	Rapid thermal annealing
SEM	Scanning electron microscope
SI	Semi-insulating
SI-SP	Semi-insulating surface plasmon
SIMS	Secondary ion mass spectroscopy
THz	Terahertz
TM	Transverse magnetic

VI	Voltage - Current
XRD	X-ray diffraction

Chapter 1

Introduction

The terahertz (THz) frequency range is the least studied and hence the least developed range in the electromagnetic spectrum, due to lack of proper light sources, detectors, and transmission lines. The THz frequencies are roughly defined as $f = 10^{12} - 10^{13} Hz$, corresponding to $\lambda = 300 - 30 \mu m$ in wavelength, and $\hbar\omega \simeq 4 - 40\ meV$ in photon energy. The THz frequency range lies between far infrared (shorter wavelengths) and sub-millimeter waves (higher frequencies), as shown in Figure 1.1. The sub-millimeter waves/microwaves are typically generated using semiconductor transistor based electronic techniques and the infrared (IR) light are generated using semiconductor laser based photonic techniques. It has been attempted to extend the electronic and photonic techniques, for generation of THz emission. Compact, coherent, tunable, and high power sources for THz wave have been desired because of many promising potential applications in the terahertz range that have long been identified. The research interest in THz technology has seen dramatic upsurge in the past decade [1, 2, 3], leading to rapid progress in the development of THz components, in particular various THz sources.

Out of all proposals for compact and coherent THz sources, semiconductor quantum cascade lasers (QCL), first demonstrated in 2002 by Kohler et al. [5], are among the

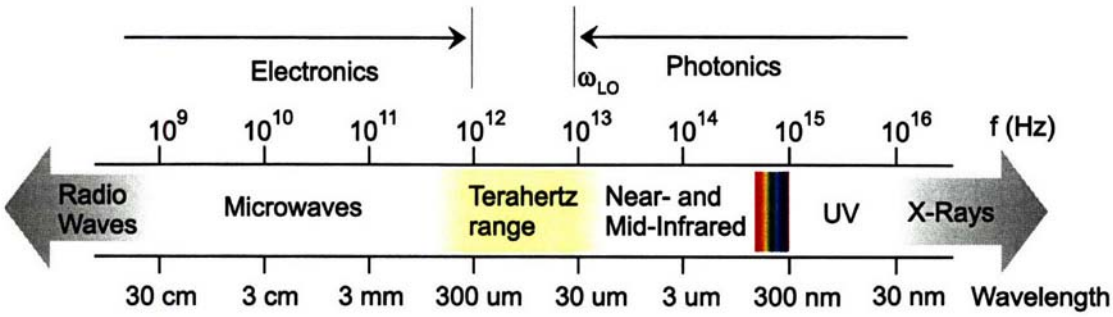

Figure 1.1: Diagram of electromagnetic spectrum showing THz region between far-IR and microwaves (adopted from [4]).

most promising options in generating high power THz wave. This thesis discusses the physics and the design behind a THz QCL device, and describes the engineering of the fabrication process to make high performance devices. This thesis presents and discusses the latest research results including intersubband charge transport, optical gain model, thermal investigation of the device, continuous wave (CW) operation of QCL devices, the investigation of modal field distribution, far-field pattern of the THz emission from THz QCLs, and design of the novel high temperature THz QCL devices.

1.1 THz Applications

The oldest application for THz waves is spectroscopy. This is mainly due to the fact that characteristic rotational and vibrational absorption lines for many chemical species and gasses are much stronger in THz range than in microwave region [6]. It is, therefore, much easier to detect different chemical agents using THz spectroscopy. The spectroscopy was historically performed using incoherent thermal sources. For the detection part, a Fourier transform infrared IR spectrometer (FTIR) combined with a cryogenically-cooled bolometer detector was used [7]. For long wavelength spectral measurements ($\lambda > 300\mu m$), long

mirror travel lengths are required in the FTIR. In such cases heterodyne spectroscopy is employed by using a CW THz source as a local oscillator. In this technique, local oscillator mixes with the incoming signal to downconvert it into an intermediate frequency in microwave/RF range for detection and consequent data processing. A tunable and narrow-band THz radiation source would be necessary in the successful transmission, absorption or reflection spectral measurements. Recently, mixing of a 2.7 THz QCL with a 182 GHz microwave source using hot electron bolometer is presented by Baryshev et al [8]. This work resulted in phase locking of the THz QCL, with the beat signal as narrow as 1 Hz.

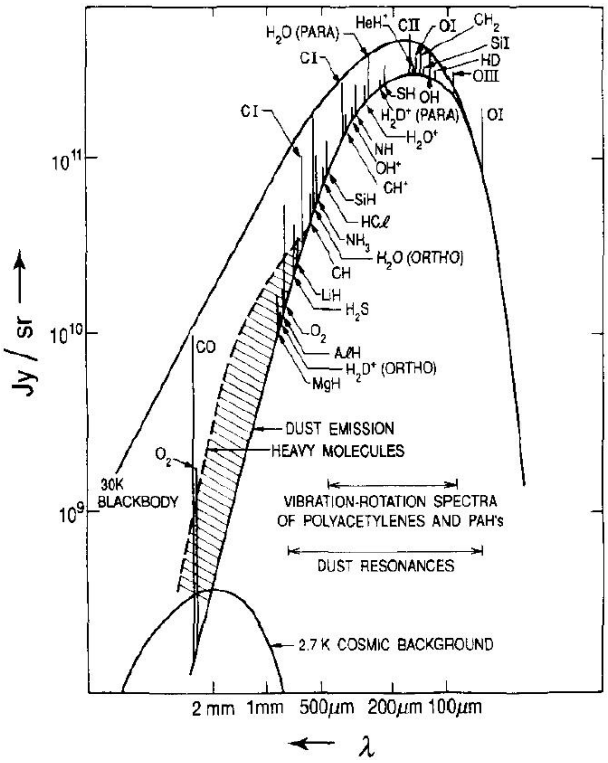

Figure 1.2: Intensity of the spectral content in the submillimeter band for an interstellar cloud. Black and bold curve shows 30 K blackbody radiation (adopted form [9]).

THz spectroscopy was also extensively applied in the fields of astronomy, in order to resolve the radiation lines received from the space [9]. Figure 1.2 shows the radiated power

versus wavelength from an interstellar cloud (dusts, heavy molecules, etc). In this figure, 30 K blackbody radiation curve and the 2.7-K cosmic background signature curve are plotted together. It is believed that interstellar dust clouds emit approximately $40,000$ individual spectral lines, only a few thousand of which have been resolved. An estimation based on the results gathered by satellites indicates that approximately one-half of the total luminosity of the galaxy and 98% of the photons emitted from the Big Bang fall into the submillimeter, THz and far-IR ranges. Much of this energy is being radiated by cool interstellar dust [3].

THz spectroscopy is also used in environmental monitoring, such as detection of various gases in the atmosphere by measuring their thermal emission [2]. Information about the ozone chemistry helps us to better understand global warming, quantify effects of how the atmospheric composition affects the climate and study the aspects of pollution in the upper troposphere. For instance, the earth observing system microwave limb sounder (EOS-MLS), onboard NASA's Aura satellite, was launched in July 2004. It has been monitoring chemical species in atmosphere (OH, HO_2, H_2O, O_3, HCl, ClO, $HOCl$, BrO, HNO_3, N_2O, CO, HCN, CH_3CN, and volcanic SO_2), cloud and ice. The thermal spectrometer measures the emission at 118, 190, 240, and 640 GHz, and 2.5 THz frequencies [2]. A summary of past, current and future space projects, along with the embedded instrument descriptions, are listed in [10]. Terahertz spectroscopy can also be used in plasma fusion diagnostics to measure the profile of plasma, as discussed in [11].

Another important application of THz wave after spectroscopy is THz imaging, which is also called the T-Ray imaging. THz imaging has gained a lot of attentions, after its first demonstration by Hu et al. in 1995 [14]. It simply used the transmission imaging technique on the materials that are opaque in visible and IR range, but are transparent in the THz region. Such technique would be diffraction limited and hence the imaging resolution confines to the wavelength. THz imaging has been demonstrated and widely used in many

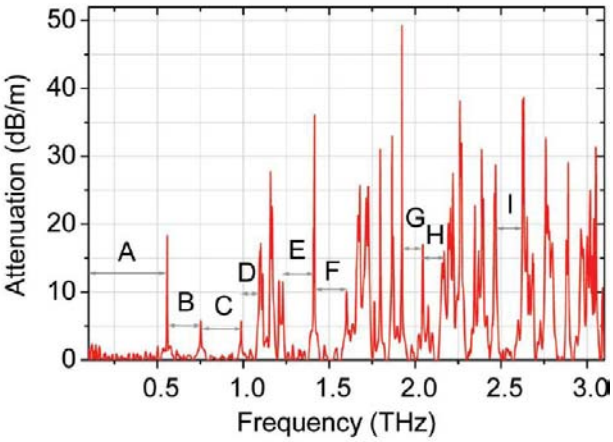

(a)

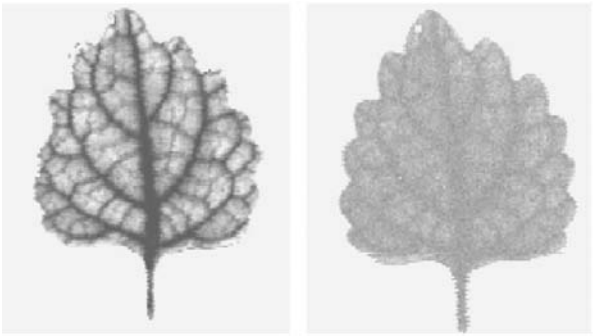

(b)

Figure 1.3: (a) Atmospheric attenuation of THz waves in the range of 0.1-3 THz and nine major THz transmission bands, at 23^oC and the relative humidity of 26%. (Adopted from [12]); and (b) THz images of a living leaf. Left picture is when the leaf was starved of water for several days and right image is for several tens of minutes after watering. The water distribution in the right image is much more uniform, indicating a dynamic uptake of water. (Adopted from [13])

areas including non-invasive medical imaging of teeth or sub-dermal melanoma; diagnosis of cancer; detection of concealed weapons and currency forgeries at airports; monitoring water level in plants (Figure 1.3-b); inspection of fat content in packaged meat, manufacturing

defects in automotive dashboards, high voltage cables, semiconductor chips and silicon solar cells [15, 16, 17, 10, 13, 2]. The three dimensional image reconstruction of the THz image has been also demonstrated [17, 18].

There are two major types of THz source used for typical diffraction limited THz imaging systems: an ultra-short THz pulse [12, 13], and THz semiconductor lasers [17, 16, 19, 20]. In the former approach, the THz pulse is generated using femtosecond optical pulse incident on a non-linear crystal. The imaging was performed by inspecting the transmitted or reflected pulse, coherent with the incident pulse, by either scanning the object in free space or using a charge coupled device (CCD) camera. Time domain spectroscopy techniques are used to detect the THz pulse. One of the major obstacles in THz free space imaging is the atmospheric attenuation, which is dominated by water vapor absorption in THz band. Figure 1.3-a shows the atmospheric attenuation in the range of 0.1-3 THz [12]. Nine different transmission windows throughout this range are indicated. Figure 1.3-b shows an example of THz transmission on a leaf, when it is fresh (left hand side)and after it is dried (right hand side). The absorption of the THz light due to water contents is clearly observed.

THz imaging is mostly dominated by the use of pulsed time domain systems. Yet, there are many potential applications for imaging with high-power CW source. The high cost of the femtosecond lasers required in the pulsed time domain systems is another motivation in using alternatives THz sources. Semiconductor THz lasers are demonstrated with CW wave and high output power (in range of few hundred milliwatts) [21]. The use of CW sources is advantageous when narrowband imaging is desired, since the short pulsed systems typically have frequencies ranged approximately from 0.5 to 2.5 THz or higher. There are recently many THz imaging works demonstrated using semiconductor lasers. In all of these cases a powerful and compact THz semiconductor laser is of great advantage.

Efforts on the application of THz QCLs have resulted in demonstration of THz commu-

nication. Theoretically, fast response time nature of intersubband based lasing transitions allows for fast modulation of QCLs [22]. Recently, Barbieri et al. demonstrated directly modulating bias voltage of a THz QCL up to 12.3 GHz, and used it to modulate the THz light [23]. In a separate work, a full communication link system using THz QCL and fast THz quantum well photodetector is demonstrated, by Grant et al [24]. In this work, an audio signal is AM modulated, carried over the THz light and transmitted over two meters in free space. The fast detector picks up the signal and demodulates it. Danylov et al. have also presented the frequency locking of single mode THz QCL, to be used in short range transmitters [25]. In reference [2] Tonouchi as proposed a roadmap for different THz applications. Federici et al. have extensively reviewed the THz and sub-THz wireless communication systems in [26].

1.2 THz Sources

The simplest THz source for a long time had been thermal black body radiation, which generates very low power, broadband, and incoherent signal. The quest for generating THz signal were started by trying to extend the microwave techniques to higher frequencies and in a parallel effort extending IR photonic techniques to longer wavelengths. Microwave techniques use semiconductor electronic devices that utilize freely moving electrons (such as transistors, Gunn oscillators, Schottky diode frequency multiplier, and photomixers) are limited by the transit time and parasitic RC time constant of the electronics. The power level of these devices decreases as $(1/\nu)^4$ with frequency. Above 1 THz, microwave based sources result in microwatt level power. On the other hand, traditional photonic devices (such as semiconductor laser diodes) generate radiation through radiative recombination of electron-hole pairs. The emission frequency of these devices is determined by the energy band gap of the semiconductor used to fabricate the laser diode. For THz emission, the band gap has to be smaller than 40 meV (corresponding to 10 THz); but narrow band

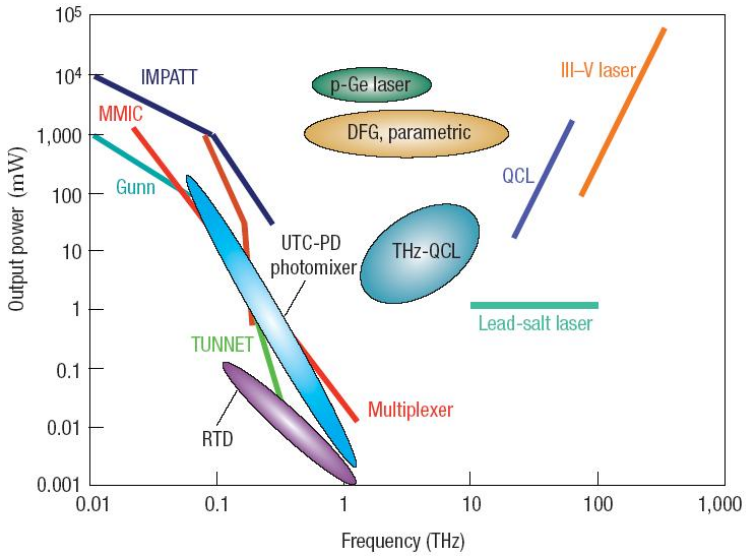

Figure 1.4: THz power versus frequency for various sources. (adopted form [3]).

gap materials are not commonly available. For example, narrow gap lead salt materials typically have a band gap greater than 50 meV [27]. In addition, it is very challenging to obtain population inversion in these narrow gap materials. This is because the lasing energy is comparable with the phonon resonant energy, which can depopulate the excited states at higher temperatures very fast.

An ideal coherent THz source would be a narrow-band, CW and high power laser working at room temperature with tunability in emission wavelength. No such source have yet been demonstrated, but many approaches have resulted in the THz source devices that fulfill some of above requirements. Figure 1.4 shows power and frequency ranges for various THz sources extending from both electronic and photonic techniques towards the THz range (IMPATT stands for impact ionization avalanche transit time diode, MMIC stands for microwave monolithic integrated circuits, RTD stands for resonant tunnel diode, and DFG stands for difference frequency generator) [2].

1.2.1 Microwave up-conversion

THz signal can be obtained by up-conversion of microwave signal using Schottky doublers and tipplers [3]. A CW THz signal can be generated using this technique, the power of which is decreasing rapidly with frequency to microwatts range for > 1.6 THz.

1.2.2 Photo-mixing

Down-converting the light from optical and IR sources using photo-mixing is another approach to generate THz radiation. It works when a fast photoconductive or nonlinear material (e.g. superconductor [28]) is illuminated with two optical lasers which are detuned by desired THz frequency. A room temperature, CW, and narrow band but low power ($< 10\mu W$) THz signal is achieved using this technique [29, 30]. Nonlinear optical materials such as $LiNbO_3$, KTP, $GaSe$, and $ZnHeP_2$ have been used in difference frequency generation (DFG) to generate pulsed THz radiation. GaSe has showed the best efficiency so far - generating $5ns$ pulse THz radiation tunable from 0.18 to 5.27 THz, with a peak power of $70W$ ($2.5\mu W$ average power) [31]. Dupont et al. used an asymmetric $GaAs/AlGaAs$ based quantum wells instead of the optical material and observed the THz generation using DFG [32]. Recently Belkin et al. have used DFG by stacking two IR QCL lasers ($\lambda = 7.6$ and 8.7 μm) on top of each other to generate THz emission at $\lambda = 60$ μm, with a small output power of 60 nW [33]. This device operates up to 150 K.

Another approach to generate THz field from photonic sources is to use optical parametric generation [34, 35, 36]. In this approach, coherent THz wave is generated from efficient parametric scattering of a laser light ($Nd:YAG$ laser for instance) by the interaction with non-linear and Raman active crystals, like $LiNbO_3$, $LiTaO_3$ and GaP. The THz light is generated parametrically based on the phase matching condition between the pump, the idler and the THz light. Therefore, the THz wavelength can be widely tuned

(λ between 140 and 310 μm) by changing the incident angle of the pump [35]. The THz light is coupled out of the crystal using prism, grating, or monolithic photonic crystal.

1.2.3 Gas lasers

The most common method to produce coherent radiation in the far-IR/THz region is by using optically pumped gas laser. In such gas molecular lasers, vibrational transition of the molecules with a permanent electric dipole are optically excited by a pump CO_2 laser to achieve population inversion between different vibrational energy levels. By this way, tens of milliwatt CW power at wavelengths from 35 μm to 2.9 mm can be generated [37]. However, the efficiency of such systems are very low ($\sim 10^{-4}$).

1.2.4 Semiconductor lasers

Semiconductor lasers for THz emission were introduced in 1987, when hot hole intersubband $p-Ge$ and $BiSb$ lasers were realized [38]. There are three important types of $p-Ge$ coherent sources. First type of $p-Ge$ device is based on hole population inversion between the light-hole and heavy-hole bands, due to a streaming motion that takes place in crossed electric and magnetic fields. The second one is a light-hole cyclotron resonance laser in crossed electric and magnetic fields, and the third one is a negative mass heavy-hole cyclotron resonance maser in parallel electric and magnetic fields [38]. Several watts of peak power have been obtained in broadband lasing (linewidths of $10-20\ cm^{-1}$) that can be tuned from 1 to 4 THz. Because of low efficiency and high power consumption, the device can work only at low duty cycles up to 5% [39].

A new type of $p-Ge$ lasers are strained $p-Ge$ resonant state laser that uses uniaxial compressive pressure to move light-hole and heavy-hole bands into resonance [40]. The population inversion takes place between these two energy states even without the presence

of a magnetic field. Tunable (2.5 to 10 THz with different pressures) and CW laser with output powers up to tens of microwatts have been achieved using this technique. A similar laser was demonstrated in 2000, where the pressure of the lattice mismatch between $SiGe$ and Si was used instead of external pressure to align the hole bands [41].

The most recent development has been the extension of QCL operation from the mid IR to the THz region. THz QCL was first demonstrated by Kohler et al. in 2002 [5]. The THz QCL device emitted at 4.4 THz in frequency, which is well below the semiconductor Reststrahlen band (8-9 THz). Since then a few groups have been pursuing design of THz QCLs and two new designs for active region were also proposed [42, 43]. This thesis focuses on improving the current performance of THz QCLs, which is very important at the time being, in order to implement exciting THz applications. Many breakthroughs are expected in this field.

1.3 Quantum cascade lasers

In traditional bipolar semiconductor lasers, the lasing emission occurs when a photon stimulates the electron relaxation from a conduction band into a valance band (interband transition) [44]. The wavelength is primarily determined by the semiconductor material band gap. Mid and far IR lasers, therefore, can hardly be designed based on interband transition of electrons, because very small band gap semiconductors ($< 0.1\ eV$) would be required for the corresponding very long wavelength ($10 - 300\mu m$) emission. Optical amplification using radiative transition of electrons between energy levels/subbands in the conduction band was proposed by Kazaronov and Suris in 1971 [45], which provided an alternative approach to tackle realization of long wavelength laser challenge. Quantized states in the conduction band can be created by using properly designed heterostructure quantum wells. Usually heterostructure quantum wells consist of thin stack of semicon-

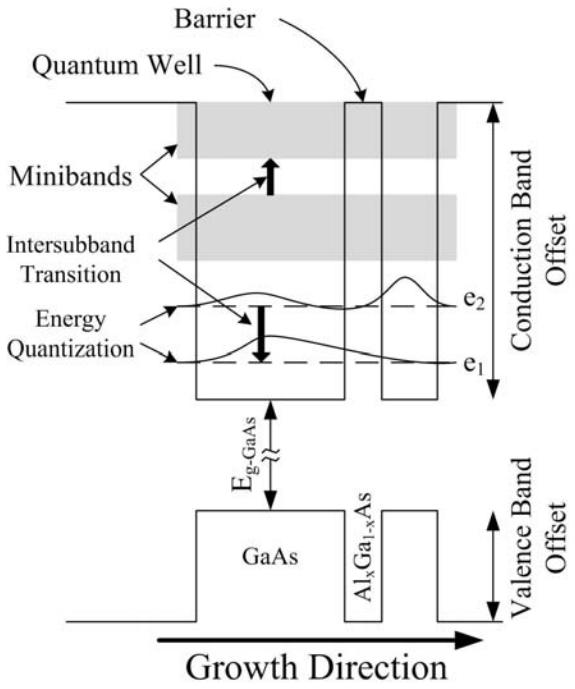

Figure 1.5: Schematic diagram of energy band profile for an arbitrary $GaAs/Al_xGa_{1-x}As$ system, showing the energy minibands, subbands and intersubband transitions.

ductor layers (nanometers in thickness) with different compositions grown on top of each other. The conduction band edge discontinuity between different materials hence results in quantum confinement of carriers in growth direction. The energy levels in the conduction band break into "subbands", Figure 1.5. In such a structure the energy of carriers is only quantized in the growth direction and follows parabolic free carrier dispersion relation along the in-plane directions (normal to the crystal growth direction), as shown in Figure 1.6-b [22]. Intersubband transition of electrons can be used for generating low energy photons ($< 0.1eV$), since the energy levels in the quantum structures can be precisely tuned by tailoring the thickness of quantum wells and barrier layers. Helm et al. were the first to observe intersubband emission in a semiconductor superlattice pumped by thermal excitation [46] and then by resonant tunneling [47]. In fact, the first intersubband emission was

observed in the THz frequency range (2.2 THz). Later on it was experimentally proven that it is much easier to operate intersubband lasers in the mid-IR region, where the radiative energy is more than the optical phonon energy [48]. In the mid-IR QCL devices, the relatively larger subband energy separations and much less free carrier absorption in the laser waveguide make it less challenging to establish carrier population inversion, which is necessary for the lasing operation [48].

A detailed history of Far IR intersubband laser proposals was reviewed by Smet [50]. The basic superlattice structure, proposed by Kazarinov [45], shows high field domains and hence is not suitable for laser design. The first quantum cascade laser was developed at Bell Labs (Capasso group) in 1994 [49], using $InGaAs/AlInAs/InP$ material system. It operated at a wavelength of 4.2 μm, only in pulsed mode at cryogenic temperatures with a high threshold current density ($\sim 14\ kA/cm^2$). Figure 1.6-b shows the conduction band energy profile and intersubband states for this QCL device, where a radiative transition is spatially diagonal. Depopulation of lower radiative state is achieved by setting the subband separation between levels 2 and 1 slightly less than the longitudinal-optical (LO)-phonon resonance energy of $InGaAs$ (34 meV). Electron-phonon scattering is a very fast process and hence efficiently depletes the electrons from level 2 to 1. Electrons of level 3 also relax into level '1' through the LO-phonon scattering mechanism, but large required in-plane momentum exchange significantly slows down this process (Figure 1.6-b). The digitally graded alloy (Figure 1.6-a) is essentially a doped quasi-classical multi-well superlattice region, which collects electrons from the lower states 2 and 1 and injects them into the excited upper radiative state in the next stage. Since the lasing mechanism in QCLs is a unipolar process, it has the ability to cascade N modules together. A single injected electron, hence, can emit many photons (ideally N photons) when flowing through the whole cascade structure. This could lead to greater-than-unity differential quantum efficiency, and is one of the biggest advantages of QCLs.

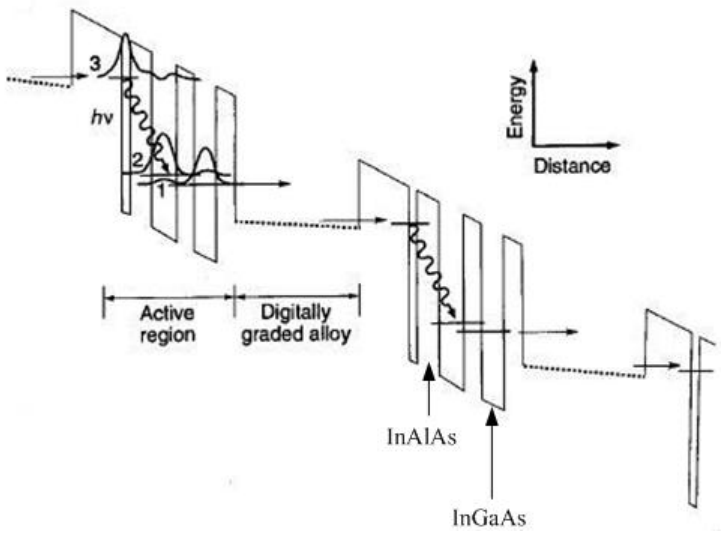

(a)

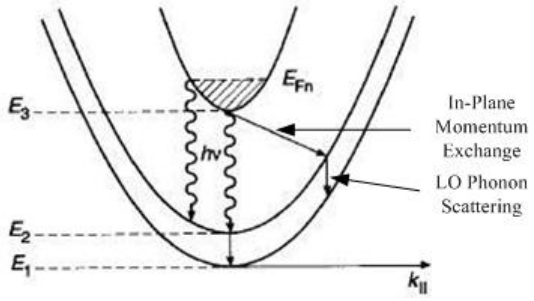

(b)

Figure 1.6: (a) Conduction band profile of first QCL, including subband energy state and electron distribution in each of them. (b) In-plane momentum space ($k_{\|}$) diagram of subbands and allowed relaxation paths via LO-phonon and photon emission (adopted form [49]).

QCLs have gained lots of attentions and the performance has improved dramatically, since its first appearance. They have become the dominant laser sources in the mid-IR spectral range. Lasing has been obtained at wavelengths between 2.6 and 24 μm in the mid-IR [51, 52, 53], and has recently been extended to far-IR and THz wavelengths

$(60 - 250\ \mu m)$. The wavelength gap in between corresponds to the Reststrahlen band. The room temperature and CW performance of mid-IR QCL lasers have been demonstrated. High output power with watt-level peak powers have also been achieved [54]. A tunable wavelength ($4.5 - 16.5\ \mu m$ with $0.2 - 1.0\ nm/K$ temperature tunability) and single-mode (30 dB of side-mode suppression) QCL has been reported [55]. Recently an efficient 5 μm mid IR QCL was reported with wall plug efficiency beyond 50% [56].

As mentioned above, the active region design of QCLs relies on band offsets between quantum wells and barriers. A typical design uses two different materials that have different band gaps and electron affinities. Many QCLs have been grown in the $InGaAs/AlInAs/InP$ material system, although QCL devices using other material systems such as $GaAs/Al_xGa_{1-x}As$ have been also demonstrated [57]. $InGaAs/AlInAs$ based mid-IR QCLs show higher performance, due to their higher conduction band offsets.

QCLs with valence band intersubband transition have also been demonstrated based on $SiGe/Si$ quantum wells [58]. Materials with larger band offsets, such as $AlGaN/GaN$, are suitable for achieving shorter wavelength (telecom wavelengths) QCLs [59]. On the far IR part of the spectrum, QCLs have extended their range into THz region. The lasing wavelength of up to 250 μm has been already achieved [60]. Maximum lasing temperature of 186 K in pulse mode [61] and 117 K in CW mode [62] has been demonstrated, separately. A detailed history of THz QCLs is discussed in the next section.

1.4 THz QCLs

THz QCL was first demonstrated in 2002, from the work of Kohler et al. at the Scuola Normale Superiore in Pisa, where a chirped superlattice (CSL) structure was employed (Figure 1.7-a) to obtain population inversion [5]. This structure was based on coupling of several quantum wells in a superlattice to create minibands at the design electric field.

In this structure, the radiative transition takes place when an electron relaxes from the bottom of the upper miniband to the top of the lower miniband. This is very similar to traditional band-to-band transition, where the radiative transition is only from states $2 \rightarrow 1$. The scattering process within the minibands (intra-miniband scattering) is dominated over inter-miniband scattering. Therefore, electrons tend to relax to the bottom of each miniband, leaving the upper part of lower miniband empty and filling lower part of upper miniband. Moreover, very narrow width of each miniband makes it difficult for LO-phonon generation and helps keeping the population inversion high. The oscillator strength, which is a measure of the lasing states coupling, for this design is typically very high, $f_{if} \sim 2-3$. Higher oscillator strength results in higher optical gain.

Despite of lower rate of LO-phonon generation in CSL design, electron-electron scattering at upper miniband reduces the population inversion. The next generation of THz QCLs used relaxation of electrons from bound upper defect state to lower miniband. This design is called bound-to-continuum (BTC), Figure 1.7-b, and reported shortly after first THz QCL demonstration in 2002 by the university of Neuchâtel / Cambridge collaboration [63]. The oscillator strength in BTC is slightly less than SCL, due to low overlap of the bound state to miniband states. The typical oscillator strength for BTC design is around $f_{if} \sim 1.5-2$. On the other hand due to strong coupling of the injector states with the bound state, the injection process becomes more selective. Hence this structure has higher operating temperature, higher output power, and lower threshold current density. The output powers up to 100 mW, and the maximum operating temperature up to 110 K at pulse mode and 80 K at CW has been reported [1]. Also lasing frequencies as low as 1.2 THz have been reported using this type of active region structure [60].

Other major type of active region design is using resonant phonon (RP)-based scheme for depopulation of the lower lasing state, Figure 1.7-c. This design was first reported by Williams et al. in 2003 by MIT / Sandia collaboration [43]. It is very similar to

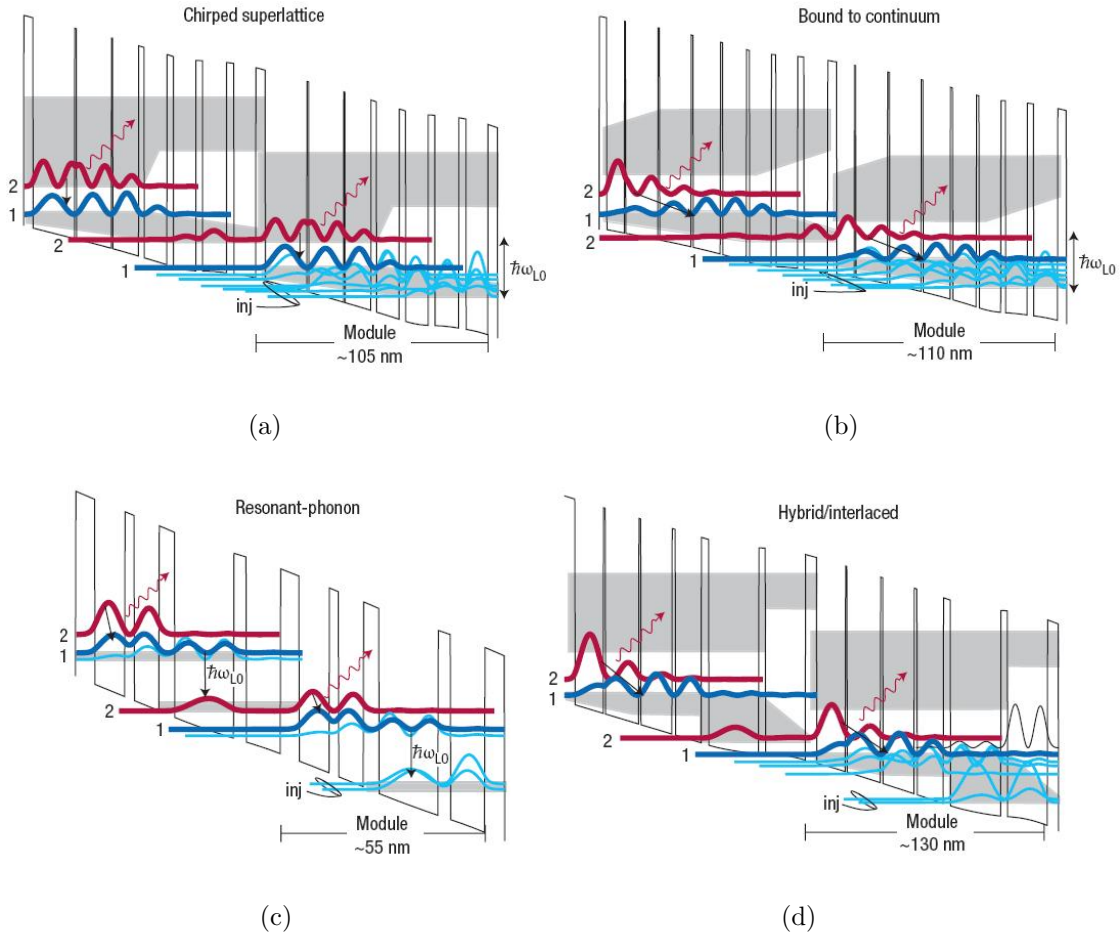

Figure 1.7: Conduction band profile and subband energy states for major THz QCL designs, (a) Chirped super-lattice, (b) Bound-to-continuum, (c) Resonant-phonon, and (d) Hybrid structure (adopted from [1]).

mid IR QCLs, as the collector and injector states are below the lower radiative states by $E_{LO} = 36\ meV$. This makes the depopulation of the lower radiative states through emission of LO-phonon, which is very fast (sub-picoseconds) and efficient. In this design the lower radiative state is in resonance with the excited state in the adjacent quantum well that makes it spreading over few quantum wells and emit LO-phonons in the phonon well. Using this technique the upper radiative state remains localized, due to small overlap

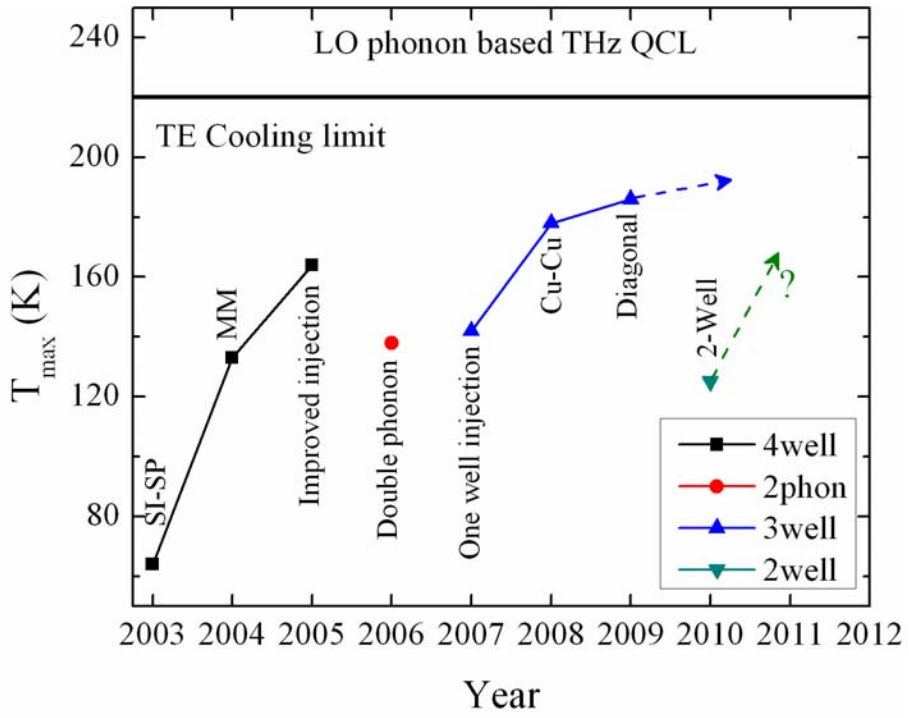

Figure 1.8: State of the art maximum operating temperature of various RP based THz QCLs.

with the injector states. The oscillator strength for this design is smaller than previous designs ($f_{if} \sim 0.5 - 1$), because of absence of minibands. However, the length of an RP module is typically half of the BTC module, and hence results in higher density of gain producing transitions [22]. This design has showed the best temperature and power performance among other THz QCL designs. Peak output powers up to 250 mW, average output power of 145 mW (both at 10 K)and maximum operating temperature up to 186 K at pulse mode and 117 K at CW has been reported using four-well RP design [1], [61], [62] and [21].

Figure 1.7-d shows active module of a hybrid (interlaced) structure, where phonon-assisted depopulation is combined with the BTC optical transition, in an effort to achieve longer wavelength [1]. The alternation of RP structure using two consecutive phonon

transitions was also reported [64], but no significant improvement was observed. Two depopulation schemes were considered in this work; firstly the two back to back phonon emission and secondly, the two spatially separated phonon remissions using a superlattice. None of the above designs improved the maximum operating temperature of the device, indicating that the thermal backfilling was not an issue. Figure 1.8 summarizes the progress of RP based design state of the arts for maximum operating temperature.

Luo et al. proposed a new structure based on RP scheme that had only three quantum wells in each module [65]. The three-well structure combined the phonon and injector wells of original four well RP design. This structure is designed to have the oscillator strength in the same range as the original RP scheme design. Three well THz QCL inherits high power and temperature performance of the RP design, but has slightly higher threshold current density. The high current of three-well design is due to inefficient injection of the carriers into upper lasing state and extraction state [66, 67]. The device lased up to 142 K in pulse mode, and no CW operation of this design have been reported so far. Belkin et al. demonstrated higher working temperature of 178 K using a similar three-well design with lower sheet doping density of (3×10^{10} cm^{-2}) and lower loss metal-metal waveguide using copper bonding [68]. Recently, Kumar et al. made the lasing transition of this design more diagonal to reduce the undesirable leakage channels and obtained the highest so far maximum operating temperature of 186 K [61].

A simple two well RP based designs have been also demonstrated, in two parallel and separate works [69, 70]. In these designs, the double lasing well is replaced by a single well and the radiative transition occurs between the only state in the lasing state (upper lasing state) and the upper state of the phonon well (lower lasing state). The depopulation of the carriers then is mediated through a fast phonon emission, from the lower lasing state to the ground state of the phonon well. As indicated in Figure 1.8, the maximum operating temperature of ~ 125 K have been observed for both designs. It is believed that the two

well designs are the simplest possible lasing scheme, which is cascade of a laser transition and a resonant tunneling [71].

Hypothetically, it was believed that achieving population inversion for intersubband transition energies less than thermal energy (κT) is not feasible. This sets the temperature limit of $\sim 150K$ ($13meV$) for 3 THz QCL. However, new active region designs have demonstrated lasing far above this limit [72]. There are many other questions about THz QCL's fundamental limits that are yet to be answered. Room temperature operation, CW operation, high power output, confined beam shape, direct frequency modulation, wavelength tunability are among the most important problems that are to be investigated. This thesis discusses these limits and propose solutions to make existing THz QCLs operate at higher temperatures with high power. Such properties are necessary to introduce the THz QCLs into the application world.

This thesis focuses on the modeling, design, fabrication and characterization of three well RP-based THz QCLs. Comprehensive discussion about improving performance of these devices will be followed. The next section overviews the materials presented and discussed in this thesis.

1.5 Thesis organization

The focus of this thesis is mainly on understanding of the intersubband charge transport and gain inside the active region of THz QCL, as well as their thermal and electromagnetic properties, in order to engineer it towards high performance operation. The thesis, therefore, consists of discussions on three main subjects: intersubband charge transport and gain modeling for designing active regions with high gains at high temperatures; thermal modeling of the device for better understanding of the heat dissipation; and electromagnetic modeling of the laser cavity for designing a lower loss waveguide and more controllable

beam pattern. These subjects are organized in this thesis as follows.

Chapter 2 introduces a theoretical framework to study the intersubband charge transport and optical gain in three-well RP based THz QCLs. This chapter starts from the basics of quantum mechanics and calculates the subband energy levels in the conduction band of the $GaAs/Al_{0.15}Ga_{0.85}As$-based active region. The tight binding approximation is used to estimate the coupling and energy detuning between the energy states involved in resonant tunneling process. The fundamental equation of motion in quantum electrodynamics is then employed, using density matrix formalism, to calculate the population of all energy states and the coherence between them. The numerical application of this model to three-well RP-based THz QCL reveals the importance of various leakage channels within the active region, including the extraction tunneling leakage. This chapter further introduces the Rabi oscillation of the laser field into the interaction Hamiltonian and uses rotating wave approximation to estimate the optical intersubband gain for three-well RP-based THz QCLs. The analytical form of the gain shows that the gain consists of a modified Lorentzian term, which is proportional to the population inversion, and two stimulated Raman like gain terms, which are proportional to the injection and extraction sides' coherence. The modified Lorentzian term dominates the gain mechanism, particularly at lower temperatures. The gain of THz QCL under study shows double peaks when either injection or extraction side tunneling coupling is strong. The Raman like shows a dispersive like gain and hence provides inversionless gain.

Chapter 3 focuses on the two commonly used waveguide structures for the THz QCLs: metal-metal (MM) and semi-insulating surface plasmon (SI-SP) waveguide structures. The details of the device fabrication, as well as the waveguide design is presented for each of the above structures. The discussion in this chapter is supported by the experimental results. Later in this chapter, the active region temperature measurement is presented and a model is proposed to explain the measurement results. The developed model is used to

design a structure with more efficient heat removal and hence results in continuous wave operation of the lasers. The second part of this chapter is focused on the SI-SP based devices, where the electromagnetic mode is loosely confined inside the active region and higher power is emitting from the laser facet. The temporal dynamics of such a high power beam is measured using a fast quantum well photodetector. The light dynamics measurement results are used to understand the dynamics of the gain and temperature, inside the active region. Later this chapter presents the design and fabrication of a THz QCL that electrically switches the lateral waveguide modes. The lateral mode switching of the laser results in the change in the emission direction. Finally this chapter presents THz transmission imaging results, as a proof of concept for concealed metallic objects.

Chapter 4 of this thesis starts with the application of gain temperature dependence on the real measured data. Through this exercise three fundamental parameters of the device (electron's heating temperature, and two pure dephasing time constants) can be fitted [66]. The fitted values are used along with the model presented in chapter 2 to design various three-well RP-based active regions. A systematic study over the effect of oscillator strength on maximum operating temperature is performed. It is shown theoretically and experimentally that the highest temperature performance is achieved for oscillator strengths of ~ 0.4. Experimentally maximum operating temperature of 176 K is achieved. The details of the design and experimental results are presented in chapter 4. Finally the conclusion of the Chapter 2 leads us to a new lasing scheme that improves the weaknesses of the RP based THz QCL designs. The new structure consists of phonon-photon-phonon emission. It can ideally provide near 100% population inversion and emit an unmodified Lorentzian gain shape, with high peak values. The carrier transport and the optical gain of the proposed structure is discussed by employing the density matrix model. Based on the model, a figure of merit is defined to design such structures. A promising design is proposed for proof of concept.

Chapter 2

Intersubband transitions and gain model in multiple quantum wells

This chapter is divided into two section. The first section mainly focuses on the theoretical fundamentals behind the physics of electronic intersubband transitions in the conduction band of multiple quantum well (MQW) semiconductor heterostructures. The second part of this chapter uses the results from the first section and applies them to a simplified density matrix model to calculate the intersubband charge transport and the optical gain in three well based RP THz QCLs. Williams proposed an emperical limit for the maximum operating temperature (T_{max}) of THz QCLs, where obtaining the optical gain at oscillating frequency ω is only possible when $\hbar\omega \geq \kappa T_{max}$ [1]. Despite the uncertainty in measuring the T_{max}, the William's limit has already been surpassed in several designs [1, 61, 72]. The analysis in this chapter reveals the fundamental limits for achieving THz QCLs that operates close to room temperatures with a reasonable power. Knowing these limits, chapter 4 introduces several intersubband schemes, for achieving optical gain close to room temperature.

This chapter first quickly reviews some properties of the 1D Schrödinger equation solu-

tions, particularly for one dimensional single quantum wells and MQWs. The tight binding formalism is used to calculate the detunings and couplings between coupled quantum wells. This section considers idealized quantum wells, which means that the electron mass (m^*) is position and temperature independent. In another word it is assumed that the band non-parabolicity is neglected. This is a valid assumption when considering the THz QCLs that have electrons occupying small energy range above the conduction band edge. However for calculating the scattering rates of the carriers, the non-parabolicity of the band will be considered. This is because when calculating the scattering rates, the *form factor* is extended up to high kinetic energy part of the band and hence it is required to integrate it over much bigger energy range [73].

After calculating the subband energy levels and respective wavefunctions, the time dependant perturbation theory is employed to calculate the carrier interaction with the system elements. It starts from quantum theory of light (quantization of electromagnetic energy), where it defines the time-dependent perturbation Hamiltonian (H'). The *Fermi's golden rule* is then used to calculate optical absorption and gain coefficient for intersubband transitions. Later the electron-phonon scattering rates will be calculated.

The second part of this chapter takes the stationary energy states and wavefunctions from the calculations in the first part and extends it to the density matrix model developed by Kazarinov and Suris [45, 74]. The model calculates the subband population and the transit time of the carriers. By further extending the model and including the laser induced coherence, the absorption / gain shape of the THz light will also be calculated [66].

This thesis mainly focuses on the modeling and the design of RP THz QCLs, with an emphasis on three-well design presented in [65]. This design uses $GaAs/Al_{0.15}Ga_{0.85}As$ material system for realization of MQW heterostructure. This THz QCL design is used as an example in the above density matrix model for understanding the basics of the lasing operation and investigating effect of various parameters of the structure on the lasing

performance.

2.1 Time independent perturbation theory

This section provides a quick review on the time independent perturbation theory to calculate the Energy states and wavefunctions in a MQW. Assume a single quantum well with barrier height of V_b and well width of L, as in Figure 2.1-a. The solution of Schrödinger equation for such a system can be analytically found as in [75]. When a small electric field ($\vec{F}$) is applied, the potential energy of the system is slightly tilted. The total Hamiltonian is such case can be written as,

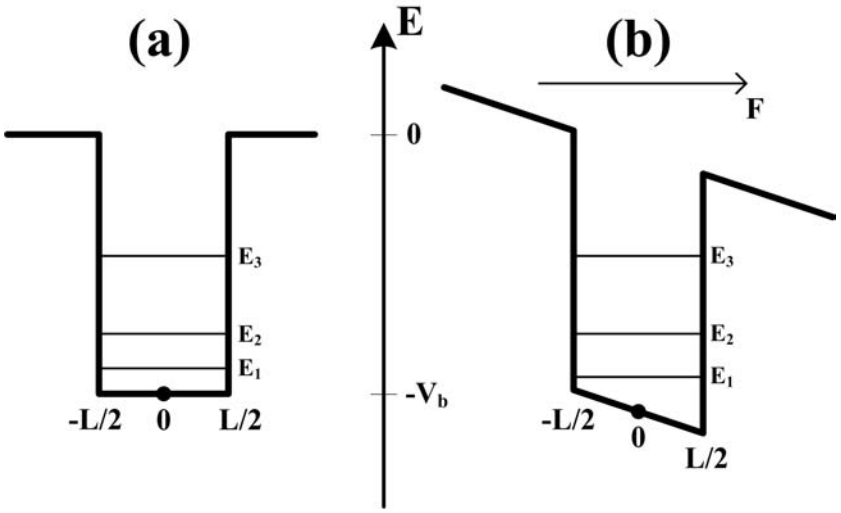

Figure 2.1: Potential energy profile for a finite square quantum well (a) unperturbed and (b) perturbed with a small electric field ($\vec{F}$).

$$H = H^{(0)} + H', \tag{2.1}$$

where, $H^{(0)}$ is unperturbed and H' is perturbation Hamiltonian value, and is simply defined

as,

$$H^{(0)} = -\frac{\hbar^2}{2m^*}\frac{d^2}{dz^2} + \begin{cases} 0 & |z| > \frac{L}{2} \\ -V_b & |z| < \frac{L}{2} \end{cases} \tag{2.2a}$$

$$H' = eFz \tag{2.2b}$$

where V_b is the potential energy and $\vec{F}$ is the applied electric field vector, as shown in Figure 2.1-b. The solution for an arbitrary perturbed Hamiltonian, like in Equation 2.1, can be numerically obtain using transfer matrix method [44]. This method assumes a piecewise constant potential and applies the boundary condition between adjacent solutions using a 2×2 matrix. The final solution is multiplication of all the matrices. The numerical solution for an arbitrary potential can also be extended for MQW structures. However it is more insightful if the solution of MQW can analytically be obtained from the existing solutions of single well. For this purpose, the *tight binding* formalism is quickly reviewed. This approach will be used in the second part of this chapter to calculate the coupling parameters between neighboring wells.

2.1.1 Tight binding model

Let's consider two un-coupled one dimensional quantum wells in Figure 2.2-a, the Hamiltonian of which are similar to Equation 2.2. It is assumed that each well is deep enough to have at least one bound state (E_l and E_r). If these two wells couple through a barrier (Figure 2.2-b), the wavefunction of the double wave state becomes a linear combination of wavefunctions before coupling as

$$\psi = \alpha\psi_l + \beta\psi_r. \tag{2.3}$$

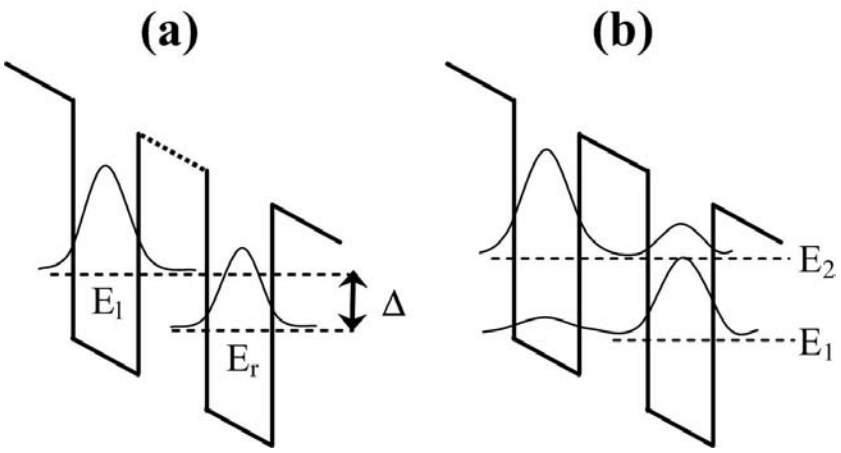

Figure 2.2: Potential energy profile for a double quantum well under a small electric field (a) before and (b) after coupling.

The α and β coefficients are obtained from

$$\begin{pmatrix} E_l - E + s_{ll} & (E_r - E)r + t_{lr} \\ (E_l - E)r + t_{rl} & E_r - E + s_{rr} \end{pmatrix} \times \begin{pmatrix} \alpha \\ \beta \end{pmatrix} = \begin{pmatrix} 0 \\ 0 \end{pmatrix}, \tag{2.4}$$

where $r,\ s$ and t are, respectively, called overlap, shift and transfer integral and are defined as [75]

$$\begin{cases} s_{ll} = \langle \psi_l | V_r | \psi_l \rangle,\ \langle \psi_r | V_l | \psi_r \rangle \\ t_{lr} = \langle \psi_l | V_l | \psi_r \rangle,\ \langle \psi_r | V_r | \psi_l \rangle \\ r = \langle \psi_l \psi_r \rangle \end{cases} . \tag{2.5}$$

The energy level of each coupled states are calculated by solving the determinant of the big matrix in Equation 2.4 equals zero. The Hamiltonian of the system in Figure 2.2-b can be approximated by a symmetric matrix as

$$H = \begin{pmatrix} E_l & \hbar\Omega \\ \hbar\Omega & E_r - \Delta \end{pmatrix}, \tag{2.6}$$

where Δ and Ω are, respectively, called *detuning* and *coupling* between the states of E_1 and E_2, and are defined as

$$\begin{cases} \Delta = (E_l + s_{ll}) - (E_r + s_{rr}) \\ \Omega = \frac{1}{2}\sqrt{(E_1 - E_2)^2 - \Delta^2} \end{cases} . \tag{2.7}$$

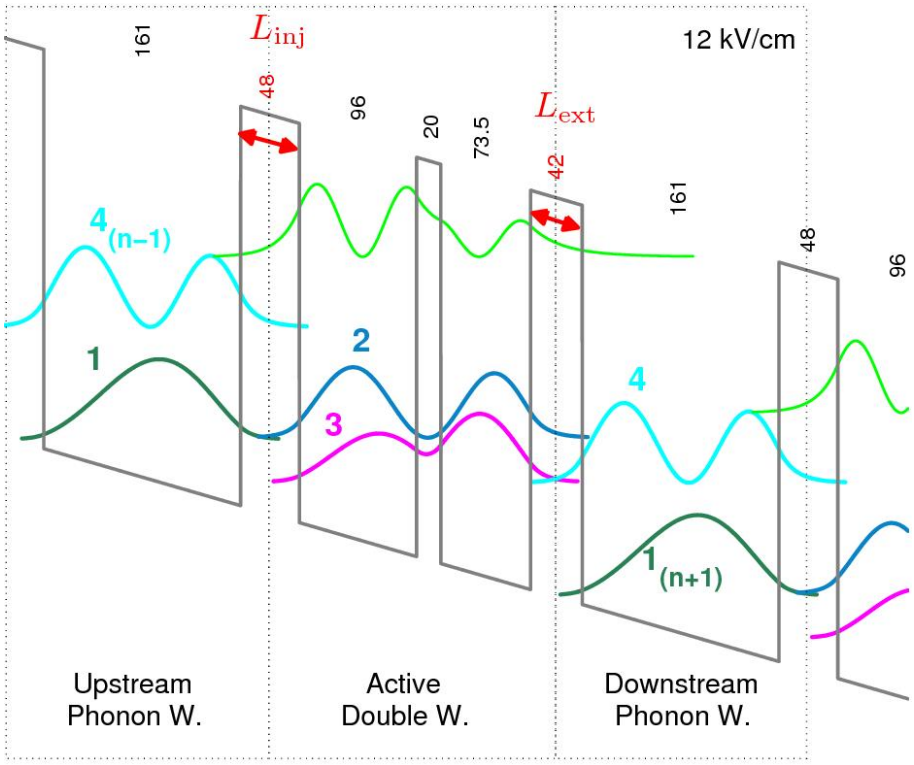

Figure 2.3: Conduction band diagram of the three-well QCL structure under study at 12 kV/cm and the square modulus of the wavefunctions of the active double-well and the upstream/downstream phonon wells when taken isolated from the adjacent quantum wells. The thickness in Angstrom of each layer is recalled in vertically oriented font. The centered 50 Å of the phonon wells are Si-doped at 7.2×10^{16} cm^{-3} for a two-dimensional carrier concentration $N_{2D} = 3.6 \times 10^{10}$ cm^{-2}.

This thesis mainly focuses on the structures similar to three-well RP THz QCL, reported for the first time by Luo et al. [65]. Such a system has four main energy states that

are playing major role in charge transport and gain mechanism of the device [66]. The Hamiltonian of the four-level system will be a 4×4 matrix. It is assumed that the wavefunctions of different quantum wells are coupled to each other by a slow tunneling process. The three-well QCL design, from now on, is considered as an optically active double-well interacting with an upstream phonon well for the carrier injection and a downstream phonon well for the extraction. The respective wavefunctions of these wells are computed separately, which means they are isolated from the neighboring quantum wells. The wavefunctions are then appropriately shifted in the growth direction, and finally plotted as shown in Figure 2.3. This figure represents the isolated wavefunctions of the three-well QCL reported in [65], at the design electric field (12 kV/cm). The relevant four states are named 1 for the injector level, 2 for the upper lasing state, 3 for the lower lasing state and 4 for the excited state of the downstream phonon well acting like an extractor level. The detuning and coupling values between all of these states can be separately calculated, under isolated well assumption. In analogy with the symmetric Hamiltonian defined for a two-level system in Equation 2.6, the symmetric Hamiltonian of the four-level system presented in Figure 2.3 can be written as

$$H = \begin{pmatrix} E_1 & \hbar\Omega_{12} & \hbar\Omega_{13} & \hbar\Omega_{14} \\ \hbar\Omega_{12} & E_2 & 0 & \hbar\Omega_{24} \\ \hbar\Omega_{13} & 0 & E_3 & \hbar\Omega_{34} \\ \hbar\Omega_{14} & \hbar\Omega_{24} & \hbar\Omega_{34} & E_4 \end{pmatrix}. \tag{2.8}$$

The wavefunction and energy level solutions of this Hamiltonian results in almost identical solution with the non-truncated solution of the 1D Schrödinger equation in [65].

From these isolated wavefunctions the tunneling coupling strengths between the four states are derived by a simple tight-binding approach [75]. Each $i \rightarrow j$ tunneling is characterized by a detuning energy, $E_{ij} = E_i - E_j$, and a coupling strength, $\hbar\Omega_{ij}$. Figure 2.4

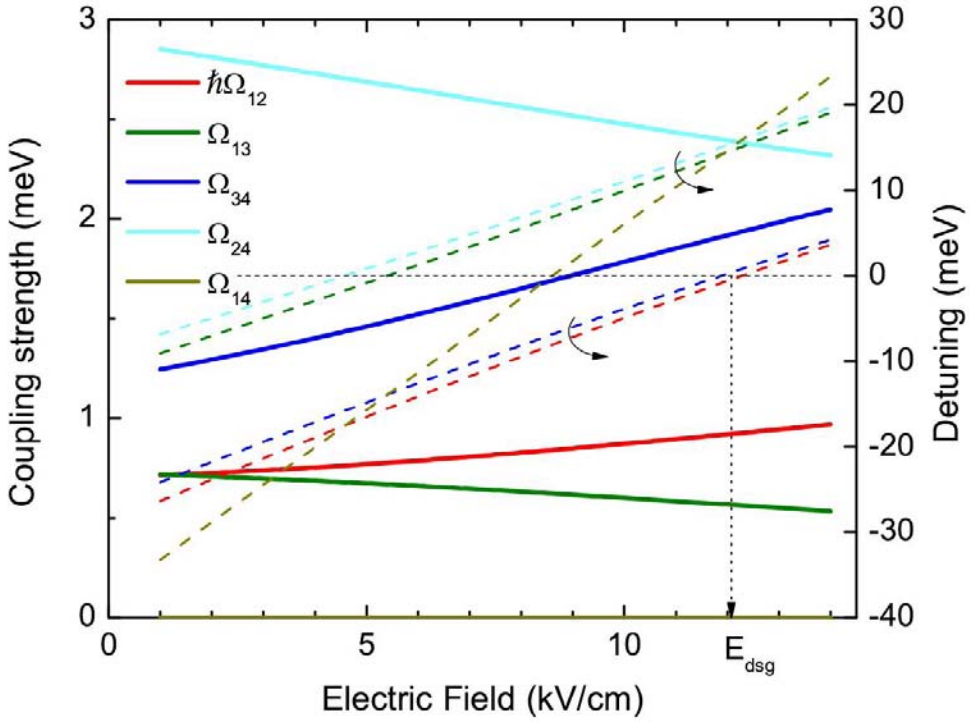

Figure 2.4: Detunings (dashed lines for right axis) and coupling strengths (solid lines for left axis) for the different tunneling processes between the four states. The same color code for the different tunneling channels applies to both vertical axis. The horizontal dashed line at zero detuning indicates the electric field for which the different tunnelings are in resonance. The vertical dashed line indicates the design electric field of the QCL. The $1-4$ coupling strength is only 0.2–0.3 μeV.

plots the detunings and couplings for all five tunnelings, versus the electric field. At the design electric field, the injection coupling is $\Omega_{12} = 0.92$ meV; the extraction coupling is $\Omega_{34} = 1.92$ meV. Ω_{34} is designed to be higher than Ω_{12} to ensure population inversion even at high temperature [65]. The wrong injection coupling, $\Omega_{13} = 0.56$ meV, is lower due to the high confinement energy of the two states 1 and 3. This observation already suggests that injection side leakage path will not play a major role around the design electric field.

On the other hand, the wrong extraction coupling, $\Omega_{24} = 2.39$ meV, is stronger than the extraction coupling. This might be a competing leakage path, particulary at low temperature, when the upper lasing time constant, τ_2, is long.
This system will be extensively studied later in this chapter and in the following chapters.

2.2 Time dependent perturbation theory

This section focuses on the quantum theory of light and discusses the light matter interaction. The interaction Hamiltonian of this interaction will be calculated and approximated using time dependent perturbation theory. Applying calculated perturbation Hamiltonian to the *Fermi's golden rule* provides us with the rate of electron-photon interaction, which will result in the absorption and gain coefficients. Later in in this section, the electron interaction with phonon will also be discussed.

2.2.1 Electron-photon interaction

When an optically active medium is illuminated by light, the Hamiltonian of the interaction between electrons and photons can be written as [1]

$$H = \frac{1}{2m^*}(\mathbf{p} - e\mathbf{A})^2 + V(r) \tag{2.9}$$

where m^* is the effective mass of the electron in the band, e is charge of an electron, $\mathbf{p}$ is the momentum vector of the electron (note that $\mathbf{p} = (\hbar/i)\nabla$), $\mathbf{A}$ is the magnetic vector potential representing the electromagnetic field, and $V(r)$ is the crystal potential discussed in Equation 2.2. In quantum electrodynamics the Hamiltonian of light matter interaction for source-free problems are usually described using choice of *Coulomb gauge*, where $\nabla.\mathbf{A} = 0$. In this case, one can found that $\mathbf{A}.\mathbf{p} = \mathbf{p}.\mathbf{A}$. Moreover, by assuming that the interacting

[1] The analysis in this section is mostly adopted from [44, 22].

electromagnetic field is small (negligible $\frac{e^2\mathbf{A}^2}{2m^*}$), the Hamiltonian in Equation 2.9 can be approximated in the weak coupling regime as summation of unperturbed Hamiltonian (H_0) and perturbed (H') Hamiltonian like

$$H_0 = \frac{\mathbf{p}^2}{2m^*} + V(r) \tag{2.10a}$$

$$H' \simeq -\frac{e}{m^*}\mathbf{A}.\mathbf{p}. \tag{2.10b}$$

In equation 2.10, it is important to use the effective mass of electrons in the band instead of free electron mass, to correctly describe the interaction.

In order to find the solution for $\mathbf{A}$, we start from the gauge invariance *Maxwell's equations* in an isotropic homogeneous medium, with spatially invariant permittivity (ε) and permeability (μ), and write it as

$$\left(\nabla^2\mathbf{A} - \mu\varepsilon\frac{\partial^2}{\partial t^2}\mathbf{A}\right) - \nabla\left(\nabla.\mathbf{A} + \mu\varepsilon\frac{\partial\phi}{\partial t}\right) = -\mu\mathbf{J} \tag{2.11a}$$

$$\nabla^2\phi + \frac{\partial}{\partial t}(\nabla.\mathbf{A}) = -\frac{\rho}{\varepsilon}. \tag{2.11b}$$

The electromagnetic fields can be described in terms of vector magnetic potential ($\mathbf{A}(\mathbf{r},t)$) and scalar potential ($\phi(\mathbf{r},t)$) with the definitions of

$$\mathbf{B} = \nabla\times\mathbf{A} \tag{2.12a}$$

$$E = -\nabla\phi - \frac{\partial}{\partial t}\mathbf{A}. \tag{2.12b}$$

However these two definitions can be also arbitrarily defined using gauge transformations of $\mathbf{A}' = \mathbf{A} + \nabla\xi$ and $\phi' = \phi - \frac{\partial}{\partial t}\xi$, and yet the observable $\mathbf{E}$ and $\mathbf{B}$ in Equations 2.12 remains the same. ξ is an arbitrary scalar function. In order to find a particular solution for Equations 2.11, it is important to specify the $\nabla.\mathbf{A}$. As mentioned above for a source free environment ($\mathbf{J} = 0$), the well-known *Coulomb gauge* is used in the quantum electrodynamics ($\nabla.\mathbf{A} = 0$). Consequently with this choice of gauge, and time independent scalar potential ($\frac{\partial\phi}{\partial t} = 0$) under static external applied bias, the Maxwell's equations in

Equations 2.11 simplifies as

$$\nabla^2\mathbf{A} - \mu\varepsilon\frac{\partial^2}{\partial t^2}\mathbf{A} = 0 \tag{2.13a}$$

$$\nabla^2\phi = -\frac{\rho}{\varepsilon}. \tag{2.13b}$$

Equations 2.13-a and b are known as the *classical wave equation* and *Poisson's equation*, respectively. These equations are completely decoupled and the solutions for $\mathbf{A}$ and ϕ can be obtained independently. The space charge density (ρ) in above equation is time-independent, which results in time-independent scalar potential (ϕ). For the optical field $\rho = 0$, and therefore the scalar potential vanishes. The vector potential for the optical field is solved from 2.13-a and results in general plane wave form of

$$\begin{aligned}\mathbf{A} &= \hat{\mathbf{e}}A_0 cos(\mathbf{k}_{op}.\mathbf{r} - \omega t) \\ &= \hat{\mathbf{e}}\frac{A_0}{2}e^{i\mathbf{k}_{op}.\mathbf{r}}e^{-i\omega t} + \hat{\mathbf{e}}\frac{A_0}{2}e^{-\jmath\mathbf{k}_{op}.\mathbf{r}}e^{\jmath\omega t},\end{aligned} \tag{2.14}$$

where $\hat{e}$ is unit vector in the direction of the optical electric field, $\mathbf{k}_{op}$ is the wave vector, and ω is the optical angular frequency. Considering the above equation for far infrared optical field, where the optical wavelength is much larger than the quantum well widths in the material system, the dipole approximation can be used to write $\mathbf{A}e^{\jmath\mathbf{k}_{op}.\mathbf{r}} \simeq \mathbf{A}$. Using Equations 2.10 and 2.14 the time-independent perturbation part of the interaction Hamiltonian can be written as

$$H'(\mathbf{r}) = -\frac{eA_0}{2m^*}\hat{\mathbf{e}}.\mathbf{p}. \tag{2.15}$$

By having the interaction Hamiltonian from equation 2.15, the optical absorption coefficient for a given photon energy can be calculated using *Fermi's golden rule*. To do so, it is required to subtract the transition rate for photon absorption and emission, calculate the net photon absorption rate, and normalize it for a given injected photon. The absorbed photon excites an electron from energy level "a" to "b", where $E_a < E_b$. For the case of intersubband transition (Figure 2.3), the energies of above states becomes

$$E_a = E_1 + \frac{\hbar^2 {k_t}^2}{2m^*} \qquad E_b = E_2 + \frac{\hbar^2 {k_t}^2}{2m^*}, \tag{2.16}$$

where k_t is the transverse component of wave vector and E_1 and E_2 are the eigenvalues of equation 2.8.

The optical absorption coefficient for the interaction described above becomes

$$\alpha(\hbar\omega) = \frac{\pi e^2}{n_r c\varepsilon_0 m^{*2}\omega}\frac{2}{V}\sum_{\mathbf{k}_a}\sum_{\mathbf{k}_b}|\hat{\mathbf{e}}.\mathbf{p}_{ba}|^2\,\delta(E_a - E_b - \hbar\omega)(F_a - F_b), \tag{2.17}$$

where n_r is refractive index of the material, c is the speed of light, V is the volume of the material interacting with optical field, the two sum functions are over all possible $\mathbf{k}_a$ for energy state "a" and $\mathbf{k}_b$ for energy state "b", and $\omega(=\frac{E_2-E_1}{\hbar})$ is the optical field oscillation frequency. The parameter $\mathbf{p}_{ba}$ is called *momentum matrix element* and is defined as

$$\begin{aligned}\mathbf{p}_{ba} &=< b|\mathbf{p}|a >\\ &= \int_{-\infty}^{+\infty}\psi_b{}^*(\mathbf{r})\mathbf{p}(\mathbf{r})\psi_a d^3\mathbf{r}.\end{aligned} \tag{2.18}$$

Moreover, the parameters F_a and F_b represent the Fermi Dirac distribution function and are defined as

$$F_{a,b} = \frac{1}{1 + e^{(E_{a,b}-E_F)/k_B T}}. \tag{2.19}$$

One can express the optical absorbtion coefficient in equation 2.17 in terms of electric dipole moment as

$$\alpha(\hbar\omega) = \frac{\pi\omega}{n_r c\varepsilon_0}\frac{2}{V}\sum_{\mathbf{k}_a}\sum_{\mathbf{k}_b}|\hat{\mathbf{e}}.\mu_{ba}|^2\,\delta(E_a - E_b - \hbar\omega)(F_a - F_b). \tag{2.20}$$

The intersubband electric dipole moment is defined as

$$\mu_{ba} = e < b|\mathbf{r}|a >= e\mathbf{r}_{ab}. \tag{2.21}$$

In equation 2.20 the momentum matrix element ($\mathbf{p}_{ba} = \jmath m^*\omega\mathbf{r}_{ba}$) is replaced by

$$\mathbf{p}_{ba} = \frac{\jmath m^*\omega}{e}\mu_{ba}. \tag{2.22}$$

Equation 2.20 suggests that the electric intersubband dipole moment is zero along transverse directions and has value only normal to the quantum well interfaces ($\hat{z}$ direction),

which results in $\mu_{ba} = e < b|z|a >= eZ_{ba}$. This is the famous intersubband selection rule, where only TM polarized electromagnetic wave can be absorbed or emitted.

Equation 2.20 is valid when the scattering relaxations are not included. In presence of scattering relaxations, the the delta function is replaced by a Lorentzian function with a linewidth of Γ and equation 2.20 becomes

$$\alpha(\hbar\omega) = \frac{\omega e^2}{n_r c\varepsilon_0}\frac{2}{V}\sum_{\mathbf{k}_{ta}}\sum_{\mathbf{k}_{tb}}|\hat{\mathbf{e}}.z_{ba}|^2\frac{\Gamma/2}{(E_a - E_b - \hbar\omega)^2 + (\Gamma/2)^2}(F_a - F_b). \tag{2.23}$$

At this point, one can define a unitless quantity for optical transition strength called the *oscillator strength* as

$$f_{ba} = \frac{2}{m^*\hbar\omega} < b|\mathbf{p}_z|a >^2 = \frac{2m^*\omega}{\hbar}{Z_{ba}}^2. \tag{2.24}$$

For an arbitrary quantum mechanical system, the oscillator strength is a measure of the strength of the optical absorption from states $a \rightarrow b$. This means that if the system is exposed with a spectrally uniform power over all transitions, f_{ab} percent of total absorbed light is due to $a \rightarrow b$ transition. The oscillator strength follows the sum rule for all initial states "a" and for the sum over all final states "b" as

$$\sum_b f_{ab} = 1. \tag{2.25}$$

Also one can conclude from equation 2.24 that $f_{ab} = -f_{ba}$, where it is positive for absorption processes and negative for emission processes. The optical absorption coefficient,equation 2.23, can be further simplified as

$$\begin{aligned}\alpha(\hbar\omega) &= \frac{\omega e^2}{n_r c\varepsilon_0}\frac{2}{V}\sum_{\mathbf{k}_{ta}}{Z_{ba}}^2\frac{\Gamma/2}{(E_a - E_b - \hbar\omega)^2 + (\Gamma/2)^2}(F_a - F_b) \\ &= \frac{\omega e^2}{n_r c\varepsilon_0}{Z_{ba}}^2\frac{\Gamma/2}{(E_a - E_b - \hbar\omega)^2 + (\Gamma/2)^2}(N_1 - N_2).\end{aligned} \tag{2.26}$$

In this simplification, the double summation is reduced to single summation using momentum conservation and finally resulted to the difference of the electron population densities

in two subbands involved in this process. In case the upper subband (E_2) holds more electron population than lower subband (E_1), it is so-called that the *population inversion* exists ($N_2 > N_1$). Population difference is defined as $\Delta N(cm^{-3}) = N_2 - N_1$, and is positive when the population is inverted. Under population inversion condition, the absorption coefficient (equation 2.26) becomes negative, meaning that the transition shows optical gain at frequency ω. In this case the net emission is higher than the net absorption, leading to *stimulated emission*. In this case one can define the intersubband gain coefficient as

$$\begin{aligned} g_{isb} &= \frac{\pi\omega e^2}{n_r c\varepsilon_0} {Z_{ba}}^2 \Delta N \mathfrak{L}(\hbar\omega - E_{ba}) \\ &= \frac{\pi\hbar e^2}{2m^* n_r c\varepsilon_0} f_{ba} \Delta N \mathfrak{L}(\hbar\omega - E_{ba}), \end{aligned} \tag{2.27}$$

where $E_{ba} = E_b - E_a$, and $\mathfrak{L}$ denotes a Lorentzian function with full width half maximum (FWHM) of Γ, and $\int \mathfrak{L}(\hbar\omega - E_{ba}) d(\hbar\omega) = 1$. Interestingly, the second form of the intersubband gain coefficient in equation 2.27 only depends on optical linewidth (Γ), population inversion (ΔN), and the oscillator strength (f_{ab}), and has no dependency on the angular frequency (ω). The optical intersubband gain, for example, at resonance ($\hbar\omega_{ab} = \hbar\omega = E_2 - E_1$) for GaAs (with $m^* = 0.067 \times m_0$ and $n_r = 3.6$) becomes

$$g_{isb}(\omega_{ab}) = 72.1 \times \frac{f_{ba}\Delta N(10^{15} cm^{-3})}{\Delta\nu(THz)} \quad (cm^{-1}), \tag{2.28}$$

where $\Delta\nu$ is the gain broadening in THz units. For a typical GaAs based active region for THz emitters with population inversion of $\Delta N \approx 1$, $\Delta\nu \approx 0.5$, and $f_{ab} \approx 0.5$, the peak of gain approximately becomes 72.1 cm^{-1}, which is enough to overcome typical waveguide loss. Later in this chapter, the population difference and the Lorentzian function for the three-well QCL shown in Figure 2.3 will be analytically discussed and calculated.

2.2.2 Electron-phonon interaction

The spontaneous emission lifetime in few THz range is typically more than microseconds. Therefore, in a typical RP based THz QCL, as depicted in Figure 2.3, the sub-threshold

carrier transport is dominated by non-radiative fast scattering mechanisms with lifetimes of below tens of picoseconds. Moreover, in the RP THz QCL, Figure 2.3, the population inversion is mediated through fast depopulation of lower lasing state using LO-phonon scattering of carriers. Therefore, to find an optimum design it is important to understand physics of LO-phonon based intersubband scattering mechanisms.

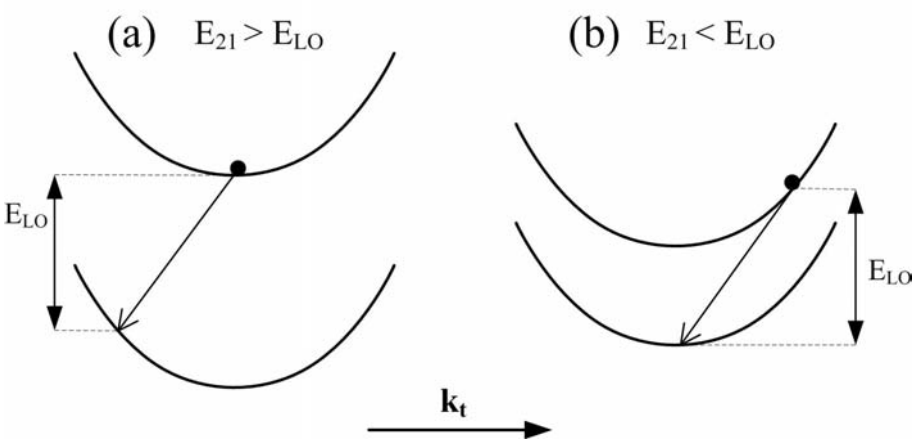

Figure 2.5: The schematic presentation of intersubband LO-phonon emission for (a) $E_{21} > E_{LO}$, and (b) $E_{21} < E_{LO}$.

Figure 2.5-a and -b shows two different cases for intersubband LO-phonon scattering of carriers. In the first case ($E_{21} > E_{LO}$), the electron-LO-phonon scattering is the dominant intersubband scattering mechanisms. The typical scattering time for such a scattering mechanism is below 1 ps. Such scattering rate (for both phonon emission and absorption) will be calculated by applying the bulk-like electron-phonon interaction hamiltonian to a quantum well structure.

When $E_{21} < E_{LO}$, the emission of LO-phonon is energetically forbidden for electrons at Γ-point. In such cases the non-radiative relaxation of carriers at low temperature is mediated through electron-electron ($\gtrsim 100\ ps$), electron-impurity ($\gtrsim 20\ ps$), and electron-interface roughness ($\gtrsim 100\ ps$)) scattering mechanisms, which are not as efficient as LO-

phonon scattering [48]. The LO-phonon emission is an efficient way to cool the electron gas temperature. Therefore, the electronic temperature tends to increase to the high energetic shoulders of the subband until it reaches the E_{LO} energy (= 36.7 meV for GaAs lattice), Figure 2.5-b. Typically for subbands with such small energy separation, the electron temperature can be 50 to 100 K higher than the lattice temperature [76]. For example micro-photoluminescence experiments on resonant phonon scattering based QCLs (Figure 2.3) have demonstrated that the temperature of lasing subbands can be $\Delta T_e \approx 100$ K higher than the lattice [77]. In calculation of scattering rate for subbands with $E_{21} < E_{LO}$, it is important to consider both electron and phonon distributions at different temperatures [73].

A brief derivation of LO-phonon scattering (absorption and emission) rates in polar semiconductor superstructures is presented.[1] It is assumed that the subband energy separation is in the range of (or slightly greater than) LO-phonon resonance energy. For two dimensional carriers, the electron-phonon interaction term is similar to the bulk material and is defined as [73],

$$\tilde{\mathcal{H}} = e \sum_{\mathbf{K}} \left(\frac{\hbar \omega P}{2|\mathbf{K}|^2} \right)^{\frac{1}{2}} \frac{e^{\jmath \mathbf{K}.\mathbf{r}}}{V^{\frac{1}{2}}}, \tag{2.29}$$

where $\mathbf{K}$ is phonon wave vector, ω is the angular frequency of the phonon, and P is

$$P = \frac{1}{\varepsilon_\infty} - \frac{1}{\varepsilon_r}, \tag{2.30}$$

with ε_∞ and ε_r being high frequency and static permittivity of the material, respectively. The $\frac{1}{|\mathbf{K}|^2}$ dependency of the phonon interaction term suggests that the interaction rate reduces when a large momentum transfer is required for the phonon scattering. Such a condition is required, for instance, when a phonon is scattered among two subbands with energy separation much greater than E_{LO}, Figure 2.5-a.

Equation 2.29 can be applied to the *Fermi's golden rule* to calculate the LO-phonon

[1] The analysis in this section is mostly adopted from [73].

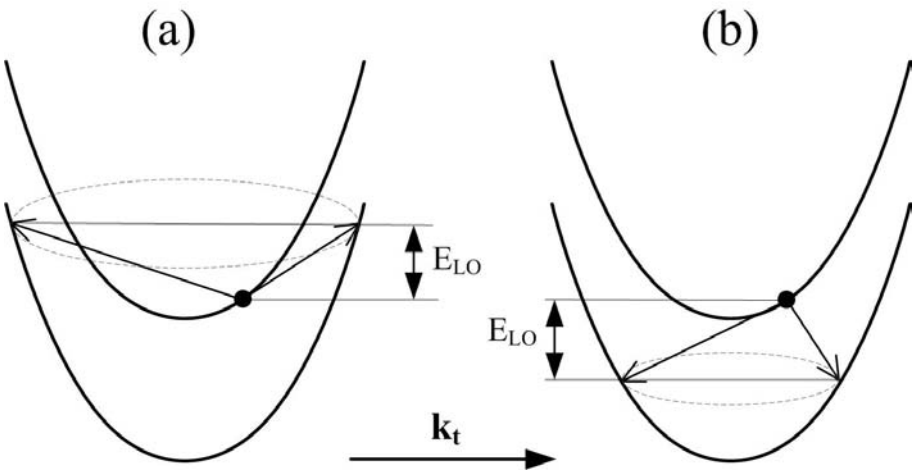

Figure 2.6: The schematic presentation of intersubband LO-phonon based (a) absorption, and (b) emission, from subband i to subband f. The dashed circle depicts all permitted in-plane wave vector in final subband. It is assumed that $E_{21} \gtrsim E_{LO}$.

transition rate between two subbands, $\tau_{i\to f}$. Generally there are two possible types of scattering mechanisms (absorption and emission) from subband i to subband f, as depicted in Figure 2.6-a and -b. By assuming the initial wave vector as k_i, the final state wave vector reads from energy conservation law as

$$k_f^2 = k_i^2 - \frac{2m^*\Delta}{\hbar^2}, \tag{2.31}$$

where $\Delta(= E_f - E_i \mp \hbar\omega)$ is the change in the kinetic energy of the scattered carrier. The upper sign accounts for the scattering process involving the absorption of a phonon and the the lower sign is for the emission. The dashed circles in Figure 2.6 depict the permitted wave vectors of the final state. After summation over all permitted final states (all permitted wave vectors), and further simplification using momentum conservation law, the LO-phonon scattering rate for a 2D carrier distribution with arbitrary wavefunctions

is extracted. The absorption rate (Figure 2.6-a) becomes like

$$W_{i\to f}^{abs} = \frac{m^* e^2 \omega P}{4\pi\hbar^2}(n_{LO})\Theta(k_i^2 - \frac{2m^*\Delta}{\hbar^2}) \times \int_{-\infty}^{+\infty} \frac{|G_{if}(K_z)|^2}{\sqrt{K_z^4 + 2K_z^2(k_i^2+k_f^2) + (k_i^2-k_f^2)^2}} dK_z, \tag{2.32}$$

and the LO-phonon emission rate (Figure 2.6-b) becomes like

$$W_{i\to f}^{em} = \frac{m^* e^2 \omega P}{4\pi\hbar^2}(n_{LO}+1)\Theta(k_i^2 - \frac{2m^*\Delta}{\hbar^2}) \times \int_{-\infty}^{+\infty} \frac{|G_{if}(K_z)|^2}{\sqrt{K_z^4 + 2K_z^2(k_i^2+k_f^2) + (k_i^2-k_f^2)^2}} dK_z. \tag{2.33}$$

Here the Θ denotes the Heaviside function, n_{LO} is the Bose-Einstein distribution factor defined as

$$n_{LO} = \frac{1}{e^{\hbar\omega/k_B T} - 1}, \tag{2.34}$$

and $G_{if}(K_z)$ is called the *form factor* and is defined as

$$G_{if}(K_z) = \int \psi_f^*(z) e^{-iK_z z} \psi_i(z) dz. \tag{2.35}$$

The form factor carries information regarding the initial and final wavefunctions and also their interaction through phonon Hamiltonian. It is a symmetric function about $K_z = 0$. It is very important for accuracy of the numerical calculation to execute the integration of $|G_{if}(K_z)|^2$ over K_z until it vanishes. The Heaviside function, Θ, in equations 2.32 and 2.33 ensures that there is non-zero rate when

$$E_i + \frac{\hbar^2 k_i^2}{2m^*} + \hbar\omega > E_f, \tag{2.36}$$

for phonon absorption and when

$$E_i + \frac{\hbar^2 k_i^2}{2m^*} > E_f + \hbar\omega, \tag{2.37}$$

for phonon emission. The power of equations 2.32 and 2.33 are in precisely calculating both intra- and intersubband phonon scattering rates. The intrasubband scattering rates

are calculated by setting $i = f$ and $\psi_i = \psi_f$, in above equations. It is important to mention that in the calculation of scattering rate, the Pauli blocking of the final state is not considered. This is a reasonable assumption, since THz QCLs are designed with low doping density.

Finally the net phonon scattering time between two subbands is calculated using a weighted average of scattering rate over the distribution of carriers in the initial subband as

$$\frac{1}{\tau_{i\to f}} = \frac{\int W_{i\to f}(E)F(E)dE}{\int F(E)dE}, \tag{2.38}$$

where $F(E)$ denotes the Fermi-Dirac distribution as defined in equation 2.19.

In the case of phonon scattering between subbands with $E_{21} < E_{LO}$, as discussed before, the scattering event will only occur at higher temperatures. At high temperature the thermally excited electrons reach the high energy tails of the subband, until reaching E_{LO} above the lower subband. Therefore the non-radiative transition of thermally-activated carrier in this condition becomes

$$\tau_{21}^{-1} = \frac{1}{\tau_{21}^{(\text{LO emi, hot e}^-)}} \exp\left(\frac{E_{21} - E_{LO}}{k_B(T + \Delta T_e)}\right) + \frac{1}{\tau_{21}^{(\text{LO abs})}} + \frac{1}{\langle\tau_{21}^{(\text{imp})}\rangle}, \tag{2.39}$$

where $\langle\tau_{21}^{(\text{imp})}\rangle$ is the intersubband $2-1$ unscreened impurity scattering time constant averaged over the Maxwell-Boltzmann distribution of carriers on level 2, E_{LO} is the LO-phonon energy, $\tau_{21}^{(\text{LO emi, hot e}^-)}$ is the LO-phonon scattering time for an electron on level 2 with a kinetic energy equal to $E_{LO} - E_{21}$, $\tau_{21}^{(\text{LO abs})}$ is the LO-phonon absorption scattering time for an electron at the bottom of subband 2 to level 1, k_B is the Boltzmann constant, and finally, $T + \Delta T_e$ is the electron temperature on level 2, T being the lattice temperature and ΔT_e the electron heating temperature.

As an example here, the non-radiative LO-phonon scattering rate of the electrons from level 2 to the level 3 in various three-well-based THz QCLs, similar to the one depicted in Figure 2.3, is discussed. Figure 2.7 depicts the plot of the non-radiative transition rates (as

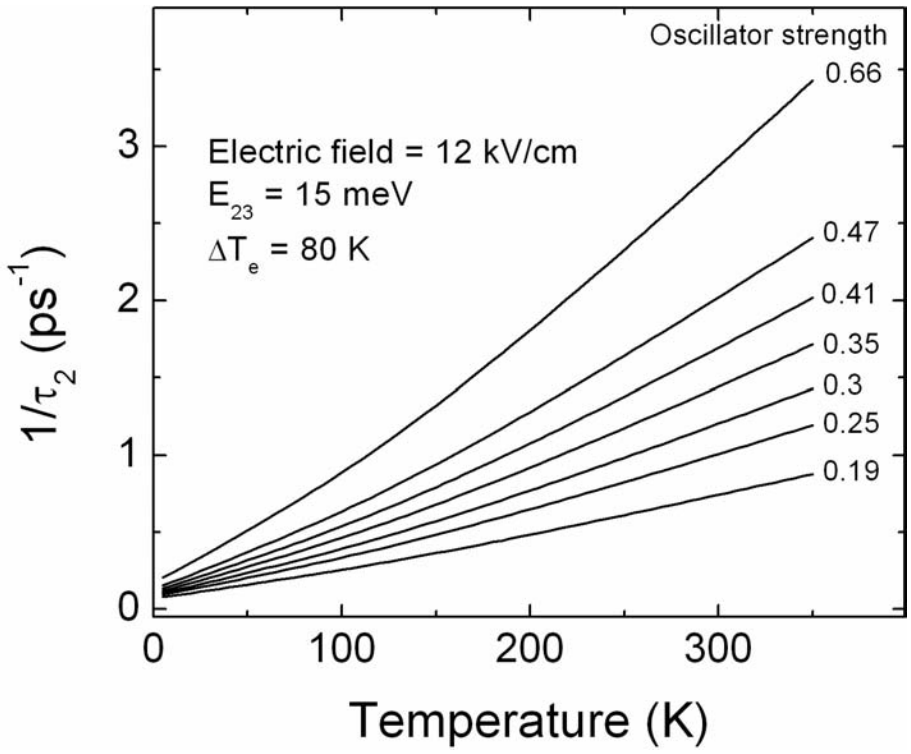

Figure 2.7: Non-radiative LO-phonon scattering rates between active photon double well of three-well THz QCLs with various oscillator strengths versus lattice temperature. Changing of the rate over the range of temperature decreases for lower oscillator strengths.

calculated in equation 2.39) versus temperature, for a range of lasing oscillator strengths between 0.19 and 0.66. In calculation of this graph, it is assumed that the quantum well structure is biased at design electric field (12 kV/cm), the photon energy is 15 meV, Lattice temperature is 5 K, and electronic temperature is $\Delta_e T = 80\ K$ higher than the lattice temperature. Seven different oscillator strength values is considered between 0.19 and 0.66. 0.66 oscillator strength corresponds to very vertical photon transition and 0.19 corresponds to very diagonal photon transition. The oscillator strength of the laser transition for original three-well THz QCL in [65] is 0.677, which is quite vertical transition.

Figure 2.7 shows that as lattice temperature increases, rate of the non-radiative tran-

sition between upper lasing state 2 to the lower lasing state3, $1/\tau_{23}$, increases. This effect potentially results in depopulating the upper lasing state at higher lattice temperatures. However, the degradation of upper lasing lifetime (τ_{23}), over the calculated range of temperatures, reduces for lasing transitions with lower oscillator strengths. The observed weak dependency of $1/\tau_{23}$ for diagonal designs, makes such structures promising for design of high temperature THz QCLs. This is because the performance of THz QCLs with diagonal double photon-well degrades less with increasing temperature [61]. However, it is important to note that the lower oscillator strength also reduces the gain cross section, as calculated from equation 2.28. Later in this chapter, a density matrix formalism is used to analytically model the population inversion and optical intersubband gain of various three-well THz QCLs. A detailed experimental study over the optimum value of the oscillator's strength will be discussed in chapter 4.

2.3 Density matrix formalism for resonant tunneling based structures

The resonant tunneling is the most important transport mechanism in three-well RP THz QCL. The injection to the upper lasing state and depopulation of the lower lasing state is mediated through resonant tunneling. Proper understanding of this mechanisms is crucial in design and optimization of THz QCLs for high performance operation. More generally the transport in THz QCLs, have attracted the attention of many theoreticians. Several useful models have been developed to predict the transport, the electron distribution, the gain and the relative importance of different scattering mechanisms. To cite only a few, the self-consistent rate equation model [78], the Monte-Carlo simulations [79, 80, 81, 82], the hybrid density matrix-Monte Carlo model [83], and finally quantum theories based on nonequilibrium Green's functions [84, 85, 86, 87, 88] or on density matrix [89, 90, 91, 92]

are a few recently developed models. Some groups have reported a remarkable agreement between the theoretical electrical characteristics and experiments [86, 92, 87, 88]. However the implementation of such models is difficult, and computationally very demanding.

Alternatively, Scalari et al. have employed a simplified density matrix model on a five-well QCL emitting at 3.7 THz. This work, after a fitting procedure of the optical and electrical characteristics, estimated the upper lasing state lifetime and relaxation time constant in the injector region [93]. All these parameters are useful for subsequent optimization. Kumar et al. have developed a similar model, which is used as a guideline tool for designing resonant LO-phonon scattering based QCLs [4, 67], as well as an analyzing tool of the laser performance [69]. With the same model, they also simulated the gain profile for different range of laser intensities. Recently Dupont et al. have demonstrated analytical solution for the charge transport and optical gain for a four level system, as in Figure 2.3, [66].

This section, first studies the simple case of two-level system using density matrix formalism. Through this simple example, many new parameters, including resonant tunneling parameters, are introduced and will be used later in the more complicated density matrix model for a four-level system, as in Figure 2.3. However before getting into the calculation details, it is useful to review the limitations of such a density matrix based model.

2.3.1 Limitations of the density matrix based model

The density matrix based models consist of solving Bloch equations of the interacting states independently of the kinetic energy of the carriers. Saying so, it means that the carriers on a particular subband behave the same, like a single particle, regardless of their kinetic energy. Therefore, the solution is not resolved in the $\mathbf{k}_{\|}$-space of subbands. With this model, tunnelings are conserving the in-plane wavevector $\mathbf{k}_{\|}$ but are not considering the Pauli's exclusion principle, which can be a severe limitation if the structures are heavily

doped. The model also ignores the Pauli's exclusion principle for the intersubband lifetime of the states. Since the THz QCLs are lightly doped, this simplification will not likely cause substantial errors.

The density matrix based model also concentrates the thermal effects only on the upper lasing time constant, τ_2. It is important to underline the fact that this model omits any thermal effects on the intrasubband component of the dephasing time constant between the states, which contributes to the linewidth of the optical intersubband transition [94]. From this point on, this component is called *pure dephasing time constant* and noted τ_{ij}^*. Simulations have suggested a strong temperature effect on intersubband transition linewidth since the electron screening length (Debye length) of the impurity Coulomb potential increases with the electron temperature [95]. However, simple models for the intrasubband scattering rate do not result in the same optical gain linewidth as the one computed by nonequilibrium Green's function based works [96, 97, 98]. Moreover, these sophisticated techniques should better predict the temperature dependance of the linewidth. Since in the density matrix based model, τ_2 carries most of the responsibility for the temperature degradation of the laser, the fitting of parameters might lead to an underestimation of τ_2, or equivalently, to an overestimation of the electronic temperature. This approximation is a serious one, which might simplify the model too much.

The upper lasing lifetime, τ_2, as defined in equation 2.39, carries the temperature dependance from the Fermi-Dirac distribution, Bose-Einstein distribution (n_{LO} from equation 2.34), and weighted averaging the scattering rates ($\tau_{i\to f}$ from equation 2.38). In equation 2.39, it is obvious that the electron heating temperature depends on input electrical power, as well as the laser intensity [99, 77, 100]. However, in order to simplify the numerical applications, its value will be kept independent of the electric field and lattice temperature. This simplification is serious and can distort the simulated current density versus electric field characteristic. Micro-photoluminescence experiments on resonant phonon scattering

based QCLs have demonstrated that the temperature of lasing subbands can be $\Delta T_e \approx 100$ K higher than the lattice [77]. The lifetime of lower lasing, extractor and injector states, Figure 2.3, are written similar to equation 2.39,

$$\tau_3^{-1} = \frac{1}{\tau_{23}^{(\text{LO emi, hot e}^-)}} \tag{2.40a}$$

$$\tau_4^{-1} = \frac{1}{\langle \tau_{41'}^{(\text{imp})} \rangle} + \frac{1}{\tau_{41'}^{(\text{LO emi})}} + \frac{1}{\tau_{41'}^{(\text{LO abs})}} \tag{2.40b}$$

$$\tau_1^{-1} = \frac{1}{\tau_{41'}^{(\text{LO emi})}}. \tag{2.40c}$$

The terms related to phonon absorption processes are not negligible at high temperatures. The phonon absorption processes from levels $1_{(n+1)}$ (which is noted $1'$ in equation 2.40) to 4, and from 3 to 2, are the reverse of the phonon emission processes $4 \rightarrow 1_{(n+1)}$ and $2 \rightarrow 3$. This is why the same term $\tau_{41'}^{\text{LO emi}}$ ($\tau_{23}^{\text{LO emi, hot e}^-}$) appears in the expression of τ_4^{-1} (τ_2^{-1}) and τ_1^{-1} (τ_3^{-1}). As will be discussed in the full model, among the absorption terms in equation 2.39 and equation 2.40, the most important term is τ_1^{-1}. This is because the phonon absorption from the heavily occupied state $1_{(n+1)}$ to state 4 acts as a backfilling process at high temperatures.

Since this model is only focused on the main states within one period, it can not predict the leakage to more remote states. For instance, at high electric fields, level 2 could be coupled to the second excited state of the next period active double-well, which is displayed by a green wavefunction in Figure 2.3.

With these obvious limitations in mind, it is clear that any fitted experiment results derived with this model should be treated with caution. Nevertheless, this simplified model can give useful insights for the effects of the different couplings on the gain. It can also be extended to structures consisting of more, or less, wells per period. Its simplicity makes the implementation very easy by experimentalists and can be used as a first-order optimization tool for new designs. In the next section, we will model the steady state populations and

static coherences without including the laser Rabi frequency, which induces oscillating coherences between states for a two-level system.

2.3.2 Density matrix model for a two-level system

Postulated of quantum mechanics make it possible to describe a physical properties of a *pure state*, such as temporal dynamics and expectation value of physical observables, but not for the *mixed states*. The density matrix formalism is an approach to solve for time evolution of quantum mechanical states. It allows for phenomenological description of arbitrary many-body system, which also includes the phase information. It is therefore widely used in solving for the coherent transport of carriers in THz QCL structures [89, 90, 91, 92, 66].

An arbitrary state $|\psi\rangle$ in Hilbert space can be expanded in it's orthonormal basis $|\phi\rangle$ as

$$|\psi(t)\rangle = \sum_n c_n(t)|\phi\rangle, \tag{2.41}$$

where $c_n(t)^2$ is the probability of having the quantum mechanical system on state $\psi_n(t)$, and therefore $\sum c_n(t)^2 = 1$. A self-adjoint (Hermitian) operator $\hat{\rho}(t)$ can be defined as

$$\hat{\rho}(t) = |\psi(t)\rangle\langle\psi(t)|, \tag{2.42}$$

which is called *density operator*. The matrix elements of $\hat{\rho}(t)$ is called *density matrix* and is clearly defined as

$$\rho_{ij}(t) = \langle\phi_i|\hat{\rho}(t)|\phi_j\rangle = c_i(t)c_j^*(t). \tag{2.43}$$

As mentioned above, the density matrix is a Hermitian operator; hence $\hat{\rho} = \hat{\rho}^\dagger$. Diagonal elements of the density matrix, ρ_{ii}, gives the probability of finding the system in its basis $|\psi_i\rangle$ that results in $Tr(\hat{\rho}) = 1$. In another word, the diagonal terms determines the

population of the particular basis state. The meaning of off-diagonal element is more subtle, where it defines the *coherence* between different states in the system. The coherence determines how well each state maintains its phase.

The density matrix elements are calculated by solving the *master equation* in the density matrix formalism,

$$\frac{\partial}{\partial t}\hat{\rho}(t) = \frac{1}{j\hbar}\left[H, \hat{\rho}(t)\right] + \mathcal{T}, \tag{2.44}$$

which is also called *quantum Liouville* equation. In this equation, the matrix $\mathcal{T}$ depends on the density matrix elements and represents the natural decay of populations and coherences when these terms are placed in nonequilibrium condition. The decay of the populations, ρ_{ii}, is given by the diagonal terms. The stimulated emission rate for the states involved are also included in this matrix.

The exponential decay of the coherences, ρ_{ij} $(i \neq j)$, is characterized by the total phase coherence time constant, $\tau_{\|ij}$, which describes how long the phase correlation is conserved during the tunneling transport from state i to j. The total phase loss rate between two interacting states i and j is half the sum of population decay rates via intersubband processes, $\tau_{i,j}^{-1}$, plus the "pure" phase randomization rate during tunneling transport or optical intersubband transition, $\tau_{ij}^{*^{-1}}$ [83]. The higher $\tau_{\|ij}^{-1}$, the more relaxed becomes the $\mathbf{k}_{\|}$-conservation law. For the sake of simplicity, one can assumed the same pure dephasing time constant for all different tunneling channels and write $\tau_{ij}^{*} = \tau^{*}$. This assumption means that the scattering potential and matrix scattering element for different pairs of states would be similar. The different total phase loss rate between states $|i\rangle$ and $|j\rangle$ reads

$$\tau_{\|ij}^{-1} = (2\tau_i)^{-1} + (2\tau_j)^{-1} + 1/\tau^{*} \tag{2.45}$$

Having a temperature independent pure dephasing time means that the broadening of tunneling or optical intersubband transition resonances with temperature will be minimal due to the thermal activation of τ_2. The intrasubband component of the linewidth at a

particular kinetic energy, $\epsilon_{\mathbf{k}_\parallel}$, and for a scattering potential, $V^{(\mathrm{sc})}$, can be written[101] as

$$\tau_{ij}^{*^{-1}}(\epsilon_{\mathbf{k}_\parallel}) = \pi \sum_{\mathbf{q}_\parallel} \left| \langle i, \mathbf{k}_\parallel + \mathbf{q}_\parallel | V^{(\mathrm{sc})} | i, \mathbf{k}_\parallel \rangle - \langle j, \mathbf{k}_\parallel + \mathbf{q}_\parallel | V^{(\mathrm{sc})} | j, \mathbf{k}_\parallel \rangle \right|^2 \times \delta(\epsilon_{\mathbf{k}_\parallel + \mathbf{q}_\parallel} - \epsilon_{\mathbf{k}_\parallel}). \tag{2.46}$$

As an example, one can consider the case that the ionized impurity scattering from Si dopants are introduced in the phonon well. With such a scattering potential, $V^{(\mathrm{sc})} = V^{(\mathrm{imp})}$, the correlated intraband scattering rate between two states should substantially change whether the states are spatially separated, like in a tunneling process, or overlapping each other, like in an optical intersubband transition in the active double-well (see equation 2.46). Therefore, in the case of tunneling process the two matrix elements relative to a state in the phonon well in equation 2.46, like $\langle 1, \mathbf{k}_\parallel + \mathbf{q}_\parallel | V^{(\mathrm{sc})} | 1, \mathbf{k}_\parallel \rangle$, is not as well compensated by the matrix element relative to a state in the active double-well, like $\langle 2, \mathbf{k}_\parallel + \mathbf{q}_\parallel | V^{(\mathrm{sc})} | 2, \mathbf{k}_\parallel \rangle$.

In the case of optical transition, the remoteness of both wavefunctions from the ionized impurity potential and the strong overlap of the two wavefunctions imply that the two matrix elements in equation 2.46 tend to cancel each other. Therefore, a different pure dephasing time constant has to be used between the two lasing states $\tau_{23}^* \neq \tau^*$. From the above discussion, with equation 2.46 and the ionized impurity scattering example, it is predicted that $\tau_{23}^* > \tau^*$.

Now for a two level system like the one in Figure 2.3, the corresponding Hamiltonian, equation 2.6, can be replaced in equation 2.44 and solved to obtain all populations and coherences. Figure 2.8 shows the schematic diagram of a two-level system. The carriers in level $|1\rangle$ are injected into the level $|2\rangle$ through a resonant tunneling process and consequently are scattered in to the level $|1'\rangle$, which belongs to the next period.

By solving equation 2.44 for the states $|1\rangle$ and $|2\rangle$, the population (ρ_{11} and ρ_{22}) and coherence (ρ_{12} and ρ_{21}) values can be obtained. The solutions depend on the tunneling

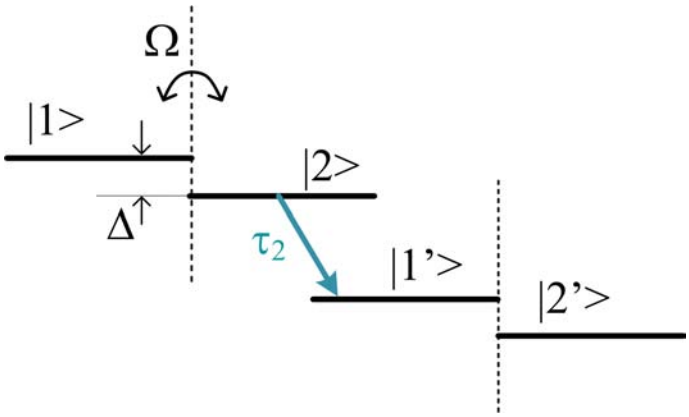

Figure 2.8: Schematic of the interaction in a two-level system. The Ω is tunneling coupling strength and Δ is the tunneling detuning between two levels $|1\rangle$ and $|2\rangle$. τ_2 is the non-radiative lifetime of the level $|2\rangle$. $|1'\rangle$ and $|2'\rangle$ depicts the energy level in the consequent period.

time between state $|1\rangle$ and $|2\rangle$ that is defined as [45, 74]

$$T_{12} = \frac{1 + \Delta_{12}^2 \tau_{\parallel 12}^2}{2\Omega_{12}^2 \tau_{\parallel 12}}, \tag{2.47}$$

where $\Delta_{12} = (E_1 - E_2)/\hbar$ is the detuning and Ω_{12} is the coupling between two states. The tunneling time of the resonant tunneling process is an important parameter and will be frequently used in the rest of this thesis. The population difference between $|2\rangle$ and $|1\rangle$ is called *population inversion* and, is calculated as

$$\Delta n (= \rho_2 - \rho_1) = -\frac{T_{12}}{T_{12} + 2\tau_2}, \tag{2.48}$$

where τ_2 is the non-radiative lifetime of the state $|2\rangle$ and can be calculated from equation 2.39. As T_{12} and τ_2 are always positive values, the population inversion of the structure in Figure 2.8 is always negative. In case, T_{12} is very short $(= 0)$or τ_2 is very long $(\rightarrow \infty)$ the population of two state becomes equal, which results in zero inversion.

The average current density of the structure shown in Figure 2.8 can be obtained from

average velocity of the carriers as [74]

$$\begin{aligned} J &= -eN_{2D}Tr\left(\rho\dot{\mathcal{Z}}\right) \\ &= -eN_{2D}Tr\left(\rho\frac{1}{\jmath\hbar}\left[H,\mathcal{Z}\right]\right), \end{aligned} \tag{2.49}$$

where $\dot{\mathcal{Z}}$ is the velocity operator, $\mathcal{Z}$ is the position operator ($z_{ij} = \langle\psi_i|\mathcal{Z}|\psi_j\rangle$), and N_{2D} is the 2D sheet doping density. The diagonal terms of the velocity operator vanishes and only non-diagonal terms contributes to the current. By assuming that the length of a period of cascaded gain medium (superperiod, L_{sp}) approximately equals to $z_{22} - z_{11} = \langle\psi_2|\mathcal{Z}|\psi_2\rangle - \langle\psi_1|\mathcal{Z}|\psi_1\rangle$, then the current density reads

$$J \approx eN_{2D}\jmath\Omega\delta\rho_{21}. \tag{2.50}$$

In this equation $\delta\rho_{21} = \rho_{12} - \rho_{21}$, which can be found from the solution of master equation, equation 2.44. After some math the current density of the two-level system results in

$$J = \frac{eN_{2D}}{T_{12} + 2\tau_2}. \tag{2.51}$$

The denominator of equation 2.51 calculates the *transit time* of the carrier over one superperiod. The current is simply total charge of carriers in one superperiod (eN_{2D}), divided by the transit time. Such a current shows a maxima where tunneling time (and hence transit time) is minimum. This happens at resonance ($\Delta_{12} = 0$). The maximum current in strong coupling regime ($2\Omega^2\tau_{\parallel 12} \gg 1$), approximately becomes $J_{max} \approx \frac{eN_{2D}}{2\tau_2}$. Beyond this maximum point the current decrease with increasing the electric field, and hence *negative differential resistance* (NDR) occurs [93]. The FWHM of the NDR is $\frac{2}{\tau_{\parallel 12}}\sqrt{1 + 4\Omega^2\tau_{\parallel 12}\tau_2}$ [93], which suggests that the FWHM decreases for high $\tau_{\parallel 12}$ or for low Ω and τ_2. Figure 2.9-a and -b show Resonant tunneling detuning versus current density for various values of pure dephasing time constant ($\tau_{\parallel 12}$) and coupling strength (Ω), calculated from equation 2.51. It clearly show that as $\tau_{\parallel 12}$ increases or Ω decreases the FWHM of the NDR reduces.

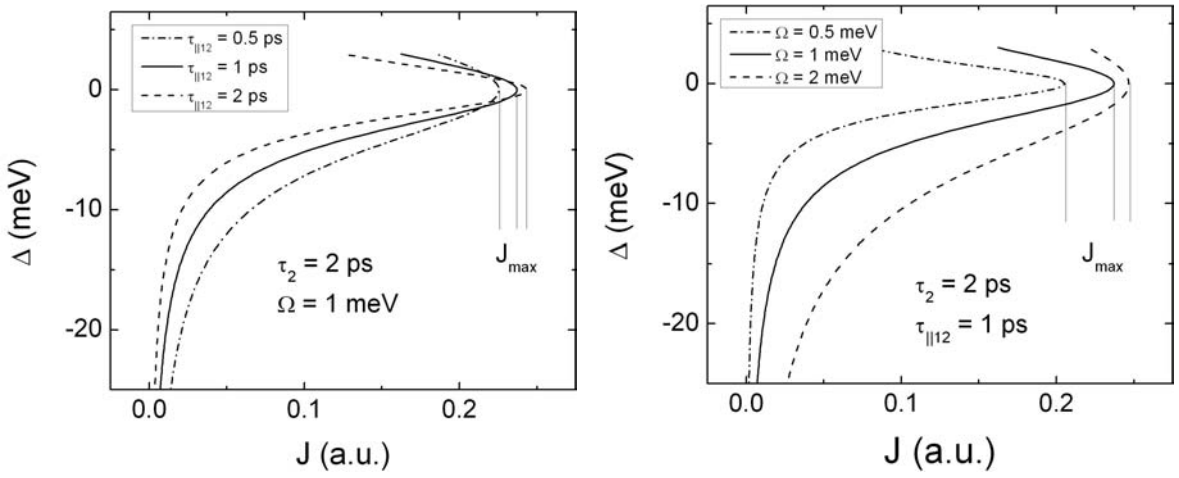

(a) (b)

Figure 2.9: (a) Resonant tunneling detuning versus current density for three different values of pure dephasing time constants ($\tau_{\|12}$ = 0.5, 1, and 2 ps); and (b) Resonant tunneling detuning versus current density for three different values of coupling strengths (Ω = 0.5, 1, and 2 meV).

2.3.3 Density matrix formalism for three-well THz QCL

Previous section showed how density matrix can describe the population and coherence values of different energy levels. This section applies the master equation in equation 2.44 for the structure shown in Figure 2.3. To do so, the tunneling and detuning values calculated in Figure 2.4 is used for the Hamiltonian at various electric fields. All possible interactions between the four states are schematically represented in Figure 2.10.

The desirable coupling strengths (green double arrows) are the injection, Ω_{12}, and extraction, Ω_{34}, tunnelings. These channels are optimum at the design electric field of the laser, E_{dsg}, i.e. close to $\sim$12 kV/cm. However, at low electric fields, the injector level can also interact with the lower lasing state, a process called the *wrong injection* channel, Ω_{13}. Similarly, carriers injected to the upper lasing state can directly tunnel towards

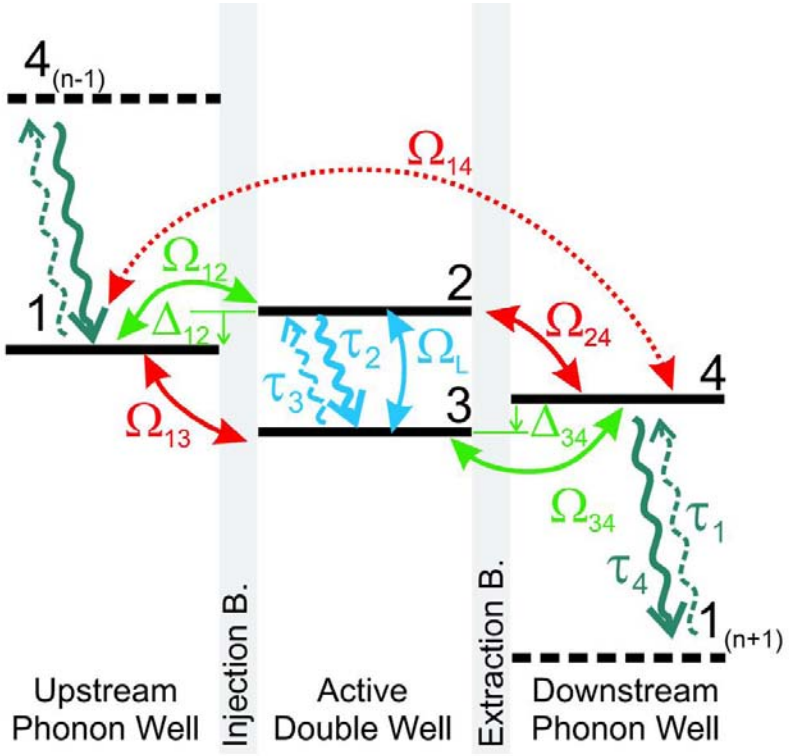

Figure 2.10: Schematic of the interactions between the four relevant states in a three-well THz QCL. The Ω_{ij} are the tunneling coupling strengths. The injection (Ω_{12}) and extraction (Ω_{34}) are represented in green as opposed to the not so desirable tunneling channels like Ω_{13} for wrong injection channel, and Ω_{24} for the wrong extraction channel. A parasitic and negligible channel Ω_{14} between 1 and 4 can also occur.

the extractor state, a process called *wrong extraction*, Ω_{24}. Less importantly, there is a weak direct *parasitic coupling* between the injector and the extractor states, Ω_{14}, which is three orders of magnitude smaller than the other four tunneling couplings. The last three couplings (double red arrows) are not desirable for the laser operation. The laser field, $\mathcal{E}_L$, as schematically represented by its Rabi frequency $\Omega_L = qZ_{32}\mathcal{E}_L/\hbar$ in Figure 2.10, puts the lasing states in interaction. This is because only this pair of states is in close resonance with the laser frequency and has a significant dipole moment. The laser field

not only induces oscillating coherences between 2 and 3, but also between $1-3$, $2-4$ and $1-4$. These interaction introduces a Raman-like gain for the structure under study, and will be discussed later in this chapter. The laser field only reduces the upper lasing state lifetime via the stimulated emission. The scattering processes between different states are represented by wavy arrows. The main relaxation processes for achieving laser operation are drawn with solid wavy downward arrows, and processes related to phonon absorption are drawn by dashed wavy upward arrows. The upper lasing state time constant, τ_2, is estimated from the $2-3$ intersubband unscreened impurity and bulk LO-phonon scattering rates, as explained in previous section.

The time evolution of the density matrix, ρ, is written as

$$\frac{d\rho}{dt} = \frac{1}{\jmath\hbar}\left[\begin{pmatrix} E_1 & \hbar\Omega_{12} & \hbar\Omega_{13} & \hbar\Omega_{14} \\ \hbar\Omega_{12} & E_2 & 0 & \hbar\Omega_{24} \\ \hbar\Omega_{13} & 0 & E_3 & \hbar\Omega_{34} \\ \hbar\Omega_{14} & \hbar\Omega_{24} & \hbar\Omega_{34} & E_4 \end{pmatrix}, \begin{pmatrix} \rho_{11} & \rho_{12} & \rho_{13} & \rho_{14} \\ \rho_{21} & \rho_{22} & \rho_{23} & \rho_{24} \\ \rho_{31} & \rho_{32} & \rho_{33} & \rho_{34} \\ \rho_{41} & \rho_{42} & \rho_{43} & \rho_{44} \end{pmatrix}\right] - \begin{pmatrix} \tau_1^{-1}\rho_{11} - \tau_4^{-1}\rho_{44} & \tau_{\|12}^{-1}\rho_{12} & & \\ \tau_{\|12}^{-1}\rho_{12} & \tau_2^{-1}\rho_{22} - \tau_3^{-1}\rho_{33} + \tau_{\text{sti}}^{-1}\Delta\rho & \cdots & \\ \tau_{\|13}^{-1}\rho_{31} & \tau_{\|23}^{-1}\rho_{32} & & \\ \tau_{\|14}^{-1}\rho_{41} & \tau_{\|24}^{-1}\rho_{42} & & \end{pmatrix}$$

$$\begin{pmatrix} \tau_{\|13}^{-1}\rho_{13} & \tau_{\|14}^{-1}\rho_{14} \\ \tau_{\|23}^{-1}\rho_{23} & \tau_{\|24}^{-1}\rho_{24} \\ \cdots & \tau_3^{-1}\rho_{33} - \tau_2^{-1}\rho_{22} - \tau_{\text{sti}}^{-1}\Delta\rho & \tau_{\|34}^{-1}\rho_{34} \\ \tau_{\|34}^{-1}\rho_{43} & \tau_4^{-1}\rho_{44} - \tau_1^{-1}\rho_{11} \end{pmatrix}, \tag{2.52}$$

where

$$\tau_{\text{sti}}^{-1} = \frac{c}{n_g}\sigma_{\text{op}}\Theta. \tag{2.53}$$

The variable Θ is the photon density in the cavity and $\Delta\rho$ is the population inversion, $\rho_{22} - \rho_{33}$. The left matrix in the commutator of equation 2.52 represents the Hamiltonian

of the two phonon wells and the active double-well interacting with each other by tunneling, as calculated in equation 2.8.

The last matrix on the right hand side represents the natural decay of populations and coherences when these terms are placed in nonequilibrium condition. The decay of the populations, ρ_{ii}, is given by the diagonal terms. For the lasing states, ($i = 2,\ 3$), these terms include the stimulated emission rate, τ_{sti}^{-1}, the expression of which is given by equation 2.53. Similar to equation 2.27, σ_{op} represents the optical intersubband cross section in cm^2, and reads as

$$\sigma_{\text{op}} = \frac{\pi e^2 n_g}{\epsilon_0 \epsilon_r c} |Z_{23}|^2 \omega \delta(\hbar\omega - E_{23}), \tag{2.54}$$

where c/n_g is the group velocity in the optical waveguide, Z_{23} is the matrix dipole moment between the lasing states, ω is the laser angular frequency. The dephasing time constants in the non-diagonal terms are calculated from equation 2.45. For the sake of simplicity one can assume the pure dephasing time constant (τ^*) for all the transitions are similar, except for the lasing transition. For the laser transition, the phase loss rate can be calculated as

$$\tau_{\parallel 23}^{-1} = (2\tau_2)^{-1} + (2\tau_3)^{-1} + 1/\tau_{23}^* \tag{2.55}$$

The current density of the system under study can be calculated using equation 2.49. After some algebra, the expression of current density, J, for the three-well THz QCL in Figure 2.10 becomes [66]

$$\begin{aligned} \frac{J}{eN_{2D}} = & \quad 2\Omega_{12}\Im(\rho_{12}) + 2\Omega_{13}\Im(\rho_{13}) + 2\Omega_{14}\Im(\rho_{14}) \\ & + \ 2\frac{Z_{22} - Z_{33}}{L_{\text{sp}}} \left(\Omega_{24}\Im(\rho_{24}) - \Omega_{12}\Im(\rho_{12})\right) \\ & - \ 2\frac{Z_{23}}{L_{\text{sp}}} \tau_{\parallel 23}^{-1} \Re(\rho_{32}), \end{aligned} \tag{2.56}$$

where , $L_{\text{sp}} \approx Z_{11} - Z_{44}$ is the superperiod of the active region, $Z_{22} - Z_{33}$ is the static dipole between the lasing states, Z_{23} is the dipole moment between the lasing states, $\Im()$

and $\Re()$ are the imaginary and real components of a complex entity. The first three terms represent the three tunneling currents departing from the injector state 1: injection Ω_{12}, wrong injection Ω_{13} and the negligible parasitic Ω_{14} channels. The fourth term is only a small correction, which takes into account the different centroids of the two lasing states in the active double-well. The structure in Figure 2.3 has relatively vertical optical intersubband transition ($f = 0.677$), and hence the static dipole is small. It ranges from -5 nm at 1 kV/cm to 2.6 nm at 14 kV/cm. The last term is directly related to the tunneling induced coherence between the lasing states. This coherence is induced by the leakage paths and the so-called *cross-terms*. The last two terms of equation 2.56 contributes to maximum of $\sim$5 % in the total current. The first two terms are the most dominant in this expression.

The solution of equation 2.52 provides all populations and coherence terms in the density matrix. The 4×4 commutation equation results in sixteen equations, one of which is linearly dependant to the rest. This equation is replaced by the charge conservation law, $\rho_{11} + \rho_{22} + \rho_{33} + \rho_{44} = 1$. The time evolution of the density matrix without laser induced coherences, therefore, can be rewritten as a 16×16 system of linear equations as $A[\rho] = C$. The complete equation set is presented in Appendix A.

Equation 2.52 can be numerically solved for the accurate solution of the density matrix elements. However, in the matrix A, if the cross-terms, $\Omega_{nm}\rho_{ij}$ with $nm \neq ij$ or ji are neglected, analytical formulas can be easily found. The cross-terms explain the indirect resonance between states 1 and 4 at 8.5 kV/cm, despite the fact that the parasitic coupling, $\hbar\Omega_{14}$, is in the μeV range. This is because several tunneling trajectories are bridging these states, which otherwise, would not be coupled if leakage paths were absent. For instance, states 2 and 3 develop a static coherence by the tunneling trajectories $2 \rightarrow 4 \rightarrow 3$ or $2 \rightarrow 1 \rightarrow 3$. These cross-terms are responsible of the pre-threshold shoulder in current-voltage characteristic that is observed in three-well designs (at $\sim$8-9 V) [102, 68, 61]. The

tunneling time of the four main tunneling channels are comparable, in the order of 1–10 ps, when levels 1 and 4 are both approximately equidistant in energy from the two lasing states. For instance, at 8.5 kV/cm the non-truncated solution of the three-well structure shows a strong mixing between levels 1 and 4 with an anticrossing energy of 0.7 meV. This strong *indirect coupling* between the injector and extractor states will be a source of leakage path. However, since the carriers falling on the extractor level are meant to be scattered efficiently to the next period injector level, the indirect leakage at 8.5 kV/cm does not alter the population inversion significantly.

The approximation of neglecting the cross-terms are justified beyond slightly below the threshold of the laser, due to the narrow resonance of this process. One can also neglect direct $1-4$ channel, due to μeV range direct coupling, $\hbar\Omega_{14}$, between levels 1 and 4 (Figure 2.4), and assume infinite T_{14}. The first two terms of equation 2.56 for the current density give

$$\begin{aligned} J &\approx eN_{2D}\frac{\hat{c}+\hat{d}\tau_2\tau_{\mathrm{sti}}^{-1}}{\hat{a}+\hat{b}\tau_2\tau_{\mathrm{sti}}^{-1}} \\ &= \frac{eN_{2D}}{\tau_{\mathrm{transit}}}, \end{aligned} \tag{2.57}$$

where

$$\begin{aligned} \hat{c}+\hat{d}\tau_2\tau_{\mathrm{sti}}^{-1} = \; & T_{13}\;\; T_{24}\big[1+\tau_2\tau_{\mathrm{sti}}^{-1}\big]+T_{24}\big[T_{12}+\tau_2+(\tau_2\tau_{\mathrm{sti}}^{-1})T_{12}\big] \\ & + \;\; T_{13}\big[\tau_2+(\tau_2\tau_{\mathrm{sti}}^{-1})T_{34}\big]+(T_{34}+T_{12})\tau_2+(\tau_2\tau_{\mathrm{sti}}^{-1})T_{12}T_{34}, \end{aligned} \tag{2.58}$$

and

$$\begin{aligned} \hat{a}+\hat{b}\tau_2\tau_{\mathrm{sti}}^{-1} = \; & T_{13}\;\; T_{24}\big[T_{34}+T_{12}+2\tau_2+2\tau_4+(\tau_2\tau_{\mathrm{sti}}^{-1})(3T_{34}+4\tau_4+T_{12})\big] \\ & + \;\; T_{24}\big[2T_{12}T_{34}+3T_{34}\tau_2+3T_{12}\tau_4+4\tau_2\tau_4+(\tau_2\tau_{\mathrm{sti}}^{-1})T_{12}(3T_{34}+4\tau_4)\big] \\ & + \;\; T_{13}\big[T_{12}\tau_2+T_{34}\tau_4+4\tau_2\tau_4+(\tau_2\tau_{\mathrm{sti}}^{-1})T_{34}(T_{12}+4\tau_4)\big] \\ & + \;\; 2T_{12}T_{34}(\tau_2+\tau_4)+4(T_{34}+T_{12})\tau_2\tau_4+4(\tau_2\tau_{\mathrm{sti}}^{-1})T_{12}T_{34}\tau_4. \end{aligned} \tag{2.59}$$

The population inversion, $\rho_{22} - \rho_{33}$, becomes

$$\Delta\rho = \frac{\hat{e}}{\hat{a} + \hat{b}\tau_2\tau_{\rm sti}^{-1}}, \tag{2.60}$$

where

$$\begin{aligned} \hat{e} &= T_{13}T_{24}\big[\tau_2 - T_{34} - \tau_4\big] - T_{24}T_{12}\big[T_{34} + \tau_4\big] \\ &\quad - T_{13}T_{34}\tau_4 - T_{12}T_{34}(\tau_4 + \tau_2). \end{aligned} \tag{2.61}$$

The ratio, $\eta_J = \hat{e}/\hat{c}$, is the product between population inversion and the transit time in the absence of laser field. $\hat{c}$ is defined from equation 2.58. It can be viewed as the *current efficiency* for inversion. By assuming a cavity mirror loss coefficient, α_M, an optical waveguide loss, α_W, and an optical mode overlap with the active region, Γ, the threshold population inversion, the threshold current, the stimulated emission rate and the total optical power, $P_{\rm op}$, easily become [66]

$$\Delta\rho_{th} = \frac{\alpha_M + \alpha_W}{N_{3D}\Gamma\sigma_{\rm op}} \tag{2.62}$$

$$J_{th} = eN_{2D}\left.\frac{\Delta\rho}{\eta_J}\right|_{th} = e\,\frac{L_{\rm sp}}{\sigma_{\rm op}\Gamma}\left.\frac{\hat{c}}{\hat{e}}\right|_{th}(\alpha_M + \alpha_W) \tag{2.63}$$

$$\tau_{\rm sti}^{-1} = \frac{\hat{a}}{\hat{b}\tau_2}\left(\frac{\Delta\rho|_{\Theta=0}}{\Delta\rho_{th}} - 1\right) \tag{2.64}$$

$$\begin{aligned} P_{\rm op} &= \hbar\omega V_c\alpha_M\frac{\hat{a}}{\hat{b}\sigma_{\rm op}\tau_2}\left(\frac{\Delta\rho|_{\Theta=0}}{\Delta\rho_{th}} - 1\right) \\ &= \hbar\omega V_c\alpha_M\frac{\hat{c}}{\hat{d}\sigma_{\rm op}\tau_2}\left(\frac{\eta_J J}{qN_{2D}\Delta\rho_{th}} - 1\right), \end{aligned} \tag{2.65}$$

where V_c is the volume of the cavity mode. The transit time before and after laser threshold reads

$$\left(\frac{1}{\tau_{\rm transit}}\right)_{I<I_{th}} = \frac{\hat{c}}{\hat{a}} \tag{2.66}$$

$$\left(\frac{1}{\tau_{\rm transit}}\right)_{I>I_{th}} = \left(\frac{\hat{c}}{\hat{a}} - \frac{\hat{d}}{\hat{b}}\right)\frac{\Delta\rho_{th}}{\Delta\rho|_{\Theta=0}} + \frac{\hat{d}}{\hat{b}}. \tag{2.67}$$

With this system, where tunneling leakage channels cannot be neglected, it is not possible to derive a simple analytical expression for the differential resistance at threshold. In a two-well QCL with one tunneling process, Kumar et *al.* have shown that the slope discontinuity of the current-voltage characteristic at threshold is simply related to the inversion population and the ratio of two intersubband scattering times[67]. With our system, one can only write a general expression for the discontinuity of the differential conductance at threshold [66],

$$\frac{1}{\widetilde{R}_{I=I_{th}^{+}}} - \frac{1}{\widetilde{R}_{I=I_{th}^{-}}} = \frac{1}{L_{\mathrm{ar}}} \left(eN_{2D}\Sigma \frac{\hat{d}}{\hat{b}}\bigg|_{E_{th}} - I_{th} \right) \frac{d(\Delta\rho/\Delta\rho_{th})}{dE}\bigg|_{th}, \tag{2.68}$$

where $\widetilde{R}$ is the differential resistance of the device, Σ is the area of the laser, and L_{ar} is the thickness of the active region. This expression involves the derivative of population inversion with respect to the electric field and the difference between the threshold current and the current at the same threshold electric field, E_{th}, of a hypothetic zero threshold device (first term inside the brackets).

The maximum operating temperature of the laser, $T_{\max}$, can be approximatively given by this condition,

$$\frac{\hat{e}}{\hat{a}}\bigg|_{E_{\mathrm{dsg}},\, T_{\max}} = \Delta\rho_{th}, \tag{2.69}$$

and the differential wall-plug efficiency is approximatively given by [66]

$$\frac{dP_{\mathrm{op}}}{dP_{\mathrm{elec}}} \approx \frac{\hbar\omega}{\hbar\omega + E_{\mathrm{LO}}} \frac{\alpha_M}{\alpha_M + \alpha_W} \frac{1}{\tau_2} \left[\frac{\hat{e}}{\hat{d}} + \frac{\widetilde{R}I}{L_{\mathrm{ar}}} \frac{d(\hat{e}/\hat{d})}{dE} - eN_{2D}\Sigma\Delta\rho_{th} \frac{\widetilde{R}}{L_{\mathrm{ar}}} \frac{d(\hat{c}/\hat{d})}{dE} \right]. \tag{2.70}$$

The internal quantum efficiency of the laser is represented by the bracket on the left hand-side of equation 2.70 divided by the upper lasing state lifetime. It can be roughly estimated by $\hat{e}/\hat{d}\tau_2$, which can be calculated by 2.58 and 2.61 and by approaching T_{13} towards infinity.

Simulated current densities, upper lasing state populations, population inversions and stimulated emission rates in the cavity are plotted in Figure 2.11. It shows different cases, where leakage tunneling paths are artificially turned on, or off, in order to visualize their

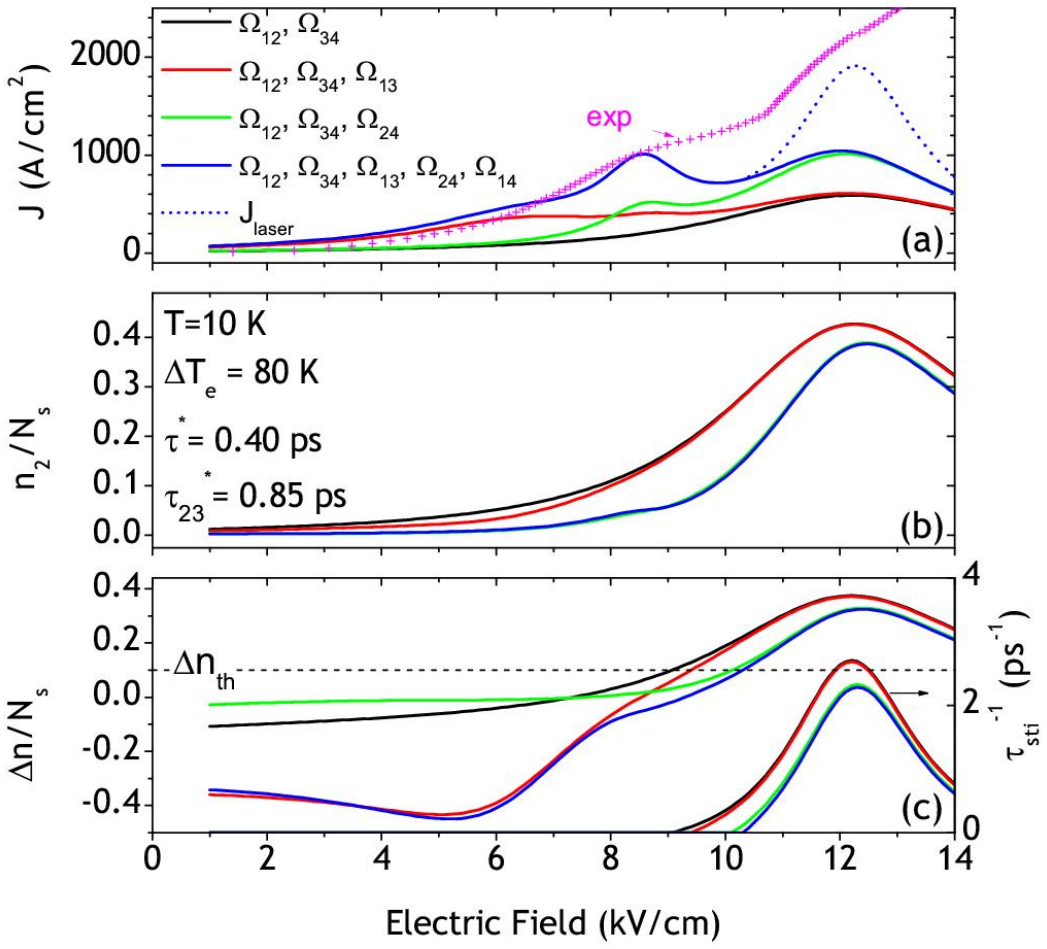

Figure 2.11: Simulation of (a) current density ; (b) upper laser state population ρ_{22}; (c) population inversion $\rho_{22} - \rho_{33}$ (left vertical axis) and stimulated emission rate $\tau_{\text{sti}}^{-1} = \sigma\Theta(c/n_g)$ (right vertical axis) without the laser induced coherence in the model. The lattice temperature is 10 K, the electron heating temperature ΔT_e is set constant at 80 K, the pure dephasing time constant in tunneling is $\tau^* = 0.4$ ps and in optical intersubband transition is $\tau_{23}^* = 0.85$ ps. In each sub-figure four cases are considered: no leakage (black curves), only injection side leakage (red curves), only extraction side leakage (green curves), and both leakage paths (blue curves). The J_{laser} is the lasing current density when $\Delta\rho_{th} = 0.1$.

impact. The values used in the simulations for the electron heating temperature (80 K), pure dephasing time constant in tunneling (0.4 ps) and optical intersubband transition (0.85 ps) were inferred by the fitting exercise in [66]. Panel (a) shows that the current density around the design electric field increases significantly by the wrong extraction channel, $2-4$, whereas the effect of the wrong injection, $1-3$, is not as severe. However, below threshold, the presence of all tunneling channels is important to model the large current increase by the aforementioned $1-4$ indirect coupling. For comparison, the electrical characteristics of a 0.1×1 mm^2 metal-metal ridge waveguide laser with a structural design identical to that reported in [65] is plotted. The kink of the experimental current density at 10.7 kV/cm and 1.4 kA/cm^2 corresponds to lasing threshold. Both contacts of this device were Ohmic with an e-beam sputter deposition and a consequent 15 s, 380°C rapid thermal annealing of Pd/Ge/Ti/Pt/Au with the thickness sequence 550/1000/250/550/5000Å. The material from [65] has been exhausted and the clone wafer (V610) shows higher threshold and lower maximum operating temperature than that of [65]. Nevertheless, the simulations with this simplified model are consistent with the experimental data: the order of magnitude for the peak current density is well predicted and the current density at the shoulder ($\sim$ 8.5 kV/cm) is close to experimental value. Figure 2.11(b) shows the depletion effect of upper lasing state by the wrong extraction, $2-4$, which results in a 14% decrease of the maximum population inversion at the design electric field, as shown in Figure 2.11(c). The last panel shows the wrong injection channel, $1-3$, is very active at its resonance (5.4 kV/cm), but looses its strength at the design electric field. For the laser action, the consequence of this channel is to delay the transparency electric field and the laser threshold slightly, without affecting the maximum population inversion and the laser emission. The picture is different for the wrong extraction channel, $2-4$, which delays significantly the transparency, the threshold and in total, affects the maximum population inversion, and hence the laser emission.

Without leakage channels, the population inversion is simply derived from equation

2.60 and given by

$$\Delta\rho\Big|_{\Omega_{13}=\Omega_{24}=0} = \frac{\tau_2 - T_{34} - \tau_4}{T_{34} + T_{12} + 2\tau_2 + 2\tau_4}, \tag{2.71}$$

and is represented by a green line in Figure 2.11(c). As mentioned in the discussion of equation 2.39, the upper lasing state lifetime τ_2 is strongly reduced at higher temperature. On the other side, the "effective lifetime" of the lower lasing state, $\tau_{\text{eff},\,3} = T_{34} + \tau_4$ [67], is weakly temperature dependent by the nature of the resonant phonon depopulation scheme. Therefore, it cannot compensate for the thermally activated τ_2. In other words, the depopulation scheme cannot sustain the increasing flow of carriers originating from the shortening of the upper lasing lifetime with temperature. This bottleneck at depopulation stage explains the degradation of population inversion with temperature.

From the above discussion, it is concluded that the wrong injection channel, on this particular design, does not severely limit the laser operation. It is showed that the $1-4$ indirect coupling is only a significant source of leakage at its resonance ($\sim$ 8.5 kV/cm). On the other hand, the wrong extraction channel increases the current density and slightly reduces the maximum population inversion. Therefore, the latter leakage channel is detrimental for CW operation and explains why the three-well design, with vertical transitions, does not work in this mode [103]. The channel $2-4$ is more to blame than $1-3$ because of the high coupling strength Ω_{24} and moreover, because of the high total phase loss rate of this tunneling, $\tau_{\|24}^{-1}$, which is limited by the fast phonon resonant scattering τ_4 (see equation 2.45). The tunneling resonance T_{24} will be broader than T_{13} and still reasonably fast at the design electric field, which means that the depletion $2 \rightarrow 4$ will be still active. In other words, at the design electric field, the upper lasing state population does not recover fully from the $2-4$ resonance taking place at 4.6 kV/cm. Of course, the effect of this shunt channel is more pronounced at higher upper lasing state lifetime, τ_2, i.e. at low temperature.

Figure 2.12(b) shows the four main tunnelings times versus electric field. At the design

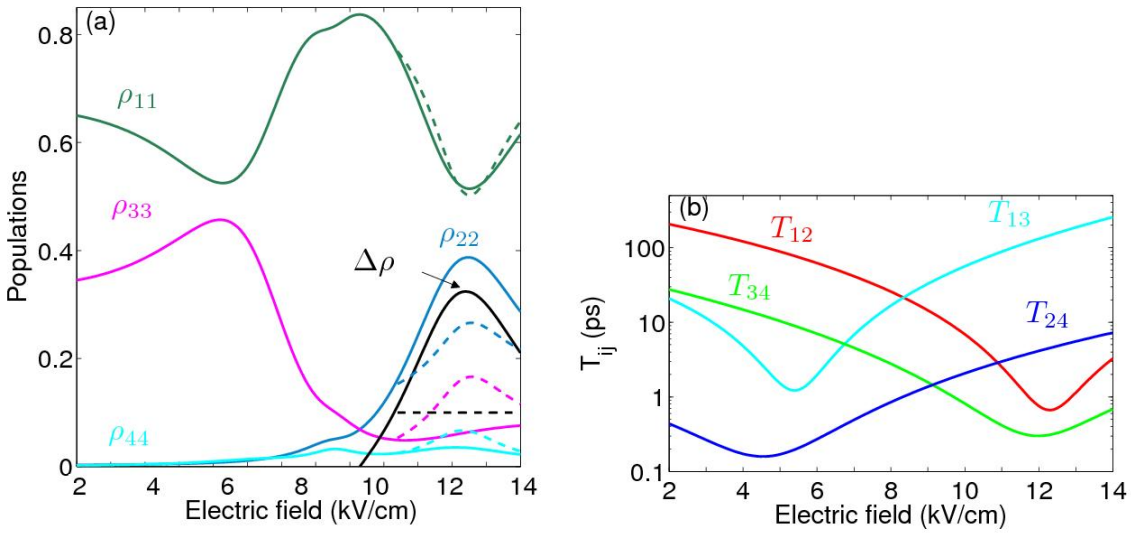

(a) (b)

Figure 2.12: Panel (a) shows the populations of all the states and the population inversion on a non-lasing device (solid lines) and on a lasing device with a threshold population inversion of 10% (dashed lines); and Panel (b) shows the four main tunneling times T_{ij} as defined by equation 2.47. Simulations are performed with the same parameters as Figure 2.11.

electric field, T_{24} is about $\sim$4 ps, while T_{13} is larger than 100 ps and hence cannot have a large influence. Around 8.5 kV/cm, the same panel shows that the four tunnelings times are comparable within an order of magnitude, which makes the building of a coherence between $1-4$ possible. The range of electric field for which these tunneling times are comparable is narrow. This explains the small fineness ($\pm$1.5 kV/cm) of the simulated indirect resonance between levels '1' and '2', $|\rho_{14}|$. Figure 2.12-a shows four populations in the non-lasing and lasing conditions. In the latter condition, the threshold population inversion, $\Delta\rho_{th}$, is fixed at 10% of the total number of carriers per period. We see that population of the injector state, ρ_{11}, quickly recovers from the resonance of the wrong injection, T_{13}. Around the resonance of the wrong extraction channel (4.6 kV/cm), level

4 is more populated than level 2. This is due to a combination of a strong resonance (high Ω_{24}) and other channels that also supply the extractor state. We see that all four populations respond around 8.5 kV/cm, where all four states are being coupled to each other to form the $1-4$ indirect resonance.

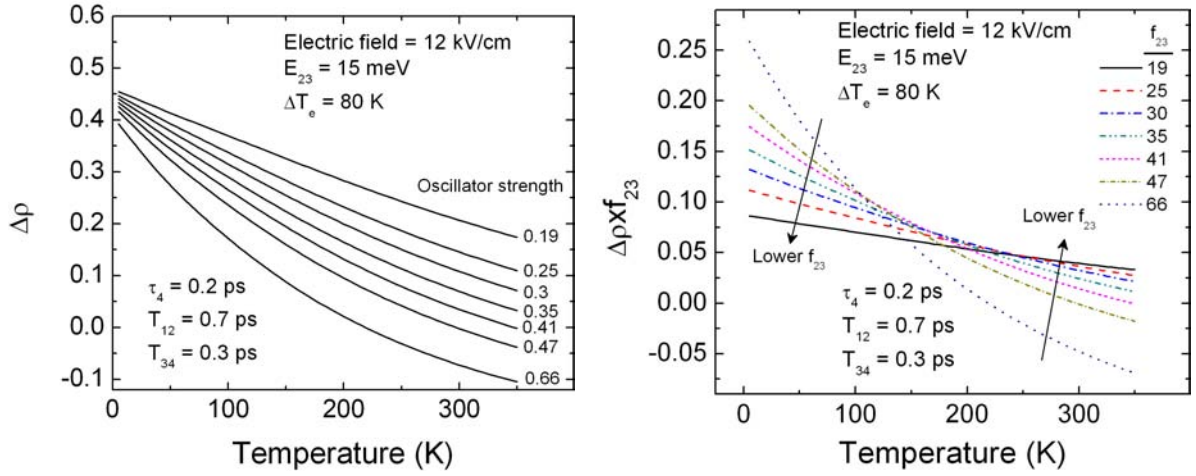

(a) (b)

Figure 2.13: (a) Population inversion between the lasing states of three-well THz QCLs with various oscillator strengths versus lattice temperature; No leakage channel is considered, as in equation 2.71. Changing of the rate over the range of temperature decreases for lower oscillator strengths. (b) Product of $\Delta\rho \times f_{23}$ versus temperature for various oscillator strengths. Around 150 K, oscillator strength values between of 0.3 and 0.47 show the highest values.

Figure 2.13-a shows the temperature dependance of the population inversion ($\Delta\rho$) for three-well THz QCL with the same degrees of diagonality as in Figure 2.7. All the graphs are calculated using equation 2.71, with phonon scattering time of $\tau_4 = 0.2$ ps, and tunneling time of $T_{12} = 0.7$ ps and $T_{34} = 0.3$ ps, which is read from Figure 2.12(b) at design electric field ($E = 12$ kV/cm). In an ideal case of $\tau_2 \to \infty$, the population inversion approaches towards 0.5. This is expected, as with the long τ_2 all the carriers are equally

distributed between levels '1' and '2'. In the discussion for Figure 2.7, it was observed that the non-radiative lifetime of carriers on level '2' is very high at low temperatures and decreases with temperature. Therefore, at low temperatures (i.e. 5 K) the population inversion of the laser is very close to but lower than 0.5. $\Delta\rho$ for designs with higher level of diagonality is closer to 0.5, due to the slightly longer τ_2. By increasing the temperature, the $\Delta\rho$ for all levels of diagonality drops. This is the main reason why THz QCL devices can be operated only at cryogenic temperatures. The same as observed in the discussion for Figure 2.71, the rate of the $\Delta\rho$ change for more diagonal designs is smaller, that results in higher $\Delta\rho$ at high temperatures for diagonal designs. The maximum operating temperature (T_{max}) of the THz QCL depends on the temperature dependence of the gain, which is proportional to the $\Delta\rho \times f_{23}$ (equation 2.27). Figure 2.13-b shows the product of $\Delta\rho \times f_{23}$ versus temperature for various oscillator strengths. The gain for very diagonal designs is reduced due to the small oscillator strength (f_{23}). For medium range of diagonality the gain stays high at higher temperatures. Around 150 K, oscillator strength values between of 0.3 and 0.47 show the highest values. This explains higher temperature operation of diagonal designs [61].

To illustrate the effect of wrong extraction around the design electric field, the approximate formulas that are derived from equations 2.57 and 2.60, with the assumption of an infinitely long tunneling time T_{13}. The transit time reads as

$$\tau_{\text{transit}} = \frac{T_{24}}{T_{24}+\tau_2}\left(T_{34}+T_{12}+2\tau_2+2\tau_4\right)+\frac{\left(T_{12}\tau_2+T_{34}\tau_4+4\tau_2\tau_4\right)}{T_{24}+\tau_2}. \tag{2.72}$$

The population inversion becomes

$$\Delta\rho = \frac{\left(\tau_2 - T_{34} - \tau_4\right) - \dfrac{T_{34}\tau_4}{T_{24}}}{\left(T_{34}+T_{12}+2\tau_2+2\tau_4\right)+\dfrac{\left(T_{12}\tau_2+T_{34}\tau_4+4\tau_2\tau_4\right)}{T_{24}}}.$$

If possible, the shunting effect by the wrong extraction channel, represented by the factor $T_{24}/(T_{24}+\tau_2)$ in equation 2.72, should be minimized. This observation brings an

additional argument for a three-well QCL design based on *diagonal* transitions, which demonstrated the record $T_{\max}$, a rather low threshold current density[61] and even CW operation [67]. The discussion in this section tried to visualize the transfer of charges versus electric field. In the next section, we will see how the gain profile is modified by the insertion of the laser interaction, Ω_L, in the Hamiltonian.

2.4 Gain spectrum model

In the Hamiltonian used for solving the master equation in previous section (equation 2.8), the coherence induced by the laser action (ρ_{23} and ρ_{32}) was not included. Therefore, the density matrix formalism could not calculate for the laser coherence term. In this section, the density matrix model is re-solved after including the laser coherence terms, and the details of the gain is discussed.

2.4.1 Derivation of the gain

When introducing the laser Rabi frequency in the master equation of time evolution of the density matrix, the equation 2.44 is written as

$$\begin{aligned}\frac{d\rho}{dt} &= \frac{1}{\jmath\hbar}\left[\begin{pmatrix} E_1 & \hbar\Omega_{12} & \hbar\Omega_{13} & \hbar\Omega_{14} \\ \hbar\Omega_{12} & E_2 & \Omega_L\cos(\omega t) & \hbar\Omega_{24} \\ \hbar\Omega_{13} & \Omega_L\cos(\omega t) & E_3 & \hbar\Omega_{34} \\ \hbar\Omega_{14} & \hbar\Omega_{24} & \hbar\Omega_{34} & E_4 \end{pmatrix}, \begin{pmatrix} \rho_{11} & \rho_{12} & \rho_{13} & \rho_{14} \\ \rho_{21} & \rho_{22} & \rho_{23} & \rho_{24} \\ \rho_{31} & \rho_{32} & \rho_{33} & \rho_{34} \\ \rho_{41} & \rho_{42} & \rho_{43} & \rho_{44} \end{pmatrix}\right] \\ &- \begin{pmatrix} \tau_1^{-1}\rho_{11} - \tau_4^{-1}\rho_{44} & \tau_{\|12}^{-1}\rho_{12} & \tau_{\|13}^{-1}\rho_{13} & \tau_{\|14}^{-1}\rho_{14} \\ \tau_{\|12}^{-1}\rho_{12} & \tau_2^{-1}\rho_{22} - \tau_3^{-1}\rho_{33} & \tau_{\|23}^{-1}\rho_{23} & \tau_{\|24}^{-1}\rho_{24} \\ \tau_{\|13}^{-1}\rho_{31} & \tau_{\|23}^{-1}\rho_{32} & \tau_3^{-1}\rho_{33} - \tau_2^{-1}\rho_{22} & \tau_{\|34}^{-1}\rho_{34} \\ \tau_{\|14}^{-1}\rho_{41} & \tau_{\|24}^{-1}\rho_{42} & \tau_{\|34}^{-1}\rho_{43} & \tau_4^{-1}\rho_{44} - \tau_1^{-1}\rho_{11} \end{pmatrix}.\end{aligned} \tag{2.73}$$

The laser field, which oscillates at the angular frequency ω, can potentially induce oscillating coherences between states that have energy spacing close to $\hbar\omega$. For small injection and extraction detuning values, $\Delta_{12} \approx \Delta_{34} \approx 0$, i.e. close to the design electric field, we can use the *rotating wave approximation* [66]. Keeping in mind that, in previous section, the static coherences between any combination of states in the absence of laser field were found. For equation 2.73, the solutions for the coherences should be in the form of

$$\rho_{12} = \rho_{12}^{(0)} \tag{2.74a}$$

$$\rho_{13} = \tilde{\rho}_{13} e^{-\jmath\omega t} + \rho_{13}^{(0)} \tag{2.74b}$$

$$\rho_{14} = \tilde{\rho}_{14} e^{-\jmath\omega t} + \rho_{14}^{(0)} \tag{2.74c}$$

$$\rho_{23} = \tilde{\rho}_{23} e^{-\jmath\omega t} + \rho_{23}^{(0)} \tag{2.74d}$$

$$\rho_{24} = \tilde{\rho}_{24} e^{-\jmath\omega t} + \rho_{24}^{(0)} \tag{2.74e}$$

$$\rho_{34} = \rho_{34}^{(0)}, \tag{2.74f}$$

where $\rho_{ij}^{(0)}$ is the static tunneling induced coherence between states i and j, and $\tilde{\rho}_{ij}$ is the laser induced coherence between the same states. Here, the populations and coherences are calculated for a vanishing Rabi frequency, which implies that the solutions are valid below threshold and slightly above (weak field regime). As expected, when Ω_L goes to zero, the static terms of the density matrix, $\rho_{ij}^{(0)}$, fulfill the previous master equation 2.52, with a vanishing stimulated emission rate, $\tau_{\text{sti}}^{-1} = 0$. If laser intensity is not negligible, the right hand side of equation 2.52 is changed and no simple analytical can be found. Kumar showed numerical solutions of gain broadening by a strong stimulated emission rate in a three-level system with one injection tunneling channel [4]. The four oscillating coherences

fulfil a simple system of linear equations,

$$\frac{\Omega_L}{2}\begin{pmatrix}\rho_{12}^{(0)}\\0\\\rho_{22}^{(0)}-\rho_{33}^{(0)}\\-\rho_{34}^{(0)}\end{pmatrix}=\begin{pmatrix}\Gamma_{13}&-\Omega_{34}&\Omega_{12}&0\\-\Omega_{34}&\Gamma_{14}&0&\Omega_{12}\\\Omega_{12}&0&\Gamma_{23}&-\Omega_{34}\\0&\Omega_{12}&-\Omega_{34}&\Gamma_{24}\end{pmatrix}\times\begin{pmatrix}\tilde{\rho}_{13}\\\tilde{\rho}_{14}\\\tilde{\rho}_{23}\\\tilde{\rho}_{24}\end{pmatrix},\tag{2.75}$$

where Γ_{ij} is the complex detuning of states i and j with respect to the laser frequency,

$$\Gamma_{ij}=(\Delta_{ij}-\omega)-\jmath\tau_{\|ij}^{-1}.\tag{2.76}$$

The solution of equation 2.75 is found as

$$\begin{aligned}\frac{\tilde{\rho}_{23}}{\Omega_L/2}=&\\&(\rho_{22}^{(0)}-\rho_{33}^{(0)})\frac{\Gamma_{13}\Gamma_{14}\Gamma_{24}-\Omega_{12}^2\Gamma_{13}-\Omega_{34}^2\Gamma_{24}}{(\Omega_{34}^2-\Omega_{12}^2)^2-\Omega_{34}^2(\Gamma_{13}\Gamma_{14}+\Gamma_{23}\Gamma_{24})-\Omega_{12}^2(\Gamma_{13}\Gamma_{23}+\Gamma_{14}\Gamma_{24})+\Gamma_{13}\Gamma_{14}\Gamma_{23}\Gamma_{24}}\\&+\rho_{12}^{(0)}\Omega_{12}\frac{\Omega_{12}^2-\Omega_{34}^2-\Gamma_{14}\Gamma_{24}}{(\Omega_{34}^2-\Omega_{12}^2)^2-\Omega_{34}^2(\Gamma_{13}\Gamma_{14}+\Gamma_{23}\Gamma_{24})-\Omega_{12}^2(\Gamma_{13}\Gamma_{23}+\Gamma_{14}\Gamma_{24})+\Gamma_{13}\Gamma_{14}\Gamma_{23}\Gamma_{24}}\\&+\rho_{34}^{(0)}\Omega_{34}\frac{\Omega_{34}^2-\Omega_{12}^2-\Gamma_{13}\Gamma_{14}}{(\Omega_{34}^2-\Omega_{12}^2)^2-\Omega_{34}^2(\Gamma_{13}\Gamma_{14}+\Gamma_{23}\Gamma_{24})-\Omega_{12}^2(\Gamma_{13}\Gamma_{23}+\Gamma_{14}\Gamma_{24})+\Gamma_{13}\Gamma_{14}\Gamma_{23}\Gamma_{24}},\end{aligned}\tag{2.77}$$

from which the gain/absorption coefficient, G_{op}, can be derived as [66]

$$G_{\text{op}}=\frac{N_{3D}e^2|Z_{23}|^2n_g\omega}{\epsilon_0\epsilon_r c\hbar}\Im\left(\frac{\tilde{\rho}_{23}}{\Omega_L/2}\right).\tag{2.78}$$

To estimate the gain with equation 2.77, it is also useful to get the analytical expressions of injection $\rho_{12}^{(0)}$ and extraction $\rho_{34}^{(0)}$ coherences, in the absence of laser field ($\Theta=0$), from

solution of equation 2.52

$$\rho_{12}^{(0)} = \frac{(\jmath + \Delta_{12}\tau_{\parallel 12})/\Omega_{12}}{2\tau_{\text{transit}}|_{\Theta=0}} \frac{T_{13}T_{24} + T_{24}(T_{34} + \tau_4) + T_{13}\tau_2 + T_{34}(\tau_2 + \tau_4)}{T_{13}T_{24} + T_{24}(T_{12} + \tau_2) + T_{13}\tau_2 + (T_{34} + T_{12})\tau_2}, \quad (2.79)$$

$$\rho_{34}^{(0)} = \frac{(\jmath + \Delta_{34}\tau_{\parallel 34})/\Omega_{34}}{2\tau_{\text{transit}}|_{\Theta=0}} \frac{T_{13}T_{24} + T_{24}(T_{12} + \tau_2) + T_{13}\tau_4 + T_{12}(\tau_2 + \tau_4)}{T_{13}T_{24} + T_{24}(T_{12} + \tau_2) + T_{13}\tau_2 + (T_{34} + T_{12})\tau_2}, \quad (2.80)$$

where $2\tau_{\text{transit}}|_{\Theta=0}$ is obtained from equation 2.66.

2.4.2 THz QCL gain behavior

To illustrate the effects of injection and extraction tunnelings on the gain, the maximum gain versus the thicknesses of injection and extraction barriers is computed, in two cases. First, a voltage independent Lorentzian gain profile with a $\hbar\tau_{\parallel 23}^{-1}$ half-width at half-maximum is considered. In this situation, the coherence $\tilde{\rho}_{23}$ depends only on population inversion, $2\tilde{\rho}_{23}/\Omega_L = (\rho_{22}^{(0)} - \rho_{33}^{(0)})/\Gamma_{23}$. The second case considers the complete model summarized in equation 2.77. The results of this calculation for $\tau^* = 0.4$ ps, $T = 50$ K, $\Delta T_e = 80$ K, $\tau_{23}^* = 0.85$ ps are plotted in Figure 2.14. On one hand, panel (a) shows that the maximum population inversion is obtained for ~ 33 Å thick barriers. On the other hand, the complete model (Figure 2.14-b) suggests further isolating the active double-well from the phonon wells, with ~ 45 Å barriers. The full model recommends to limit the tunneling interferences by increasing the barriers, even if these larger barriers decrease the population inversion (see equation 2.71). Getting the correct extraction barrier is more critical than the correct injection barrier, as a thick extraction barrier can penalize the depopulation mechanism. It is also observed that the peak gain with the complete model is significantly smaller than the one predicted with a Lorentzian model, which is classically observed for laser diodes [44].

The full gain spectra, as in equations 2.77 and 2.78, at 10 K for different electric

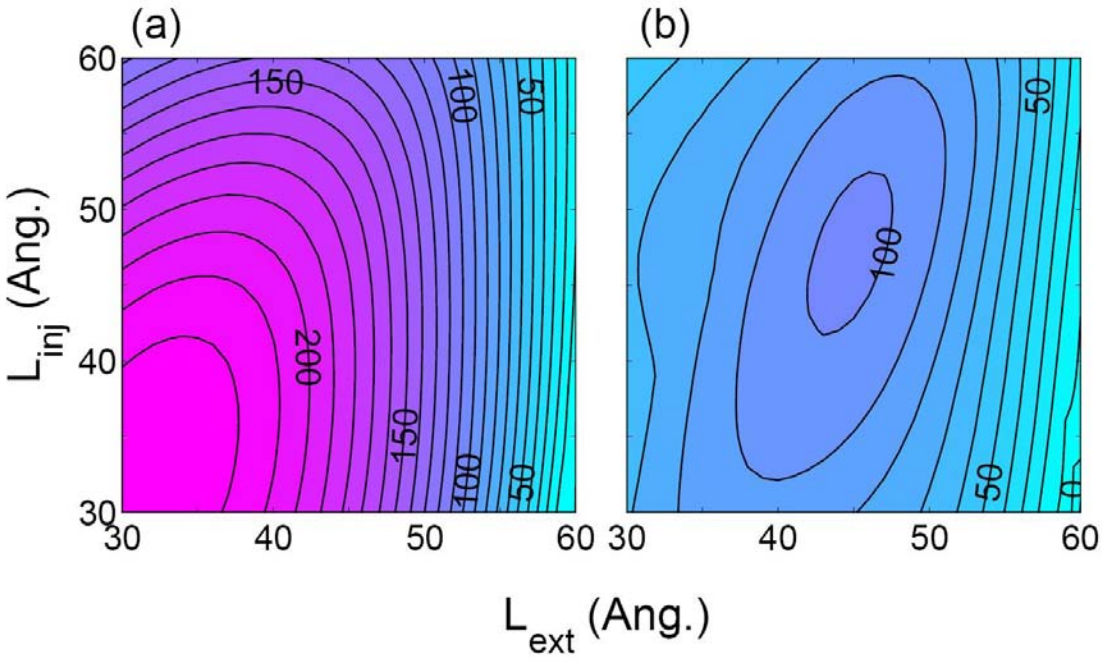

Figure 2.14: Simulation results for the maximum gain (in cm^{-1}) as a function of injection and extraction barrier thicknesses, with $\tau^* = 0.4$ ps, $\tau_{23}^* = 0.85$ ps, $T = 50$ K and $\Delta T_e = 80$ K. In panel (a), the gain spectrum is assumed to be a voltage independent Lorentzian with a $(\pi\tau_{23}^*)^{-1} = 0.375$ THz full-width at half-maximum. In panel (b) the complete gain model of equation 2.77 is used. For the sake of comparison, the same color scale is used in both panels.

fields, as well as the peak position and the two half-width at half-maximum points, are displayed in Figure 2.15. In this figure, L_{inj} and L_{ext} denote the injection and extraction barrier thicknesses, repressively. The broadest spectra are obtained around the design electric field. At this bias, the curves show a 5 meV FWHM, a value between $2\hbar\Omega_{34}$ and $2\hbar(\Omega_{12} + \Omega_{34})$. Below the design electric field, the gain shows a peak at a photon energy higher than E_{23}, and above the design electric it is red-shifted relatively to E_{23}.

Equation 2.77 can be decomposed into several terms that are associated with different

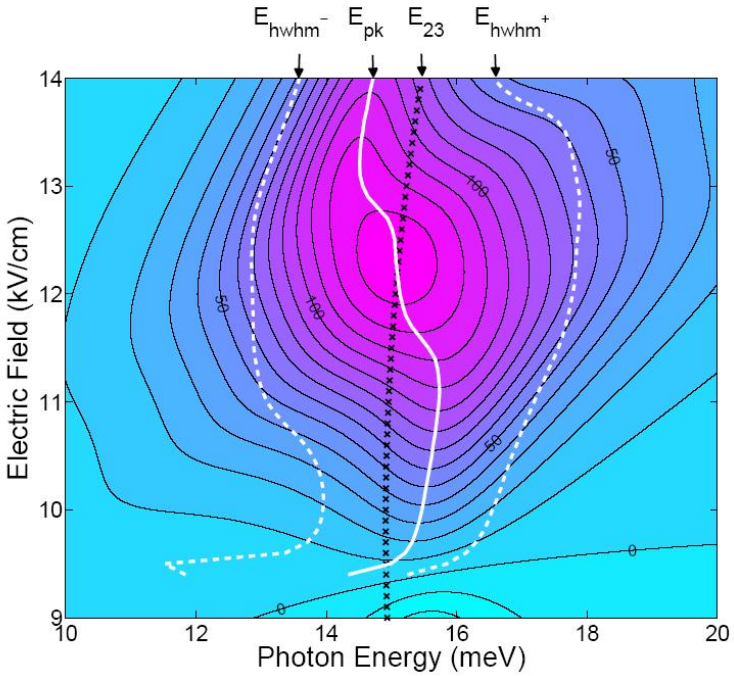

Figure 2.15: Contour plot of the gain spectrum for different electric fields. The lattice temperature is 10 K, the electron heating temperature ΔT_e is fixed at 80 K, the pure dephasing time constant in tunneling is $\tau^* = 0.4$ ps and in optical intersubband transition is $\tau_{23}^* = 0.85$ ps. The crossed-dotted line represents the position of $E_2 - E_3$ as a function of electric field (quadratic Stark effect). The white-solid line represents the position of the peak gain. Relatively to E_{23}, the peak gain is blue-shifted before the design electric, and red-shifted after. The white-dashed lines represent the position the two points at half-width at half-maximum. The full-width at half-maximum is 5 meV at 12.5 kV/cm. The unit of gain is cm^{-1}.

physical processes. From this point on, the first term on the right-hand side of eqaution 2.77 proportional to population inversion is called the *linear* component of the gain. It is the dominant component and represents a strongly modified Lorentzian gain profile under the effect of coherent injection and extraction. The two other terms, which are not linked

to the population inversion, are called the *nonlinear* components of the gain.

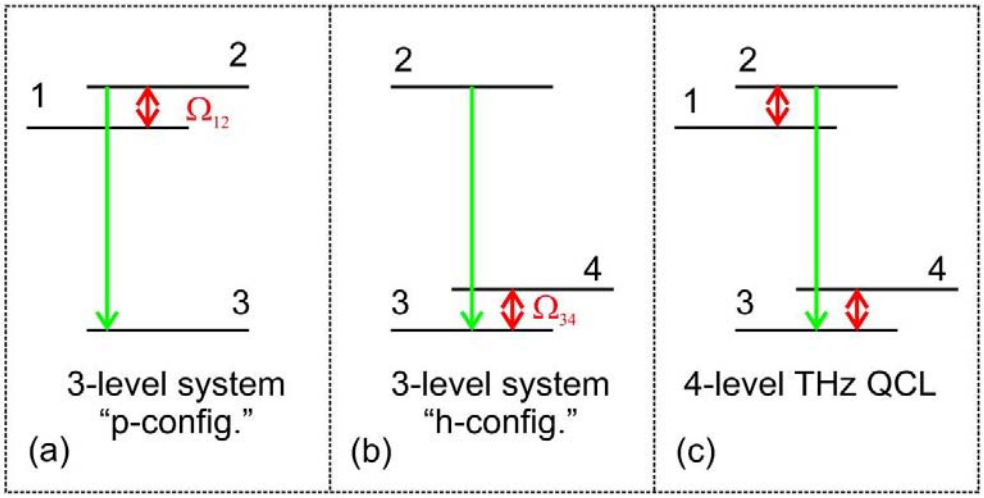

Figure 2.16: (a) Schematic representation of a 3-level system in p-configuration, where the coherence between the two highest states is determined by a field (laser, tunneling) with a coupling strength Ω_{12}. (b) Schematic of h-configuration, where the coherence between the two lowest states is determined by a field Ω_{34}. (c) Schematic representation of a 4-level system, such as the three-well THz QCL, which can be viewed as the sum of p and h-configurations.

If the extraction coupling Ω_{34} and the extractor state 4 are ignored in equation 2.77, and if the non-desirable tunneling couplings, $\Omega_{13,\,24,\,14}$, are neglected, one finds the gain of a three-state system with one injection tunneling as demonstrated in [104],

$$\frac{\tilde{\rho}_{23}}{\Omega_L/2} = \frac{(\rho_{22}^{(0)} - \rho_{33}^{(0)}) - (\rho_{11}^{(0)} - \rho_{22}^{(0)})\dfrac{\Omega_{12}^2}{\Gamma_{12}\Gamma_{13}}}{\Gamma_{23} - \dfrac{\Omega_{12}^2}{\Gamma_{13}}}, \tag{2.81}$$

where Γ_{12} is the complex detuning at the injection side, $\Delta_{12} - \jmath\tau_{\|12}^{-1}$. It is interesting to note that this latter expression reminds the gain of a three-level system in the p-configuration, in which the coherence between the two highest levels, 1 and 2, is prepared by an external pump laser field (see Figure 2.16-a). This system has been extensively studied for

its potential in amplification without population inversion [105]. Recently, lasing by an intersubband Stokes Raman process was demonstrated inside a mid-infrared QCL acting like a pump [106]. The gain of this Raman laser is modeled like equation 2.81. In our lasers, the only difference comes from the injection tunneling Rabi frequency, which drives the coherence between states 1 and 2. The second term of the numerator in equation 2.81, proportional to $\rho_{11}^{(0)} - \rho_{22}^{(0)}$, is associated with a stimulated anti-Stokes scattering process. For positive population difference, $\rho_{11}^{(0)} - \rho_{22}^{(0)} > 0$, this nonlinear gain term is maximum around $\hbar\omega \approx E_{13}$ and is highly dispersive. Similar to [104], the second term of equation 2.77 can be identified as a third order process which resonantly scatters carriers from the injector level 1 to lower lasing state 3 under the "injection field" Ω_{12}.

Similarly, when ignoring Ω_{12} and the injector level 1 in equation 2.77, and neglecting the same tunneling couplings, an expression very similar to equation 2.81 is derived as

$$\frac{\tilde{\rho}_{23}}{\Omega_L/2} = \frac{(\rho_{22}^{(0)} - \rho_{33}^{(0)}) - (\rho_{33}^{(0)} - \rho_{44}^{(0)})\dfrac{\Omega_{34}^2}{\Gamma_{34}\Gamma_{24}}}{\Gamma_{23} - \dfrac{\Omega_{34}^2}{\Gamma_{24}}}, \tag{2.82}$$

where Γ_{34} is the complex detuning at the extraction side, $\Delta_{34} - \jmath\tau_{\|34}^{-1}$. This expression reminds us the gain of a three-level system in the h-configuration [105], in which the coherence between the two lowest levels, 3 and 4, is prepared by a pump laser (see Figure 2.16-b). For positive population difference, $\rho_{33}^{(0)} - \rho_{44}^{(0)} > 0$, the nonlinear gain term is maximum around $\hbar\omega \approx E_{24}$. The third term of equation 2.77 represents the stimulated scattering from the upper lasing state 2 to the extractor level 4 via the "extraction field" Ω_{34}.

The expression of equation 2.77 is, therefore, simply modeling the sum of p and h-configurations, where two coherences between two highest and two lowest energy states are electrically driven by tunneling (see Figure 2.16-c). The effects of the non-desirable tunneling couplings, $\Omega_{13,\,24,\,14}$, on the gain are hidden in $\rho_{22}^{(0)} - \rho_{33}^{(0)}$, $\rho_{12}^{(0)}$ and $\rho_{34}^{(0)}$.

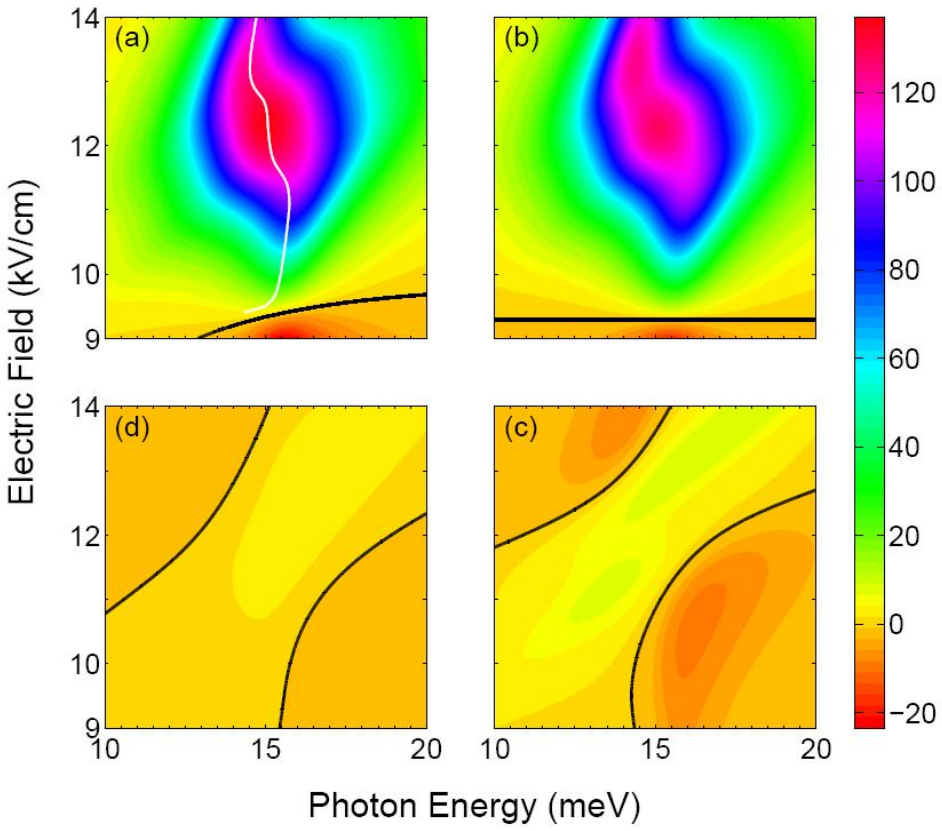

Figure 2.17: Four contour plots of the total gain (a) at 10 K, showing all three components as decomposed in equation 2.77. The first term depending on $(\rho_{22}^{(0)} - \rho_{33}^{(0)})$ is displayed in panel (b), the second term depending on $\rho_{12}^{(0)}$ is on panel (c), and finally, the third term depending on $\rho_{34}^{(0)}$ is on panel (d). The dispersive nonlinear gain in panel (c) is strong enough to change the linear gain contour (panel (b)) into a different total gain contour (panel (a)). The iso-gain lines at 0 cm^{-1} are displayed by a solid black line. The same parameters as in Figure 2.15 are used in the simulations. The thin white line on panel (a) shows the position of the peak gain versus electric field. Globally, the total gain is characterized by a negative Stark effect, i.e. a decrease of peak frequency with electric field. The unit of gain is cm^{-1}.

It is instructive to report the relative strength of the three terms in equation 2.77. Figure 2.17 displays the contribution of each term (panels b-d) to the total gain (panel a). The input parameters used during the simulation are $T = 10$ K, $\tau^* = 0.4$ ps, $\tau_{23}^* = 0.85$ ps and $\Delta T_e = 80$ K. By comparing the total gain (panel a) and the linear gain (panel b), one can see that the nonlinear gain of the second term (panel c) has an non-negligible impact. This term gives an additional anti-Stokes gain at the photon energy around E_{13}, and is strongly dispersive. The maximum of the sum of two nonlinear terms is about $\sim$10% of the maximum linear gain. This is small, but the relative contribution of nonlinear gain is actually higher below or above the design electric field, i.e when the population inversion is not maximum. At the design electric field, the peaks of the linear and nonlinear gains coincide in energy, but the linear gain has a slight negative Stark effect, and the nonlinear gain shows a strong positive Stark effect [66]. This observation suggests that the nonlinear component can potentially induce extra structures in the gain spectrum (shoulder, additional peak) when levels are not aligned, i.e. below or above the design electric field. Our numerical applications confirm the nonlinear terms of the gain are more active in the THz than in the Mid-IR QCLs because of the relatively long dephasing time. Unlike in Mid-IR QCLs, the dephasing time is not limited by interface roughness scattering in THz devices [104]. In THz QCLs, the coupling strengths $\Omega_{12,\,34}$ are comparable to the dephasing rates $\tau_{\parallel 12,\,34}$ and therefore, enhances the contribution of the nonlinear gain. At 10 K, the third term is about one third of the second term because of the smaller coherence $\rho_{34}^{(0)} < \rho_{12}^{(0)}$, which comes from $\tau_4 \ll \tau_2$ and $\Omega_{34} > \Omega_{12}$ (see equations 2.79 and 2.80).

Figure 2.18 shows that, as the temperature is raised to 140 K and the population inversion is lowered, the relative contribution of the two nonlinear gain terms increases significantly. The same figure shows that below (above) 10.9 (13.5) kV/cm and for photon energies lower (higher) than E_{23} the gain is positive, while the population inversion is negative. Close to the maximum operating temperature, the THz QCL works in a regime where the nonlinear gain plays an important role. At 140 K, the peak gain is blue-shifted with the

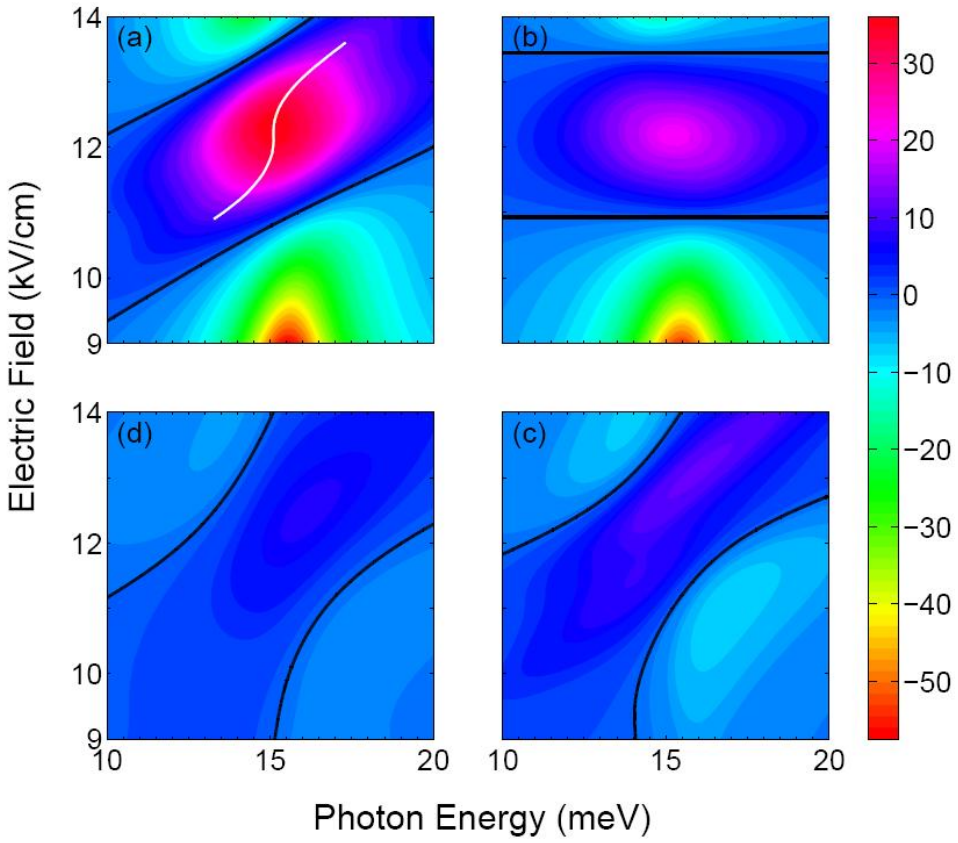

Figure 2.18: Contour plots of the total gain and its three components, like in Figure 2.17, but at $T = 140$ K. The thin white line on panel (a) shows the positive Stark effect of the peak gain, i.e. an increase of peak frequency with electric field.

electric field (Figure 2.18-a) because of the stronger contribution of nonlinear terms. At 10 K, the opposite situation is expected, the peak is mostly red shifted (Figure 2.17-a) by the large contribution of the linear component. Therefore, measurement of spectra voltage dependance for different temperatures might be able to confirm the contribution of the nonlinear gain.

2.4.3 Double-peaked gain

As explained in [67], the large gain linewidth mainly comes from the extraction tunneling mechanism. More precisely, it comes from the anticrossing between 3 and 4, and from the fast "effective lifetime" for the lower lasing state, $\tau_{\text{eff},\,3} = T_{34} + \tau_4$, which also depends on the extraction coupling. In the same reference, a convenient criteria was given for double-peaked gain around the design electric field. Several groups have observed dual-wavelength operation of THz QCLs, with modes 2.5–3 meV apart [67, 107]. This has been attributed to the anticrossing on the injection side[107] or extraction side[67].

The analytical model presented in this chapter can identify which term is at the origin of a multi-peaked gain spectrum. Figure 2.19 shows the number of peaks of the imaginary part of the linear gain term of equation 2.77, as a function of the injection and the extraction coupling strengths. This calculation is performed at perfect injection and extraction resonance conditions, i.e. $\Delta_{12} = \Delta_{34} = 0$. This "phase diagram" shows that a double-peaked gain behavior occurs if, at least, one of the coupling strengths, Ω_{ij}, is larger than a limit value, $\widehat{\Omega}_{ij}$. The higher the coupling on the injection or extraction side, the higher the ratio $\Omega_{ij}/\widehat{\Omega}_{ij}$ on the other side is required to obtain a double-peaked linear gain. It is observed, when two tunneling couplings from injector and extractor sides have comparable strengths, the gain spectrum shows single peak. Qualitatively, this can be explained by the large broadening of the transitions and the small photon energy difference, $2|\Omega_{12} - \Omega_{34}|$, between the doublets on the injection and extraction sides. But, as the coupling strengths become unbalanced in favor of either one of the sides, the double peak behavior associated with either the injection or extraction appears. In this case, it means that the coherent injection or extraction is sufficiently strong to reveal the existence of its associated dressed states in the gain spectrum.

In case the resonance conditions are not perfectly met, $\Delta_{12} \neq 0$ and/or $\Delta_{34} \neq 0$, we intuitively expect the double peak behavior to appear later, i.e. for stronger coupling

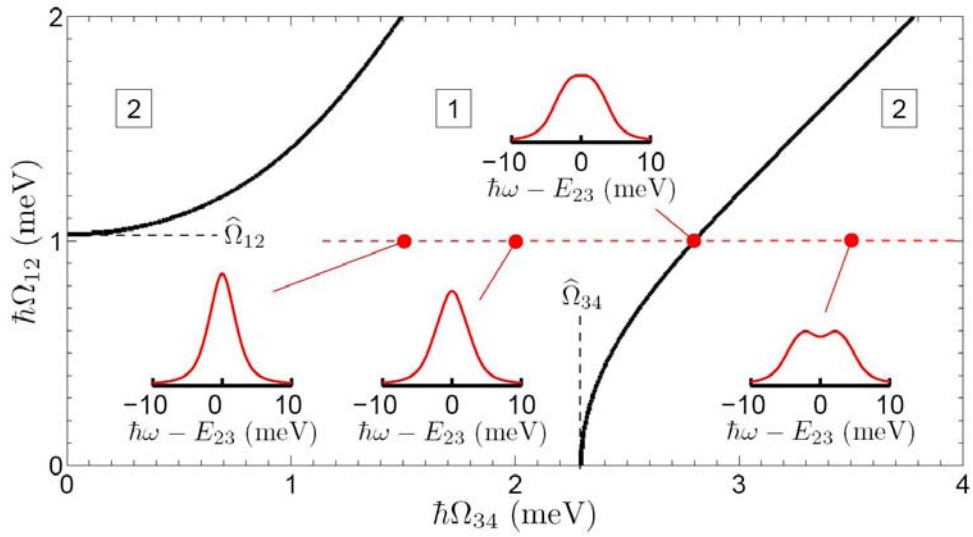

Figure 2.19: The "phase" diagram of number of peaks in the spectrum of the linear component of gain versus the extraction and injection couplings. The number of peaks are indicated in square boxes. The calculation is performed for perfect alignment of states at the injection and extraction, $\Delta_{12} = \Delta_{34} = 0$. The parameters used are $\tau^* = 0.4$ ps, $\tau_{23}^* = 0.85$ ps and $\tau_2 = 2$ ps. Four examples of gain spectra are given at $\Omega_{12} = 1$ meV, for different extraction couplings $\Omega_{34} = 1.5,\ 2,\ 2.8,\ 3.5$ meV. At $\Omega_{34} = 2.8$ meV, the linear gain is at the boundary of having between 1 or 2 peaks. For the sake of comparison, the graphs in the insets are plotted with the same vertical scale. The broadening of the gain by the extraction coupling is obvious.

strengths. In such a case, in a phase diagram like Figure 2.19, the domain of single-peaked gain is enlarged.

To understand such a behavior, the linear gain of a three-level system in the p- and h-configurations, have to investigated. In either of these cases, only tunneling coupling at one of the barrier is considered, in resonance condition. One can demonstrate that the imaginary part of the linear gain in equation 2.81 and 2.82 shows double peak behavior

when

$$\Omega_{12} > \widehat{\Omega}_{12} = \frac{\tau_{\|13}^{-1}}{\sqrt{2+\frac{\tau_{\|13}}{\tau_{\|23}}}} \tag{2.83}$$

$$\Omega_{34} > \widehat{\Omega}_{34} = \frac{\tau_{\|24}^{-1}}{\sqrt{2+\frac{\tau_{\|24}}{\tau_{\|23}}}}. \tag{2.84}$$

These equations impose a strong coupling between the interacting states to overcome the total phase loss rate $\tau_{\|13}^{-1}$ or $\tau_{\|24}^{-1}$. Of course, the coupling limit on the extraction side, $\widehat{\Omega}_{34}$, is larger than that of injection, $\widehat{\Omega}_{12}$, due to the resonant phonon scattering from level 4. The strong coupling ensures bigger splitting between the states involved in the corresponding tunneling process and hence, the transitions between each of these states to the third level can be distinguished. From simplistic arguments, in a four-level system like the one represented in Figure 2.16-c, the double-peaked gain should then appear when $|\Omega_{12} - \Omega_{34}|$ reaches $\widehat{\Omega}_{12} + \widehat{\Omega}_{34}$. This criteria is conservative, as Figure 2.19 shows that a double-peaked gain occurs well before this simplistic criteria is met. As mentioned above, it requires a larger coupling strength to observe double-peaked gain, when the resonance condition becomes loose. The plots displayed as insets of Figure 2.19 show the linear gain spectrum at $\Omega_{12} = 1$ meV, and for four different extraction couplings $\Omega_{34} = 1.5,\ 2,\ 2.8,$ and 3.5 meV. The first two have a single-peaked behavior, the third is marginally double-peaked and the last one shows a double-peaked gain. These insets illustrate the broadening of linear gain and the decrease of the peak gain by the extraction coupling strength. Typically, our three-well QCL are designed for $\Omega_{12} \sim 1$ meV and $\Omega_{34} \sim 2$ meV, therefore with single-peaked linear gain, but close to the boundary between single and double-peaked linear gain.

This discussion suggests that the dual frequency operation with a 0.6 THz separation reported in [67] is not due to the linear gain, but rather to the nonlinear gain. This term can be substantial and give rise to some structures at $\hbar\omega \approx E_{13}$ in the total gain

spectrum, outside the resonance condition. For instance, the complete gain model reveals multi-peaked spectra when $\tau^* \geq 0.6$ ps for $\tau_{23}^* = 0.85$ ps, mainly thanks to the contribution of the second term of equation 2.77. However, with these new parameters the linear gain stays in the single-peak phase.

2.5 Summary and conclusions

In this chapter, firstly the solutions of Schrödinger equation for multiple quantum well heterostructures, followed by tight binding model were presented and used to calculate the coupling strength and detuning values between various energy levels . Later the description of light-matter interaction Hamiltonian was discussed and applied towards extraction of the gain coefficient of the intersubband optical transition from first principles. Moreover, the intersubband non-radiative relaxation were extracted. Interestingly for the case that the subband energy spacing was smaller than the phonon energy, it is observed that the temperature dependence of the transition lifetime becomes weaker as the transition gets more diagonal. In such designs although diagonality compromises the gain, the population inversion sustains at higher temperature, leading to higher T_{max}. This effect will be later used in the next chapter, for designing THz QCL for high temperature operation.

In the second part of this chapter, the calculated diagonalized Hamiltonian of three-well based THz QCL was applied to density matrix formalism, with two separate assumptions. Once the model excluded the coherence between the lasing state. This makes the laser field only acting on the population of the states, but is very useful to find the population and coherence values for various energy subbands in weak field regime. Later the laser-induced coherence values were properly added, by including the laser Rabi frequency in the model. The gain / absorption spectrum of the radiative transition was found for the three-well THz QCL.

Applied to a three-well design with vertical transitions at 3.6 THz, the model concludes that the wrong injection channel is not a major issue, while the wrong extraction channel from the upper lasing state to the extractor state is undesirable, particulary for CW operation. If possible, this leakage path should be minimized, for instance by using diagonal transitions [61]. Under certain approximations, analytical solutions were found, the gain profile equation being probably the most useful. Equation 2.77 shows that the gain spectrum is seriously broadened by both injection and extraction tunnelings. This problem could be minimized by removing one tunneling process, for instance by using a resonant phonon scattering mechanism for injection [108] or a two-well design[69, 107]. Two nonlinear terms in the gain were identified, they are associated with stimulated scattering processes in a tunneling driven system. Their contribution to the total gain is not negligible, especially as the temperature is raised. These terms can also be at the origin of dual-frequency operation of THz QCL which has been encountered by several groups.

Chapter 3

THz QCL structure design, fabrication and characterization

This chapter presents the optimization of fabrication process, waveguide design and heat removal mechanism for THz QCLs. Several new active region designs will be proposed and discussed in chapter 4. Demonstrating the full performance capacity of these new designs requires a structure with optimized waveguide and heat removal mechanism. In the existing chapter, the active region similar to the original three-well THz QCL [65] (Figure 2.3) is selected for the optimization process. As explained in [65], the phonon well width is designed to provide energy spacing of the LO-phonon energy between first two energy states. The injection and extraction barrier thicknesses are picked to have ~ 1 meV and ~ 2 meV coupling strength, respectively. The active double phonon well in this design is intended to give very high oscillator strength, and hence the laser transition is quite vertical. As calculated in chapter 2 the oscillator strength for this structure is 0.677. Such a vertical transition results in very effective leakage channels (particularly extraction leakage channel, Figure 2.4). It is, therefore, expected to see high current levels for this design. The double laser well widths and laser barrier are designed for vertical transition with the lasing energy

spacing, at the design electric field (12 kV/cm). The designed layer thicknesses are **48**/ 96/ **20**/ 74/ **42**/ 161 $\AA$ and the barriers are indicated in bold fonts [65]. The whole QCL structure consists of 216 repeats of this module in sandwich between a 50 nm top and 400 nm bottom n^+ GaAs layers doped to 5×10^{18} cm^{-3} and 3×10^{18} cm^{-3},respectively. The quantum well of 161 $\AA$ is doped with Si dopants to a two-dimensional carrier concentration of 3.6×10^{10} cm^{-2} per module. $GaAs/Al_{0.15}Ga_{0.85}As$-based MQW structure is grown on a semi-insulating (SI) (100) GaAs substrate using molecular beam epitaxy (MBE) [1]. It is desirable to grow the epitaxial layers as thick as possible. However, due to instability and non-uniformity during a long time growth (MBE growth rate $\sim 0.5 - 1.0$ $\mu m/hr$), the thickness of the epitaxial layers is typically grown under around $10 - 15$ μm to avoid quality degradation. Photoluminescence mapping of the wafer with $\sim 10\mu m$ film shows quite reasonable uniformity. X-ray diffraction data and secondary ion mass spectroscopy of the wafer also confirm that doping levels, aluminum composition and thickness of each layer of the $10\mu m$-thick epitaxial layers accurately agree with the original design. From now on this MBE grown wafer is called as "V610".

The threshold gain (g_{th}) of the laser is the minimum gain required from the gain medium to overcome losses, and is defined as [44]

$$g_{th} = \frac{\alpha_w + \alpha_m}{\Gamma}, \tag{3.1}$$

where α_w is the waveguide loss, α_m is the mirror loss and Γ is the confinement of the mode inside the cavity. There are two major waveguide structures, to confine the THz laser field in a relatively low loss cavity, for THz QCLs: semi-insulating surface-plasmon (SI-SP) [5, 43] and metal-metal (MM) [109] structures. The SI-SP structures confines the mode within the active region by sandwiching it between top metal and bottom n^+ surface plasmon. Due to the small modal overlap with lossy regions, SI-SP waveguide offers very low waveguide loss, and also rather low confinement factor. The SI-SP structure shows

[1] Dr. Zbignew Wasilewski provided the MBE grwon wafers

relatively high mirror loss values (reflectivity of ~ 0.33, as for the GaAs-air interface), and hence it is used to achieve high power Thz QCLs. On the other hand, the MM structure confines the mode between a sandwich of top and bottom metals and hence offer very high confinement factor and very high waveguide loss as well. The MM structure offers very low threshold gain and hence is used to achieve high temperature operation for THz QCLs.

As mentioned above, both waveguide structures for THz QCLs are widely used, depending on the requirements of various applications (either high temperature or high power). This chapter separately studies the design and fabrication details of both THz QCL structures. For this purpose, the detailed fabrication process, waveguide design details, and heat removal engineering will be presented, for both structural types. Once the structural design of the laser is optimized in terms of the waveguide and heat dissipation mechanisms, it can be applied to active regions with high temperature and high gain behavior, and demonstrate high performance THz QCLs. At the end of the chapter, such high performance THz QCLs will be used to demonstrate a few simple THz transmission imaging experiments.

3.1 Metal-metal waveguide structure

The MM structure proposed first time by Williams et al. in [109], where they found big improvement in the maximum operating temperature (T_{max}) and threshold current density (J_{th}). The most challenging part in processing THz QCLs in MM configuration is bonding the MBE-grown material to a metal deposited substrate, which is called "substrate removal", and will be addressed in this section.

Equation 3.1 suggests that lasing performance improvement is due to highly confined laser field to the active region. However, strongly confining long wavelength field ($\lambda \sim 70 - 200\ \mu m$) within sub-wavelength thick active region ($t \sim 10\ \mu m$) extends the mode

slightly more into the plasmon (doped and metal) regions. The higher overlap of the mode with lossy plasmon regions translates into the higher waveguide loss for the MM based structures. This section theoretically and experimentally studies the effect of metal choices on the laser performance.

3.1.1 Device fabrication

After the MBE growth, wafers are cut into 1 $cm \times 1$ cm pieces and then cleaned using a standard Isopropanol (IPA) / Acetone / deionized (DI) water cleaning process in an ultrasonic cleaner. Organic contaminations and native oxide are removed afterwards through an oxygen plasma descum treatment followed by $HCl : H_2O$ (1 : 10) dip. An stack of $Ti/Pt/Au$ (250/550/10000 $\mathring{A}$) metal (unless otherwise noted) is then deposited on top of the 10 μm-thick epi-layer using an electron beam evaporator. In parallel, a silicon doped n^+ ($\sim 1 \times 10^{18}$ cm^{-3}) GaAs substrate is coated with a $Pd/Ge/Pd/In$ (250/100/250/10000 $\mathring{A}$) metal stack, which will be used as the receptor substrate in the subsequent wafer bonding process. These two wafers are reactively bonded ($In-Au$ bonding) under 0.5 Mpa pressure at 200 $^\circ C$ for 90 minutes (Figure 3.1-a), during which In atoms diffuse into the Au layer to form $In - Au$ alloy. The $In - Au$ alloy has a melting point of 340 $^\circ C$ and is mechanically strong at room temperature. It is very crucial to maintain the highest degree of cleanness during the wafer bonding process. Any small particles and other surface contamination could result in failure of wafer bonding.

After the wafer bonding step (Figure 3.1-a), the original 600 μm thick GaAs substrate of the QCL wafer is removed by mechanical lapping followed by selective wet etching process. The bonded wafer piece (1×1 cm^2) is mounted on a glass holder using wax. In the mechanical lapping process, around 550μm of the $GaAs$ substrate is removed. The rest ($\sim 50\mu m$) of the $GaAs$ substrate is etched chemically in a citric acid: H_2O (4 : 1) solution (etch rate $\sim 0.3\mu m/min$). This selective etch will stop at an underneath etch stop layer

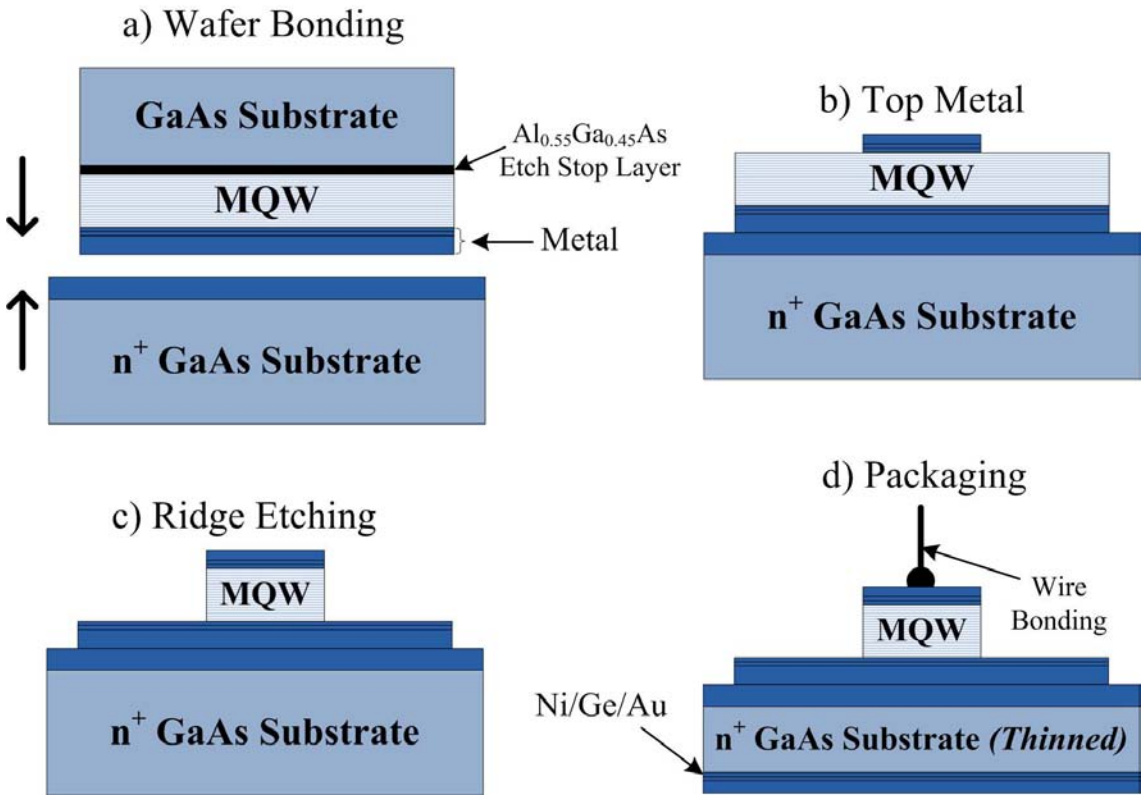

Figure 3.1: Schematic diagram of fabrication process for MM QCL with metal-metal structure.

($Al_{0.5}Ga_{0.45}As$). The etch stop layer is then removed using hydrofluoric acid (HF) in one minute. Finally the sample is dismounted from the holder, thoroughly cleaned and is then ready for photolithography and metallization steps.

The next fabrication step (Figure 3.1-b) is to define the waveguide ridge pattern on top of the sample using conventional photolithography techniques. Great cares need to be taken to ensure that the ridge pattern is parallel to the major flat (crystallographic orientation) of the wafer. At the end of fabrication, this parallel orientation makes it easier to cleave light emission facets perpendicular to the laser ridges. Two photolithograph masks are used in the process. Mask 1 is used to pattern a bi-layer photoresist coating

for a metal lift-off process. $Ti/Pt/Au$ (250/550/3000 $\AA$) (unless otherwise noted) is then deposited on top of the patterned bi-layer photoresist, and lifted-off using NMP at 80 $^{\circ}C$ (Figure 3.1-b). The sample is then annealed at 350 $^{\circ}C$ for 15 seconds in N_2 ambient in a rapid thermal annealing (RTA) process to alloy the top metals for an Ohmic contact. Next step is to etch the MQW layers in regions that are not covered by the top metal to form the waveguide ridges. Mask 2 is used to define window openings for the etching.

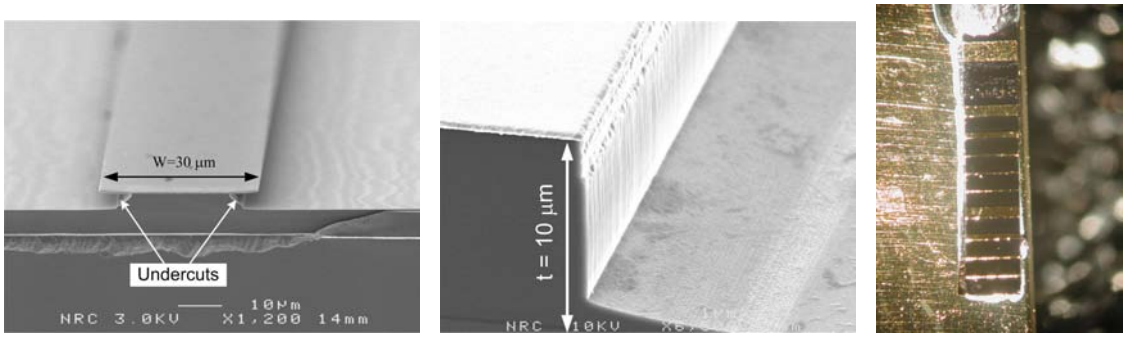

(a) (b) (c)

Figure 3.2: SEM micrograph for fabricated THz QCL using (a) wet etch, and (b) dry etch processes. Panel (c) shows the image of a cleaved and packaged device.

It is required to etch the entire 10 μm MQW region to avoid spreading of current (Figure 3.1-c). Either wet etching or dry etching can be used to define the laser ridge. Wet etching of MQWs is performed using $NH_4OH : H_2O_2 : H_2O$ (2 : 1 : 10). This etchant removes the MQW $GaAs/AlGaAs$ structure fairly isotropically along all crystal orientations, so etching 10 μm in vertical direction also yields to 10 μm undercut from sidewalls as well. This undercut can be very critical for narrow ridge widths. To minimize the undercut effect, the ridge is only etched down to 5 μm in vertical direction. Figure 3.2-a shows scanning electron microscope (SEM) images of a fabricated QCL devices with a ridge width of 30 μm. One can see that the undercut is quite substantial in the 30 μm wide ridge. Dry etching of MQW is performed on a cooled substrate (10 $^{\circ}C$) at low pressure (4 $mTorr$) in BCl_3 environment using both RIE (50 W) and ICP (400 W) powers. An end

point detection system is used to stop the etch at the bottom metal contact. Figure 3.2-b shows the SEM micrograph of a fabricated QCL device using dry etching. In this device the top metal is used as etching mask. This process causes roughness on the sidewalls, particularly on the higher parts closer to the top metal. This is believed to be due to the RIE plasma field concentration around the top metal, during the dry etching process. Although the long THz emission wavelength ($\sim 100\mu m$) is much larger than the size of the roughness features, it is desirable to minimize them. Experimentally it is found that using photoresist instead of metal for the mask eliminates the roughness issue during the dry etching. However when using photoresist mask, it is required to mask the sample few microns outside of the top metal. This leaves edges of the top of the mesa uncovered (as shown in Figure 3.5-b). Such a structure is actually desired for single mode operation of MM THz QCLs, as will be discussed in section 3.1.2.

The last step of the fabrication is device packaging (Figure 3.1-d). First, the n^+ GaAs substrate is thinned down to $\sim$ 150 μm to facilitate the heat dissipation through the substrate. The bottom of the wafer is also used as a ground contact. The heavily doped n-type GaAs receptor substrate is expected to yield a very small contact resistance. A stack of $Ni/Ge/Au$ (250/550/3000 $\mathring{A}$) metal is then deposited onto the back of the substrate and annealed at 350 $^{\circ}C$ for 15 seconds in N_2 ambient using RTA. After that, the sample piece is cleaved into $\sim$ 1 mm long Fabry-Perot resonator laser bars. Figure 3.2-a and -b show the atomic flat quality of cleaved facets. Each laser bar is In soldered (epi-layer side up) on an Oxygen-free copper package, as shown in Figure 3.2(c). The emission facet of laser ridges is carefully placed as close as possible to the edge of the mount. Thin Au wires are used to connect the top metal contact on the ridge of each device to different electrical pins of a 16-pin package. The package is placed on a cryostat cold finger for low-temperature measurements.

The RP-based THz QCLs typically require a very high current to yield sufficient optical

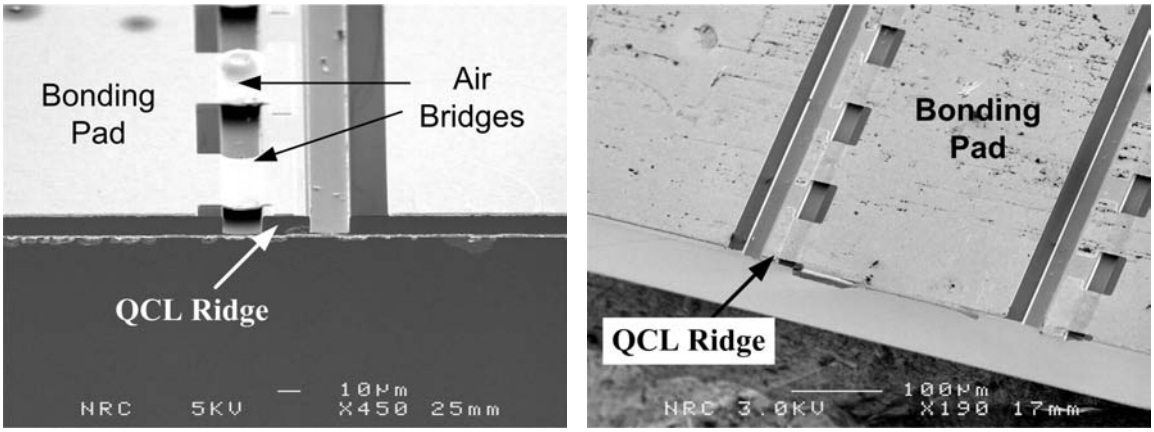

(a) (b)

Figure 3.3: micrograph for air bridge structure QCL after cleaving.

gain for lasing operation at design electric field ($E \sim 12\ kV/cm$, equivalent to $V = 12\ V$ for a 10 μm thick active region). As a result, multiple Au wires must be bonded to the top contact metal layer of each device to apply the external high current. This multiple Au wire bonding scheme, however, does not apply to narrow ridges with a width smaller than 50 μm because each Au wire bonding foot takes an area of at least $50 \times 50\ m^2$. The alternative solution is to use an air bridge structure in the narrow ridge devices. The air bridge structure, as shown in Figure 3.3, first connects the narrow laser ridge to a very wide bonding pad (250 μm) on its side using a metallic bridge structure. The Au wires then connect the wide bonding pad to package pins. Through this technique, one can make electrical connection to QCLs with a ridge width as narrow as 20 μm. Figure 3.3-a and -b show SEM images of fabricated QCL devices with a 20 μm ridge width, connected to a series of air bridges. The air bridge is 50 μm in width, with a 50 μm gap between two neighboring bridges, along the longitudinal direction.

Figure 3.4 shows the schematic diagram of air bridge structure fabrication steps. These processes are carried out after the wafer bonding and substrate removal (Figure 3.1-b) are finished. After patterning the top metal, a SiO_x layer is deposited on the top surface and

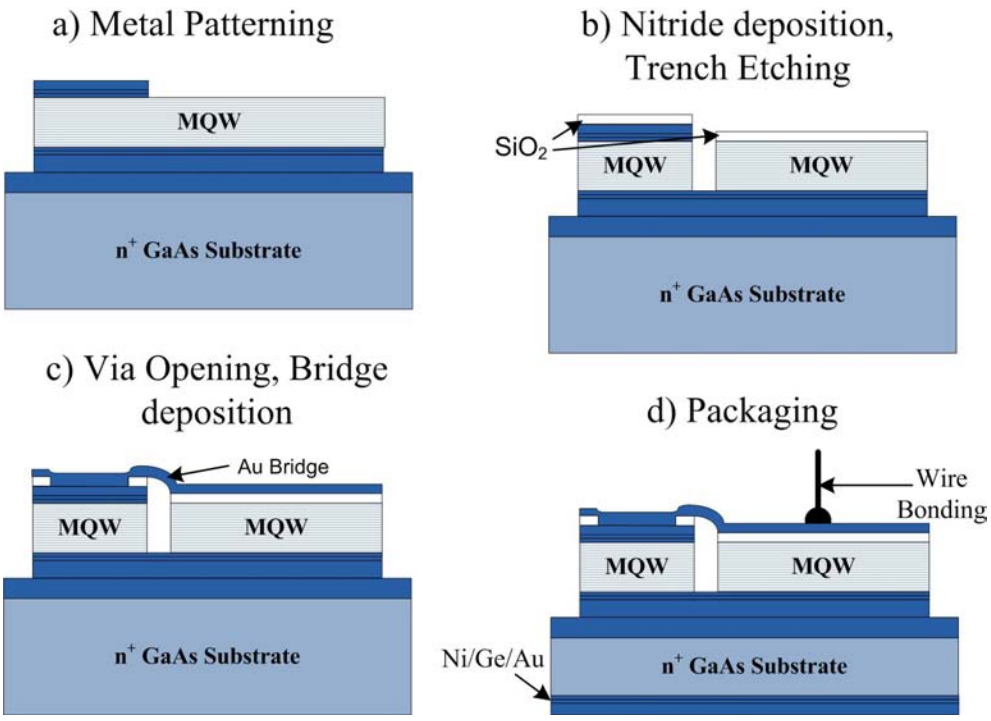

Figure 3.4: Schematic diagram of fabrication process for air bridge QCL structure. Steps shown after substrate removal.

is patterned to serve as mask for following etching. Dry etching is employed to form almost 10 μm deep trenches (for electrical isolation) and opening contact via is formed on top of the ridge. A thick photoresist film is spun to fill up the trenches and forms a convex arc which defines the shape of the metal bridge. A gold metal layer is then deposited and after metal lift-off, leaving the connection air bridges as shown in Figure 3.4-d [1].

3.1.2 Waveguide design

This section discusses the effects of waveguide design in the MM structures on the performance of an RP-based 3.6 THz QCL device, as shown in Figure 2.3. Kohen et al. has

[1]Mr. Sylvain R. Laframboise aided for developing the processes and the fabrication

extensively calculated and discussed the 1D electromagnetic modeling of the THz QCL waveguide, for both MM and SI-SP structures at different frequencies [110]. It is well-known that the MM waveguide demonstrates the lowest threshold gain (G_{th}) for THz QCL structures. However, the low threshold gain along with wide ridge width result in excitation of higher order transverse modes. Such multi-mode structures do not show predictable and hence controllable light versus current (LI) characteristics. Here a 2D simulation of the waveguide structure is discussed using COMSOL Multiphysics finite element solver. The 2D solution of the waveguide structure provides new information on the higher lateral modes of the ridge waveguide, which can be significant for wider ridges.

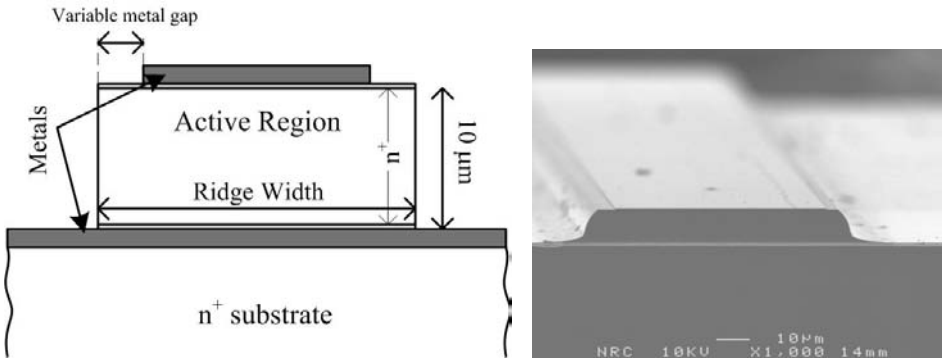

(a) (b)

Figure 3.5: (a) Schematic presentation of the simulated MM THz QCL structure. The laser ridge width and the metal gap distance vary for simulating different waveguide mode allocations. (b) The SEM micrograph for the fabricated structure with a 5 μm metal gap, after cleaving.

As mentioned before, this chapter discusses on the $V0610$ wafer with the design similar to the one reported in [65]. The waveguide simulations model the 10 μm active region using GaAs, doped to an average doping density of 6×10^{15} cm^{-3}. The entire active region structure is sandwiched between a 50 nm top and 400 nm bottom n^+ $GaAs$ contact layers doped to 5×10^{18} cm^{-3} and 3×10^{18} cm^{-3},respectively. The simulations consider

a metal layer and an n^+ GaAs substrate below the active region (Figure 3.5-a). The MM structure mainly supports the transverse magnetic (TM) modes, due to electric field boundary conditions at the metal interfaces [44]. As other types of modes (rather than TM) can also weakly exist in such waveguides, the real mode inside the MM waveguide becomes TM-like. Based on the intersubband selection rule, however, the gain medium only provides gain for TM polarized wave inside the active region, and makes other propagating modes weaker compared to pure-TM mode. Therefore, the rest of this thesis uses the TM notation instead of TM-like, for easier expression.

Gellie et al. have suggested in [111] that introducing a gap between edge of the top metal and ridge suppresses the higher order modes in a wide MM ridge. From now on this gap is referred as "metal" gap. The ridge waveguide structure used in the simulation is depicted in Figure 3.5-a. Figure 3.5-b shows the SEM micrograph of a fabricated ridge with a 5 μm metal gap.

The effective complex permittivity of the semiconductor layers are dominated by free carrier absorption and are calculated using Drude-Lorentz approximation from [110]

$$\epsilon(\omega) = \epsilon_{core}(\omega) + \jmath \frac{ne^2\tau}{\omega m^*(1 - \jmath\omega\tau)}, \tag{3.2}$$

where $\epsilon_{core}(\omega)$ is the permittivity of the material at given frequency, n is the total number of conduction electrons per unit volume, and τ is the Drude relaxation time. The electrical permittivity of the contact metal layers and n^+ $GaAs$ layers are calculated using Drude model with relaxation times of 60 fs and 100 fs, respectively. For the active region the Drude relaxation time of 500 fs is used [110].

To calculate the waveguide loss, the complex effective refractive index of the waveguide is first obtained using COMSOL. The simulator finds the 2D eigenmode solution of the Maxwell's equation for the given structure. The waveguide power loss is given by $2 \times \Im(\beta)$, where β is the complex propagation constant and $\Im(\beta)$ is the imaginary part of β.

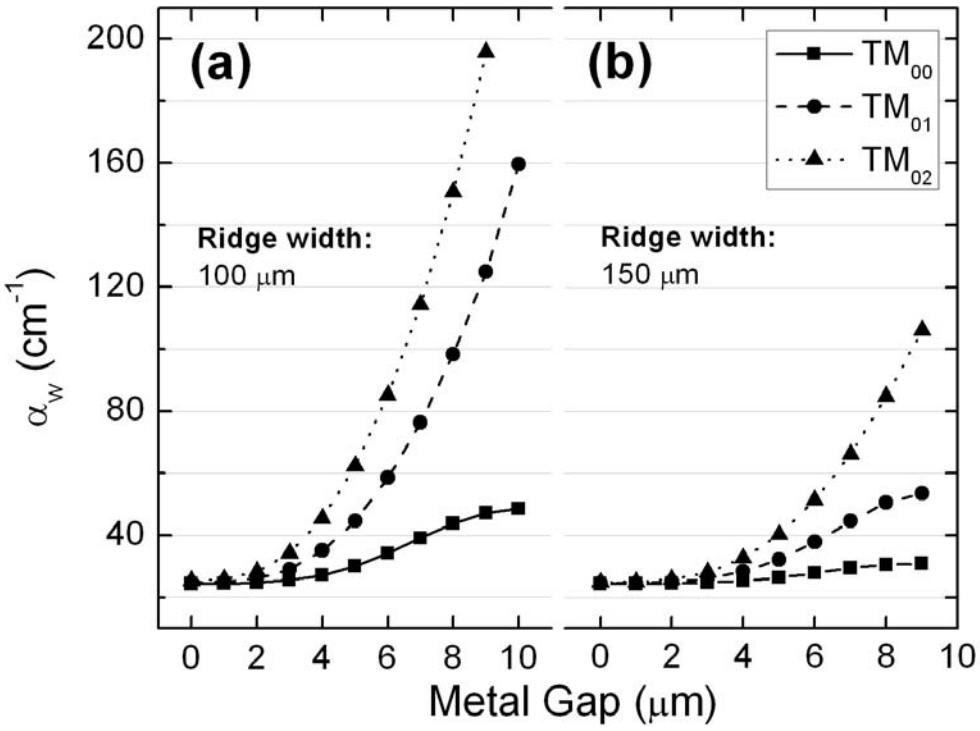

Figure 3.6: Effect of metal gap on the modal waveguide loss (α_w) for MM ridge waveguide with (a) 100 μm and (b) 150 μm widths. Both graphs clearly show that the waveguide loss for higher order modes increase for bigger metal gaps.

Figure 3.6 shows the calculated waveguide loss for two various waveguide widths of 100 and 150 μm, versus the metal gap distance. As expected from the calculations in [110], the waveguide loss for a wider ridge is lower, for all metal gap distances. The waveguide loss for various transverse modes are calculated and depicted in Figure 3.6. By increasing the metal gap from zero up to 2 μm, the waveguide loss for first three modes does not change significantly and remains very close to each other. By further increasing the gap, the loss of all modes including the fundamental mode (TM_{00}) increases. However the introduction of the metal gap increases the loss of the higher order modes much more than the lower order modes. For instance, an 8 μm gap on a 150 μm ridge increases the loss of fundamental

mode from 25 cm^{-1} to 30 cm^{-1}, while it increases the loss of TM_{01} and TM_{02} modes to 50 and 84 cm^{-1}, respectively. The increase of modal loss is more pronounced in the narrower ridge (Figure 3.6-a). In the following, MM THz QCLs with and without top metal gap are fabricated and the LI characteristics of MM THz QCLs devices will be experimentally discussed.

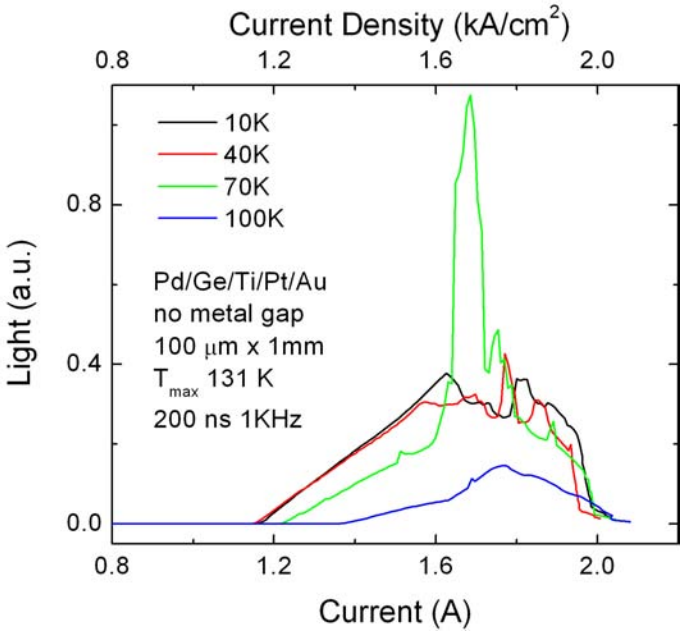

Figure 3.7: The collected THz light (optical output power) versus current curves for MM THz QCLs with no metal gap. The device is biased in pulsed mode (pulse width = 200 ns and repetition rate = 25 Hz). Existance of higher order modes results in non-predictable LI behavior at different temperatures.

Figure 3.7 shows the the LI characteristics of a 100 μm wide ridge fabricated using $Pd/Ge/Ti/Pt/Au$ (550/1000/250/550/3000 $\mathring{A}$) metal contacts, with no top metal gap. The device shows threshold current density of less than 1.2 kA/cm^2 at 10 K and lases up to 131 K. This metal combination provides Ohmic contacts on both sides of the device. Slightly above threshold, where the gain of the active region is low, it is expected to just

excite the fundamental mode. By increasing the current, the gain of the active region increases and consequently higher order modes also gets excited. Figure 3.6 suggests that without metal gap, the waveguide loss of first three fundamental modes are very close to each other. Therefore at high current injection levels, the higher order modes can be excited (Figure 3.7). In such condition, the LI curve shows two slopes and many kinks, which is indication of mode competition inside the laser cavity.

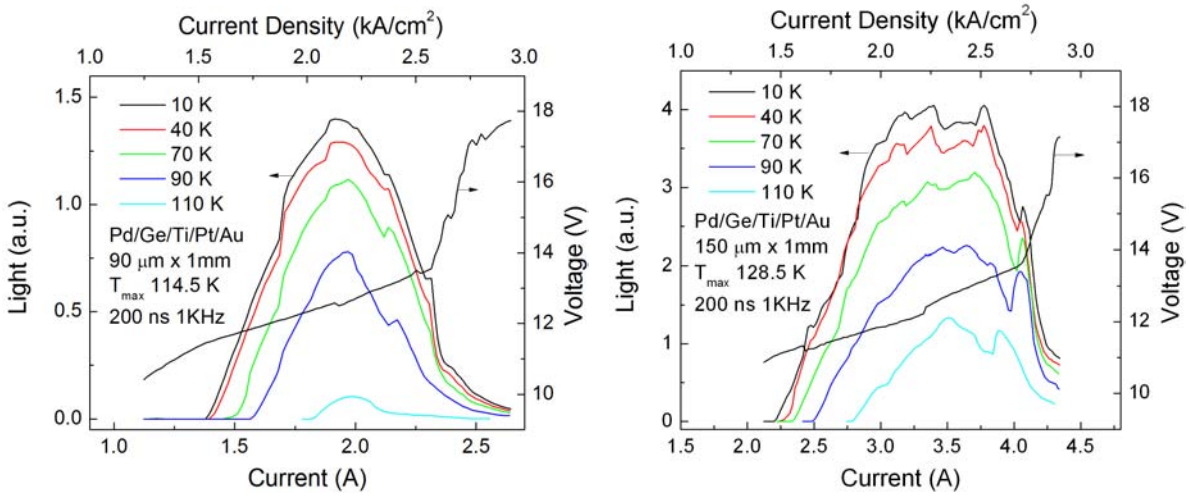

(a) (b)

Figure 3.8: The collected THz light (optical output power) versus current curves for MM THz QCLs with 5 μm metal gap and (a) 90 μm and (b) 150 μm wide and 1 mm long device at different heat sink temperatures. The device is fabricated using $Pd/Ge/Ti/Pt/Au$ metal contacts and is biased in pulsed mode (pulse width = 200 ns, repetition rate = 1 kHz).

As observed in Figure 3.6, the increase of waveguide loss with increasing metal gap is more prominent for TM_{01} and TM_{02} modes. Ideally in order to obtain single mode operation for THz QCL devices, choosing a larger metal gap is more suitable. However, a large metal gap also results in high waveguide loss for desirable fundamental mode and compromises the T_{max}. The metal gaps between 5 to 10 μm is found to offer reasonable mode differentiation, with yet low fundamental mode loss. Figure 3.8 shows the experimental

light-current-voltage (LIV) results for two ridge widths of 90 (a) and 150 μm (b), using $Pd/Ge/Ti/Pt/Au$ metal contacts and $\sim$ 5 μm top metal gap. The IV of both panels, shows a small NDR at $\sim$ 12 V, and then a big NDR occurs at $\sim$ 13.5 V. The current density at which the maximum output power is emitted (J_{max}) coincides with the first NDR at $\sim$ 12 V, which is also near the design electric field. The reason for having the bell-shape LI is related to the non-zero detuning value at injection and extraction tunneling barriers (Figure 2.4), [93] and [66].

The narrower ridge (Figure 3.8-a) shows almost perfect bell-shaped LI curve, indicating dominance of fundamental mode inside the waveguide. This device shows the threshold current density of 1.4 kA/cm^2 at 10 K and lases up to 114.5 K. Comparing this with the case without metal gap in Figure 3.7, the threshold current density is increase and the T_{max} is decreased, indicating elevated waveguide loss. Figure 3.8-b shows the experimental LIV results for a 150 μm wide ridge with the 5 μm metal gap. This device shows comparable threshold current density of 1.5 kA/cm^2 at 10 K but higher T_{max} of 128.5 K, which is expected due to lower waveguide loss (Figure 3.6). The shape of the LI curve shows a few small kinks, meaning that the higher order modes are prominent in the wider waveguide ridge. However unlike the no-gap case, the LI behavior is quite smooth and looks like the famous bell-shape.

In conclusion, introducing the top metal gap increases the higher order modes' loss and leaves the laser cavity with mainly fundamental mode. This makes the LI curve shape smooth, with expense of slightly higher loss for the fundamental mode. This might slightly reduce the T_{max}, but makes the LI curve experimentally repeatable. It was found that the top metal gaps with width of 5 to 10 μm for ridges below 150 μm eliminates the higher order mode losses without significantly changing the fundamental mode loss. From now on, all the MM devices will be fabricated with top metal gaps of 5 to 10 μm metal gap.

3.1.3 Effect of metal on device performance

It was discussed in the previous section that the MM waveguide confines the mode between two metals with a sub-wavelength spacing. The waveguide loss in such a structure comes from two major parts: the overlap of the mode with doped semiconductor region, and the tails of the mode penetrating into the metal layers. In order to reduce the waveguide loss associated to the active region doping, one can reduce the doping level it. However, as the gain of the material is directly proportional to the available carriers (equation 2.78), reducing the doping of the active region might deteriorate the device performance. There has been many studies over the doping of the active region, where the concentration of δ-doping has been varied to find the doping level in which the loss and gain are balanced [112, 113]. The doping concentration for V610 wafer is chosen at the optimum value of $3.6 \times 10^{10}\ cm^{-2}$. Figure 3.9-a shows the schematic presentation of the MM waveguide structure, based on V610 wafer. The active region is sandwiched between top 400 nm $3 \times 10^{18}\ n^{+}\ GaAs$ and bottom 50/10 nm $5 \times 10^{18}/5 \times 10^{19}\ n^{+}\ GaAs$ layers for contact purposes. These layers further increase the waveguide loss above the value calculated for the ideal case in [68].

Another important factor to be considered to lower the waveguide loss of the MM structure is the choice of the metal stack. Despite the tiny penetration depth of the electromagnetic mode inside the metal, high tangent loss of metals in THz regime significantly increases the loss. Belkin et al. have compared the stack of Td/Cu with Ti/Au and found that at 3 THz the Td/Cu have a lower loss, and hence improved the T_{max} of the THz QCL from 168 K to 178 K [68]. It is important to note that both of these contacts are Schottky contacts and during operation of the laser $\sim 5\ V$ drops across the contacts, which can locally heat the active region and reduce the T_{max}.

Figure 3.8 already showed the LIV results of 90 and 150 μm THz QCL devices fabricated using $Pd/Ge/Ti/Pt/Au$ (550/1000/250/550/3000 $\mathring{A}$) metal contacts. This contact metal

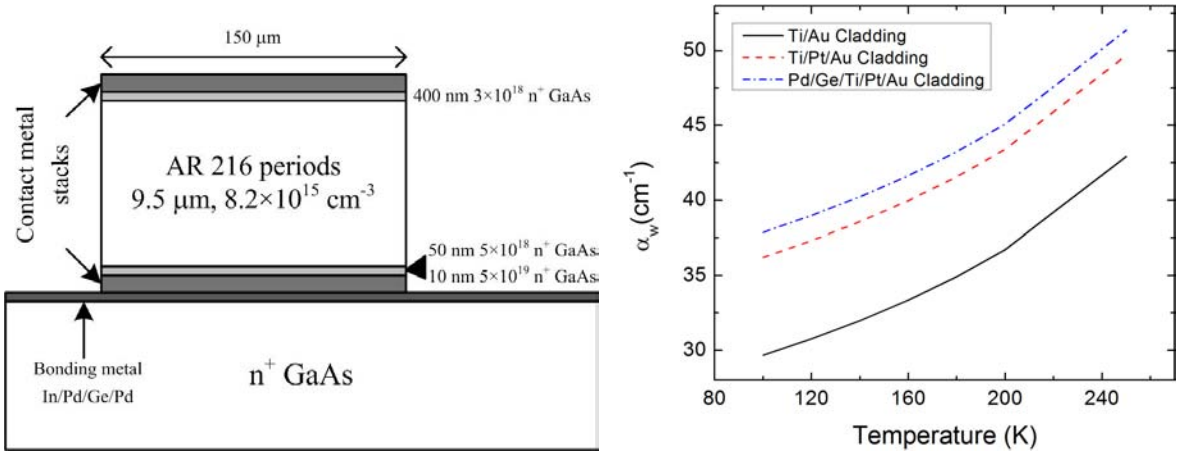

(a) (b)

Figure 3.9: (a) The schematic structure of the MM structure used for the waveguide simulations. The top and bottom metal stack are changed accordingly for each simulation. (b) Simulated temperature dependence of the waveguide loss for three different metal stacks of Ti/Au, $Ti/Pt/Au$, and $Pd/Ge/Ti/Pt/Au$. The waveguide with Ti/Au contact metal shows the lowest loss in all temperatures.

stack provides Ohmic contacts for the device and hence there is very small amount of heat generated on the contacts. This section further studies the device performance for $Ti/Pt/Au$ (250/550/3000 $\mathring{A}$) and Ti/Au (50/3000 $\mathring{A}$) metal contacts, as well, both of which makes Schottky contact. Due to limited resources for Copper deposition the Td/Cu devices could not be processed for this study. For the contacts with Schottky barrier, there is $\sim 1-3\ V$ voltage drop across the contacts. Such a voltage drop on the contacts of a typical device working at 2 A generates $\sim 2-6\ W$ of Joule heat. For CW operation such Joule heat, generated in vicinity of the active region, becomes considerable. On the other hand for the short pulse operation, the Joule heat is neglected and hence the metal contacts with lower waveguide loss can used for high temperature operation.

Figure 3.9-b shows the calculated waveguide loss versus temperature for the V0610-

based MM THz QCLs with three different metal stacks. The full details of the waveguide structure, including the thin highly-doped GaAs layers below and above the 10 μm thick active region were taken into account in the simulation. The waveguide losses were calculated from simulating 10 μm thick and infinitely wide metal-metal THz QCL waveguide at a lasing frequency of 3.75 THz. The temperature dependant permittivity and mobility of the active and n^+ regions were calculated using the data in [114, 115], respectively. The optical constants for the metals (plasma and carrier collision frequencies) were assumed temperature independent and were taken from [116] and the complex permittivity of various layers were calculated using the Drude-Lorentz approximation (equation 3.2). Titanium, Platinum, Palladium, and Germanium are all poor conductors; they are modeled in the waveguide calculation as one metal with a 70000 cm^{-1} plasma frequency and a short 12 fs Drude model electron collision lifetime. Below 80 K the results become very sensitive to the deposited metal quality [68], and hence is not calculated in this graph. The graph shows that for all temperatures Ti/Au metal stack offers the lowest waveguide loss. Therefore it is expected to see the lowest threshold current density and highest T_{max} from devices with this waveguide. The calculated results shown in Figure 3.9-b calculates the loss much higher than the calculated results in [68]. The high calculated loss in Figure 3.9-b is due to considering the full details of the waveguide structure as shown in Figure 3.9-a.

Table 3.1: Summary of metal study results on V610 based THz QCLs.

	T_{max}(K)		$J_{th}(kA/cm^2)$		V_{NDR}(V)	
Width (μm)	**90**	**150**	**90**	**150**	**90**	**150**
$Pd/Ge/Ti/Pt/Au$	114.5	128.5	1.53	1.47	13.55	13.6
$Ti/Pt/Au$	110	134.5	1.53	1.51	15.4	15.5
Ti/Au	124.5	128	1.27	1.3	14.3	14.6

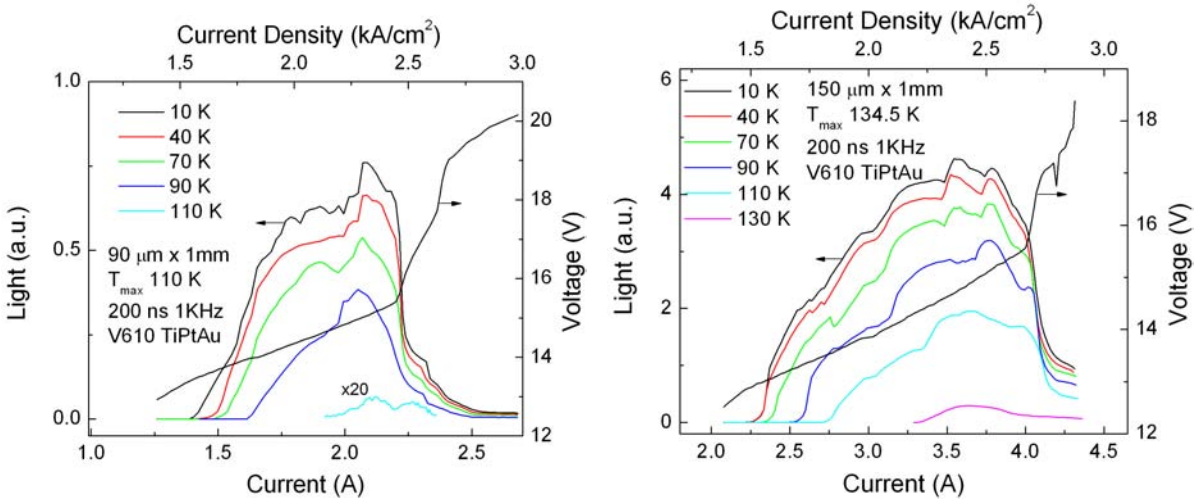

Figure 3.10: The collected THz light (optical output power) versus current curves for MM THz QCLs with 5 μm metal gap and (a) 90 μm and (b) 150 μm wide and 1 mm long device at different heat sink temperatures. The device is fabricated using $Ti/Pt/Au$ metal contacts and is biased in pulsed mode (pulse width = 200 ns, repetition rate = 1 kHz).

Figure 3.10-a and -b show the LIV characteristics of 90 and 150 μm THz QCL devices with $Ti/Pt/Au$ (250/550/3000 $\mathring{A}$) metal contacts. The 90 μm device shows the threshold current density of 1.55 kA/cm^2 and T_{max} of 110 K, while the 150 μm device shows the comparable threshold current density of 1.56 kA/cm^2 and higher T_{max} of 134.5 K. As it is expected the device with wider ridge lases up to higher temperatures, but the threshold current did not change much. Figure 3.11-a and -b show the LIV characteristics of 90 and 150 μm THz QCL devices with Ti/Au (50/3000 $\mathring{A}$) metal contacts. In this sample the absorbing metal layers before gold are minimized to lower the waveguide loss. For both of the $Ti/Pt/Au$ and Ti/Au devices the low temperature $In-Au$ bonding process is used for the metal-metal wafer bonding to avoid un-controlled annealing of the contacts during the bonding. For the Ti/Au based devices, the 90 μm sample shows the threshold current density of 1.28 kA/cm^2 and T_{max} of 124.5 K, while the 150 μm device shows slightly higher

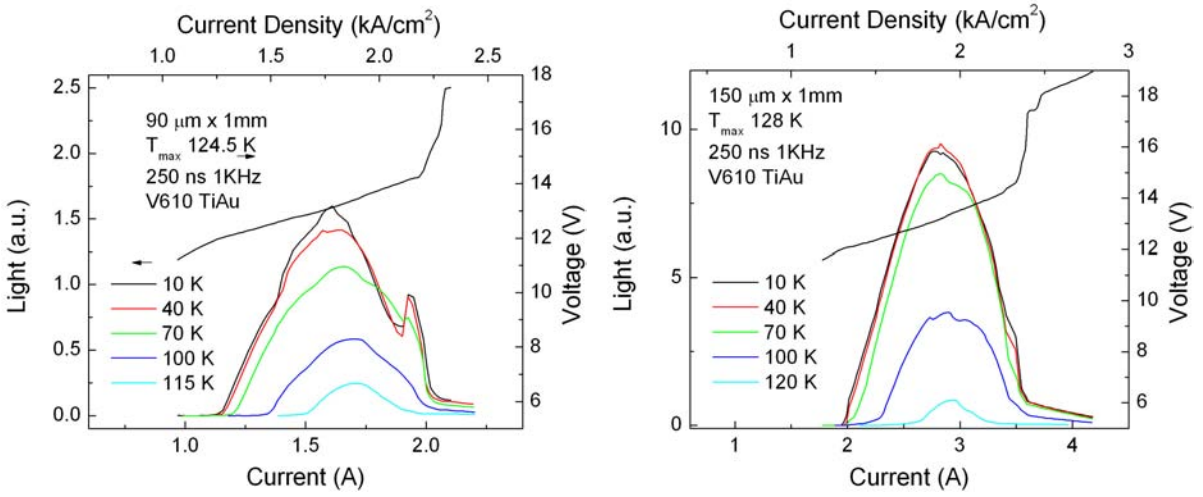

(a) (b)

Figure 3.11: The collected THz light (optical output power) versus current curves for MM THz QCLs with 5 μm metal gap and (a) 90 μm and (b) 150 μm wide and 1 mm long device at different heat sink temperatures. The device is fabricated using Ti/Au metal contacts and is biased in pulsed mode (pulse width = 250 ns, repetition rate = 1 kHz).

threshold current density of 1.3 kA/cm^2 but higher T_{max} of 128 K. This results clearly show that the waveguide loss for the MM THz QCL with $InAu$ contacts is much lower that other metal choices. In the pulse mode, threshold gain improvement compensates high Joule heat generated at non-ohmic contacts and demonstrates higher T_{max}. Table 3.1 summarizes the T_{max}, J_{th} and NDR voltage values for the devices tested in metal waveguide loss study.

3.1.4 Continuous wave operation

The continuous wave operation of THz QCL is of crucial importance in many applications such as imaging, free space communication, etc. In this section after brief presentation of pulse mode characteristics of a fabricated THz QCL, obstacles for achieving CW operation

of QCLs will be discussed. The three-well based THz QCLs show relatively higher threshold current density compared to four-well based devices [65, 62]. Therefore achieving CW operation using three-well devices required refining the heat dissipation from the active region. To demonstrate the THz QCL CW operation a four-well based active region, replica of [62] with optimized doping from [112], is grown and processed. Compared to thre–well design results, this design shows much lower threshold current density of $\sim 550\ kA/cm^2$ for $\sim 1\ mm$ long laser ridges [112].

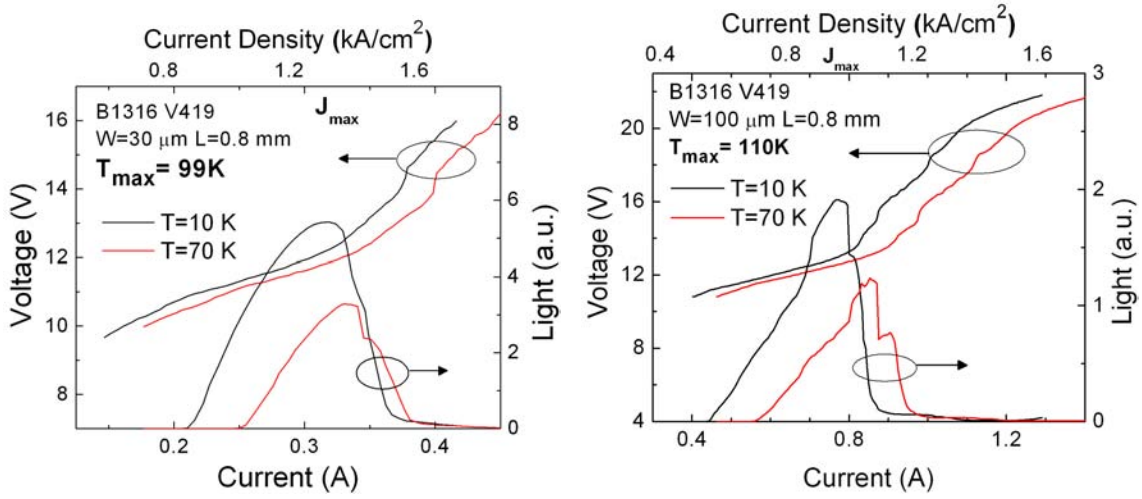

(a) (b)

Figure 3.12: The collected THz light (optical output power) versus current curves for air-bridge MM THz QCLs with (a) 30 μm and (b) 100 μm wide and 0.8 mm long device at different heat sink temperatures. The device is fabricated using $Ti/Pt/Au$ metal contacts and is biased in pulsed mode (pulse width = 2 μs, repetition rate = 1 kHz).

THz QCL devices with different widths were fabricated, using air-bridge structure discussed earlier in the fabrication section. The lasers were cleaved into 0.8 mm bars. The QCLs were biased in pulse mode with a 1 kHz repetition rate and a 2 μs pulse width. Figure 3.12-a and -b show LIV measurement results for V419 QCL with 100 μm and 30 μm device widths, respectively. The 30 μm device shows the threshold current density

of $\sim 0.8\ kA/cm^2$ and T_{max} of 110 K, while the 100 μm device shows much lower threshold current density of $\sim 0.5\ kA/cm^2$ and lower T_{max} of 99 K. This clearly shows that the narrow device is experiencing much higher waveguide loss, however due to its very low current the total dissipated Joule heat for 30 μm device is within the cooling power of the cryostat and can be used for CW operation. The 40 μm device were also tested that showed he threshold current density of $\sim 0.65\ kA/cm^2$ and T_{max} of 109 K, in pulse mode.

For the pulse mode operation of a narrow THz QCL device with voltage bias of around 12 V, current of around 0.5 A, duty cycle of 0.02% (200 ns and a 1.0 kHz repetition rate), the electric power ($P_{elec} = V \times I \times \text{DutyCycle}$) is calculated to be 1.2 mW, which is negligible comparing to the cooling power of the cryostat. In this case the Joule heat can quickly be dissipated to the heat sink, and the active-region temperature of the QCL device remains almost the same as that of the heat sink. In CW operation of THz QCLs, a DC electrical bias (duty cycle of 100%) results in generation of at least 6 W Joule heat in a small active region volume ($10 \times 30 \times 1000\ m^3$), which exceeds the cooling power of the liquid Helium cryostat. The cooling power of closed-cycle cryostats decrease at lower temperatures. For the existing cryostat in our lab, the cooling power is less than 2 W at temperatures below 20 K. When the Joule heat generation from the operating QCL device surpasses the cooling power, the heat sink temperature of the cryostat starts to rise until reaching a balance point where the device heat load equals to the cooling power.

In order to obtain the CW operation for a THz QCL device, two major issues have to be addressed. The first one is to reduce Joule heat generated in lasing operation, which is already archived by fabricating narrow air bridge devices. However due to device fabrication and waveguide loss constrains, the ridge of the QCLs can not be fabricated narrower than 20 μm while still maintaining a reasonable good yield. The Joule heat can be further reduced by optimizing the active region to obtain better current injection efficiency and hence lower current. In addition, optical losses (including waveguide loss and mirror loss)

can be further minimized by improving device waveguide design. These optimization measures will enable the QCLs to operate at a higher temperature. For example, the QCLs with a four well QCL resonant phonon depopulation scheme and a metal-metal waveguide exhibit a lower threshold current as well as the highest CW operating temperature comparing to our other designs so far [62].

The second problem that has to be solved is to enhance the cooling process, that is, to dissipate the heat as fast as possible away from the existing THz QCL device. For this purpose, the laser bar was mounted on an Oxygen free Copper package (thermal conductivity $K \sim 400\ W/m.K$) that leads to reasonable thermal conductance between n^+ substrate and cryostat cold finger. A 300 mm thick $n^+\ GaAs$ substrate of the QCL device, which has thermal conductivity of $K \sim 150\ W/m.K$, is thought to be the main limiting component for heat dissipation out of the active region. Consequently, to improve the overall thermal conductance between the QCL active region and the cold finger, $n^+\ GaAs$ substrate was thinned down to 140 mm by lapping. This step is done before the backside metal deposition step. The substrate thinning process improves the thermal conductance of substrate by more than twice. To further improve the thermal conductance, the bonding metal composite used in flip chip bonding is changed from $In-Au$ alloy to $Au-Au$ bonding system [48]. Using this technique, the THz QCL device benefits even more from higher thermal conductivity of pure metallic bonding compared to In-Au alloy [62].

Figure 3.13-a and -b show the CW measurement result for the V419 based QCL ridges with 30 and 40 μm widths, respectively. These results have obtained using the CW characterization setup, described in Appendix B. The threshold current densities for 30 and 40 μm ridge at 10 K are 640 and 680 A/cm^2, respectively. Similar to what was observed in pulse mode, the threshold current density increases with temperature until it reaches J_{max} at T_{max}, where lasing stops. J_{max} does not show strong dependence on temperature and remains almost constant for all temperatures. This suggests that carrier transport

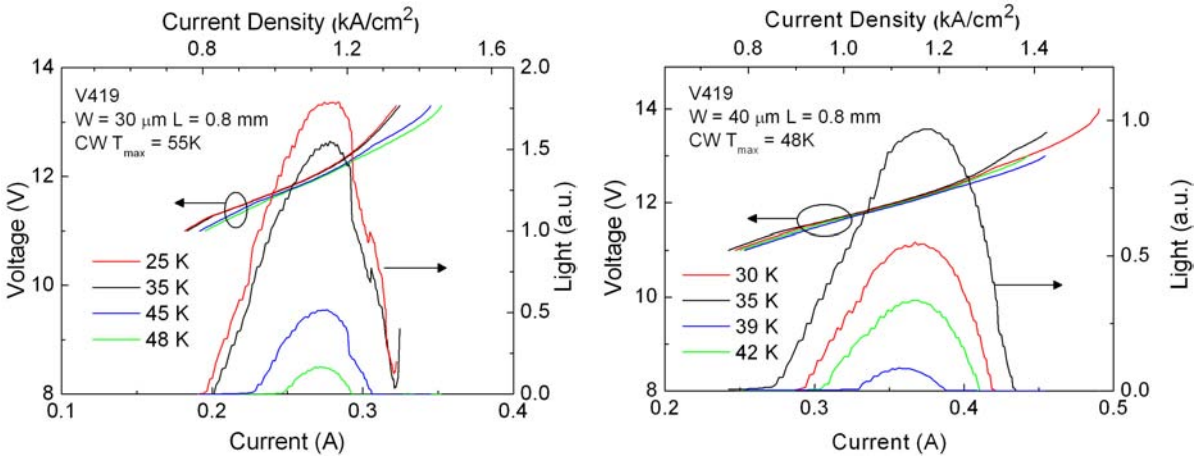

(a) (b)

Figure 3.13: The collected CW THz light (optical output power) versus current curves for air-bridge MM THz QCLs with (a) 30 μm and (b) 40 μm wide and 0.8 mm long device at different heat sink temperatures.

is limited by incoherent sequential tunneling through the injector barrier [62]. For the 30 μm ridge device T_{max} is 99 K for pulsed mode and 55 K for CW, while for the 40 μm ridge device it is 109 K for pulsed mode and 48 K for CW. The interesting point is that, comparing to the 30 μm device, the 40 μm device lased up to a higher temperature in pulse mode but up to a lower temperature in CW. The reason is that the wider device has 33% more current in CW, assuming both devices have the same current density at T_{max}, and hence generates 33% more heat, which leads to a hotter active region, and more limited cryostat cooling power. As mentioned above, the active region and heat sink are approximately at the same temperature when the device is operated in pulse mode, due to very tiny generated Joule heat. This section showed that the T_{max} for the pulsed mode and for the CW mode are quite different, indicating that the active region temperature when the device is in CW mode is much higher than the heat-sink temperature.

3.1.5 Active region temperature measurement and modeling

As mentioned in previous section, the active region temperature of THz QCL in CW operation could be much higher than the heat sink temperature. This is due to the high DC electrical power, most of which converts to Joule heat. In this section an in-situ active region measurement technique is used to measure two different samples with two thicknesses of the n^+ $GaAs$ substrate. The substrate of the samples in group A was thinned down to 140 μm, which is expected to better facilitate heat dissipation from the active region to an underneath heat-sink, the substrate of the samples in group B remained intact (300 μm thick). CW operation was achieved only with the devices of group A (thinner substrate), which lased up to a heat sink temperature of only $\sim$ 55 K. This is $\sim$ 44 K ($99 - 55 = 44$) lower than the maximum operating temperature in pulse mode. The fact that for example for sample V419, a four well design device with 30 μm width, T_{max} is 99 K in pulse mode and 55 K in CW suggests that the active region temperature of the device operating in CW operation might be 44 K higher that in pulse mode. It is therefore postulated that when the device is operating in CW mode at a heat sink temperature of 55 K, the actual active region temperature could be 99 K. This can explain the difference in T_{max} of pulse and CW modes. The only way to prove this speculation is to measure the actual active region temperature of an operating QCL device in CW mode. Unfortunately, lateral temperature profile drops rather quickly due to trenches in air bridge structure, and hence active region temperature can not be measured using a mounted probe (e.g., a Silicon diode) in direct contact with the ridge. A well known microprobe band-to-band photoluminescence (PL) technique is employed to measure the active region temperature [117]. The spatial resolution of this technique depends on the beam spot size of a probing laser (the $HeNe$ laser in Figure 3.14) used for measuring PL. The beam size of the probing laser can be reduced down to 5 μm at its focus point. The PL peak of the semiconductor material shifts to lower energies (longer wavelengths) at higher temperatures [117, 118].

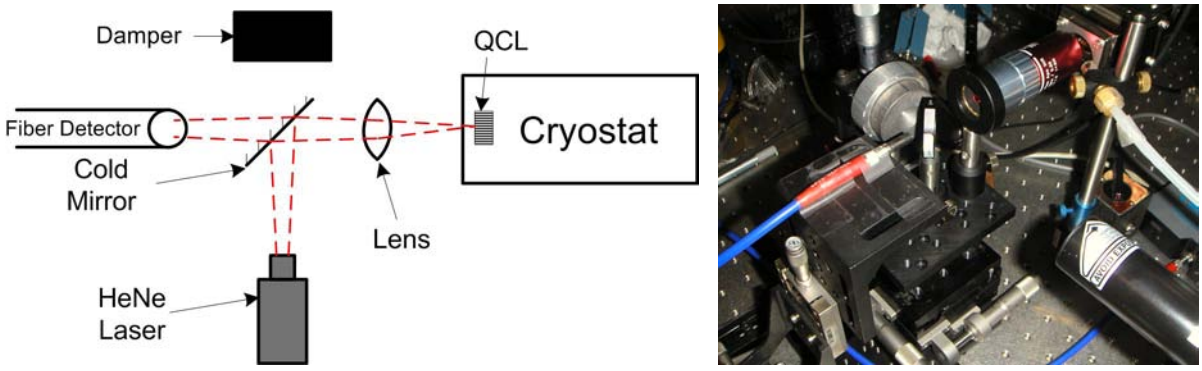

(a) (b)

Figure 3.14: QCL photoluminescence measurement setup (a) schematic diagram and (b) picture.

Figure 3.14-a shows the schematic diagram used for measuring the PL signal of the active region of an operating QCL. A low power $HeNe$ laser (632.8 nm) is used for optical excitation. The power of the probing laser needs to be controlled to avoid local heating, altering the active region temperature. A 45° cold mirror reflects the laser beam toward the cryostat, where the QCL device under test was operating in CW mode at low temperature. The cold mirror used for this experiment reflects wavelengths shorter than 660 nm and passes through wavelengths longer than that. The beam was focused on the QCL facet using a lens. The spot size in order of 5 μm was achieved. However, due to the mechanical vibration of the cryostat, which moved the device-under-test up and down relative to the probing beam, the focused beam spot swept over a much larger area including $GaAs$ substrate as well. This relative movement also reduces the intensity of PL signal. Tightly fixing the cryostat on an optical table helped control the vibration and partially solved the problem. The PL signal emitted from the QCL facet transmitted through the cold mirror and was coupled into an optical fiber. An Ocean Optics S2000 USB spectrometer was employed to measure the PL spectrum. The carbon doped damper behind cold mirror is installed to block the HeNe laser beam transmitted through the cold mirror. Figure

3.14-b shows a digital picture of the experimental setup. The alignment is obtained using a three-dimensional translation stage as shown in the picture.

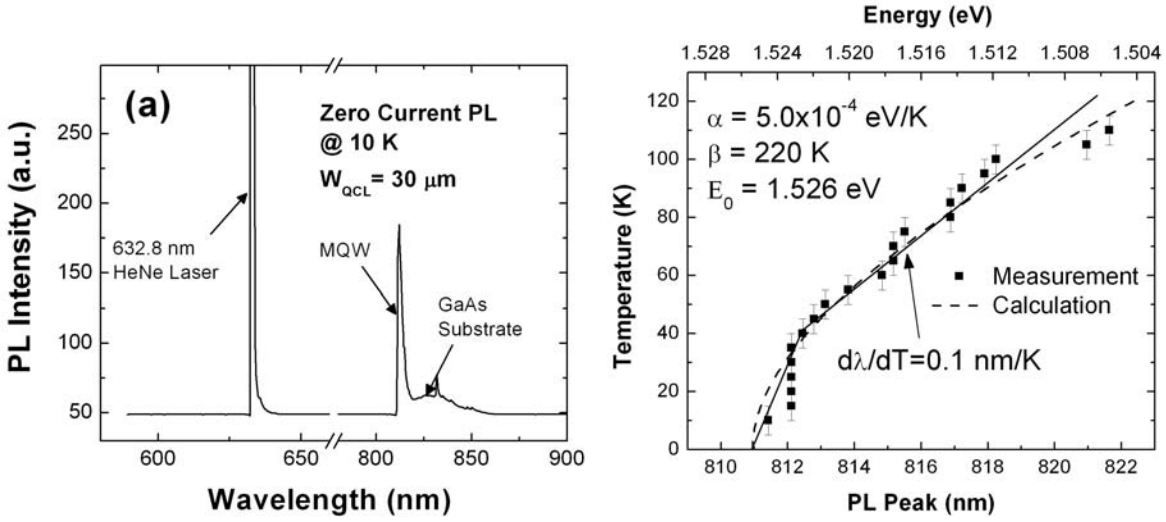

(a) (b)

Figure 3.15: (a) Photoluminescence graph of 30 μm wide QCL laser ridge at 10 K, when no current is flowing. Both MQW and $GaAs$ peaks are observed. (b) Measured and calculated calibration curve of a QCL device active-region temperature versus peak wavelength of the PL emission from the corresponding active region. The heat sink temperature increases from 10 K to 110 K. The device is under zero bias, as a result the active region temperature is expected to be the same as the heat sink temperature at thermal equilibrium.

PL spectrums of a QCL device with a 30 μm wide ridge at various heat-sink temperatures up to 110 K were obtained, while the device was under zero bias. PL peaks from both MQW active-region and $GaAs$ substrate were observed, Figure 3.15-a. As the heat-sink temperature increases, both peaks shift to lower energy values (red-shift). The red-shift of the PL peak of the MQW region is more prominent. Figure 3.15-b shows a calibration curve of the MQW PL peak wavelength versus the active-region temperature (assuming that it is equal to the heat-sink temperature as the device was under zero bias). It was obtained

by gradually increasing the heat sink temperature up to 110 K. Measured calibration curve agrees well with Varhsi's empirical equation for bulk $GaAs$ bandgap temperature dependence [114]

$$E(T) = E_0 - \frac{\alpha T^2}{T + \beta}, \tag{3.3}$$

where E_0 is the bandgap at 0 K and α and β are empirical parameters. Figure 3.15-b plots the Equation 3.3 (dashed line) using a parameter set of $E_0 = 1.526\ eV$, $\alpha = 5 \times 10^{-4}\ eV/K$, and $\beta = 220\ K$. These parameter set is within 10% of reported values set in [114]. The discrepancy is mainly due to MQW band structure and also slightly different material system in our experiment ($GaAs/Al_{0.15}Ga_{0.85}As$).

For temperatures below 35 K, the PL peak wavelength does not change much and shows quadratic dependence on temperature. Above 40 K the peak starts to shift linearly to longer wavelengths with a rate of approximately 0.1 nm/K. Using the calibration curve, we could derive the actual active-region temperature of an operating QCL device by measuring the MQW PL peak wavelength. It should note that the PL peak wavelength of the MQW active region can be shifted with the change of device bias due to Stark effect [22]. However, this Stark shift is negligible ($< 0.2\%$) even under the maximum applied electric field of 9.5 kV/cm based on our simulation results. We therefore use the calibration curve obtained from an unbiased device to derive the in-situ active-region temperature of actively-biased devices.

Figure 3.16 shows measured active-region temperature versus applied DC power for two QCL devices (one each from the two groups). The two devices are otherwise identical (same MM waveguide and active-region design) except the substrate thickness. As shown in Figure 3.16, the active-region temperature of the device with a 300μm-thick substrate (group B) is at least 10 K higher than that of the one with a 140μm-thick substrate (group A) under the same bias condition. It also shows that the active-region temperature increases much faster than the heat-sink temperature with the increase of applied DC

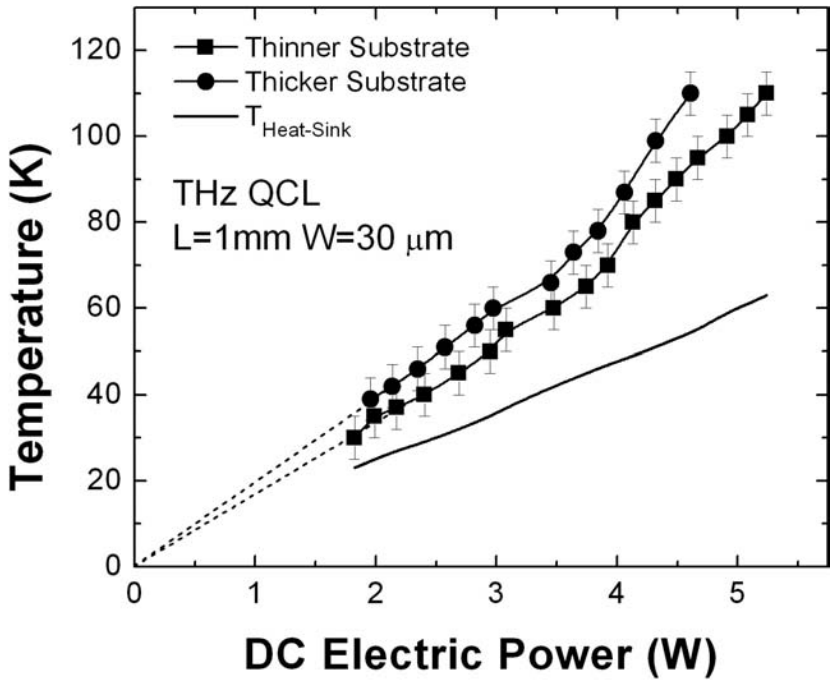

Figure 3.16: Measured active-region temperature and heat-sink temperature versus electrical power applied to THz QCL devices with thinner (140 μm) and thicker (300 μm) substrates.

power. At an input electric power of $\sim 4.7\ W$, the temperature difference between the active region of the device of group A and the heat sink is around $95 - 55 = 40\ K$, which agrees well with the postulated value of 44 K. The active-region temperature increases approximately linearly with the DC power in the low power range up to 3 W. Beyond this point, the temperature growth accelerates because of limited maximum cooling power of the cryostat ($\sim 3\ W$). We, therefore, limit the discussion in the rest of this paper to the linear region below 3 W. The slope of the linear portion in Figure 3.16, which is 60 mW/K for the thinner sample (group A) and 50 mW/K for the thicker sample (group B), defines the overall heat conductance of the whole system (QCL device, package, interfaces, cold-finger of the cryostat, etc). Because of limited cooling power of the cryostat and finite thermal

mass of the cold-finger of the cryostat (the heat sink onto which the device was mounted), the heat-sink temperature increased with the input electric DC power, as shown in Figure 3.16. This effect can be modeled by using a finite thermal resistance, R_{HS}, attached to an ideal heat-sink that has an infinite thermal conductance and a constant temperature. Based on the slope of the heat-sink temperature curve in Figure 3.16, we can obtain $R_{HS} = 11.5\ K/W$.

Assuming the thermal resistance of the substrate of the thinner sample (140 μm) is R_A and the thermal resistance of the rest of the device including active region, wafer bonding metal layer, device package, etc, is R_B, we have,

$$R_A + R_B + R_{HS} = \frac{1}{60\ mW/K} = 16.6\ K/W. \tag{3.4}$$

For the device with a thicker substrate (300 μm), we can approximate the thermal resistance of its substrate is $(300/140)R_A$ by assuming that thermal resistance is proportional to the thickness of the substrate. The thermal resistance of the rest of the device should roughly remain the same, as R_B, we have,

$$\frac{300}{140}R_A + R_B + R_{HS} = \frac{1}{50\ mW/K} = 20\ K/W. \tag{3.5}$$

By using R_{HS} measured value from Figure 3.16 and solving equations 3.4 and 3.5, we find,

$$R_A = 3\ k/W, \quad R_B = 2.1\ K/W. \tag{3.6}$$

This result indicates that the thermal resistance of the $GaAs$ substrate is $3/(3+2.1) = 59\%$ that of the device. In other words, the thermal resistance of the MQW active region and other parts except substrate counts $100\% - 59\% = 41\%$ that of the device. This implies that further thinning of the substrate will continue to improve heat dissipation efficiency of the device. However, processing and handling thinner substrates will become much more challenging.

An interesting behavior of the curves in Figure 3.16 is that if we extrapolate them to zero, they all intercept at origin. This implies that the QCL can be simply modeled by using a first-order thermodynamic partial differential equation (PDE). A numerical simulation of the temperature profile of the QCL device by solving steady state thermodynamic differential equations will be presented in next section and compared to the experimental results.

A 2D heat flow equation can be solved to obtain the steady state temperature profile inside an operating QCL device. Because of the relatively long ridge length ($\sim 1\ mm$) compared to the width and the thickness, it is reasonable to assume that the temperature along the QCL waveguide ridge is constant, that is,

$$\frac{\partial T}{\partial z} = 0, \tag{3.7}$$

where z is the axis along the waveguide ridge. A 2D heat flow PDE can be then written as

$$\nabla.(k\nabla T) + P = 0, \tag{3.8}$$

where k is thermal conductivity with a unit of $W/m.K$, T is temperature with a unit of K, and P is input power density with a unit of W/m^3. Thermal conductivity of $GaAs$ varies with temperature to some extent. However, the simulation is only investigating the linear region of Figure 3.16 that corresponds to temperatures between 35 K and 60 K. Therefore for simplicity, a constant value of 150 $W/m.K$ is used for n^+ $GaAs$ substrate thermal conductivity [119]. Thermal conductivity of the bonding metal (gold-gold bonding) and the MQW active region are defined as 2000 and 100 $W/m.K$, respectively. Thermal conductivity of different MQW active region varies with the quality and periodicity of the MQW interfaces, due to diffusive scattering of phonons by interfaces [62, 120]. A PDE solver software called FlexPDE is employed to find the numerical solution to equation 3.8. Figure 3.17-a shows the definition of the QCL device structure used in the simulation. The 30 μm wide ridge waveguide is located at the top-center of a 500 μm wide substrate. Two

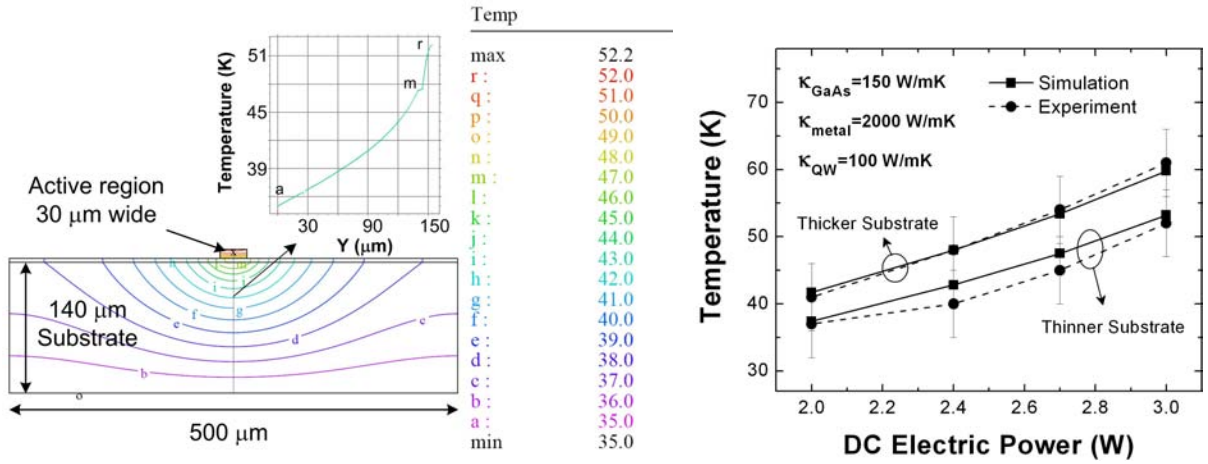

(a) (b)

Figure 3.17: (a) 2D simulated temperature contours of a QCL device with a 30 μm wide ridge waveguide and a 140 μm thick substrate. The device in the simulation was biased with an input DC electric power of 3 W. The heat-sink temperature was kept at 35 K. The inset shows the temperature gradient across the line drawn in (a) from bottom of the substrate (point a) to the top of active region (point r). (b) Simulated and measured active-region temperature vs. device input electrical power for QCL devices with a thinner (140 μm) and a thicker (300 μm) substrate. Solid circles are measured data, squares represent simulation results.

substrate thicknesses, 140 and 300 μm, are used in the simulation. The boundary condition at the bottom of the substrate is first set to a constant temperature (Figure 3.17-a), which implies infinite cooling power. Other boundaries of the device are set to being thermally isolated from outside (no heat exchange).

Figure 3.17-a shows a numerical solution of temperature contours within the substrate of a 30 μm wide ridge waveguide and a 140 μm thick substrate QCL device. The device in the simulation was biased with a constant input DC electric power of 3 W. The heat-sink temperature was kept at 35 K. It is clear that lateral heat flow in substrate does not vanish

until around 200 μm away from the edge of the ridge. Therefore, a device with narrower substrates will have a higher active-region temperature because of impeded lateral heat dissipation. The inset of Figure 3.17-a shows the temperature gradient along a vertical line connecting bottom of the substrate to the top of the active region. It is clear that most temperature gradient is observed at the region closest to the active region. Only 34% of the temperature difference drops across bonding and MQW regions (above contour line m). This result is slightly less than the 41% (= 100% − 59%) as implied by the thermal resistance result that was calculated after equation 3.6. This is because R_B also includes the chip bonding and package thermal resistance as well. The remaining 7%(= 41% − 34%) of the total thermal resistance is likely attributed to the thermal resistance of chip bonding region and measurement errors.

Figure 3.17-b shows simulation results of the maximum active-region temperature at four different input DC powers ($< 3\ W$, all in the linear portion of Figure 3.16), together with the experimental data, for QCL devices with a thinner and a thicker substrate. The temperature at the bottom of the substrate is changed at each given DC power point based on experimental readings (taken from Figure 3.16) to take into account of the limited cooling power of the cryostat (i.e., the increasing cold finger temperature in actual experiments). The simulation results are in good agreement with the experimental data, validating the linear model of heat conductivity inside the device.

The heat dissipation can be facilitated by increasing the thermal conductivity of each component layer of the QCL device. Enhanced thermal conductivities of the active region and the substrate can reduce the active-region temperature of a device under a constant condition. Figure 3.18-a shows simulation results of active-region temperature as a function of material thermal conductivities for a QCL device at a constant bias power of 3 W and a constant heat sink temperature of 35 K. By increasing the thermal conductivity of the substrate from 100 $W/m.K$ to 200 $W/m.K$ while keeping the thermal conductivity

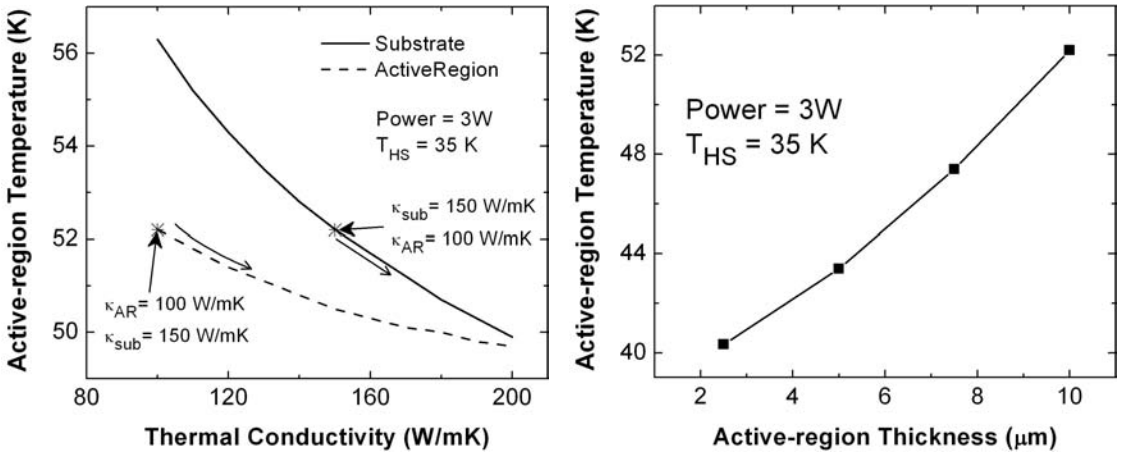

(a) (b)

Figure 3.18: (a) Simulation results of active-region temperature as a function of active-region thermal conductivity (dash line, in which the substrate thermal conductivity remained constant at 150 $W/m.K$) and substrate thermal conductivity (solid line, in which the active-region thermal conductivity remained constant at 100 $W/m.K$). The device was biased at a DC input power of 3 W. (b) Simulation results of active-region temperature as a function of active-region thickness. Input electric power of the device in simulation was scaled according to different active region thickness. The heat-sink temperature was kept at 35 K, in both parts.

of the active region at 100 $W/m.K$, the active-region temperature drops from over 56 K to below 50 K (solid line). By increasing the thermal conductivity of the active region from 100 $W/m.K$ to 200 $W/m.K$ while keeping the thermal conductivity of the substrate at 100 $W/m.K$, the active-region temperature drops from $\sim$ 52 K to $\sim$ 50 K (dash line). It shows improving substrate thermal conductivity is more effective than improving active-region thermal conductivity. Figure 3.18-b shows the simulation results for QCLs with different active-region thicknesses. In this simulation the input DC electric power is scaled according to different thickness of the active region to ensure the same power density input in the device. All other parameters are remained unchanged. It shows that thinning

of the active region facilitates the heat dissipation, drastically reducing the active-region temperature. However, the optical performance of a QCL device with such a thin active region could significantly be degraded, which may render the device eventually inoperable.

3.2 Semi-insulating surface plasmon waveguide structure

As discussed in the beginning of the chapter, the SI-SP waveguides have high facet reflectivity of 0.33 that corresponds to a mirror loss of $\sim$ 11 cm^{-1} for a typical 1 mm long laser bar. Combining this with low confinement of the laser field inside active region ($\Gamma \approx 0.3$), the waveguide results in much higher threshold gain, compared to the MM structure. Therefore, it is expected to have SI-SP THz QCLs work up to lower T_{max}. The high reflectivity of the facet also leads in the portion of the laser field emitting out of the facet, whereas in MM waveguides most of the field is confined inside the ridge. Therefore, SI-SP structures emit higher power and are suitable for high power applications. This section studies dirrerent aspects of SI-SP THz QCLs, such as device fabrication, waveguide design, thermal modeling and etc.

3.2.1 Device fabrication

The fabrication of SI-SP THz QCL does not require the metal-metal bonding. The devices is processed on the SI-GaAs wafer, as grown. Firstly a standard IPA / Acetone / DI water cleaning process in an ultrasonic cleaner followed by organic contaminations and native oxide removal using an oxygen plasma descum treatment and $HCl : H_2O$ (1 : 10) dip is performed. Mask 1 is used to pattern a bi-layer photoresist coating for a metal lift-off process. An stack of $Ti/Pt/Au$ (250/550/10000 $\AA$) metals (unless otherwise noted) is then

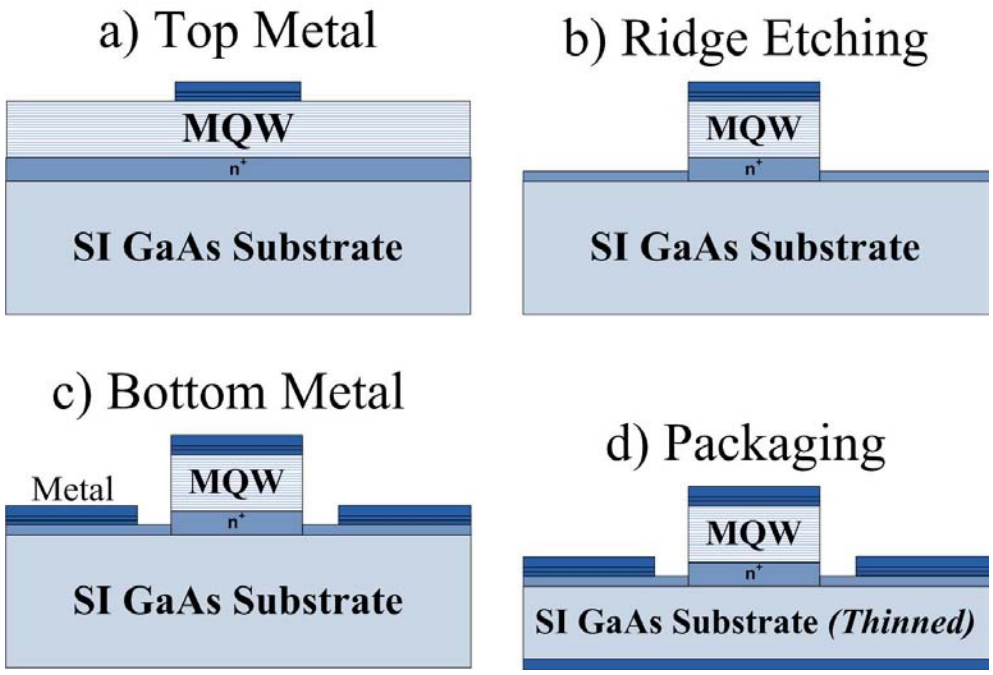

Figure 3.19: Schematic diagram of fabrication process for SI-SP QCL with metal-metal structure.

deposited on top of the patterned bi-layer photoresist and 10 μm-thick epi-layer using an electron beam evaporator (Figure 3.19-a). The sample is then annealed at 350 $^{\circ}C$ for 15 seconds in N_2 ambient in a RTA process to alloy the top metals for an Ohmic contact. Next step is to etch the MQW layers in regions that are not covered by the top metal to form the waveguide ridges. The top metal is used as the mask against etching, until exposing the bottom n^+ GaAs layer. The 10 μm active region is etched on both sides of the ridge using a dry etch process, to access the bottom n^+ layer for electrical contact (Figure 3.19-b). Dry etching of MQW is performed on a cooled substrate (10 $^{\circ}C$) at low pressure (4 $mTorr$) in BCl_3 environment using both RIE (50 W) and ICP (400 W) powers. An end point detection system is used to stop the etch at the bottom metal contact. A reasonably thick n^+ layer is therefore required to rule out the uncertainty in end-point detection of the

dry etch process and make sure that the bottom contact does not exhaust. After exposing

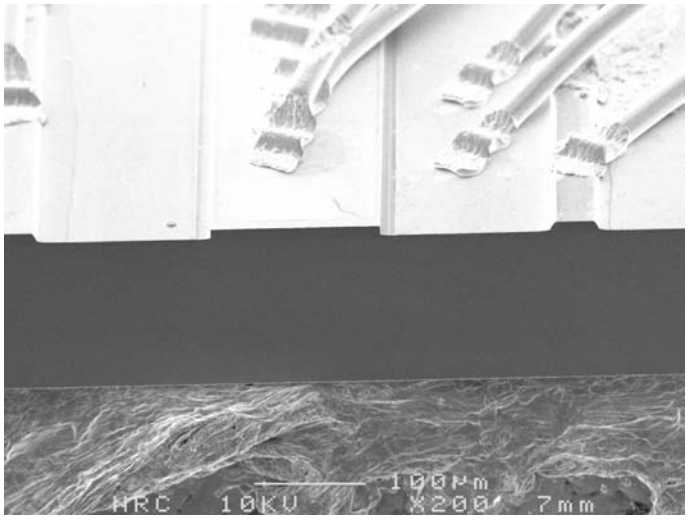

Figure 3.20: SEM micrograph of a fabricated SI-SP THz QCL. The side metal contacts and the Gold wire bond wire is visible in the picture.

the bottom contact n^+ layer, the mask 2 is used to define the opening windows for the side contacts. The spacing of the side metals with the ridge impacts the waveguide loss. If it is defined and deposited closer than 10 μm to the ridge, it can increase the waveguide loss significantly [110]. The side contact far away from ridge also incorporates a high contact resistance. Optimally, spacing of $\sim 15\mu m$ is picked for defining the side contact window. A stack of $Ni/Ge/Au$ (250/550/3000 $\mathring{A}$) metals are then deposited, to form the bottom contacts (Figure 3.19-c). After this, the back side of the $SI\ GaAs$ wafer is thinned down to $\sim 150\ \mu m$ to facilitate the heat dissipation. After that, the sample piece is cleaved into $\sim 1\ mm$ long Fabry-Perot resonator laser bars. Each laser bar is In soldered (epi-layer side up) on an Oxygen-free copper package. The emission facet of laser ridges is carefully placed as close as possible to the edge of the mount. Thin Au wires are used to connect the top metal contact on the ridge of each device to different electrical pins of a 16-pin package. The package is placed on a cryostat cold finger for low-temperature measurements. Figure

3.20 shows the SEM micrograph of the cleaved and wire-bonded SI-SP THz QCL ready to be tested.

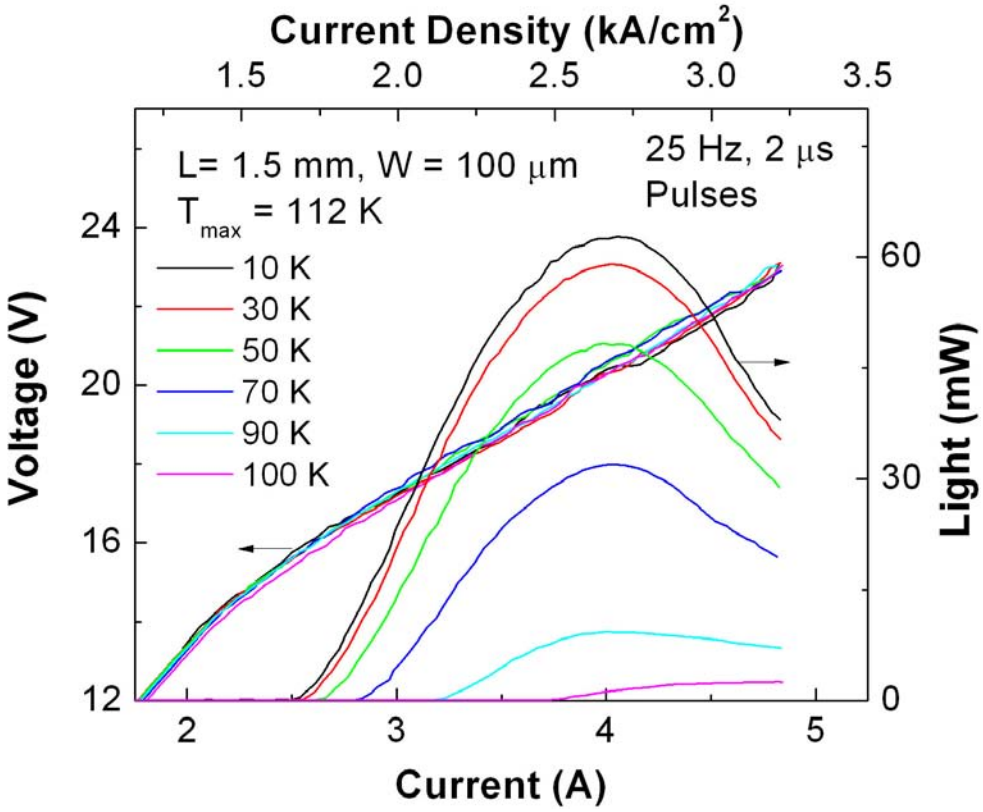

Figure 3.21: The collected THz light (optical output power) versus current curves for a 100 μm wide and 1.5 mm long THz QCL at different heat sink temperatures. The device is biased in pulsed mode (pulse width = 2 μs and repetition rate = 25 Hz).

Figure 3.21 shows the LIV characteristics of a SI-SP THz QCL based on V610 active region. As compared to the MM device fabricated with the same material, the SI-SP device lases at higher threshold current density at 10 K (= 1.66 kA/cm^2) and up to lower T_{max} (= 112 K). The THz light is calibrated using a Golay cell (the procedure of calibration is explained in Appendix B). The peak output power of the QCL device is measured to be as high as 60 mW, which decreases gradually with increasing the temperature.

3.2.2 Waveguide design for single mode operation

The laser field inside a SI-SP based waveguide is confined between the metal on top and the n^+ surface plasmon layer at the bottom of the active region. The doping of the n^+ layer determines the plasma frequency, which along with the thickness of this layer confines the mode inside the active region. A thick and highly doped n^+ confines the mode within the active region. Consequently it increase the overlap of the mode with very absorptive and thick n^+ layer. Therefore the doping and thickness of bottom n^+ layer can not be arbitrarily increased. This section uses the COMSOL MultiPhysics simulator to solve the 2D waveguide structure for the eigen-solutions. The simulation in this section mainly focus on the fundamental TM_{00} mode. The simulation is performed for a SI-SP THz QCl structure as shown in Figure 3.19-d, with 10 μm thick active region, 150 μm wide ridge, 50 nm of 5×10^{18} cm^{-3} doped top n^+ layer, side contacts at 20 μm away from ridge (as suggested by [110]), and various doping levels and thicknesses for bottom n^+ layer.

Figure 3.22 shows the COMSOL simulation results for various bottom n^+ layer thicknesses and doping values. The confinement factor is defined as the portion of the power confined inside the active region for the fundamental mode. The mirror loss and the waveguide loss for different modes in cm^{-1} are given by $\alpha_m = ln(R)/L$ and $\alpha_w = 2\beta \times \frac{2\pi}{\lambda}$, where $R = (\frac{n_{eff}-1}{n_{eff}+1})^2$ is the reflectivity, n is the calculated effective index of mode, and β is the imaginary part of the propagation constant [110]. Figure 3.22-a shows that the confinement of the mode inside the ridge (Γ) increases for the thicker bottom n^+ layer. At very thin n^+ layers, the confinement factor weakly depends on the n^+ layer doping. However as the thickness of the n^+ layer increases, the confinement factor increases faster with decreasing doping. Figure 3.22-b depicts the simulated waveguide loss, where it increases for thicker n^+ layer. Figure 3.22-c shows the same trend for the mirror loss, which was calculated for a 2 mm long ridge. Including all these results into the equation 3.1 results in the final figure of merit for the design of waveguide structure, as shown in Figure 3.22-d. It shows that

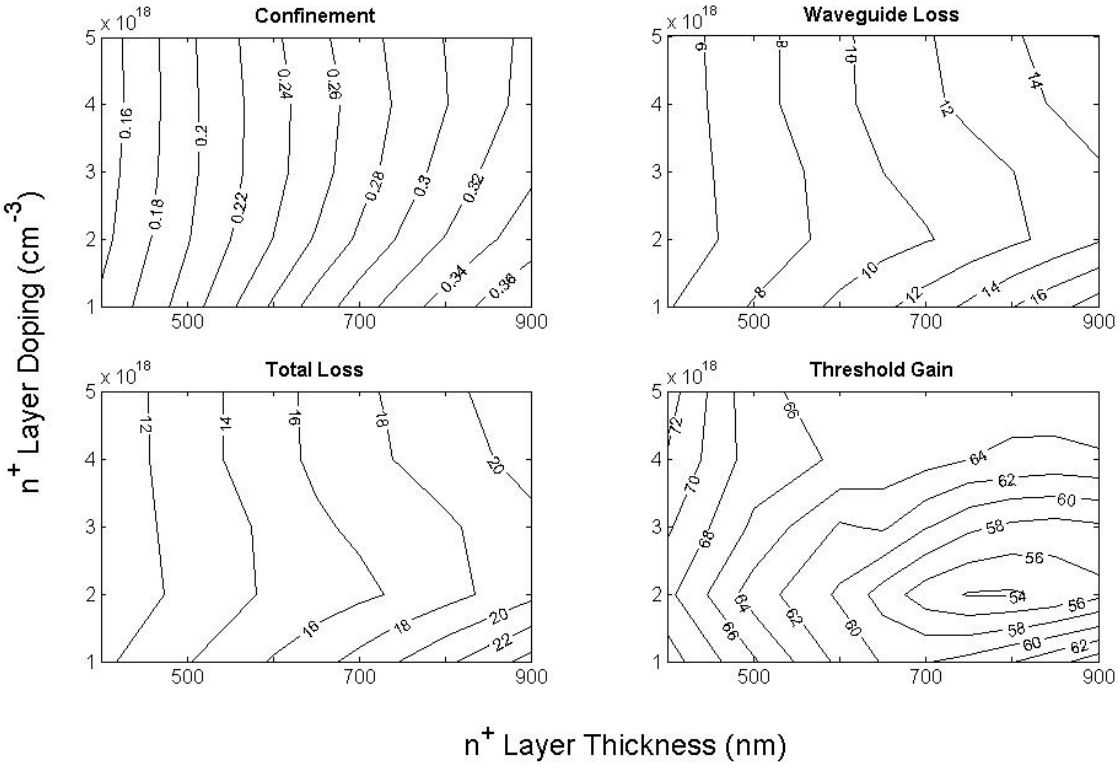

Figure 3.22: Simulated (a) confinement factor (b) waveguide loss (c) total loss (d) threshold gain for a 150 μm wide and 2 mm long SI-SP THz QCL, for various bottom n^+ parameters, using COMSOL. The top n^+ thickness is 50 nm with the doping of 5×10^{18} cm^{-3}. The loss and gain values are in cm^{-1}.

doping concentration of 2.5×10^{18} cm^{-3} and thickness of 750 nm is the optimum point for the bottom n^+ layer, which yields in ~ 50 cm^{-1} for threshold gain. The SI-SP THz QCL fabricated based on the V610 wafer (Figure 3.21) has a bottom n^+ doping concentration of 3×10^{18} cm^{-3} and thickness of 400 nm that results in 20 cm^{-1} higher threshold gain. The fundamental mode loss of this wafer is so high that becomes comparable with the first excited mode (TM_{01}) and makes it possible to also excite the TM_{01} mode, as will be

discussed in Section 3.2.4.

3.2.3 Thermal quenching of lasing operation

THz QCLs are often biased at high electric current and voltage for lasing operation. Only a small portion of the injected current contributes to useful optical output power, most of the input electric power eventually convert to Joule heat, increasing the temperature of the active region of the devices. At elevated temperatures, non-radiative optical phonon scattering from upper to lower lasing state can be thermally activated, leading to depopulation of upper lasing state and hence diminishing population inversion and radiative transition efficiency [66]. Thermally-induced leakage current becomes more substantial at higher temperatures, further deteriorating device performance. In low duty-cycle pulsed mode, the Joule heat generated in the active region can adequately be dissipated to a heat sink. The active region therefore remains in thermal equilibrium with the heat-sink. In CW operation mode the Joule heat is continuously generated in the active region and if the current injection is high, heat generation could outpace heat dissipation, resulting in the accumulation of Joule heat and the active-region temperature being well above the heat-sink temperature [121, 103].

Investigation of the thermal dynamic behavior of operating THz QCLs is therefore of crucial importance for pinpointing the main mechanisms responsible for observed performance degradation as well as for further optimizing device performance for high-temperature, high-power and CW operation. While some pertinent issues can be tackled via numerical modeling, the phenomenon remains to be observed directly in real time via experiment. Direct observation of thermal quenching and temperature rise of the active region has already been reported in mid-infrared lasers [122]. The two major candidates for fast detection of THz radiation are $Ge:Ga$ photodetectors and THz quantum well photodetectors (QWP). The $Ge:Ga$ detector is based on shallow donor levels and has shown response times as low

as 2 ns [123]. On the other hand QWP is based on electronic process in quantum wells, and in principle can be much faster [124]. Our group has demonstrated the background limited performance of the latter detector [125]. The temporal response time of a THz QWP could be trimmed down to nanoseconds or even shorter in contrast to milliseconds attainable with Si bolometers or Golay cells in which the detection mechanism is based on slow thermal processes. This could lead to experimentally resolving fast dynamic processes in operating THz QCLs and shedding light into underlying mechanisms which are responsible for dynamic performance of THz QCLs.

This section studies THz QCLs thermal dynamics, in details. An experimental method, in which a spectral-matching QWP was employed to measure stimulated radiation pulses from a 3.4 THz single surface plasmon QCL, is developed. Only then were we able to carry out a systematic suite of experiments to elucidate the inner operation of this laser under modulation. This part of the thesis resolves the temperature evolution in the active region of THz QCL under pulsed electric biases. A theoretical model based on thermodynamic differential equations is employed to simulate the dynamic temperature profile inside the active region of the devices. It is concluded that the optical output contribution from each of the cascaded quantum well modules of the THz QCLs is highly differentiated and the dynamic response of the devices is strongly affected by thermal effects.

Details of the device under study and experiment setup

The device used for the study in this section is similar to the SI-SP THz QCL presented in Figure 3.21. Before packaging, the SI $GaAs$ substrate of the samples is thinned down to 130 μm to facilitate heat dissipation from the active region to a heat sink underneath. The sample is then cleaved into laser bars with a $\sim$ 1 mm long Fabry-Perot resonator and a stack of $Al_2O_3/Ti/Au$ (300/25/100 nm) high reflective (HR) coating is grown on the rear facet of the laser. The laser bars are Indium soldered (epi-layer side up) on an oxygen-free

copper package and then mounted in a Janis closed-cycle cryostat for measurements.

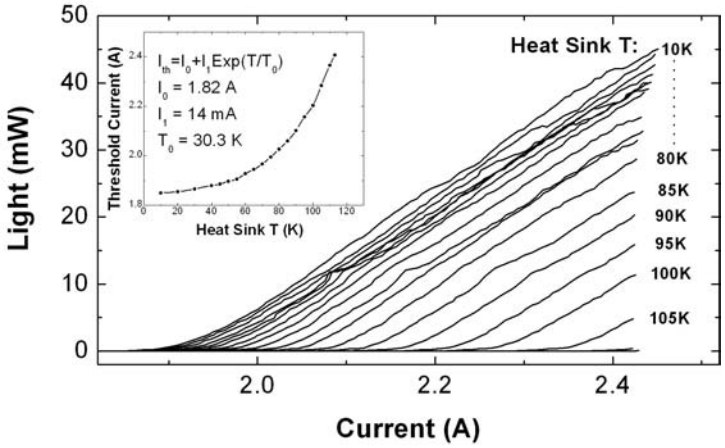

(a)

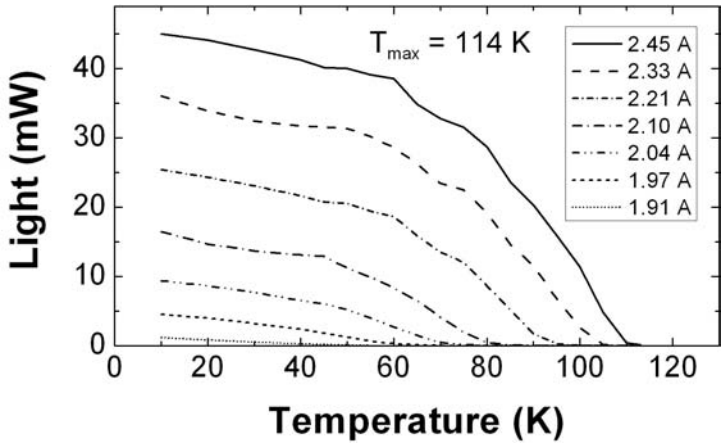

(b)

Figure 3.23: (a) The collected light (optical output power) versus current curves for a 100 μm wide and 1 mm long THz QCL at different heat sink temperatures. The device is biased in pulsed mode (pulse width = 150 ns and repetition rate = 25 Hz). The inset depicts threshold current density versus heat sink temperature. The lasing is observed up to a maximum temperature of 114K. (b) Collected light versus temperature graph under various current injection levels of the same device.

Figure 3.23-a shows the LI curves of the QCL device in pulsed operation (with a 25 Hz

repetition rate and a 0.15 μs pulse width) and under different heat-sink temperatures ranging from 10 K to 105 K. The device lases up to T_{max} of 114 K when biased in this low-duty-cycle pulsed mode. The Joule heat generated in the device is negligible due to low average electric input power ($< 9\ mW$) under low duty-cycle operation (0.015%). Since the duty-cycle is very low, the average input electric power is well below the maximum cooling power of the heat sink to which the device is mounted, and it is reasonable to assume that the active-region temperature of the device equals the nominal heat-sink temperature. The inset of Figure 3.23-a plots the threshold current versus heat sink temperature. The threshold current as function of temperature follows the well-known empirical equation,

$$I_{th} = I_0 + I_1 exp(T/T_0), \tag{3.9}$$

where $I_0 = 1.82\ A$, $I_1 = 14\ mA$ and $T_0 = 30.3\ K$ for the device under test. Reorganizing the experimental data in Figure 3.23-a, the curves of light (optical output power) versus active-region temperature under different electrical current injection can be plotted as in Figure 3.23-b. It clearly shows that for a given current injection, the optical output power quickly drops to zero as the temperature rises. For a higher injected current, the lasing of the device stops at a higher temperature.

Figure 3.24 shows measured voltage versus current characteristics of the device at 4.2 K. The small bump (at I = 1.2 A) shows the voltage at which energy levels on the injector side becomes aligned [66]. This means that after this voltage, carriers are selectively injected in the upper lasing state. Therefore, this bump in the figure represents the onset of population inversion and gives an estimate of the transparency current. Later we will use this parameter in calculating the quenching time. Also note that this electrical characteristic is weakly temperature dependant. The emission wavelength of the THz QCL devices is $\sim 89.3\ \mu m$ (or $f = \sim 3.37\ THz$ in frequency), as indicated on the inset of Figure 3.25.

The THz QWP device is based on a $GaAs/AlGaAs$ multiple quantum well structure grown by molecular beam epitaxy. The width of the GaAs quantum well is 22.1 nm and

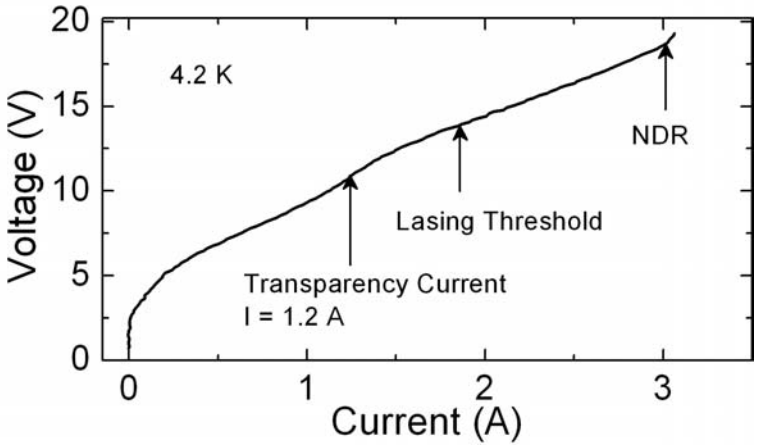

Figure 3.24: The voltage versus current characteristic of the device under test at 4.2 K. The bump around 1.2 A is a signature of the energy level alignment at the injector side, which is onset of gain. This current gives the approximate value of the transparency current. The rightmost arrow shows the NDR point, at which the energy levels are out of alignment.

the width of $AlGaAs$ (1.5%Al composition) is 95.1 nm. This structure was described in [125]. The doping concentration in the quantum well is 3×10^{16} cm^{-3}. The device consists of 23 repeats of such quantum well/barrier module. The whole $GaAs/AlGaAs$ MQWs are sandwiched between 400 nm top and 800 nm bottom $GaAs$ contact layers doped with Si to 10^{17} cm^{-3}. A 1.5×1.5 mm^2 mesa with a $Ti/Pt/Au$ metal mirror layer on the top is fabricated onto the epi-layers. The substrate is cleaved in the vicinity of the mesa and one facet is polished to 45 degree with respect to the plane of the device. Incoming THz radiation is focused onto this 45 degree facet to ensure the light is absorbed and the intersubband transition is excited in the quantum wells. The fabricated THz QWP is then glued onto the edge of a Kovar package and mounted inside another liquid-helium cryostat. The THz QWP is biased at 30 mV and 10 μA by a SR570 Stanford Research Systems current amplifier, and the detected photocurrent is amplified with a gain of 1 mA/V and a

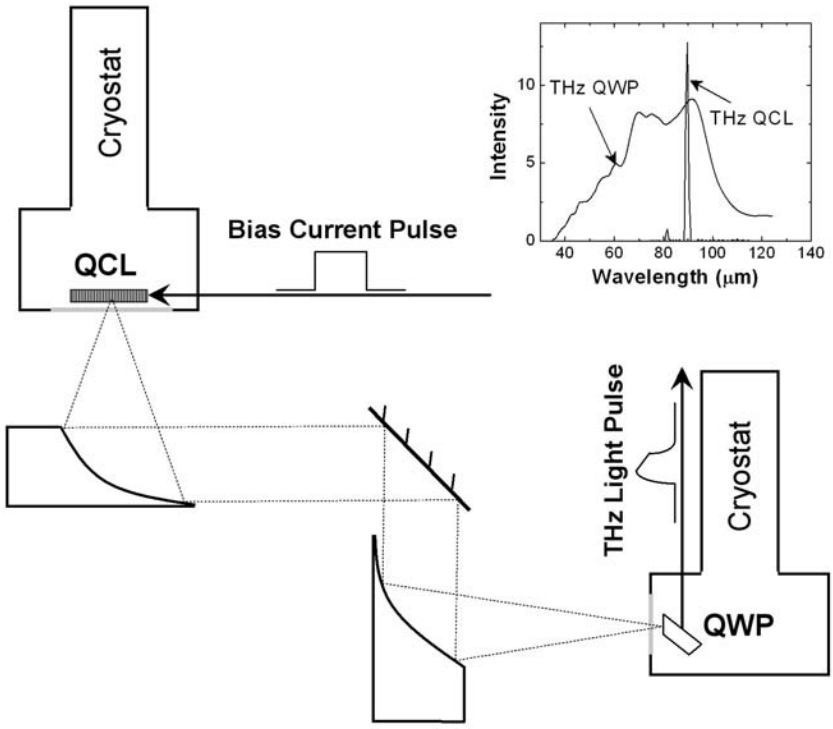

Figure 3.25: The schematic diagram of the experimental setup used for direct detection of THz radiation from the QCL device using the THz QWP device. The dashed lines show the THz optical path from the QCL to the QWP. The inset shows spectra of the THz QCL (lasing) and the THz QWP (responsivity). Both QCL and QWP are tested at 10 K and biased above lasing threshold. This shows that the lasing wavelength of the THz QCL is right in spectral response range of the THz QWP.

bandwidth of 1 MHz. This bandwidth limits the time resolution ($\sim 400\ ns$) in measuring the THz signal. The chosen bias of 30 mV is below the barrier breakdown voltage (40 mV) of the device [126]. The measured spectral response of the THz QWP device is shown in the inset of Figure 3.25. It shows that the device responds to a wide wavelength range from 40 to 100 μm. The device exhibits maximum responsivity at 93 μm that is very close to the lasing wavelength of the THz QCL under test (89.3 μm).

The beam pattern of the THz QCL is wide and divergent due to the sub-wavelength size of its ridge waveguide structure [127]. Two parabolic mirrors are deployed to collimate and re-focus the THz beam directly from the THz QCL device to the THz QWP device, Figure 3.25. No significant vapor absorption along the optical path is observed. The THz QCL device is electrically biased by a pulse generator (HP 8114A), with a measured rise time of below 40 ns. The pulsed electrical signal from the THz QWP is measured using an oscilloscope (TDS 3012).

Experimental results

With the set-up described above, the thermal dynamic behavior of lasing THz QCLs have been investigated. During this experiment the thermal quenching of the lasing operation in the duration of electrical current pulses is directly observed, by measuring the temporal evolution of the optical power of the device. The time-resolved optical output power of the THz QCL under pulsed electric current injection ($I = 2.45\ A$ and $V = 16.3\ V$) is measured using the spectral-matching THz QWP detector. In the measurements the device starts with an initial active-region temperature of 10 K (i.e., the heat-sink temperature), unless otherwise specified. Figure 3.26-a shows the detected THz radiation pulses for various electric pulse widths ranging from 3 to 90 μs. The repetition rate of the electric current pulses is increased to remains the same (25 Hz). It can be observed that the optical output power rises quickly to the maximum upon the application of an electric current. The maximum optical output power remains almost unchanged through the whole pulse duration for short pulses (e.g., 3 and 5 μs). As the electric pulse width extends from 10 to 70 μs, the optical output power of the device starts to gradually decrease in time and drops to zero when the electric pulse is switched off. The falling time constant of the curves is around 400 ns. This is constrained by the 1-MHz-bandwidth current amplifier that is part of the detection system and also by the slow RC time constant of the circuit.

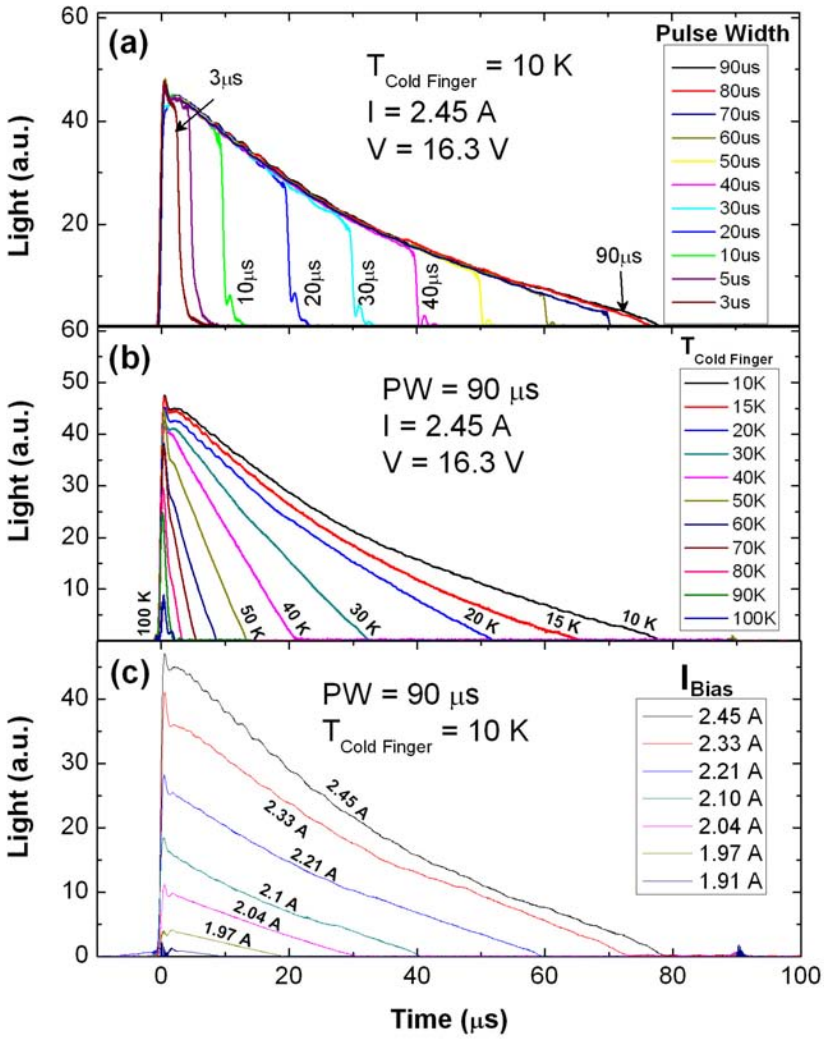

Figure 3.26: (a) Measured THz radiation pulse under different bias pulse widths ranging from 3 μs to 90 μs. The device is biased at current injection level of 2.45 A and the heat-sink temperature of 10 K. (b) Measured THz radiation pulse at different heat-sink temperatures varying between 10 K and 100 K. The device is biased at a current injection level of 2.45 A with 90 μs-long pulses. (C) Measured THz radiation pulse under different injection current levels. The device is biased with 90 μs-long pulses and heat-sink temperature is set at 10 K.

THz QWPs are believed to have much faster response time [124]. As for pulse widths of 80 and 90 μs, the optical output power descends to zero before the electric pulse is shut down. The diminishing optical output power for longer electric current pulse width is due to thermal quenching of THz emission at elevated active-region temperatures. The Joule heat generated in the active region upon higher duty-cycle electric current pulses is not dissipated fast enough, leading to heat accumulation and hence the increase of the active-region temperature.

Figure 3.26-b shows the optical output power of the device as a function of time as the initial active-region temperature varies from 10 K to 100 K. The device is biased in pulsed mode, at a constant injection current of 2.45 A. It shows that the maximum of the optical output power decreases with the increase of the initial active-region temperature. All curves show a declining slope, nevertheless, it takes longer time for the optical output power to descend to zero when the device starts with a lower temperature. For example, when the active-region temperature of the device starts from 90 K, it takes only 3 s before the lasing quenching is observed, while starting from 15 K, the lasing operation lasts for ~ 64 μs. Figure 3.23-b shows that the device stops lasing at a maximum temperature of 114 K under the same current injection of 2.45 A (in low-duty-cycle pulsed mode). It is therefore postulated that the lasing quenching observed in Figure 3.26-b occurs around a similar temperature as the average active-region temperature increases with time upon the application of electric current injection.

Figure 3.26-c shows the optical output power of the device as a function of time upon the application of different electric current injection ranging from $I = 1.91$ A to $I = 2.45A$, with a constant pulse width of 90 μs. The slope of the curves (dL/dt), for instance at 10 μs, appears smaller at lower current injection levels but more linear than that at higher current injection levels. Since the slopes (dL/dT) are similar at low T for different currents (Figure 3.26-b), the faster drop of power at high current (i.e. $I = 2.45$ A) in Figure 3.26-c compared

to lower current (i.e. $I = 2.1\ A$) suggests a faster temperature increase at the first 20 μs of the pulse during higher current injection. Besides, this measurement shows that the temperature increase in active region slows down in time, particularly for large biases. Indeed, the decrease of emission in Figure 3.26-c, dL/dt, is about constant or slightly decreases with time while we know the emission drops severely at higher temperatures and large biases (Figure 3.26-b). Figure 3.26-b shows that the drop of emission with temperature is more critical at large biases, which suggests that the slowing down of active region temperature rise during long pulses is more pronounced at higher biases.

Thermal dynamics modeling

A time dependant 2D heat flow equation is numerically solved to obtain the dynamic temperature profile and evolution inside an operating QCL device upon the application of current injection. Because of the relatively long ridge length (1 mm) compared to the width and the thickness, it is reasonable to assume that the temperature along the QCL waveguide ridge is constant. As a result, the system can be treated as a two dimensional system [121]. Inset of Figure 3.27 shows the device model used in the simulation. The device model only consists of a $10 \times 100\ \mu m^2$ MQW active region and a 130 μm-thick undoped GaAs substrate. Joule heat is assumed to be uniformly generated only in the MQW active region and is dissipated to the heat sink through the $GaAs$ substrate. We assume a uniform current distribution between the two contact layers and hence a uniform heat generation in the active region. The conductivity of the bottom n^+ contact layer can challenge this assumption, by modifying the current distribution in the active region and by inducing an electric resistance between the edge of the laser and the ohmic contact. Temperature dependence and anisotropic nature of the thermal conductivity and the heat capacity of the materials are taken into account in the numerical simulation. We assume prefect interface layer between the heat sink and the chip. Therefore the boundary condition at the bottom

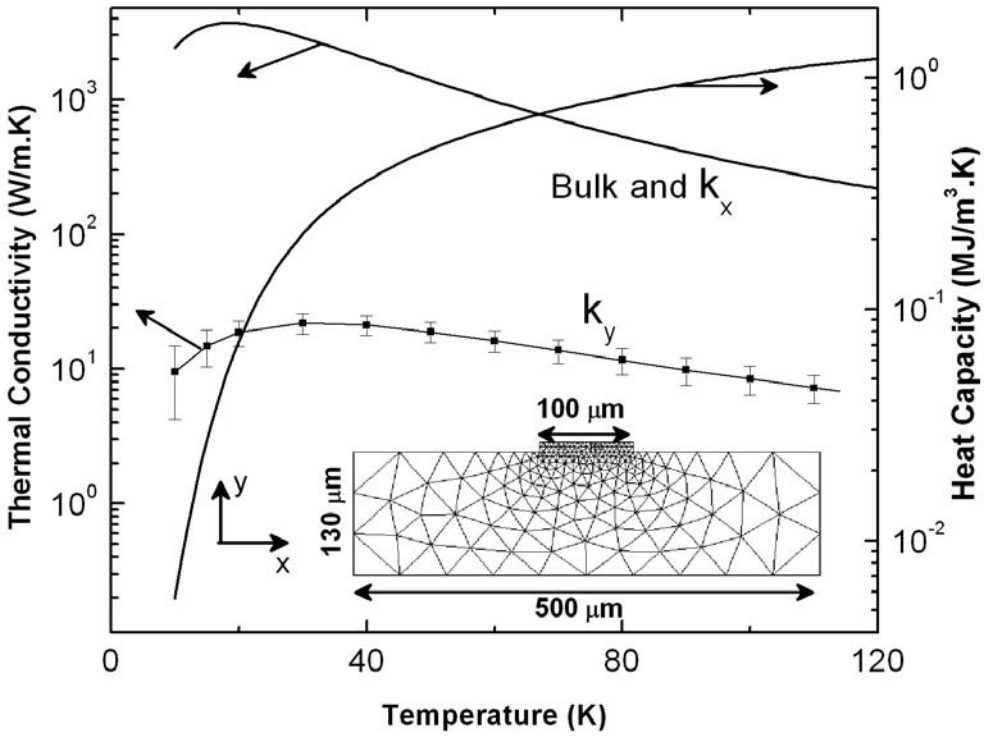

Figure 3.27: The temperature dependence of thermal conductivity and heat capacity of the active region of the THz QCL used for numerical simulation. The error bars for the active region thermal conductivity define the 10% mean square error region for quenching time curve using gain criterion. The inset shows the mesh diagram of the device model defined for the numerical simulation.

of the substrate is set to a constant temperature, which implies infinite cooling power. Other boundaries of the device are set to being thermally isolated from outside (no heat exchange). The 2D dynamic heat flow PDE can be then written as

$$\nabla.(k_x \frac{\partial T}{\partial x} + k_y \frac{\partial T}{\partial y}) + P = c \frac{\partial T}{\partial t}, \tag{3.10}$$

where k_x and ky are respectively thermal conductivity along horizontal and vertical directions with a unit of $W/m.K$, c is heat capacity for each region with a unit of $J/m^3.K$, T is temperature with a unit of K, and P is input power density with a unit of W/m^3.

The I-V characteristic at 4.2 K (Figure 3.24) to calculate the power density, P, which was considered temperature independent for the sake of simplicity. Thermal conductivity and specific heat of $GaAs$ varies with temperature. 3.27 depicts the temperature dependence of bulk $GaAs$ thermal conductivity and specific heat [114]. It is well-known that the thermal conductivity of the active region is anisotropic, and the vertical thermal conductivity (k_y) is lower than the horizontal and bulk values [128, 129, 120]. For the sake of simplicity, the horizontal thermal conductivity (k_x) and the heat capacitance of the active region are chosen the same as $GaAs$ substrate. Therefore, the only fitting parameter of this model is active region vertical thermal conductivity (k_y). We adjust the vertical thermal conductivity of the quantum well region (k_y) to fit the measured thermal quenching times from Figure 3.26-b. A simple way to estimate the quenching time from the 2D thermal simulation results is to compare the average temperature of active region with the $T_{max} = 114\ K$. This approach is valid only if gain profile across active region follows the same shape as the temperature distribution. As the temperature profile across the active region is not uniform when the device is under high current injection, the optical contributions from individual cascade modules become highly non-uniform because the threshold current strongly depends on temperature (inset of Figure 3.23-a). In order to get better measure of quenching time, we propose a criterion that calculates the total gain of the active region, based on the given temperature distribution across the active region.

In the QCL, the current flowing through each of the cascaded modules (I) is the same. Nevertheless, the local threshold current of each of the module ($I_{th-i}(T)$, depending on the exact temperature at that point) is different due to the nonuniform temperature profile. As a result, some modules (the lower temperature side) are operating above the corresponding local threshold point (net photon emission) and some modules (at higher temperature side) are operating below the corresponding local threshold point (net photon absorption). We define a parameter R that denotes the ratio of the total reserve of optical gain (gain margin, G_{res}) against the total waveguide optical loss (α). It is reasonable to assume that the gain

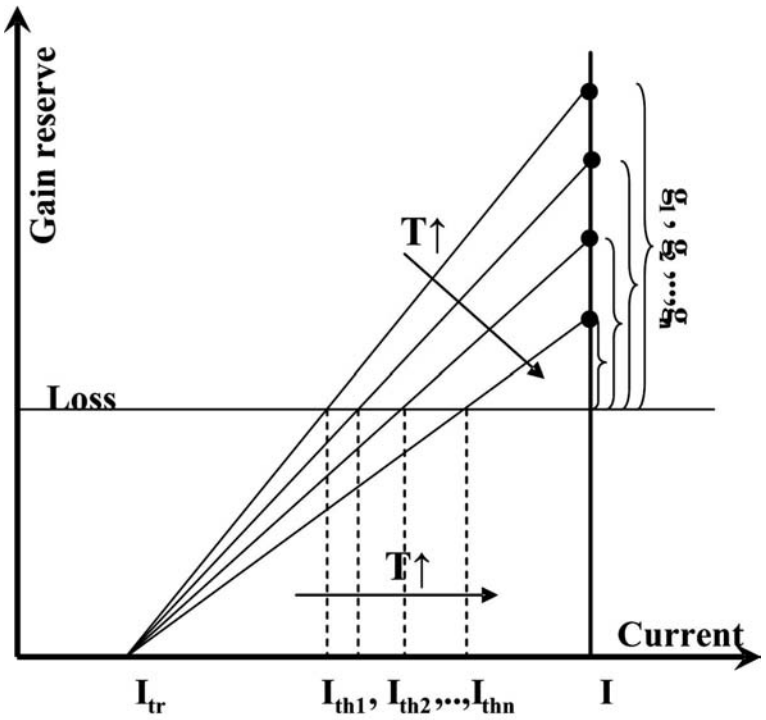

Figure 3.28: The schematic presentation of the gain model calculation. It is assumed that the gain for each active region module increases linearly with current above transparency current. The threshold current for n-th module (I_{thn}) increases with the temperature, resulting in decrease of the gain for corresponding module (g_n). The total gain is the sum of the gain for all the modules.

of a quantum cascade module is linearly dependent on the current, when the device is biased above its transparency current (I_{tr}): $G_{res} \propto (I - I_{tr})$, see 3.28. By using above assumptions, the overall ratio (R) of total reserve of gain to the total optical waveguide loss is calculated by summing up the gain to loss ratio for each period of the cascaded structure, as

$$R = \frac{G_{res}}{\alpha} = \frac{1}{n}\sum_{i=1}^{n}\frac{I - I_{tr}}{I_{th-i} - I_{tr}}, \tag{3.11}$$

where $n = 216$ is the number of the quantum cascade modules, I_{th-i} is the temperature-

dependent local threshold current at the i-th cascade module, and I_{tr} is the transparency current (Figure 3.24). Equation 3.11 assumes identical waveguide mode overlap in each module, which is a reasonable approximate for surface plasmon devices. The model also assumes a temperature independent transparency current for the sake of simplicity. This approximation is based on the small sensitivity of I-V with temperature. One can combine equations 3.10 and 3.11 and use the temperature distribution profile found by solving the 2D thermal diffusion model to obtain the value of gain criterion. For ease of calculation we converted the sum to an integral as,

$$R = \frac{1}{z_2 - z_1} \int_{z_1}^{z_2} \frac{I - I_{tr}}{I_0 - I_{tr} + I_1 exp(T(z)/T_0)} dz, \tag{3.12}$$

where z_1 and z_2 are the terminal coordinates at the top and bottom ends of the active region, respectively. The ratio $R = G_{res}/\alpha$ can be used as an unambiguous indicator on whether lasing can be observed. When the device is under a given current injection (I) that is initially above the lasing threshold at the starting temperature, the ratio (R) is greater than unity and lasing can be observed. With the increase of the active-region temperature, the value of total reserve of gain drops as the local threshold current at each cascaded module (I_{th-i}) increases and thus the ratio (R) decreases with time. The device stops lasing (i.e., quenched) when the ratio drops below unity ($G_{res} < \alpha$). The lasing quenching time (how long the lasing lasts) can therefore be derived by calculating the time evolution of the ratio of R.

A PDE solver software is employed to find the numerical solution to equation 3.10. The device is initially in thermal equilibrium with a heat sink. A 90 μs-long electric current pulse ($I = 2.45\ A$) is applied to the device model at time $t = 0$. Vertical thermal conductivity of the active region (k_y) is successively adjusted from higher temperatures to lower temperatures, using quenching time calculated by gain criterion. As the k_y value for higher temperature is found, it is used for fitting the quenching time at lower temperatures. Figure 3.27 shows the derived values for the vertical thermal conductivity of active region

(k_y), with 10% error in quenching time prediction. The vertical thermal conductivity for active region is less than two orders of magnitude lower than the bulk value, which is consistent with an earlier report [120]. The error bar increases at lower temperatures because the device stays most of the time at high temperature before quenching.

The temporal evolution of the ratio R is calculated based on equations 3.9, 3.10, 3.11 and 3.12 and the results are plotted in Figure 3.29-a. In the simulation, the device is under current injection of $I = 2.45\ A$, the pulse width is all set to 90 μs. The heat-sink temperature is set in a range from 10 K to 90 K. The electric current pulse is turned on at $t = 0$. One can see that the ratio R at $t = 0$ is greater than unity for all temperatures. As a result, lasing can be observed. After that the ratio starts to drop due to the increase of the active-region temperature. It takes different length of time before the ratio R decreases to unity, where lasing is quenched, for different initial heat-sink temperatures. The quenching time is derived and plotted in the Figure 3.29-c. The simulated quenching time results using the gain criterion show good agreement with the experimental data.

The evolution of the average temperature across the active region above the substrate is plotted in Figure 3.29-b. It increases very rapidly at the beginning and then gradually saturates. Figure 3.29-b shows, when starting from various initial temperatures ($10-90\ K$), the temperature curves reach the maximum lasing temperature (denoted by a horizontal line across the diagram) at different times. For example, it takes 4 μs to rise from 90 K to 114 K and 59 μs from 15 K to 114 K. The quenching time using the active region averaged temperature criterion is plotted as well in the Figure 3.29-a. The results are also in good agreement with the experimental data that are drawn from Figure 3.26-b and the gain criterion results. The good agreement indicates the average temperature can well represent an "effective" active-region temperature in nonuniform temperature profile cases. The interesting observation in Figure 3.29-b is the faster slope (dT/dt) of the curves for lower temperature values, particularly at $t = 0\ s$. This is due to high thermal conductivity

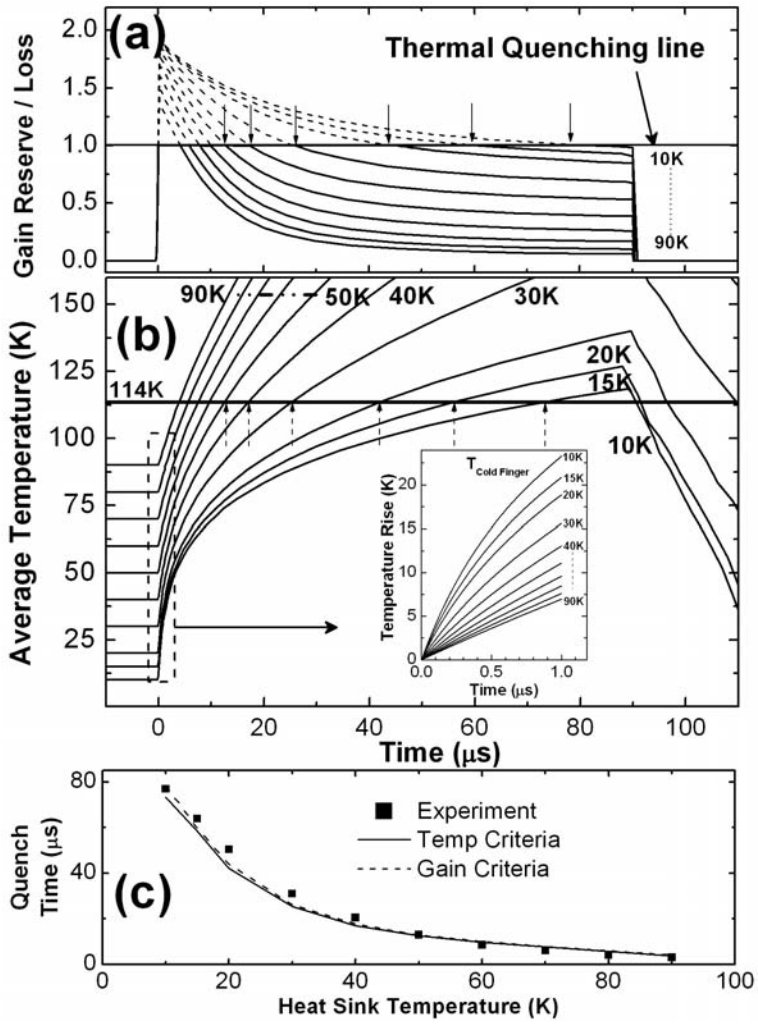

Figure 3.29: (a) Temporal evolution of the ratio R; the dashed lines depict the lasing region. the bias current is $I = 2.45\ A$ in the simulation. (b) Simulated average temperature evolution profile of the device active region for different heat-sink temperatures. The bold horizontal line denotes the maximum lasing temperature, beyond which the device stops lasing. The inset shows the rise of the active region average temperature zoomed in below 1 μs. (c) The comparison of simulated and measured lasing quenching time under different heat-sink temperatures.

and low heat capacity values at lower temperature in Figure 3.27. The inset of Figure 3.29-b shows the simulated average temperature growth in active region for various heat sink temperatures below 1 μs. It confirms the faster slope (dT/dt) at lower temperature.

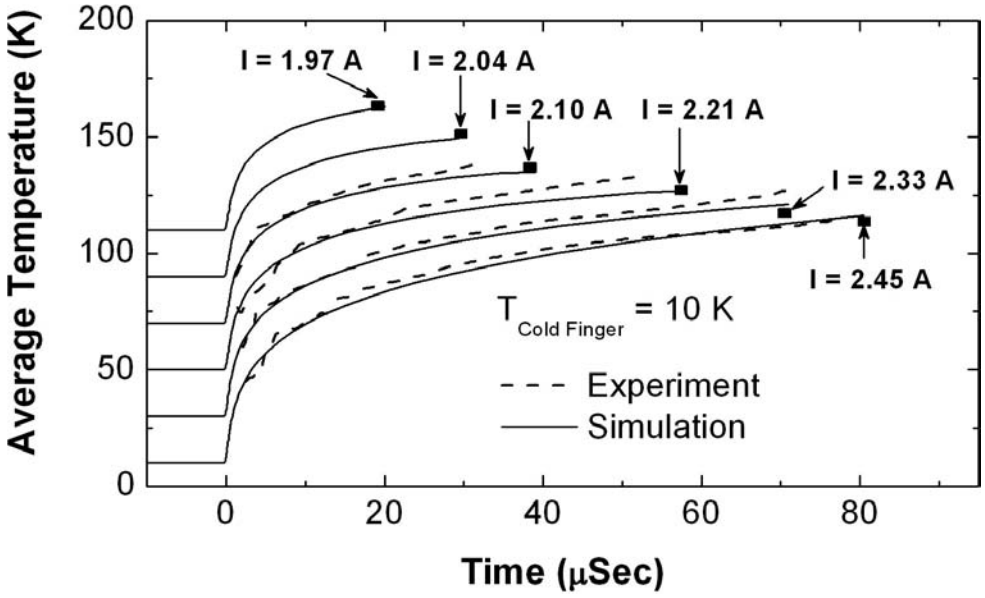

Figure 3.30: Comparison of simulation and experimental data for active region temperature evolution ($T_{heat-sink} = 13\ K$) at device biases of $I = 2.45$, 2.33, 2.21, and 2.1 A. The bold square dots denote the quenching point for each bias, based on the data on 3.26-b. Each curve is shifted by 20 K for better visibility.

The Figure 3.30 shows comparison of simulated average active region temperature evolution curve ($T_{heat-sink} = 10\ K$) and the corresponding experimental data for four different injection current bias values. The experimental curve of temperature vs. time is put together by combining the experimental curve of optical output power versus temperature (in Figure 3.23-b) and the experimental curve of optical output power vs. time (in Figure 3.26-c). In order to eliminate the effect of light pulse transient (observed in Figure 3.26-c) on the experimental graph in Figure 3.30, we considered the light values after 2 μs, and used the simulated temperature value at 2 μs for the starting point. One can see

good agreement between the experimental data and the simulation results, particularly for higher injection currents. This demonstrates that the diminishing optical output power is a result of increasing active-region temperature during the pulse. The existing discrepancy in Figure 3.30 is mainly due to larger error bars for active region thermal conductivity in the inset of Figure 3.27 For lower injection currents, average active region temperature is lower and hence the simulation discrepancy increases. The uncertainty in thermal conductivity value for active region at lower temperature also affects the data shown in Figure 3.29-c, where the calculated thermal quenching time is lower than experimental points for lower temperatures. Figure 3.30 also verifies the earlier discussion about the pace of temperature increase at different injection biases. By looking at the slope of the curves at $t = 10\ \mu s$ in Figure 3.30, it is clear that the active region temperature rises faster with increasing the bias current. Also the slope of curves right before thermal quenching confirms that at higher bias, the slowing down of temperature increase is more pronounced. This is mostly due to large effective heat capacity to thermal conductivity ratio (c/k_y) at higher temperatures (see Figure 3.27).

3.2.4 Waveguide design for Bi-modal operation

After roughly a decade of intense research on THz QCLs, the prototype devices are getting closer to be deployed for various THz applications [61]. Due to sub-wavelength dimension of the laser structure, the emission pattern of the device is inherently diffractive (wide-angle beam) [130]. Focused and controllable emission beam profiles are crucial for many applications [2]. Engineering the laser emission beam pattern is demonstrated using grating [131, 132], photonics crystals [133] and external mode converters such as horn antennas [134, 135], Si lenses [136], plasmonics [137] and hollow dielectric waveguides [138]. The THz beam with a divergence angle as low as eight degrees has been recently reported by employing a third order grating on a ridge waveguide [139]. Although the beam shape

of the laser has been engineered and steered using different designs of photonic crystal structures, dynamically controllable beam emission from a single THz QCL has not been achieved yet. This section studies the bias-controlled tuning of the emission direction of a THz QCL. Beam switching is achieved by selectively exciting different waveguide transverse modes under different current injection schemes [140].

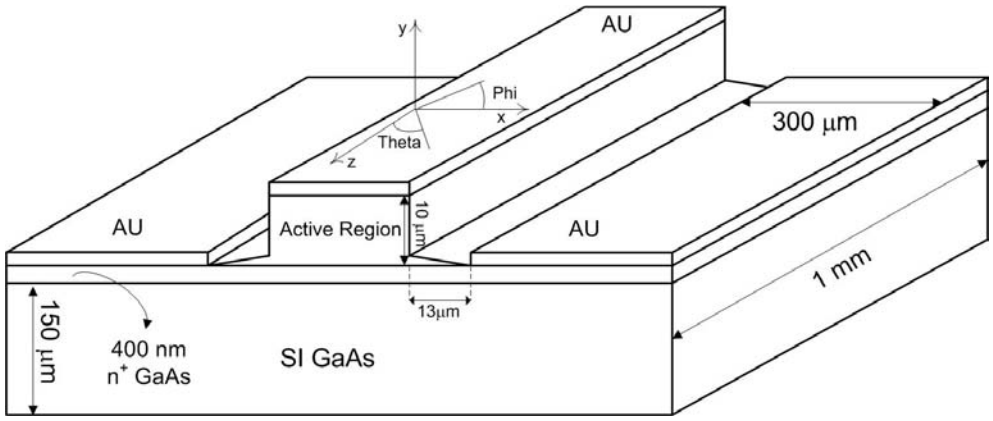

Figure 3.31: Schematic presentation of the THz QCL structure: The *Au* contacts on the sides are 13 μm away form each side of the ridge. Definition of the angles for far-field measurement and simulation is shown in the graph.

The focus will be on a SI-SP THz QCL, where the optical mode profile extends to the semi-insulating substrate and hence is not tightly confined in the active region. The device shows relatively less divergent emission patterns and also higher output power at the expense of higher optical loss [127]. The top contact is a metal layer directly on the top of the ridge waveguide and the bottom contacts consist of two Au metal layers besides the ridge waveguide, sitting on a 400 nm thick n^+ $GaAs$ layer which is underneath the QCL active region (see Figure 3.31). As discussed in section 3.2.2, with such a SI-SP waveguide design the fundamental mode (TM_{00}) loss gets so high that becomes comparable with the second mode (TM_{01}). The substrate is electrically insulating, the current is therefore laterally injected into the quantum-well active region from both sides of the laser ridge

through the thin bottom n^+ $GaAs$ layer. The side current injection leads to laterally non-uniform distribution of the injected current and electrical potential, giving rise to a laterally non-uniform gain profile. The local gain profile, even though non-uniform, is laterally symmetric due to current injection equally from both sides of the ridge. The lateral non-uniformity of the gain profile plays an important role in deciding which transverse mode can be excited, because of the different extent to which the transverse modes overlap with the gain profile. As a result, quasi-TM_{00} or quasi-TM_{01} may be selectively excited under different current injection. For simplicity from now on, these quasi-TM modes are called as TM mode.

Device fabrication and results

The fabrication procedure details are the same as explained in section 3.2.1 for SI-SP THz QCLs. A sufficient wide ridge waveguide is needed to accommodate TM_{01} lateral mode. The 150 μm wide ridges is selected for this purpose. With this ridge width, loss of TM_{00} and TM_{01} are comparable and are lower than TM_{02} mode loss. The bottom contacts are 13 μm away from the edges of the ridge on both sides, respectively, to yield efficient and laterally symmetrical current injection. The SI $GaAs$ substrate of the samples is then thinned down to 150 μm to facilitate heat dissipation from the active region to a heat sink underneath. The sample is then cleaved into laser bars with a ~ 1 mm long Fabry-Perot resonator.

Figure 3.32-a shows the LI and voltage-current (VI) characteristics of the QCL device in pulsed operation (with a 25 Hz repetition rate and a 200 ns pulse width) and under different heat-sink temperatures ranging from 10 K to 90 K. The V-I plot is measured using a four point technique, in which the four contact points are on the device to and side metal contact pads. The Golay cell detector collects 40° cone of the output THz light. The inset of Figure 3.32-a shows light collection scheme. The laser device starts to lase

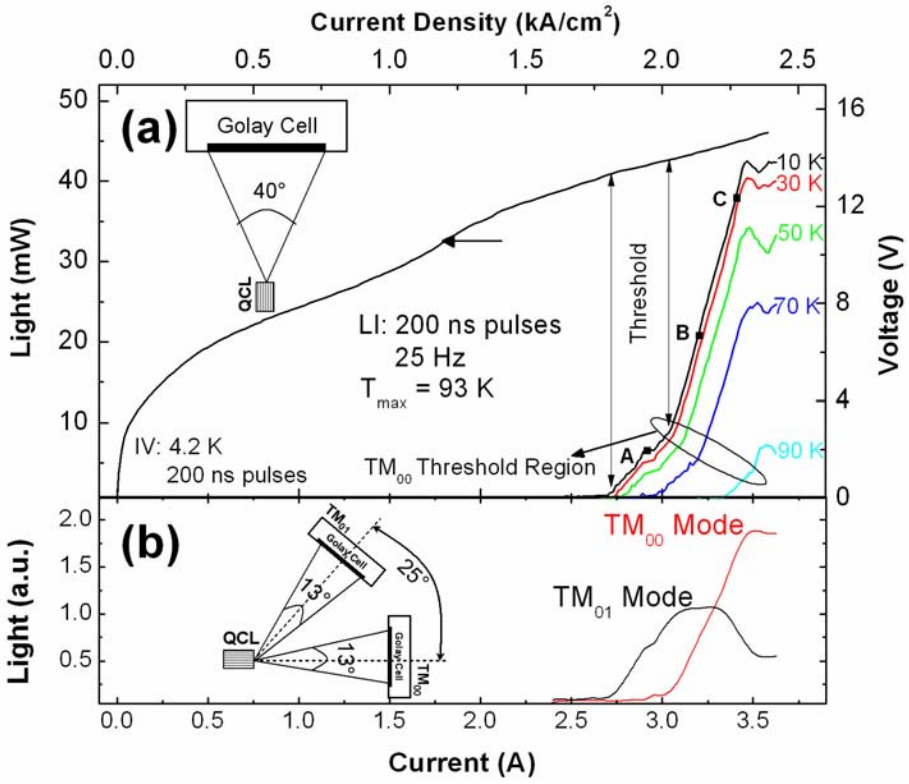

Figure 3.32: (a) The collected THz light (optical output power) versus current curves for a 150 μm wide and 1 mm long THz QCL at different heat sink temperatures. The IV characteristic is measured at 4.2 K using 200 ns pulses. The light is collected within a 40° emission cone. The slope change in L-I curve is attributed to the change of the mode excited inside the laser ridge waveguide. Lasing is observed up to a maximum temperature of 93 K. The horizontal arrow highlights the transparency current on V-I curve. (b) The collected THz light versus current curves for each mode. The TM_{00} is collected directly in front of the facet and the TM_{01} is collected by moving the detector off the normal direction by 25°. The collection cone in each case is 13°.

at $J_{th} = 1.83\ kA/cm^2$ (13.4 V), at 10 K. As the current density further increases to $\sim 2.0\ kA/cm^2$ (13.9 V), the L-I curve shows a kink - an increase in slope efficiency. This

L-I kink at 2.0 kA/cm^2 is not related to the alignment of subbands between neighboring cascade modules, because no significant kinks are observed in the VI curve in the corresponding current density region. The slope kink is consistently observed in the L-I curves at temperatures ranging from 10 K to 90 K. As will be revealed by further experimental and theoretical studies, the two distinct slopes in the L-I curves are attributed to the excitation of two different transverse modes (TM_{00} and TM_{01}) in the laser device. The kink in the V-I curve at $V \approx 10\ V$ and $J \approx 1.2\ kA/cm^2$ is due to the indirect coupling of the injector state with the collector state, where the transparency condition is approximately reached (highlighted by horizontal arrow in Figure 3.32-a) [66].

An iris is then used to confine THz emission inside a collection cone with a solid-angle of 13°. This experiment measures angular-resolved L-I curve, with a confined collection cone angle. Figure 3.32-b shows two L-I curves measured at 10 K along two different emission directions. The TM_{00} mode curve is measured along the normal direction of the laser facet and the TM_{01} mode curve is measured at an angle of 25° off the normal direction (see the inset of Figure 3.32-b). The two L-I curves show different threshold current density. The TM_{01} mode curve has a threshold current density of 1.83 kA/cm^2, which is the same as the one of the non-angular-resolved L-I curve in Figure 3.32-a. The TM_{00} mode curve has a higher threshold current density of $\sim 2.0\ kA/cm^2$, matching the current density at which the kink is observed in the non-angular-resolved L-I curve in Figure 3.32-a.

The observed change of THz emission direction suggests different transverse modes are excited when the device is biased at different currents [111, 141]. To confirm this hypothesis of transverse mode change, we use a FLIR Photon 640 micro-bolometer camera to capture the near-field emission pattern at the laser facet. The original lens of the camera is replaced by a Tsurupica lens with 80% transparency at the lasing wavelength. A biconvex spherical lens with a focal length of 50 mm and diameter of 45 mm was chosen for this experiment. The lens tube is purged using dry Nitrogen in order to minimize

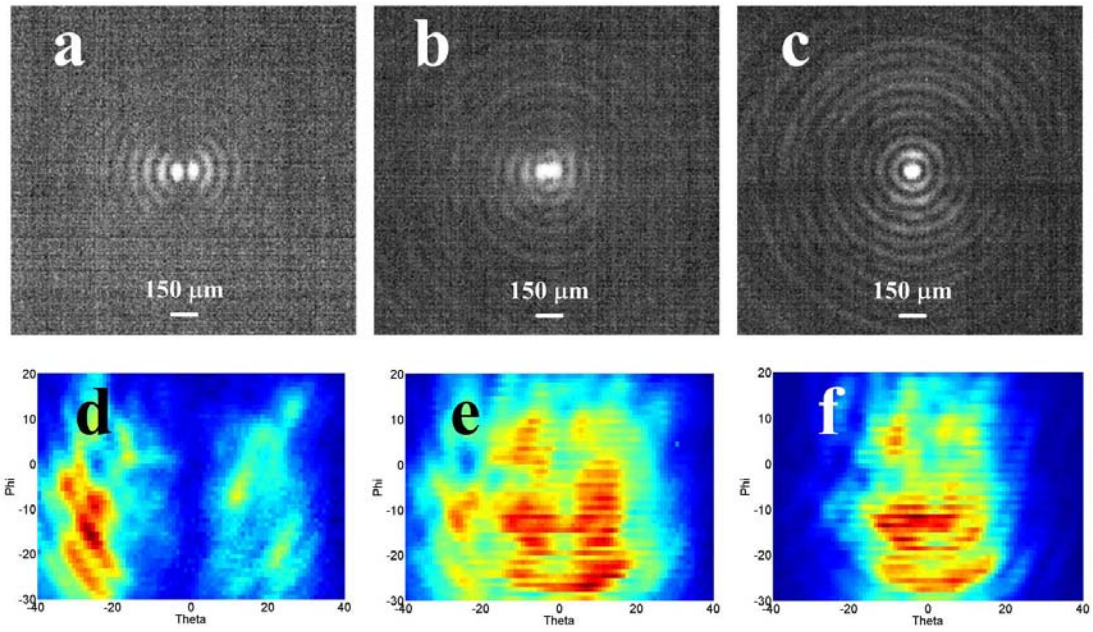

Figure 3.33: (a)-(c) Near-field image of the 150 μm THz QCL ridge at different current injection levels (a- 2.9 A, b- 3.2 A, and c- 3.4 A). At lower current levels the clearly visible two lobes confirm the existence of only the TM_{01} mode (a). By increasing the current the fundamental mode catches up (b) until at very high current mainly the TM_{00} mode is excited (c). (d)-(f) Far-field measurement results of the THz QCL at various current levels (d- 2.9 A, e- 3.2 A, and f- 3.4 A). At lower current level ($I = 2.9\ A$), when only the TM_{01} mode is excited the beam pattern emits to angles beyond 20° (d). At $I = 3.2\ A$ by exciting the fundamental mode, the normal direction of the far-field is filled up (e). Further increase of the current up to $I = 3.4\ A$ leaves mainly the fundamental mode operating and the far-field beam pattern is focused within angles of ±20°.

atmospheric vapor absorption. By ignoring spherical aberration, the spatial resolution of the optical system, as defined by diffraction, is already 150 μm. Therefore, the shape of the modal field can not be well resolved. The recorded images are dominated by diffraction effect of the lens (at the origin of the concentric rings). For high order modes the image

is dominated by interferences between the different sections of the opposite signed field. Despite the fact the optical setup could be further improved, for convenience we call these images as "near-field"; they are useful to qualitatively identify the excited lateral modes. The near-field pattern images at the laser facet are captured with a 2.5 time magnification (numerical aperture of 0.64). Figure 3.33-a to -c shows the near-field pattern measurement under different current injections (a: $I = 2.9\ A$; b: $I = 3.2\ A$; and c: $I = 3.4\ A$), corresponding to the A, B, C points, labeled in the L-I curve in Figure 3.32-a.

Figure 3.33-a shows clearly that the transverse mode at the laser facet at ($I = 2.9\ A$, point A) has two lobes ($\sim 90\ \mu m$ apart), indicating a TM_{01} mode is excited in the waveguide. On the contrary, Figure 3.33-c ($I = 3.4\ A$, point C) shows only one strong lobe at the center of the ridge, which is assigned to a TM_{00} mode. As for the intermediate current injection at $I = 3.2\ A$ (point B), the observed near-field pattern appears as the combination of the TM_{01} and TM_{00} modes. The measured near-field patterns show with no doubt that the different transverse modes are excited at different current injections. The TM_{01} mode is first excited at a lower current, while the TM_{00} mode (the fundamental mode) is excited at a higher current. The TM_{01} and TM_{00} modes can co-exist at an intermediate current injection.

The far-field emission pattern is the direct Fourier transform of the corresponding transverse modes at the laser emission facet. The two lobes in the TM_{01} mode are theoretically supposed to have opposite phase [141]. The two opposite-phase lobes of the TM_{01} mode should lead to destructive interference along the normal direction of the laser facet ($\phi = 0^\circ$ and $\theta = 0^\circ$, as defined in Figure 3.31) at far-field, which can be verified by experimentally measuring the far-field emission patterns of the device. The results are shown in Figure 3.33-d to -f. As expected at a lower injection current ($I = 2.9\ A$) when only the TM_{01} mode is excited, the far-field beam pattern (Figure 3.33-d) shows a minimum along the normal direction of the laser facet ($\theta = 0^\circ$). The laser emission is diverged to off-normal

directions at angles of $\theta = \pm 25^{\circ}$ and beyond, respectively. This suggests that two lobes of TM_{01} mode have opposite phase and are located approximately $\frac{\lambda}{2sin\theta} \approx 94\ \mu m$ apart. The non-symmetric far-field pattern might be caused by packaging asymmetry, where non-similar environment exists on each side of the waveguide facet. Along the vertical direction (ϕ) the far-field beam pattern is mainly distributed under the active region junction plane ($\phi < 0$). This is because a big portion of the transverse mode extends from the active region into the underneath semi-insulating substrate. When the device is biased at 3.4 A, only the fundamental mode TM_{00} is excited. Correspondingly, the far-field patter is mainly focused at the angle of $\theta = 0^{\circ}$ (Figure 3.33-f). At the intermediate current injection level ($I = 3.2\ A$) when both TM_{00} and TM_{01} co-exist, the far-field beam pattern (Figure 3.33-e) displays combined features, as shown in Figure 3.33-d and -f.

Angular-resolved lasing spectra of the device at 10 K measured at the aforementioned three injection current levels once again reveal that two different transverse modes are excited. The spectra are measured along two different directions: $\theta = 0^{\circ}$ and $\theta = 25^{\circ}$ along which the TM_{00} and TM_{01} modes are found to radiate strongest, respectively. The two sets of spectra (in total 6) are shown in Figure 3.34. All spectra are normalized to unity in peak intensity. The two spectra at $I = 2.9\ A$ ($\theta = 0^{\circ}$ and $\theta = 25^{\circ}$) have a main peak at 124.3 cm^{-1} and a much weaker Fabry-Perot (FP) side mode at 121.8 cm^{-1}. The FP longitudinal wavelengths are given by [44]

$$\lambda_m = \frac{2nL}{m}, \tag{3.13}$$

where n is the effective refractive index of the transverse mode, L the cavity length and m the FP mode number. The free spectral range (FSR) of the FP modes is hence 1.25 cm^{-1}. The two normalized spectra (Figure 3.34-A) looks similar to each other, while the absolute power at $\theta = 0^{\circ}$ is much weaker than that at $\theta = 25^{\circ}$. The two lasing peaks at 124.3 and 121.8 cm^{-1} belong to the same longitudinal Fabry-Perot mode family of the TM_{01} transverse mode. As the current rises to $I = 3.2\ A$, a new peak at 120.9 cm^{-1} appears in

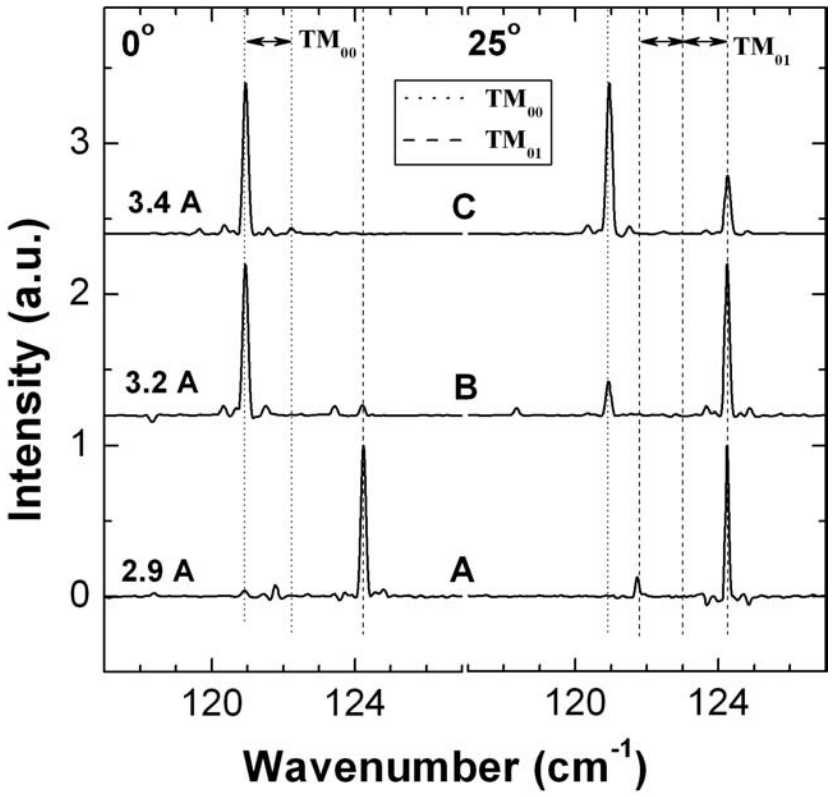

Figure 3.34: Lasing spectra of the THz QCL at 10 K for various injection currents measured at 0° and 25° angles. Two families of Fabry-Perot modes are identified with the equal spacing (double-end arrows). By increasing the injection current the TM_{01} mode diminishes and the TM_{00} mode emerges. The resolution of the spectra is 0.1 cm^{-1}.

both angular-resolved spectra (Figure 3.34-B). The wave number difference between this new peak and the peak at 124.3 cm^{-1} is 3.4 cm^{-1}, which is not an integer product of the TM_{01} FP mode spacing (1.25 cm^{-1}). Apparently, they do not belong to the same FP longitudinal mode family. The lasing emission at 120.9 cm^{-1} has the main peak at $\theta = 0°$ direction, while it is much weaker at $\theta = 25°$, indicating that this lasing wavelength is from the TM_{00} transverse mode. The peak at 124.3 cm^{-1} of the $TM)01$ mode dominates at $\theta = 25°$, while is very weak but still observable at $\theta = 0°$ direction. The spectrum

measurement result again confirms the co-existence of TM_{00} and TM_{01} modes at this current injection level ($I = 3.2\ A$). The different FP longitudinal wavelengths of the TM_{00} and TM_{01} modes are attributed to slightly different effective refractive indices of these two transverse modes. With further increasing the current to 3.4 A, the peak at 120.9 cm^{-1} dominates at both $\theta = 0°$ and $\theta = 25°$ directions. The peak at 124.3 cm^{-1} disappears at $\theta = 0°$, however, it is still observable at $\theta = 25°$. The lasing spectra show that even at $I = 3.4\ A$, both TM_{00} and TM_{01} are excited in the laser waveguide, nevertheless the TM_{00} is dominant. The results of the angular-resolved lasing spectra agree with the earlier observation of the near-field and far-field patterns.

Far field simulation

To confirm that the experimental observations of the far-field pattern measurements are really due to the excitation of the TM_{00} and TM_{01} modes, the HFSS (Finite Element Method) simulation software is employed to calculate the far-field beam patterns from the 3D model of ridge waveguide structure as depicted in Figure 3.31. HFSS was used as a 3D Driven-Modal solver. The first two modes of SI-SP waveguide were separately calculated by an embedded 2D eigenmode solver. These two modes were then separately used to excite one facet of the laser structure. Exact truncation boundary conditions were considered for the other facets. As compared to most published analysis based on simplifying assumptions, in this work, the far radiation fields are rigorously calculated from the modal field distributions over the entire 1 mm length of the structure. The conductivity of the contact metal and n^+ $GaAs$ layers is calculated using Drude model with relaxation times of 60 fs and 100 fs, respectively [110]. The active region is modeled as a 10 μm thick $GaAs$ layer with a background doping concentration of $8.15 \times 10^{15}\ cm^{-3}$ and a Drude relaxation time of 500 fs. Despite the considerable computational complexity due to large mesh size and multi-resolution nature of the structure for the 3D simulation, the full length

of the laser ridge (1 mm) is used in the accurate simulation of the fringes [130]. Figure 3.35-a shows the simulated far-field pattern of the TM_{00} mode. The laser beam is mainly focused in an emission cone around $\theta = 0°$ and $\phi = -10°$ direction, which agrees well with the experimental results shown in Figure 3.33-f. Figure 3.35-b shows the simulated far-field pattern of TM_{01} mode. The multiple-ring pattern of the simulated results resembles the experimental observation, whereas the experimental result (Figure 3.33-d) only shows the central-most ring due to the angular limit of the experimental setup collection cone. The simulation results confirm that the excited modes in the laser waveguide are TM_{00} and TM_{01} modes.

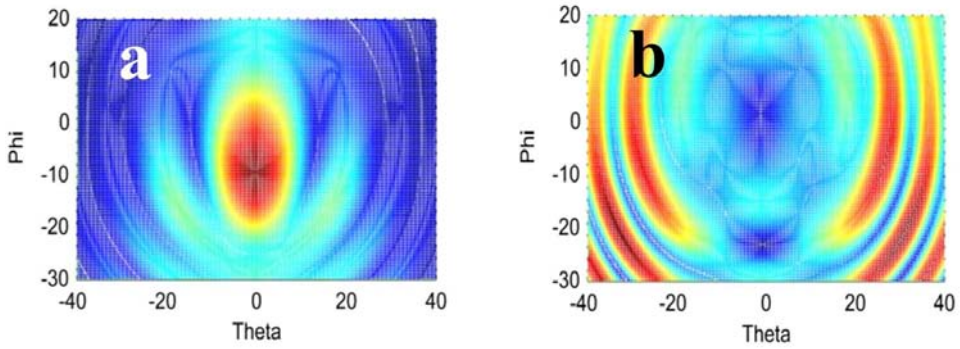

Figure 3.35: HFSS simulation results for the far-field of the THz QCL depicted in Figure 3.31 for (a) the TM_{00} and (b) the TM_{01} modes. The radiation wavelength for each mode is read from Figure 3.34.

Modal gain calculation

As mentioned before, the laser ridge is sufficiently wide ($w = 150\ \mu m$) to support multiple transverse modes. However, among these, the particular transverse mode, which is excited, is the one with sufficient optical modal gain G_{ij} given by [44, 142],

$$G_{ij} = \int_{AR} M_{ij}(x, y) g(x, y) dx dy, \tag{3.14}$$

where M_{ij} is the waveguide mode and is defined as

$$M_{ij}(x,y) = \frac{\mathfrak{Re}\left(E_{ij}(x,y) \times H^*_{ij}(x,y)\right).\hat{z}}{\int_{total} \mathfrak{Re}\left(E_{ij}(x,y) \times H^*_{ij}(x,y)\right).\hat{z}dxdy}, \tag{3.15}$$

where x and y are along the transverse directions, z is along the propagation direction (as shown in Figure 3.31), $E_{ij}(x,y)$ and $H_{ij}(x,y)$ are the lateral electric and magnetic field profile of the ij^{th} transverse mode respectively, $M(x,y)$ is the normalized 2D mode power density, and $g(x,y)$ is the local non-uniform gain. Equations 3.14 and 3.15 assume the gain is proportional to the fraction of power that overlaps with the gain medium. As pointed out by Robinson et al. in [142], this is correct for TM or quasi-TM modes, as long as the lateral confinement of the mode is not too strong. Because the SI-SP modes are mostly confined in the substrate, equation 3.15 results in less than 2% error.

In order to calculate the 2D non-uniform gain profile, $g(x,y)$, first voltage and current distribution is calculated by solving the 2D Poisson's equation as

$$\frac{\partial}{\partial x}\left(\sigma_x \frac{\partial V}{\partial x}\right) + \frac{\partial}{\partial y}\left(\sigma_y \frac{\partial V}{\partial y}\right) = 0, \tag{3.16}$$

where σ_x and σ_y are lateral and vertical conductivities, respectively. Isotropic conductivity for all the regions, except the active region, is assumed. For the n^+ $GaAs$ region equal values of $\sigma_x = \sigma_y = 96000\ (\Omega.m)^{-1}$ are used from Hall mobility measurement. The lateral conductivity of the active region (σ_x) is calculated using the weighted average of the bulk conductivities of $GaAs$ and $Al_{0.15}Ga_{0.85}As$, with the given average doping [143]. The vertical conductivity of active region (σ_y) depends on the applied vertical electric field (E_y) [143]. To measure the vertical conductivity of the active region, it is required to conduct a four point measurement of the V-I curve of a device (preferably a non-lasing device), in which current is injected and flows vertically. For this purpose, a fabricated THz QCL with a MM waveguide structure and the same active region material is employed. In such a structure, the current flows vertically through the active region from the top metal contact to the bottom metal contact without lateral spreading. As the current simulation results

will be eventually used to calculate the gain, it is important to use the V-I of a non-lasing device to derive the conductivity. For this purpose, we fabricated a small micro-disc and cleaved it in half. Such a structure is expected to show very high waveguide loss, and hence destroy or strongly damp the lasing; nevertheless we observed very weak lasing from it. The vertical conductivity of the active region material is derived form measured V-I curve of this device. The final vertical conductivity used for the active region is in form of

$$\sigma_y = f(E_y). \tag{3.17}$$

The inset of Figure 3.36 shows the measured DC vertical conductivity of the active region versus vertical electric field. We used COMSOL simulator to solve the equation 3.16 and calculate the current spreading at various applied voltages, for the 2D structure shown in Figure 3.31. Figure 3.36 shows the lateral distribution of the vertical current, J_y, under different applied voltages, across the middle of the active region (5 μm below the top of the ridge). Two dashed lines show the corresponding current density levels, at which the TM_{01} and TM_{00} modes reach the lasing threshold (Figure 3.32). Due to the bottom current injection configuration of the laser device, the lateral current density distribution, $J_y(x)$, is not uniform. As observed in Figure 3.36, $J_y(x)$ is maximum at the two lateral edges of the ridge and is minimum at the center. The inset of Figure 3.36 also compares the measured V-I curve shown in Figure 3.32-a with the simulated one. The simulated current agrees with the measurement results with a less than 1.5% mean square error.

In order to link the simulated current density to the local gain distribution, $g(x, y)$, it is required to estimate the intrinsic gain of the active material versus the vertical current density. To do so, we started from the L-I characteristic of a MM THz QCL, where the current distribution in the active region is uniform. The threshold gain for such a device is estimated to be 40 cm^{-1} [66]. It is also shown in [66] that the transparency current density occurs after the alignment of the injection and collector states. The alignment is indicated by the bump in Figure 3.32 2-a V-I (horizontal arrow). For the gain material under study,

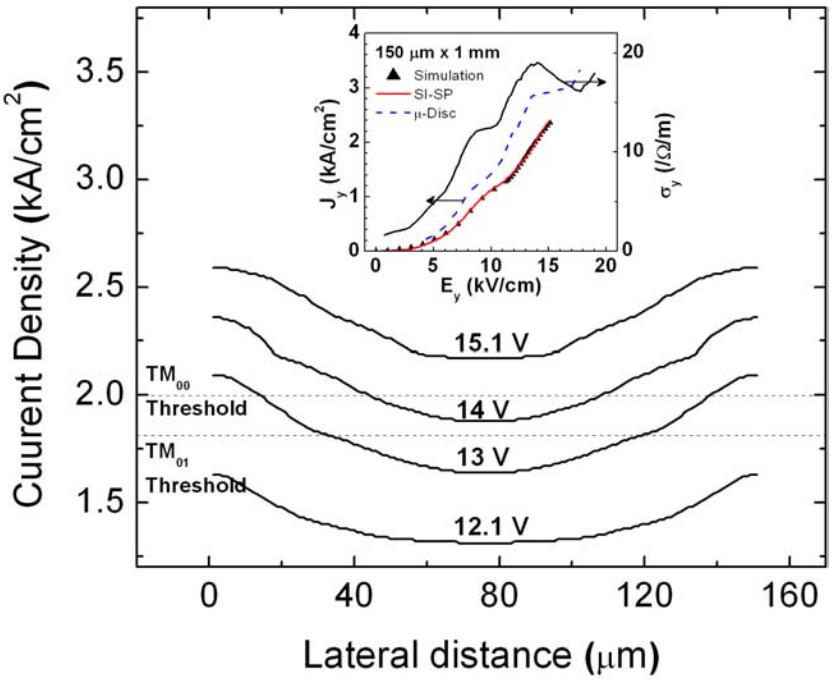

Figure 3.36: Simulated vertical current density (J_y) profile at four different applied voltages (12.1, 13, 14, and 15.1 V). The current density profile is plotted though a cross section that is 5 μm below the top of the ridge. The two dashed lines show the corresponding current density at threshold for TM_{01} and TM_{00} modes. The inset shows the measured vertical conductivity of the active region versus the vertical electric field as measured from a MM ridge laser. The inset also compares the simulated vertical current density with the experimental current in Figure 3.32-a, and current of the micro-disc used to calculate the conductivity.

the transparency current density (J_{tr}) is $\sim$ 1.2 kA/cm^2. Assuming the Lorentzian gain model for the THz QCL active region, the gain becomes proportional to the population inversion (Δn). If the leakage tunneling time from the upper lasing state to the excited state of the phonon well, called wrong extraction channel, is much larger than the upper lasing state lifetime, the current efficiency for population inversion, $\Delta n/J$, is weakly dependent

on the electric field, and therefore, population inversion increases linearly with current. For the sake of simplicity, we used such a linear approximation between the transparency point and threshold, even though we have demonstrated theoretically that the shunting effect by the wrong extraction channel cannot be neglected in our three-well design with vertical transitions [66]. Above the threshold, we assumed the emitted power is proportional to $(\Delta n/\Delta n_{th} - 1)$, where Δn is the population inversion if no photon were present in the cavity, and Δn_{nth} is the population inversion at threshold. Even though not strictly correct according to our ballistic model [66], this last approximation is reasonable.

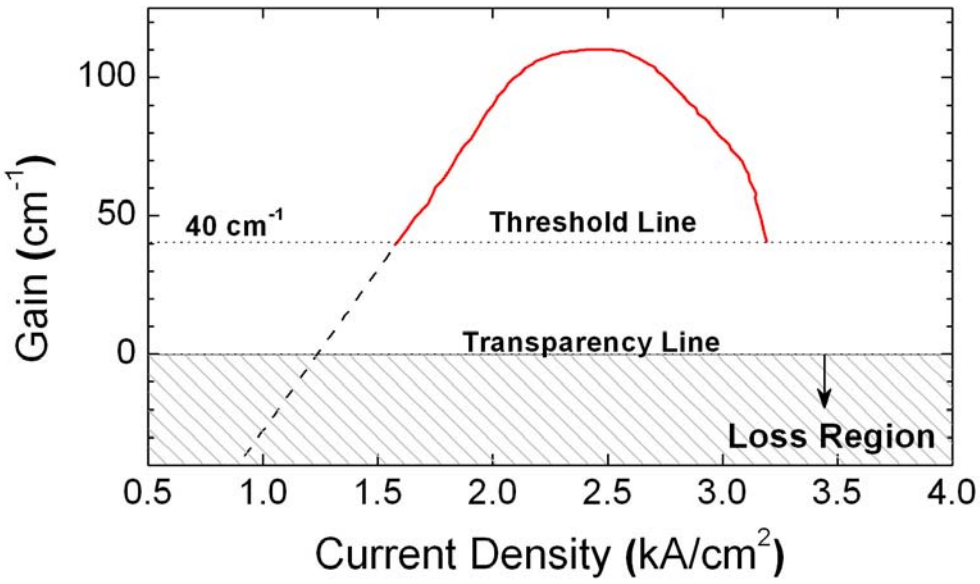

Figure 3.37: Estimated intrinsic gain of the active region versus current density for three well RP-based THz QCL active region. The curve is extracted from the L-I characteristic of a metal-metal device that is made of the same active region material. The negative differential resistance of this device is at 3.15 kA/cm^2.The curve is employed to calculate the net modal gain of the TM_{00} and TM_{01} modes.

By applying all of above assumptions and combining with the measured L-I curve, the intrinsic gain versus current density is extracted and shown in Figure 3.37. This curve is

Table 3.2: Calculated modal waveguide and mirror loss values in cm^{-1}

	α_m	α_w	$\alpha_{tot} = \alpha_m + \alpha_w$
TM_{00}	9.67	5.31	14.98
TM_{01}	7.76	4.00	11.76

used to calculate the 2D local gain distribution at various applied voltages, in combination with simulated 2D current density profile. For current densities below 2 kA/cm^2, at which $g(x,y) \propto (J_y(x,y) - J_{tr})$, the local gain distribution, $g(x,y)$, has a similar lateral profile as that of $J_y(x,y)$. At higher current densities (> 2.5 kA/cm^2) and below the negative differential resistance of the laser, the local gain diminishes probably due to the different detuning at the injection and extraction sides [93]. Since TM_{00} and TM_{01} modes have different distribution profile along the lateral direction of the device ridge, they overlap with the laterally non-uniform material gain profile to different extents, leading to different modal gains of these two modes. By controlling the current injection, one can favor one modal gain, while hold up the other one. As a result, the TM_{00} and TM_{01} modes can be selectively turned on under different biases.

In the last step, we simulate the 2D mode profile for each mode, as defined in equation 3.15. The inset of Figure 3.38 shows the simulated mode profile in the active region for the TM_{00} and TM_{01} modes, using the COMSOL simulator. These two mode distributions are inserted into the equation 3.14, together with the calculated voltage dependant non-uniform local gain distribution to calculate the total reserve of gain. Each mode (TM_{ij}) reaches the threshold when the reserve of gain increases up to the total modal loss ($\alpha_{tot-ij} = \alpha_{m-ij} + \alpha_{w-ij}$). We call such a figure of merit the net modal gain of the material and define it as

$$G_{ij-net} = \int_{AR} M_{ij}(x,y) g(x,y) dxdy - \alpha_{tot-ij}. \tag{3.18}$$

To estimate the waveguide loss for each mode, we use the imaginary parts of cor-

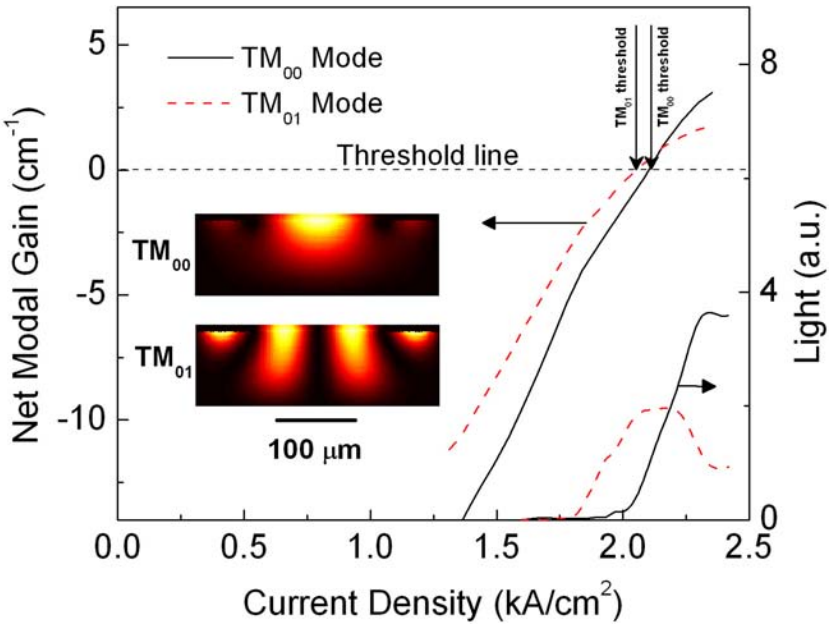

Figure 3.38: Net model gain versus different applied voltage, calculated for the TM_{00} and TM_{01} modes. The TM_{01} mode reaches the threshold around the voltage of 2.04 kA/cm^2 (13.95 V). TM_{00} mode reaches the threshold around the voltage of 2.11 kA/cm^2 (14.13 V). The arrows show the threshold for each mode. The right axis re-plots the modal light curve versus voltage, from Figure 3.32, to compare the simulated modal threshold with the experiments. The inset shows the 2D mode profiles of the TM_{00} and TM_{01} modes. The two main opposite phase lobes of TM_{01} are 85 μm apart.

responding effective index from the eigenmode solution of the Maxwell's equation. The modal mirror loss (α_m) is directly related to the modal reflectivity at the laser facet, which depends on the modal index and angle. A good approximation of the modal reflectivity is obtained by decomposing the main component of the electric field in a series plane waves by 2D Fourier transform. The coefficient of each of these waves is multiplied by the Fresnel reflection coefficient applied separately for contributions parallel and perpendicular to the plane of incidence. The total reflected field is then reconstructed by inverse Fourier trans-

form; and the reflectivity is estimated by averaging the ratio of the reflected field intensity over the incident field. The mirror loss and the waveguide loss for different modes are, therefore, given by $\alpha_m = ln(R)/L$ and $\alpha_w = 2\beta\frac{2\pi}{\lambda}$, where R is the calculated reflectivity and β is the imaginary part of the propagation constant [141]. Table 3.2 lists the calculated modal waveguide and mirror loss values. Lower mirror loss of TM_{01} can be explained using ray optics approach for a polarization perpendicular to the plane of incidence; the higher order mode impinges on the facet at a larger incident angle and hence is more reflective [141]. Lower waveguide loss of TM_{01} mode originates from smaller overlap of this mode with the active region and the n^+ layer underneath it.

Figure 3.38 shows the calculated net gain versus applied voltage for each mode. When the device is biased at a lower bias (lower current injection), the gain profile has maxima near the edges of the waveguide, which spatially overlaps more with the TM_{01} mode than with the TM_{00} mode. As a result, the TM_{01} mode possesses higher net gain than the TM_{00} mode and reaches the lasing threshold first. This explains why the experimental results show that the TM_{01} mode has a lower simulated threshold current density of $J_{th} = 2.04\ kA/cm^2$ (compared to experimental value of $J_{th} = 1.83\ kA/cm^2$) and starts to lase first. As the current injection continues to increase, the local gain in the center part of the ridge increases, which contributes more to the modal gain of the TM_{00} mode and brings it to the threshold point. According to this simplified model, the TM_{00} mode starts to lase at $J_{th} = 2.11\ kA/cm^2$ which is close to experimental ($J_{th} = 2\ kA/cm^2$). Further increase of the current injection renders the local current density at the lateral edges of the waveguide to exceed the maximum current density - beyond which the quantum wells become absorptive rather than emissive. Consequently, the net modal gain of the TM_{01} mode degrades and the lasing emission from the TM_{01} mode saturates. The TM_{00} mode is less affected by this gain-reduction process, because the maxima for lateral distribution of the current (on the edges) and TM_{00} mode profile (on the center) do not overlap. As observed in Figure 3.32-a, the TM_{00} mode dominates at a current injection of $J =$

2.25 kA/cm^2 ($V \approx 14.5\ V$), which is also consistent with the simulated graph in Figure 3.38. The discrepancy between the simulated and the measured J_{th} for each mode can be attributed to various sources of error such as, underestimation of the total loss (particularly for TM_{01} mode) and the estimated intrinsic gain of the active region, etc.

This section discussed design and fabrication of a high power THz QCL, with the capability of electrically switching the output beam using a symmetric side current injection scheme. The angular resolved LI measurements, near-field and far-field patterns and angular-resolved lasing spectra all confirm that the TM_{01} transverse mode lases first and dominates the lasing operation at lower current injection, while the TM_{00} mode lases at a higher threshold current density and becomes dominant at high current injection. Because of the different near-field patterns at the laser emission facet of the TM_{00} and TM_{01} transverse modes, the far-field of the laser shows two lobes of radiation at horizontal angles of $\theta = \pm 25^\circ$ when operating in TM_{01} mode under lower current injection and single lobe radiation at $\theta = 0^\circ$ when operating in TM_{00} mode under higher current injection. The THz emission beam of the device can be easily and dynamically maneuvered by switching the applied device bias. The experimental results are in qualitatively reasonable agreement with the results of the simplified model of the modal gain.

3.2.5 THz transmission imaging

The optical link built between a high power THz QCL and a THz QWP, like the one in Figure 3.25, can be also used for THz transmission imaging, which is the simplest possible type of imaging [3]. The fast response time of the THz QWP potentially makes it possible to perform time-resolved imaging, which can be used in imaging of living species. This section presents a simple proof-of-concept for transmission imaging using a pair of THz QCL and QWP. A similar THz QCL as in the section 3.2.3 was used for this experiment. In order to extract high THz power from the laser, the laser was biased using 2.4 A and

50 μs wide pulses at 10 K (refer to Figure 3.23-a). Similar to the setup in Figure 3.25, the THz beam is bent, focused and directed towards the THz QWP (Figure 3.39-a). For imaging purpose, it is required to tightly focus the beam within a small region. For this purpose, an elliptical mirror with focal lengths of 8 inch is used. The large focal length gives it enough space for scanning the imaging subject. The THz light focus smaller than 1 mm^2 is achieved, that defines the "imaging point". An iris is used to eliminate unwanted beam outside of the imaging point. The imaging subject is scanned around this point, until the entire area is covered The transmitted THz light through the subject. The THz loght is then bent and refocused on a THz QWP, using two parabolic mirrors. The entire THz path remains unpurged, during the imaging. The THz QWP is placed with 45° angle to satisfy intersubband selection rule and is biased at 30 mV voltage and 10 μA current. In order to increase the time resolution of detected pulse and increase the signal to noise ratio, a trans-impedance amplifier is designed in-house with $\sim$ 30 MHz bandwidth (Appendix C). This bandwidth is already more than 30 times higher than the current amplifier used in section 3.3.3.

Figure 3.39-b shows the THz transmission image of a metallic scissor hidden behind a paper. The signal at each pixel is integrated for $\sim$ 1 s. The metal perfectly blocks the THz light and hence the regions that the scissor overlaps with light, the THz QWP reads a signal as low as noise level, Figure 3.39-b. The output of THz QWP was similar to THz pulses in Figure 3.26. These pulses were collected and integrated using a lock-in amplifier. However, one could analyze the temporal response of a moving subject (i.e. living species), by dynamically analyzing the trans-impedance amplifier's output. This section was only to show a proof-of-concept experiment. The further discussions and experiment on the imaging are not within the scope of this thesis.

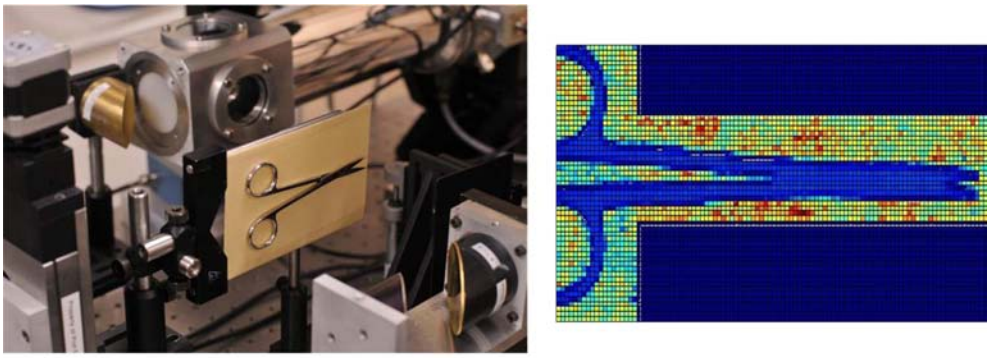

(a) (b)

Figure 3.39: (a) Image if experimental setup for imaging a metallic scissor. The THz Beam is focused out of a THz QCL in to a $< 1\ mm^2$ spot using an elliptical mirror (left). The scissor is places at the focused point and scanned for imaging. The transmitted THz light through the object is then bent and focused on a THz QWP using two parabolic minors. (b) THz transmission image of a scissor behind the envelope paper.

3.3 Summary and conclusions

This chapter discussed the fabrication, the waveguide design and the thermal behavior of the MM and SI-SP THz QCLs, in detail. Firstly, the fabrication of MM structure was discussed. Then the waveguide design considerations for achieving a single mode MM THz QCL were analyzed. The experimental results showed that introducing side absorbers make the LI of the laser very smooth and predictable, by just allowing fundamental mode propagation inside the ridge. Later the effect of different metal combination for the mode confinement were studied. The $Pd/Ge/Ti/Pt/Au$ contact resulted in an Ohmic contact and hence the lowest voltage, and Ti/Au contact resulted in the lowest waveguide loss, and hence highest T_{max}. The MM device discussions were followed by the experimental and analytical thermal behavior study, where the optimum structure for the laser device heat dissipation were discussed.

The second part of this chapter extensively studied the SI-SP THz QCLs. After a short description of the device fabrication, the waveguide design for single mode operation of these devices were presented. The high power nature of SI-SP devices made it possible to pair it with a fast THz QWP, where the THz beam dynamics were revealed. Based on the temporal beam dynamics, a time-resolved temperature model were developed that can explain the temporal features of the THz beam. Later this section presented the design and implementation of a bi-modal device. Each of the first two modes has distinguishable beam pattern in a different angle. The transverse mode of the bi-modal device could be controlled electrically, which resulted in electrically switching of the direction of THz emission. At the end of the chapter, a high power SI-SP THz QCL were paired with a fast THz QWP to demonstrate a proof-of-concept fast imaging experiment.

The results in this chapter provides us with key tools to understand the device performance and fabricate an optimized structure for various applications. For instance, the new active region designs presented in the next chapter will be fabricated using a low loss MM waveguide that has single mode operation. The developments discussed in this chapter are yet to be improved for even higher temperature and power.

Chapter 4

THz QCL active region designs

Chapter 2 theoretically discussed a density matrix based model to explain the carrier transport and optical gain in three-well based THz QCLs. The first part of this chapter implements the density matrix model (developed in chapter 2) and compares the theoretical results with the existing experimental results. The focus have been on the gain and current calculation for the three-well RP based THz QCLs. A theoretical practice to find optimum values for injection and extraction barrier thicknesses have been presented. The results of this calculation is being compared and confirmed with the similar experimental work by Luo et al. [102, 144]. This practice will be used for optimizing the new designs. For all the calculations, the pure dephasing time constants and the electron heating temperature values were borrowed from the fitting procedure presented by Dupont et al. in [66].

The second part of this chapter optimizes the three-well RP based active regions by investigating different diagonality levels for high power and high temperature operation of THz QCLs. Kumar et al. have recently reported a three-well based THz QCL with a diagonal radiative transition, lasing up to 186 K [61]. This improvement stems from the fact that the population inversion and the gain are less sensitive to the temperature change for the active regions with more diagonal lasing transition, as discussed in chapter

2. With these backgrounds in mind, seven different three-well based THz QCL designs with different levels of diagonality have been presented and theoretically studied, in this chapter. Since the different designs have different oscillator strength (f), this study is referred as "f-series study" from now on. The experimental results for the f-series study have also been presented and discussed, in this chapter.

The two major drawbacks of the three-well RP based based THz QCLs, as discussed in chapter 2, are the limitation of maximum population inversion to 50%, and the resonant tunneling enhanced wide gain spectrum that results in substantially lowered gain peak. At the end of this chapter, a totally new design that is based on phonon-photon-phonon design will be explored. The density matrix formalism for the proposed active region will be presented, calculating the gain and the carrier transport. This new design, which is called "double-phonon" design, shows very high gain even at high temperatures.

4.1 Original three-well THz QCL

Dupont et al. in [66] have discussed an approach to estimate the pure dephasing time constants and the electron heating temperature. It uses the comparison of the density matrix model results with the experimental data on laser performances versus injection barrier thickness [102]. The extraction barrier thickness data in [144] is not as comprehensive as the injection barrier one. Besides, the thin active region of the wafer used in the extraction barrier study would increase the waveguide loss [4]. The high waveguide loss for the devices studied in [144] makes the fitting exercise more sensitive to the permittivity of the lossy metals, which are not precisely known. Therefore, this section mostly focuses on the injection barrier study results. The 200 μm wide and 1 mm long ridge lasers reported in the injection barrier study have been re-measured with shorter current pulses (200 ns) and better control of the electrical reflections. Compared to the published data [102], an

increase of the T_{max} on the samples with thinner injection barriers is observed.

This section presents the details of the optimization practice to find appropriate injection and extraction barrier thicknesses. The process is similar to the process presented by Dupont et al. in [66]. This practice will be used later in this chapter, for designing optimum three-well RP based THz QCL active regions.

4.1.1 Tunneling barrier thickness optimization for three-well THz QCLs

As mentioned above, the experimental optimization results for injection barrier thickness are presented in [102]. In this section the theoretical optimization process is employed to find these experimental results. Through this practice, the density matrix model parameters (pure dephasing time constant in intersubband transition, τ_{23}^{*}, tunneling pure dephasing time constant, τ^{*}, and electron heating temperature, ΔT_e) are estimated. This process is similar to Dupont et al. approach [66], where the calculated maximum gain for the different injection barrier thicknesses were fitted to the maximum operating temperatures of the six series of devices studied in [102]. The fitting procedure for the structure presented in [102] uses the total waveguide loss coefficient of $\alpha_M + \alpha_W \sim 40\ cm^{-1}$, see Figure 3.9. The waveguide loss of 40 cm^{-1} might be overestimated. As a result, the fitting procedure is likely to lead to an overestimation of upper lasing state lifetime (or to an underestimation of electron heating temperature). The fitting procedure results in the parameters $\tau^{*} = 0.4\ ps$, $\tau_{23}^{*} = 0.85\ ps$, and $\Delta T_e = 80\ K$ for the threshold gain of 40 cm^{-1}. The high electron temperature for the three-well based THz QCL is already expected from the results in [77].

Figure 4.1 illustrates the fit with the estimated parameters for $\alpha_M + \alpha_W \sim 40\ cm^{-1}$. The experimental results of various extraction barrier thicknesses [144] align on the 55 $\pm$

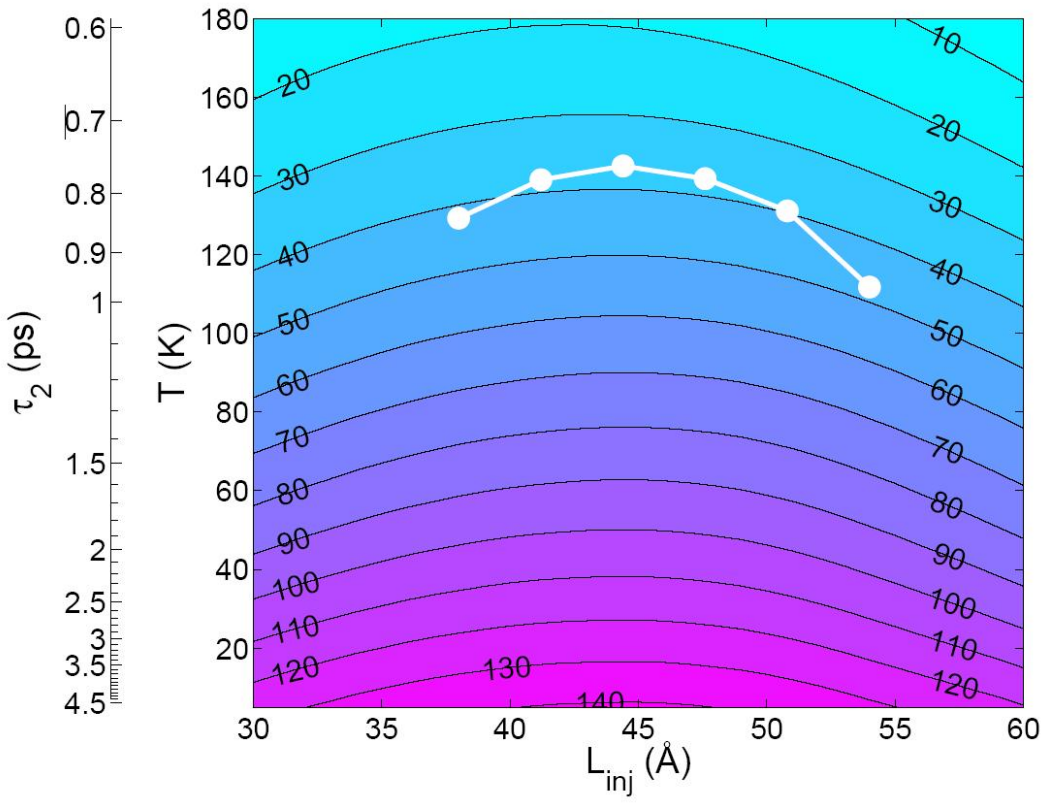

Figure 4.1: Contour plot of the maximum gain (in cm^{-1}) versus the thickness of injection barrier and lattice temperature for $\tau_{23}^{*} = 0.85\ ps$, $\Delta T_e = 80\ K$, $\tau^{*} = 0.4\ ps$. The re-measured maximum operating temperature for the six devices with various L_{inj} are plotted with white dots. At the six experimental points, the standard deviation of the maximum gain from the expected total waveguide loss 40 cm^{-1} is 3.7 cm^{-1}.

2.5 cm^{-1} iso-gain line, calculated from the model with the same input parameters. This should be compared with 64 cm^{-1}, the simulated total waveguide loss of a thin 100-period structure. In calculating the gain in Figure 4.1, the effect of backfilling by phonon absorption from $1_{(n+1)}$ to 4 is not negligible. Indeed, if phonon absorption is arbitrary removed from the model, the fitted electron heating temperature would be $\sim$ 10 K higher and the pure dephasing time constant would be $\sim 0.33\ ps$.

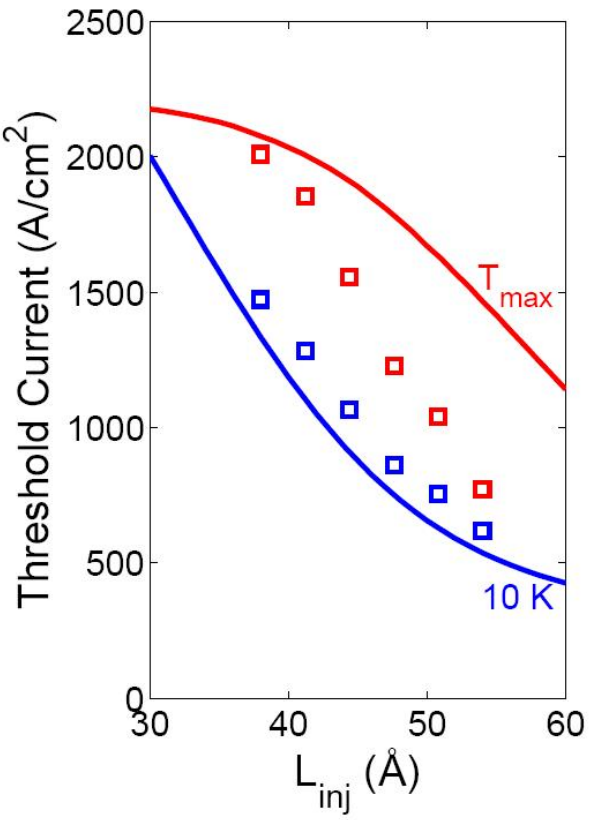

Figure 4.2: Comparison between theoretical threshold current densities (solid lines) and experimental points (open squares) at 10 K and at the simulated maximum operating temperature. The simulations are performed for $\tau_{23}^{*} = 0.85\ ps$, $\Delta T_e = 80\ K$, $\tau^{*} = 0.4\ ps$ and total waveguide loss $\alpha_M + \alpha_W = 40\ cm^{-1}$.

Figure 4.2 compares the simulated threshold current density at 10 K, and at T_{max} for 40 cm^{-1} total waveguide loss, with the experimental values. The agreement at 10 K is more satisfactory than at T_{max}. At 10 K, the laser threshold is reached at around 10 kV/cm, an electric field for which the current is mainly limited by the injection tunneling time, rather than the upper lasing state lifetime, τ_2, or the choice of ΔT_e. At T_{max}, the laser barely operates at design electric field, i.e. close to negative differential resistance where the current depends greatly on τ_2, and therefore on the electronic temperature of subband

2. The disagreement between experiment and simulation being more pronounced for thick barriers suggests that the assumption of a constant ΔT_e for the six devices, independently of the current might be too far from reality. The electron-heating temperature for devices with the thicker injection barrier might be slightly lower.

Although there are limits to which this simplified density matrix-based model can be pushed to fit experimental data, it can reasonably predict the gain at T_{max} and explain the carrier transport and optical gain in the studied intersubband device. The next section uses the model developed in chapter 2 to identify the limits that the original three-well based THz QCL in [65] faces towards reaching high temperature operation and suggests several active region schemes to improve this criteria. The optimization of the new intersubband gain mediums are performed using the estimated parameters in the current section.

4.2 Optimization of diagonal three-well THz QCL

Remembering from discussion for the calculated coupling and detuning values of the original three-well RP based THz QCL (Figure 2.4), it was discovered that for this active region design the coupling for wrong extraction channel (Ω_{24}) is stronger than the coupling for desired extraction channel (Ω_{34}). This unwanted leakage channel results in low current injection efficiency and hence smaller population inversion of ~ 0.3, compared to the maximum achievable population inversion for three-well based structure (0.5), see equation 2.71. Figure 2.11 shows and discusses the effect of wrong extraction channel and wrong injection channel on the current density and population inversion. Kumar et al. have proposed a solution to increase the population inversion by making the optical transition in the double well more diagonal [61]. This work shows that by increasing the diagonality of reducing the oscillator strength from $f_{23} = 0.67$ (original design) to $f_{23} = 0.36$, the upper lasing state lifetime increases (as expected from the discussion of Figure 2.7) and also current density

for a given electric field decreases. In the same work, Kumar et al. reported a world record of 186 K for T_{max}. More diagonal optical transition (lower oscillator strength) reduces the overlap integral of the upper lasing state 2, and upper phonon well state 4 (see equation 2.5), resulting in reduction of wrong extraction coupling. The same argument applies for the injection side, where the wrong injection channel becomes weaker as the diagonality level increase. The weakening of the wrong extraction and also injection channels result in increasing of the injection efficiency and hence higher population inversion (see Figure 2.13-a and b). Figure 2.7 also pinpoints that the non-radiative lifetime of the carriers at the upper lasing state becomes less temperature sensitive as the diagonality of the transition increases. Consequently Figure 2.13-a shows that the population inversion for the designs with higher diagonality of the optical transition is higher and diminishes less at higher temperature. On the other hand, the gain cross section of the intersubband transition is directly proportional to the oscillator strength (see equation 2.28) and very diagonal optical transitions do not generate enough optical gain for the laser. These two arguments suggest that there should be an optimum for the level of diagonality (oscillator strength), for three-well based THz QCLs. This section presents the design of f-series study study with seven different oscillator strengths of $f_{23} = 0.67,\ 0.47,\ 0.41,\ 0.35,\ 0.3,\ 0.25,$ and 0.19, at 12 kV/cm design electric field. The details of the design optimization and the experimental results for $f_{23} = 0.47,\ 0.35,$ and 0.25, will be presented in this chapter. The extraction and injection barrier widths for each design is optimized using the density matrix model, discussed in chapter 2; the optimization details (including the parameters used in the model) are identical to the approached discussed in section 4.1.

For the sake of comparison, it is decided to design all of the structures for 15 meV ($= 3.75\ THz$) photon energy, at 12 kV/cm. The design procedure for each given oscillator strength starts from designing ensemble of all possible double photon wells with 15 meV, and matching phonon wells. The choice of phonon well thickness is not very flexible, since it contains only one well and specific energy spacing between 35 and 40 meV is required

Table 4.1: Details of the well and barrier thicknesses for f-series study. all thicknesses ar in $\mathring{A}$, and the temperatures are in K.

f_{23}	phonon well	injection barrier	left well	barrier	right well	collector barrier	T_{max}
0.67	163	40	96.5	19.3	77	35	**165**
0.47	160	43	89	24.6	81.5	41	**170**
0.41	160	44	88	27	82.5	43	**170**
0.35	159	45	87	29.1	83	44	**165**
0.30	158	46	86	31.7	83	46	**155**
0.25	158	47	86	33.9	83.5	48	**145**
0.19	157	52	85	38.3	83	53	**130**

between the first two energy levels. Therefore, the choice of phonon well is limited to widths between 157 to 163 $\mathring{A}$. From the fitting procedure of $V610$ samples, it is concluded that the gain is maximized when the detuning values on both extraction and injection sides are very small. Therefore, for each pair of double well and phonon well, the extraction and injection barrier thicknesses are calculated to obtain zero detuning on both tunneling barriers. Only the solutions with reasonable barriers thickness ($30\ \mathring{A} < L_{inj,ext} < 60\ \mathring{A}$) are kept in the solution ensemble. The selection of particular solution is not quite trivial. It requires calculating the gain for all possible solutions and selecting the one with the highest gain at high temperatures. By selecting a double photon well and a matching phonon well, the optimization process for the extraction and injection barrier thicknesses (similar to the one discussed in section 4.1) are performed, and the optimum structure is designed for each oscillator strength. It is important to mention that this optimization process is performed using $N_{2D} = 3.6 \times 10^{10}\ cm^{-2}$ and $40\ cm^{-1}$ threshold gain assumption, similar to the section 4.1. Such an assumption may introduce disagreement between the calculated

and experimentally measured T_{max}, particularly when slightly different waveguide is used for the fabrication. Table 4.1 lists the details of designed structures for each level of diagonality, and compares their T_{max}. The middle three designs will be discussed in detail in the subsequent subsections.

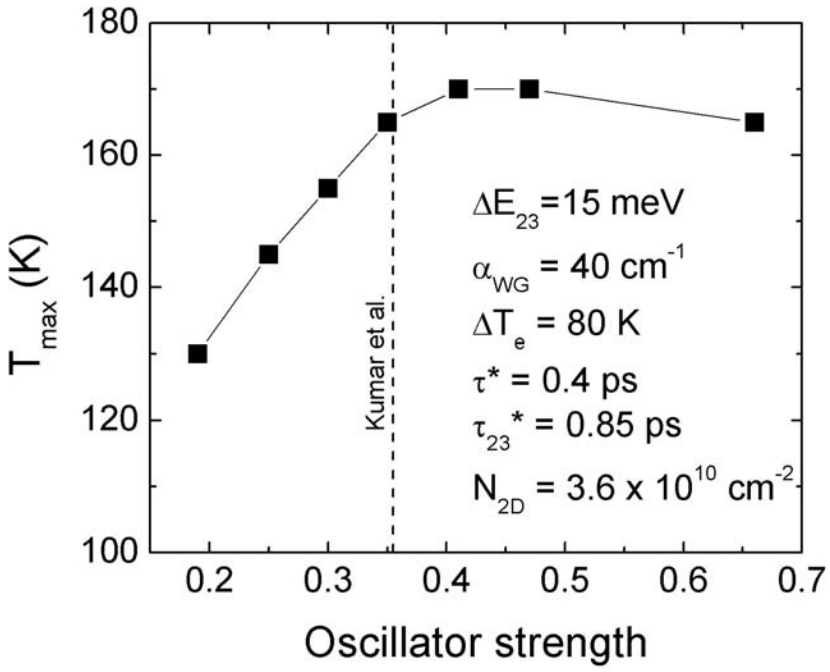

Figure 4.3: Calculated maximum operating temperature for f-series active region designs versus oscillator strength. The dashed line highlight the oscillator strength from Kumar et al., holding the record of 186 K.

Figure 4.3 visually plots the T_{max} for various designs of f-series study. The design with 0.67 oscillator strength shows higher T_{max} compared to the original three well design discussed in section 4.1. This is due to iterative optimization method, which provides us with the highest T_{max} value. Figure 4.3 clearly shows that the T_{max} gradually increases, as the oscillator strength is reduced from 0.67 (value of the original three-well device from [65]) to 0.4. This increase is attributed to the increase of population inversion. For the

oscillator strengths lower than 0.4, the gain coefficient starts to lower the total gain, due to reduced oscillator strength. Figure 2.13-b predicted that the oscillator strength values between of 0.3 and 0.47 have the highest $\Delta\rho \times f_{23}$, which is in good agreement with the results in Figure 4.3. The peak of the Figure 4.3 highly depends on the waveguide loss value. In order to rule out the waveguide value uncertainty, three oscillator strength of $f_{23} = 0.47,\ 0.35,$ and 0.25 are selected for MBE growth and fabrication. The detailed design and optimization process for these three designs are hence brought in the following.

4.2.1 f47

Figure 4.4 shows the conduction band diagram of the three-well based THz QCL design with $f_{23} = 0.47$ at 12 kV/cm. The material system used for this design is $GaAs/Al_{0.15}Ga_{0.85}As$. The active region module consists of lasing double well and the downstream phonon well. The radiative transition occurs by electron transition between upper and lower states in the double well, the energy spacing of which is designed for 15 $meV = 3.75\ THz$ photon energy, at 12 kV/cm. Similar to the original three-well design discussed after Figure 2.3, the electrons are injected into and extraction out of lasing states by resonant tunneling through the corresponding barriers. As explained in chapter 2, all the tunneling coupling and detuning values have been calculated using the tight binding approximation for given electric field. On the other hand all the non-radiative emission and absorption lifetimes are calculated for all the electric fields. Having the tunneling and scattering parameters for each electric field, a similar optimization procedure as the procedure discussed after Figure 4.1 is performed to obtain optimum injection and extraction barrier thicknesses. Similar to the earlier optimization practice the threshold gain is assumed to be 40 cm^{-2}. Also the sheet doping density of $3 \times 10^{10}\ cm^{-2}$ is picked for this design. It was shown in [112, 113] that the optimum doping level for four-well based THz QCLs is $3.6 \times 10^{10}\ cm^{-2}$, Belkin et al. showed that for three-well based THz QCLs the best performance is with sheet doping

density of $3 \times 10^{10}\ cm^{-1}$ [68].

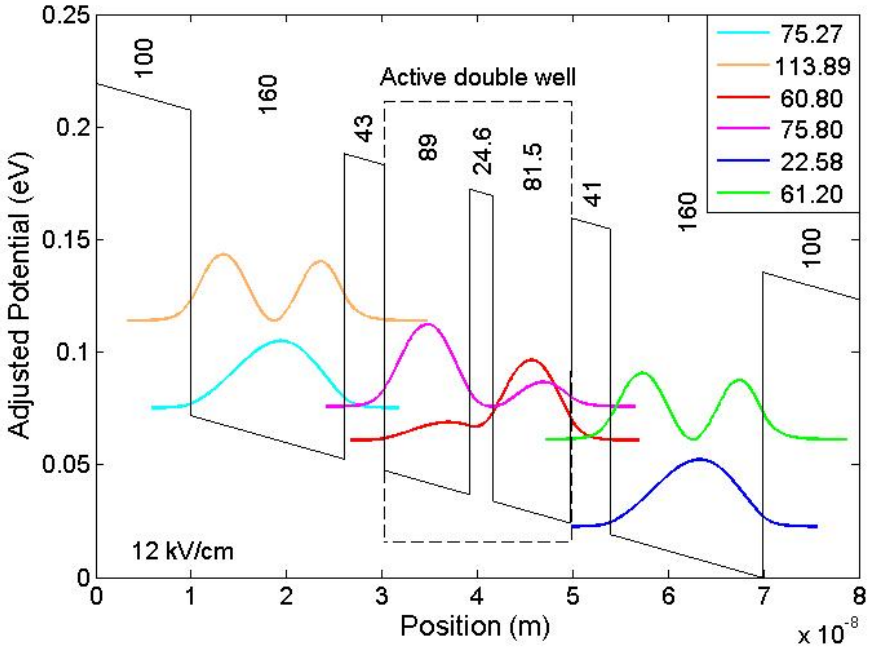

Figure 4.4: Conduction band diagram of the three-well QCL with $f_{23} = 0.47$ at 12 kV/cm and the square modulus of the wavefunctions of the active double-well and the upstream/downstream phonon wells when taken isolated from the adjacent quantum wells. The thickness in Angstrom of each layer is recalled in vertically oriented font.

Figure 4.5 shows the gain contour plot versus temperature for various injection and extraction barrier thicknesses. The optimization practice for $f47$ design uses the fitted values for electron heating temperature, radiative and non-radiative pure dephasing time constants that was calculated for the $V0610$ design in [66] ($\tau_{23}^{*} = 0.85\ ps$, $\Delta T_e = 80\ K$ and $\tau^{*} = 0.4\ ps$). Considering the 40 cm^{-1} contours, the barrier thicknesses for the optimum performance is found to be $L_{inj} = 41\ \mathring{A}$ and $L_{ext} = 43\ \mathring{A}$ (as listed in Table 4.1) that results in maximum operating temperature of $T_{max} = 170\ K$. Figure 4.5 also shows that for the optimum values of barrier thicknesses, 10 cm^{-1} improvement in the waveguide loss

results in $\sim 35\ K$ improvement of maximum operating temperature to $\sim 205\ K$.

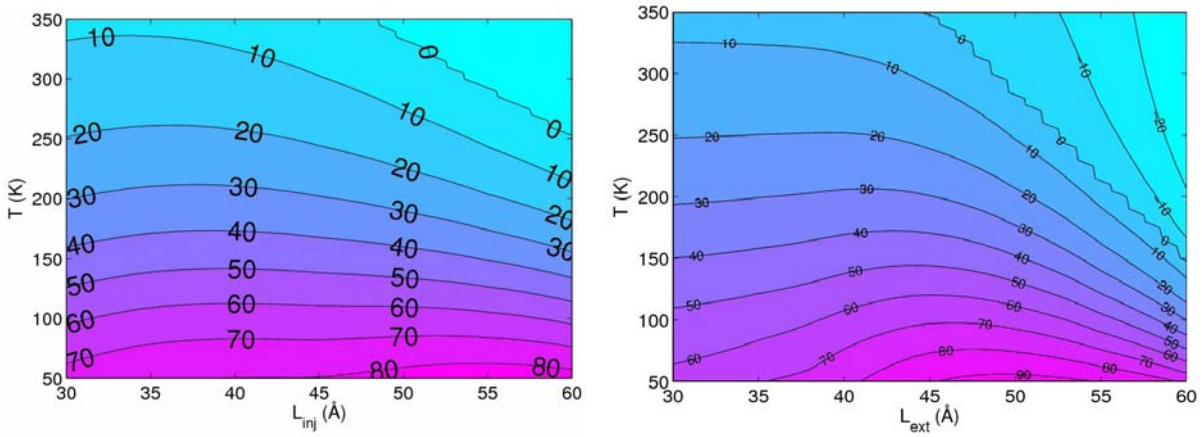

(a) (b)

Figure 4.5: Contour plot of the maximum gain of the $f_{23} = 0.47$ design (in cm^{-1}) versus lattice temperature and the thickness of (a) injection barrier (with $L_{ext} = 41\ \mathring{A}$) and (b) extraction barrier (with $L_{inj} = 43\ \mathring{A}$) for $\tau_{23}^{*} = 0.85\ ps$, $\Delta T_e = 80\ K$, $\tau^{*} = 0.4\ ps$.

The structure shown in Figure 4.4 was grown using V90 MBE system ($V0775$). The cascade module was repeated 228 times and sandwiched between bottom 100 nm and top 50 nm, $5 \times 10^{18}\ cm^{-1}$ n-doped $GaAs$. The thickness of grown MQW is about 10 μm. The doping is implemented by doping the center 50 $\mathring{A}$ of the phonon well, with doping concentration of $6.0 \times 10^{16}\ cm^{-3}$ (resulting in $6.83 \times 10^{15}\ cm^{-3}$ average doping density). After the growth, the quality of the growth was tested using X-ray diffraction (XRD), and secondary ion mass spectroscopy (SIMS) to measure the MQW layer thicknesses and level of the doping, where no considerable discrepancy were observed.

The standard MM fabrication process, as discussed in chapter 3, is employed to fabricate devices using $V0775$ wafer. For the sake of comparison with chapter 3 results the similar three metal combinations $Pd/Ge/Ti/Pt/Au$ (550/1000/250/550/3000 $\mathring{A}$), $Ti/Pt/Au$ (250/550/3000 $\mathring{A}$) and Ti/Au (50/3000 $\mathring{A}$) are processed for top and bottom metal con-

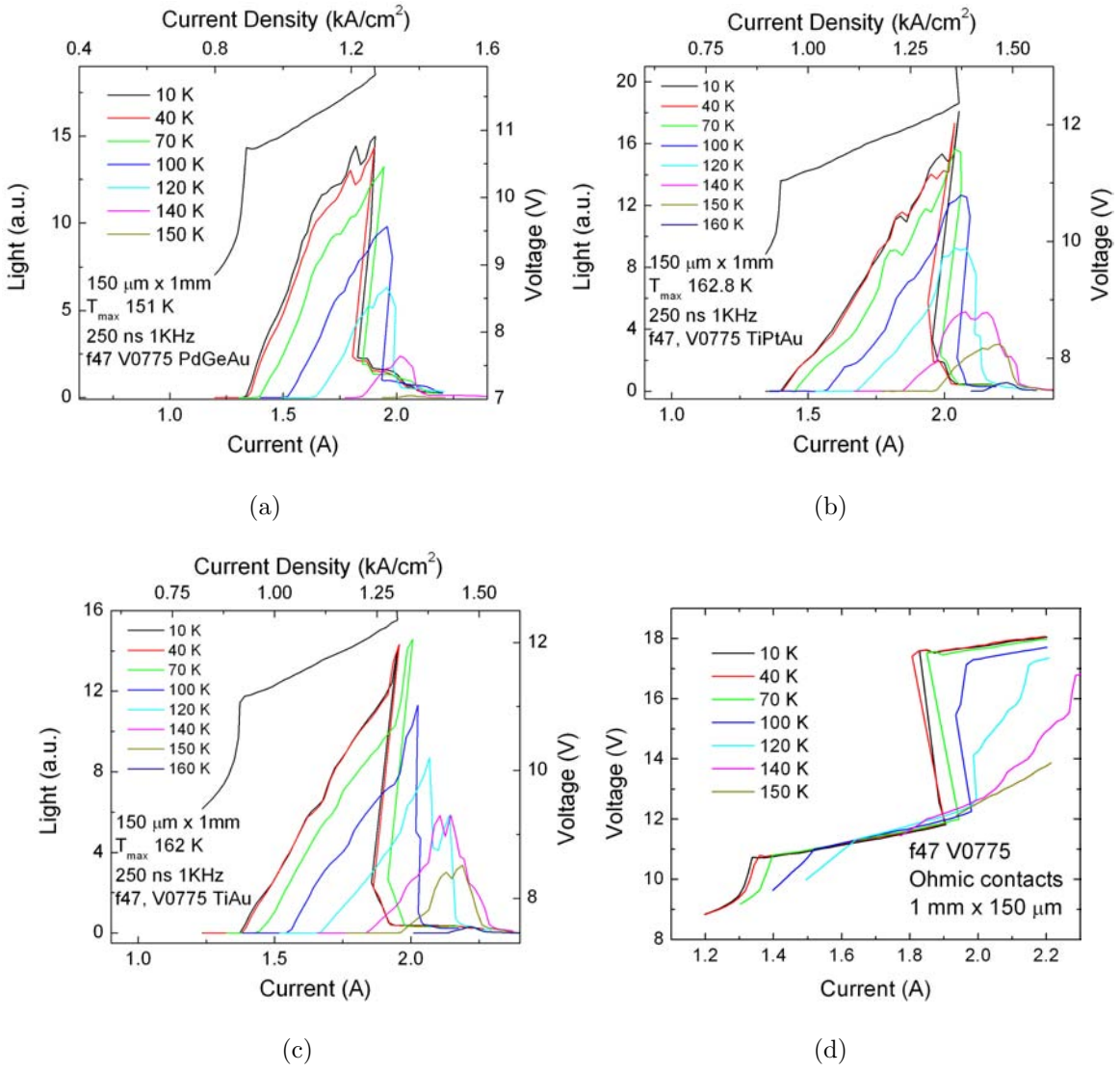

Figure 4.6: The collected THz light (optical output power) versus current curves for MM THz QCLs samples with $f_{23} = 0.47$ ($V0775$) active region design, at different heat sink temperatures. The devices are 150 μm wide, 1 mm long device and are fabricated using (a) $Pd/Ge/Ti/Pt/Au$, (b) $Ti/Pt/Au$ and (c) Ti/Au metal contacts. The bias is applied in pulsed mode (pulse width = 250 ns, repetition rate = 1 kHz). (d) The current-voltage of the $Pd/Ge/Ti/Pt/Au$ based device at various temperatures.

tacts. THz QCL devices are fabricated in 150 μm ridges with the top metal indented ~ 10 μm from ridge edges, to achieve single mode operation. All of the devices are cleaved into ~ 1 mm long Fabry-Perot cavity bars and mounted inside the cryostat for measurement. Figure 4.6 shows the pulsed LIV results for three $f47$ ($V0775$) based THz QCLs with three metal combinations. Pulses as short as 250 ns are used to avoid heating of the active region. Figure 4.6-a shows the results for $Pd/Ge/Ti/Pt/Au$ based devices, where it is expected to obtain ohmic contacts, but poor waveguide performance. This device operated up to 151 K, with threshold current density of 0.91 kA/cm^2 at 10 K. The kink at the beginning of the lasing is very strong, revealing the high efficiency of the carrier injection into the lasing states. Figure 4.6-b shows the LIV results for $Ti/Pt/Au$ based devices, at various temperatures. The lasing is observed up to 162.8 K with threshold current density at 10 K similar to the part a. Finally Figure 4.6-c shows the LIV results for Ti/Au based devices, where the lasing is observed up to 162 K.

The NDR of the $Pd/Ge/Ti/Pt/Au$ device at 10 K occurs at 11.8 V. Considering non-ohmic nature of the contact, it is concluded that the NDR occurs well before the design value of 12 V. The IV of the laser at the NDR shows a sudden and bistable jump in the voltage (Figure 4.6-d). The similar effect is also observed in low doped superlattices, where the IV shows a jump in voltage [145]. This kind of bistable NDR is believed to be because of the current source nature of the driving circuit. The driving circuit is basically not able to bias the device close to the real NDR, and instead skips this region by jumping to the higher voltage region for a given current level, Figure 4.6-d. This effect occurs before reaching the design voltage and prevents the device from reaching the design electric field. The sudden voltage jump close to the NDR disappears at higher temperatures, i.e. 140 K, and higher, and makes it possible to achieve design electric field before getting into the NDR.

Figure 4.7 shows the measured spectra of the device with Ti/Au metal contacts (the

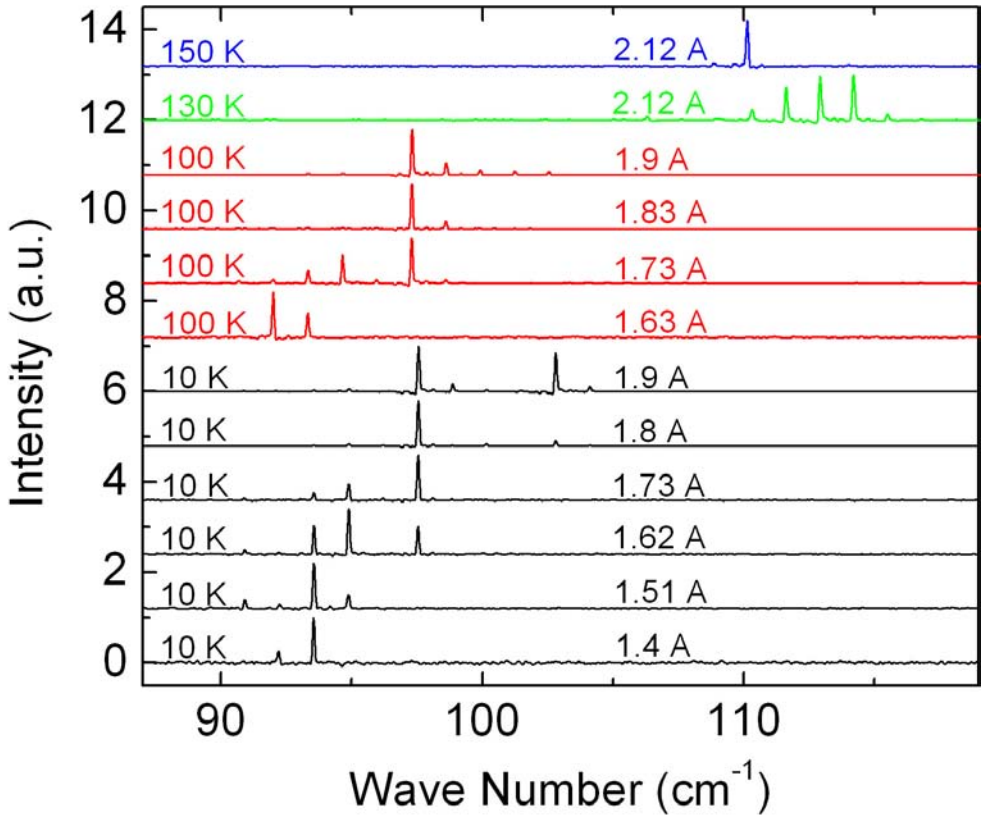

Figure 4.7: Lasing spectra of the THz QCL with $f_{23} = 0.47$ at various injection currents and temperatures. The device with Ti/Au metal contact is picked for spectrum measurements.

device shown in Figure 4.6-c), at various temperatures and current injection levels. The spectrum measurements show that the device covers a wide spectrum range from 91 cm^{-1} up to 115 cm^{-1} (covering 0.7 THz of the EM spectrum). Such a big variation of lasing wavelength is expected for the lasers with smaller oscillator strength (more diagonal lasing transition). This is because for transitions with smaller oscillator strength, the lasing states are coupled less and hence move more with the change of applied electric field. At temperatures below 100 K, the spectrum is locked below 105 cm^{-1}, which is believed ti be due to the bistable IV behavior. As discussed above, the bistable behavior in the IV translates into operating far from the design electric field (real NDR). At higher temperatures

the sudden jump in the IV disappears (as observed in Figure 4.6-d) and the active region gets closer to the design electric field. This is the reason, why at higher temperature the photon energy increases, but still is far from the designed 125 cm^{-1}.

4.2.2 f35

Figure 4.8 shows the conduction band diagram of the three-well based THz QCL design with $f_{23} = 0.35$ at 12 kV/cm. The material system used for this design is also $GaAs/Al_{0.15}Ga_{0.85}As$. The lasing mechanism is identical to the $f47$ design, except that the lasing transition is designed to have lower oscillator strength, or in another word higher diagonality. The energy spacing of the radiative transition is designed to be 15 meV = 3.75 THz, at 12 kV/cm. The design procedure for the $f35$ design is identical to the procedure discussed for the $f47$ design. A similar sheet doping density of 3×10^{10} cm^{-2} is picked for the growth.

Figure 4.9 shows the gain contour plot versus temperature for various injection and extraction barrier thicknesses. The optimization practice for $f35$ design also uses the fitted values for electron heating temperature, radiative and non-radiative pure dephasing time constants that was calculated for the $V0610$ design in [66] ($\tau^*_{23} = 0.85$ ps, $\Delta T_e = 80$ K and $\tau^* = 0.4$ ps). Considering the 40 cm^{-1} contours, the barrier thicknesses for the optimum performance is found to be $L_{inj} = 45$ $\AA$ and $L_{ext} = 44$ $\AA$ (as listed in Table 4.1) that results in maximum operating temperature of $T_{max} = 165$ K. Figure 4.9 also shows that for the optimum values of barrier thicknesses, 10 cm^{-1} improvement in the waveguide loss results in ~ 45 K improvement of T_{max} to ~ 210 K. The effect of waveguide loss reduction on the maximum operating temperature of the device is obvious. But above calculations indicate that the maximum operating temperature improves more for the devices with higher levels of diagonality. Such an effect is expected from the discussion of Figure 2.13-a, where the $\Delta\rho$ shows weaker temperature dependance for higher levels of diagonality (flatter curve).

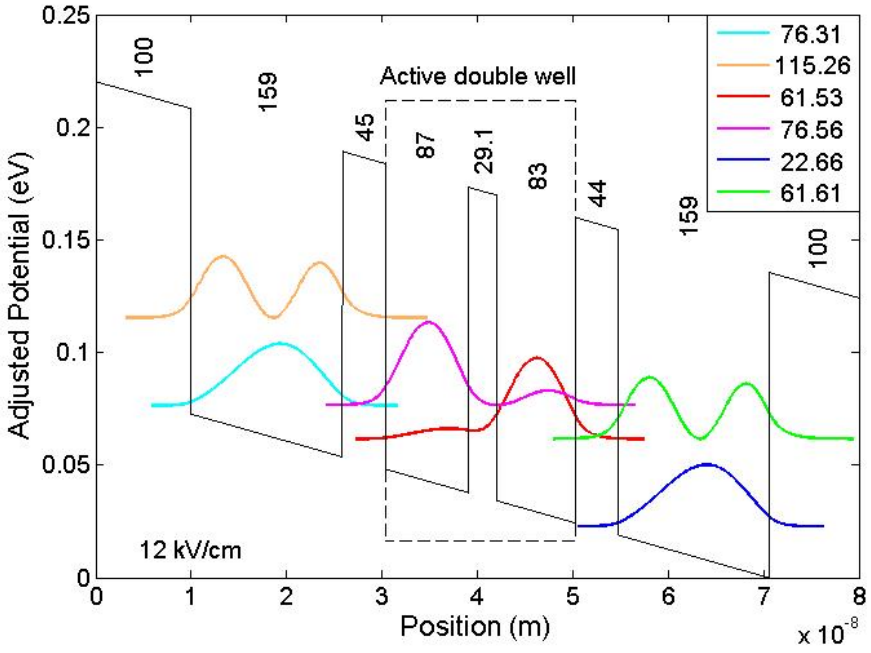

Figure 4.8: Conduction band diagram of the three-well QCL with $f_{23} = 0.35$ at 12 kV/cm and the square modulus of the wavefunctions of the active double-well and the upstream/downstream phonon wells when taken isolated from the adjacent quantum wells. The thickness in Angstrom of each layer is recalled in vertically oriented font.

Therefore slightly improving the waveguide loss (or slightly lowering the $\Delta\rho_{th}$) translates into bigger temperature improvement.

The structure shown in Figure 4.8 was grown using V90 MBE system ($V0774$). The cascade module was repeated 224 times and sandwiched between bottom 100 nm and top 50 nm, 5×10^{18} cm^{-1} n-doped $GaAs$. The thickness of grown MQW is about 10 μm. The doping is implemented by doping the center 50 $\AA$ of the phonon well, with doping concentration of 6.0×10^{16} cm^{-3} (resulting in 6.7×10^{15} cm^{-3} average doping density). After the growth, the quality of the growth was tested using XRD, SIMS to measure the MQW layer thicknesses and level of the doping, and no considerable discrepancy were

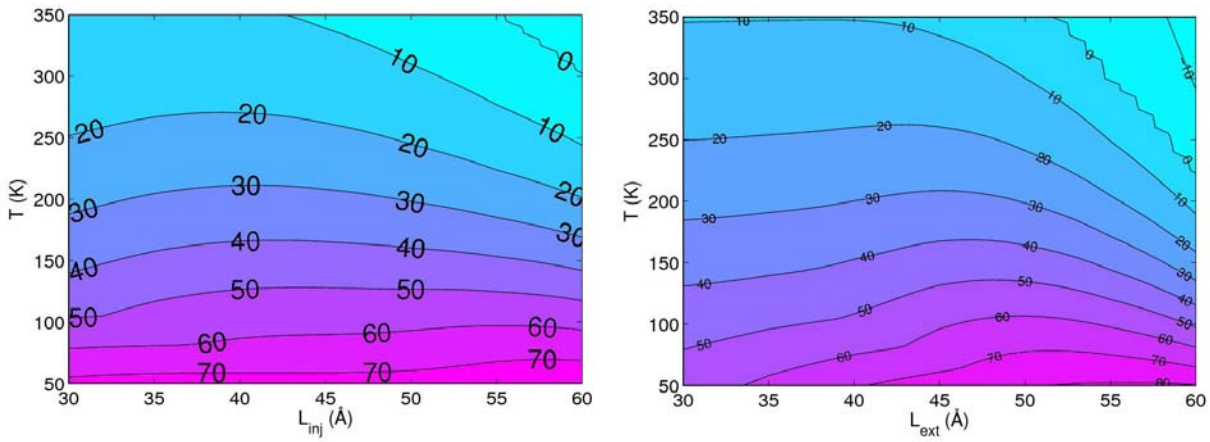

(a) (b)

Figure 4.9: Contour plot of the maximum gain of the $f_{23} = 0.35$ design (in cm^{-1}) versus lattice temperature and the thickness of (a) injection barrier (with $L_{ext} = 44$ $\mathring{A}$) and (b) extraction barrier (with $L_{inj} = 45$ $\mathring{A}$) for $\tau_{23}^{*} = 0.85$ ps, $\Delta T_e = 80$ K, $\tau^{*} = 0.4$ ps.

observed.

The standard MM fabrication process, as discussed for $f47$ sample, is employed to fabricate devices using $V0774$ wafer. Three metal combinations of $Pd/Ge/Ti/Pt/Au$ (550/1000/250/550/3000 $\mathring{A}$), $Ti/Pt/Au$ (250/550/3000 $\mathring{A}$) and Ti/Au (50/3000 $\mathring{A}$) are processed for top and bottom metal contacts. THz QCL devices are fabricated in 150 μm ridges with the top metal indented $\sim$ 10 μm from ridge edges, to achieve single mode operation. All of the devices are cleaved into $\sim$ 1 mm long Fabry-Perot cavity bars and mounted inside the cryostat for measurement. Figure 4.10 shows the pulsed LIV results for three $f35$ ($V0774$) based THz QCLs with three metal combinations. Pulses as short as 250 ns are used to avoid heating of the active region. Figure 4.10-a shows the results for $Pd/Ge/Ti/Pt/Au$ based devices, where it is expected to obtain Ohmic contacts, but poor waveguide performance. This device operated up to 132 K, with threshold current density of 0.77 kA/cm^2 at 10 K. The kink at the beginning of the lasing is also very

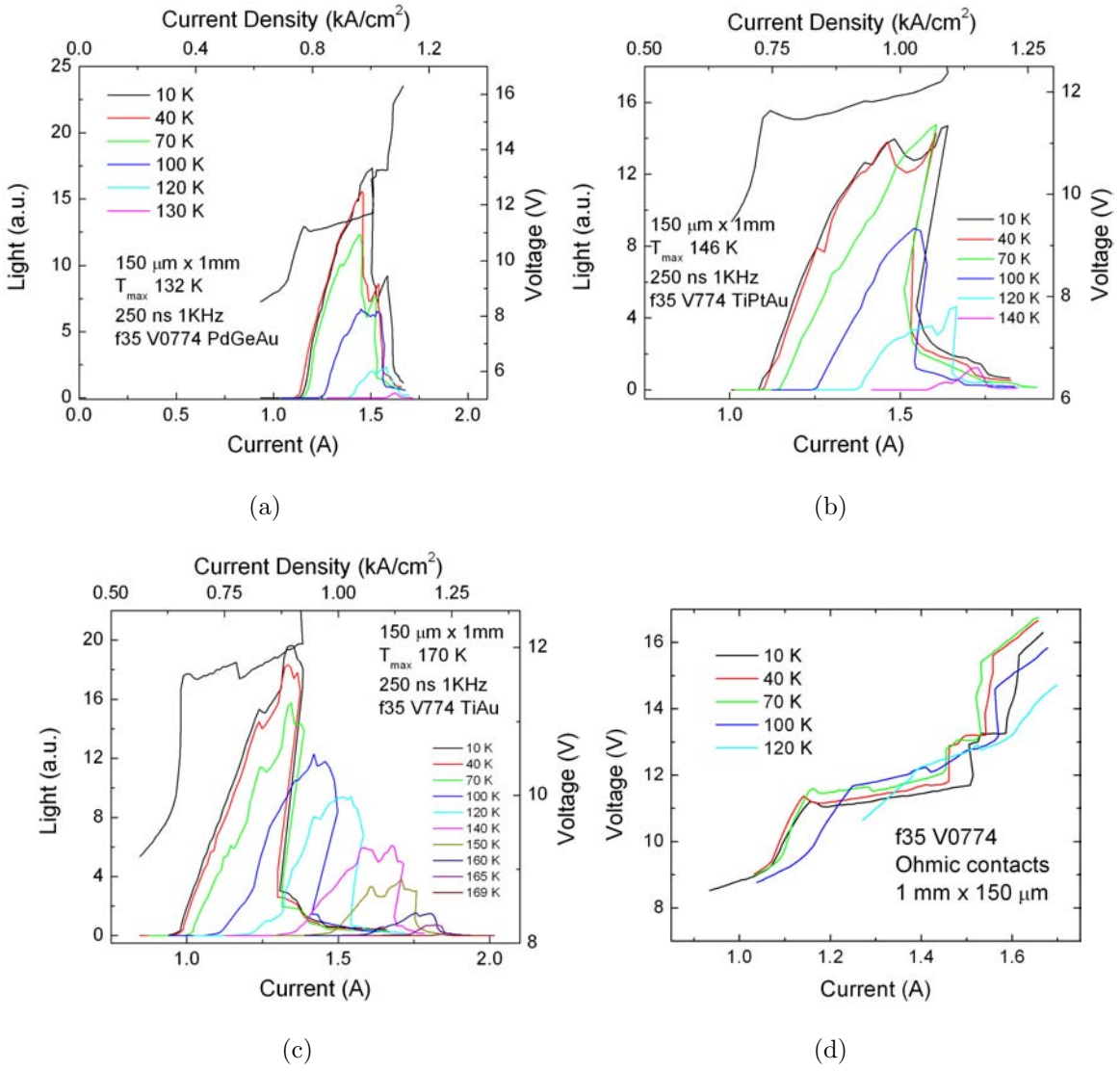

Figure 4.10: The collected THz light (optical output power) versus current curves for MM THz QCLs samples with $f_{23} = 0.35$ ($V0774$) active region design, at different heat sink temperatures. The devices are 150 μm wide, 1 mm long device and are fabricated using (a) $Pd/Ge/Ti/Pt/Au$, (b) $Ti/Pt/Au$ and (c) Ti/Au metal contacts. The bias is applied in pulsed mode (pulse width = 250 ns, repetition rate = 1 kHz). (d) The current-voltage of the $Pd/Ge/Ti/Pt/Au$ based device at various temperatures.

strong, revealing the high efficiency of the carrier injection into the lasing states. Figure 4.10-b shows the LIV results for $Ti/Pt/Au$ based devices, at various temperatures. The lasing is observed up to 146 K with threshold current density at 10 K similar to the part a. Finally Figure 4.10-c shows the LIV results for Ti/Au based devices, where the lasing is observed up to 170 K. The threshold current density for this device is 0.63 kA/cm^2 at 10 K. The higher operating temperature and lower threshold current density for Ti/Au based device is due to its lower loss (Figure 3.9). By employing Ti/Au metal to replace $Pd/Ge/Ti/Pt/Au$, the optical loss of the waveguide is reduced, as a result the T_{max} is improved by 38 K, from 132 K to 170 K. The T_{max} improvement in the $f35$ series devices is much more substantial than that in the $f47$ series devices (which is only 11 K, from 151 to 162 K). This improvement is mainly due to its diagonal nature of the optical transition, which makes the device performance improvement more sensitive to waveguide loss reduction. Although the mirror loss in MM waveguides are small fraction of total loss, in an attempt to slightly reduce the total loss the mirror loss can be easily reduced by increasing the Fabry-Perot cavity length. Consequently higher T_{max} is expected. A 2 mm laser bar from the same batch of devices were cleaved, mounted and tested for maximum operating temperature. The device showed T_{max} of 174.5 K, which is considerable improvement, given tiny improvement made in the value of waveguide loss.

In another attempt to further reduce the waveguide loss and hence improve the T_{max} of the $f35$ design, a sample with copper metal contacts is fabricated. It was shown in [68] that the copper waveguide offers lower waveguide loss in THz region. The $Ta/Cu/Au/Pt/Au$ (10/500/100/55/250 nm) metal stack is used for the $In-Au$ wafer bonding. The Pt layer is inserted to protect the inner gold layer from being alloyed by indium atoms. The rest of the fabrication details are identical as Figure 3.1. A 150 $\mu m \times 1$ mm laser bar is packaged and mounted in the cryostat for test. Figure 4.11 shows the LI results of the $Cu-Cu$ device; it lases up to 172 (2 K higher than the Ti/Au device), which is not much higher than the Ti/Au device. The $Cu-Cu$ device shows the lowest threshold current

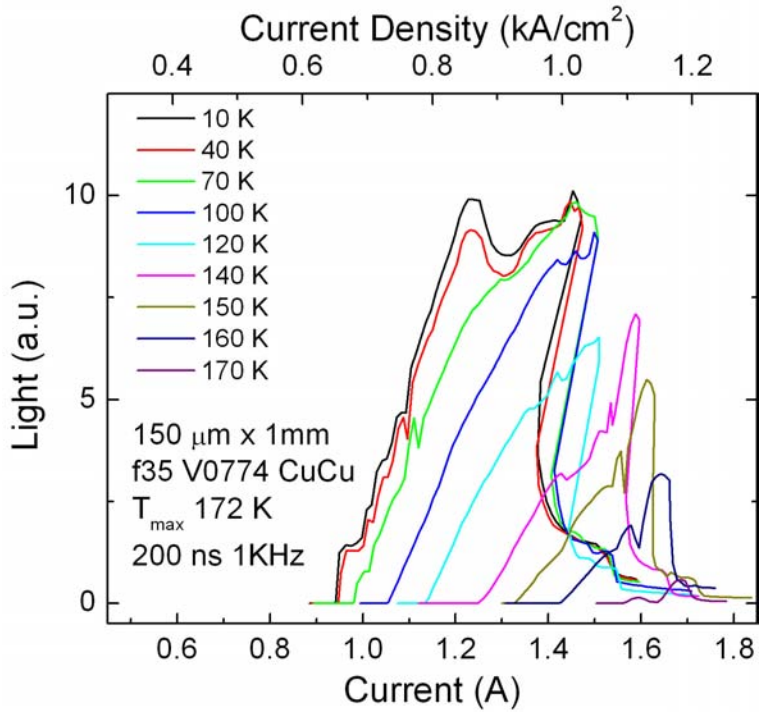

Figure 4.11: The collected THz light (optical output power) versus current curves for MM THz QCLs samples with $f_{23} = 0.35$ ($V0774$) active region design, at different heat sink temperatures. The devices are 150 μm wide, 1 mm long device and are fabricated using Ta/Cu metal contacts. The bias is applied in pulsed mode (pulse width = 200 ns, repetition rate = 1 kHz).

density of 0.63 kA/cm^2, at 10 K. A 2 mm laser bar from the same batch of devices were also cleaved, mounted and tested for maximum operating temperature. The device showed T_{max} of 176 K, which is ~ 2 K higher than the Ti/Au counterpart.

The NDR of the $Pd/Ge/Ti/Pt/Au$ device occurs at 10 K is 11.7 V and at 100 K is 13.2 V (Figure 4.10-d). The IV of the laser at the NDR again shows a sharp and sudden jump in the voltage at lower temperatures. Figure 4.12 shows the measured spectra of the device with Ti/Au metal contacts (the device shown in Figure 4.10-c), at various

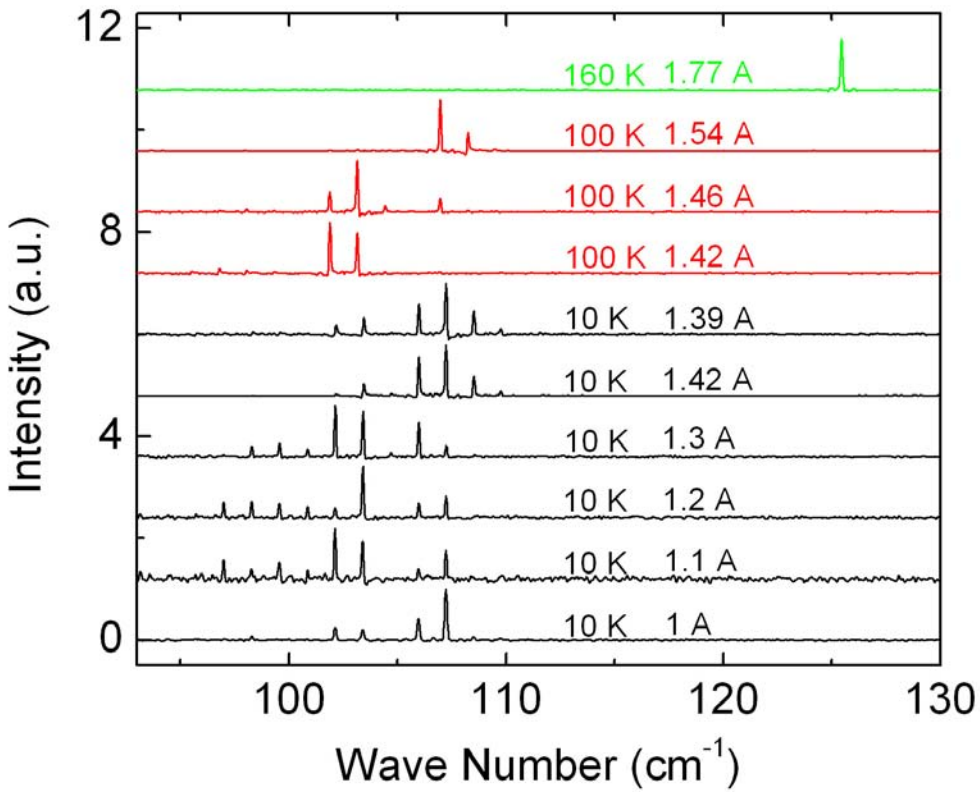

Figure 4.12: Lasing spectra of the THz QCL with $f_{23} = 0.35$ at various injection currents and temperatures.

temperatures and current injection levels. The spectrum measurements at temperatures lower than 100 K show that the device covers the spectrum range from 97 cm^{-1} up to 110 cm^{-1} (covering 0.4 THz of the EM spectrum), which is an indication of operating far from the design electric field (as discussed after the observed sudden jump in the IV). At higher temperatures the sudden jump in the IV disappears and the active region can get closer to the design electric field. This is the reason, why at 160 K the lasing frequency increases up to the designed value of 125 cm^{-1}.

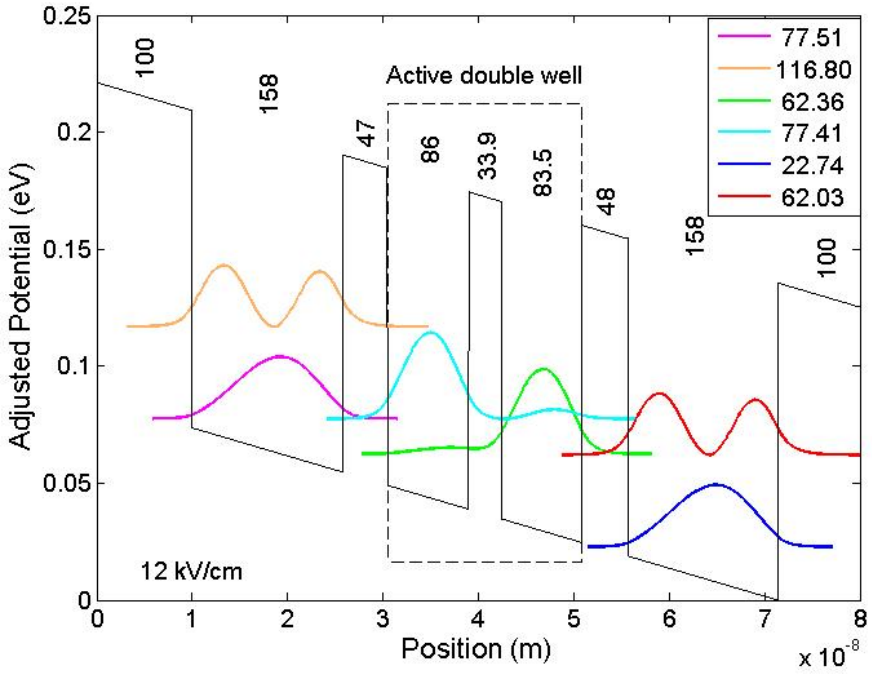

Figure 4.13: Conduction band diagram of the three-well QCL with $f_{23} = 0.25$ at 12 kV/cm and the square modulus of the wavefunctions of the active double-well and the upstream/downstream phonon wells when taken isolated from the adjacent quantum wells. The thickness in Angstrom of each layer is recalled in vertically oriented font.

4.2.3 f25

Figure 4.13 shows the conduction band diagram of the three-well based THz QCL design with $f_{23} = 0.25$ at 12 kV/cm. The material system used for this design is also $GaAs/Al_{0.15}Ga_{0.85}As$. The lasing mechanism is identical to the previous three-well based devices, except that the lasing transition is design to have lower oscillator strength, or in another word higher diagonality. The energy spacing of the radiative transition is designed to be 15 $meV = 3.75\ THz$, at 12 kV/cm. All the tunneling coupling and detuning values are calculated using the tight binding approximation for various electric field levels. I the

same time, all the non-radiative emission and absorption lifetimes is also calculated for the given electric fields. Having the tunneling and scattering parameters for each electric field, a similar optimization procedure as the procedure discussed after Figure 4.1 is performed to obtain optimum injection and extraction barrier thicknesses. The sheet doping density of $3 \times 10^{10}\ cm^{-2}$ is picked.

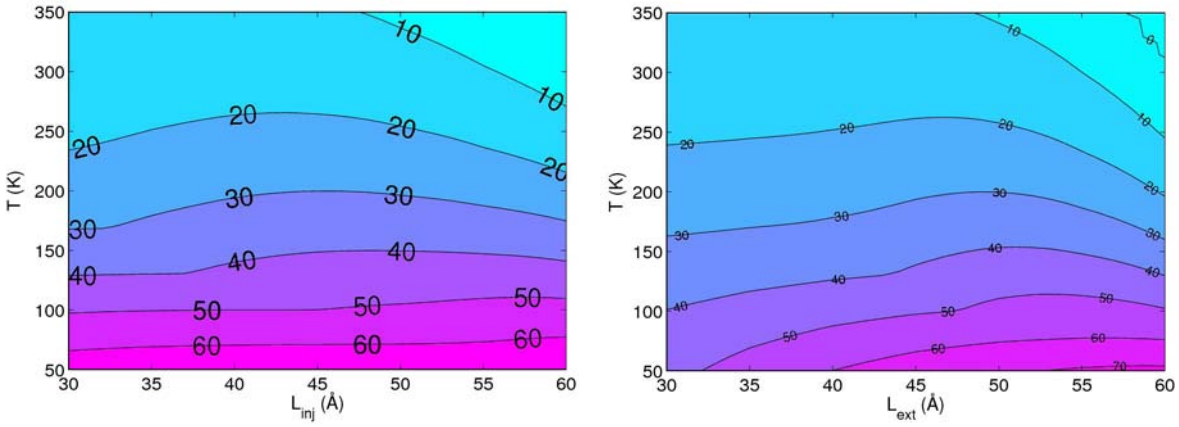

(a) (b)

Figure 4.14: Contour plot of the maximum gain of the $f_{23} = 0.25$ design (in cm^{-1}) versus lattice temperature and the thickness of (a) injection barrier (with $L_{ext} = 48\ \mathring{A}$) and (b) extraction barrier (with $L_{inj} = 47\ \mathring{A}$) for $\tau_{23}^{*} = 0.85\ ps$, $\Delta T_e = 80\ K$, $\tau^{*} = 0.4\ ps$.

Figure 4.14 shows the gain contour plot versus temperature for various injection and extraction barrier thicknesses. The optimization practice for $f25$ design also uses the fitted values for electron heating temperature, radiative and non-radiative pure dephasing time constants that was calculated for the $V0610$ design in [66] ($\tau_{23}^{*} = 0.85\ ps$, $\Delta T_e = 80\ K$ and $\tau^{*} = 0.4\ ps$). Considering the 40 cm^{-1} contours, the barrier thicknesses for the optimum performance is found to be $L_{inj} = 47\ \mathring{A}$ and $L_{ext} = 48\ \mathring{A}$ (as listed in Table 4.1) that results in maximum operating temperature of $T_{max} = 145\ K$. Figure 4.14 also shows that for the optimum values of barrier thicknesses, 10 cm^{-1} improvement in the waveguide loss results in $\sim 55\ K$ improvement of T_{max} to $\sim 200\ K$. The maximum operating temperature for $f25$

design improves even more than $f35$ design, due to even weaker temperature dependency of $\Delta\rho$. Therefore slightly improving the waveguide loss (or slightly lowering the $\Delta\rho_{th}$) translates into even bigger temperature improvement.

The structure shown in Figure 4.13 was grown using V90 MBE system ($V0773$). The cascade module was repeated 220 times and sandwiched between bottom 100 nm and top 50 nm, 5×10^{18} cm^{-1} n-doped $GaAs$. The thickness of grown MQW is about 10 μm. The doping is implemented by doping the center 50 $\mathring{A}$ of the phonon well, with doping concentration of 6.0×10^{16} cm^{-3} (resulting in 6.57×10^{15} cm^{-3} average doping density). After the growth, the quality of the growth was tested using XRD, SIMS to measure the MQW layer thicknesses and level of the doping, and no considerable discrepancy were observed.

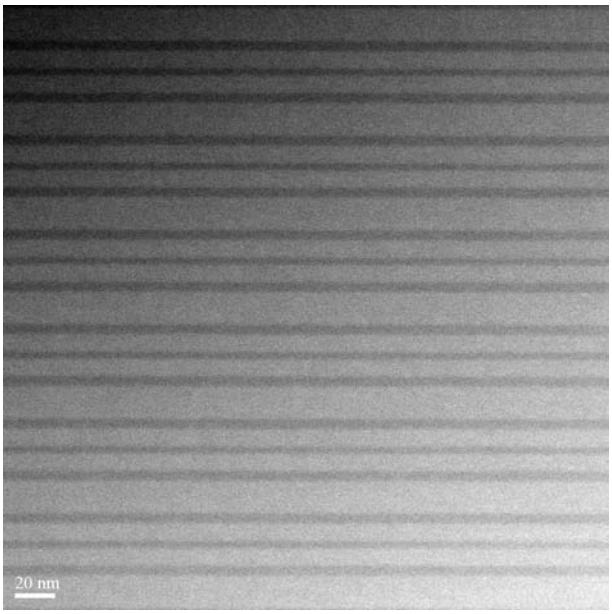

Figure 4.15: The TEM image of the $V0773$ ($f25$) wafer, showing six cascaded periods. The barriers ($Al_{0.15}Ga_{0.85}As$) look darker than the wells ($GaAs$) in the image.

The standard MM fabrication process, as discussed in for previous samples, is employed

to fabricate devices using $V0773$ wafer. Three metal combinations of $Pd/Ge/Ti/Pt/Au$ (550/1000/250/550/3000 $\mathring{A}$), $Ti/Pt/Au$ (250/550/3000 $\mathring{A}$) and Ti/Au (50/3000 $\mathring{A}$) are processed for top and bottom metal contacts. THz QCL devices are fabricated in 150 μm ridges with the top metal indented $\sim$ 10 μm from ridge edges, to achieve single mode operation. All of the devices are cleaved into $\sim$ 1 mm long Fabry-Perot cavity bars and mounted inside the cryostat for measurement. Although the model predicts lasing up to 145 K, the measurements showed that none of the devices reached the threshold gain and lased, even at 10 K. During design, growth and fabrication of the THz QCLs, each of above factors can cause failure in the lasing action. The fabrication flaw is ruled out, since it is repeated separately for three metal combinations and none lased. The SIMS and TEM results on the $V0773$ ($f25$) wafer also showed no significant deviation of the doping level, or interface roughness. Figure 4.15 shows the TEM image for the $V0773$ wafer. However, the fitting of the heterostructure layers using XRD showed that the layer thickness are slightly off from the original design shown in Figure 4.13. Starting from the injector barrier, the grown structure is measured to be (**46**/83.5/**33**/81/**46.5**/153 $\mathring{A}$), with the barriers in the bold fonts. Such a deviation in the layer thickness results in $\Delta_{12} = 1.3\ meV$ and $\Delta_{34} = 1.6\ meV$, which significantly reduces the gain. Due to very weak temperature dependency of the $f25$ gain (Figure 2.13-b), lowered gain does not get recovered even at 10 K, and results in non-lasing device. Very diagonal lasing transition in the $f25$ design also results in highly electric field dependant photon energy, where makes the the photon energy at the threshold much lower than design electric field. This translates into longer wavelength at the threshold (as observed in the spectrum of the $f35$ and $f47$ samples),and requires reconsideration of the doping level in the waveguide of very diagonal structures.

4.3 Lasing based on phonon-photon-phonon scheme

The analytical model presented in chapter 2 predicted that the population inversion in the three-well RP based THz QCL designs are ideally limited to 50% (equation 2.71). This is due to existence of the injector level (lower level in the phonon well), where the carriers are waiting to get injected into the upper lasing level. The upper lasing level ideally holds as many carriers as the injector level, which is half of the total available carriers. In the real cases, with presence of scattering channels, the population inversion is even lower than 50% (Figure 2.11). The model also predicted that the presence of injection and extraction tunneling couplings reduce the gain peak value, by modifying the Lorentzian gain shape (equation 2.77 and Figure 2.19). Above two reasons lead to limited temperature performance for three-well based designs. The previous section extensively discussed various designs for the three-well RP based THz QCLs, where the optimum values for oscillator strength, injection and extraction tunneling barrier thicknesses were found. It was experimentally demonstrated that oscillator strength of 0.35 shows the highest $T_{max} = 176\ K$.

4.3.1 Density matrix model for phonon-photon-phonon lasing scheme

Further pushing of the T_{max} towards room temperatures requires increasing the intersubband gain, particularly at higher temperatures. To do so, a structure is proposed in this section (as schematically shown in Figure 4.16) that injects the carriers into the upper lasing state (2) and out of lower lasing (3) state using resonant LO phonon assisted relaxation and ideally holds all the carriers in the upper lasing level. The proposed scheme in this section is very similar to Kumar et al. work in [72]. In such an active region design the injected carriers from upstream periods are collected by an excited state (level 1), and

quickly relaxed to the upper lasing state (2). A photon is emitted when a carrier on the upper lasing state relax down to the lower lasing state (3), spaced by the desirable photon energy. Once the carriers are relaxed down to the lower lasing state through photon emission, they quickly depopulate to the ground state (4), through phonon emission. In this structure, the resonant phonon assisted relaxation of carriers are used to populate the upper lasing state and depopulate the lower lasing state, the lifetime of which is in order of 0.1 ps. Due to absence of resonant tunnelings, a Lorentzian gain shape with high gain peak is expected from such structure. Further increase of the gain is achieved by increasing the population inversion, using very diagonal lasing transition. The diagonal lasing transition results in lower LO phonon relaxation rate. Since the population and depopulation processed are very fast, the majority of the carriers occupy the energy level 2 and results in ideally 100% population inversion. However, various leakage paths and phonon absorption processes reduce the population inversion lower than the ideal value.

Figure 4.16 schematically shows all possible electron relaxation and excitation paths by non-radiative LO phonon emission and absorption, respectively. The desired channels are $1 \rightarrow 2$ (phonon emission), $2 \rightarrow 3$ (photon emission) and $3 \rightarrow 4$ (phonon emission) electron relaxations. Therefore this structure is called phonon-photon-phonon design, from now on. The rest of electron relaxations and all the electron excitation paths are undesirable, and cause reduction of the population inversion. In order to damp all the leakage paths, it is important to reduce the spatial overlap of all the wavefunctions. However very low spatial overlap results in inefficient phonon emission for population and depopulation processes and low oscillator strength between the lasing states. An optimization process is, therefore, required to design a working active region using this scheme.

Here the density matrix model is adopted for the system schematically shown in Figure 4.16. The symmetric Hamiltonian of the phonon-photon-phonon system, without laser

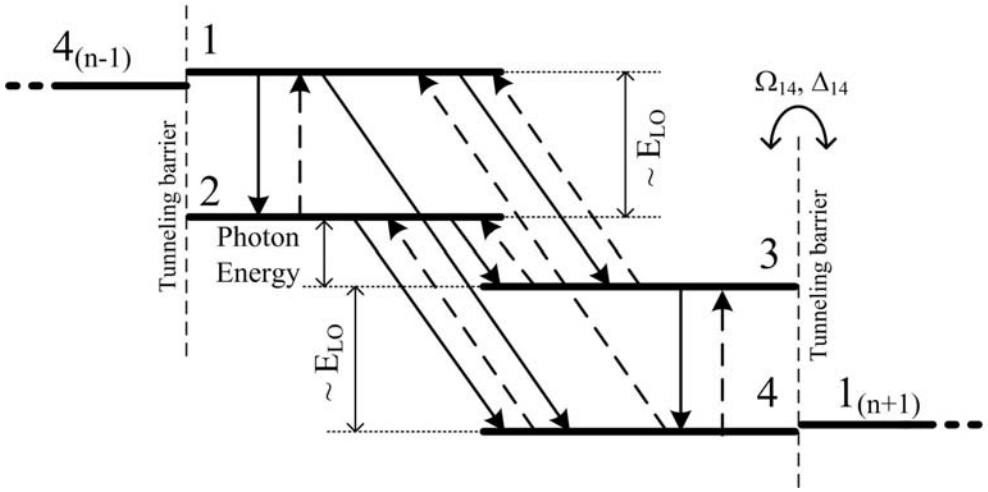

Figure 4.16: The schematic diagram of a THz QCL active region using phonon-photon-phonon scheme. The population inversion is expected to form between state 2 and 3. The upstream and downstream levels are separated by tunneling barriers. All possible non-radiative resonant phonon emission (solid arrows) and absorption (dashed arrows) scattering channels are also plotted.

coherence terms, can be written as

$$H = \begin{pmatrix} E_1 & 0 & 0 & \hbar\Omega_{14} \\ 0 & E_2 & 0 & 0 \\ 0 & 0 & E_3 & 0 \\ \hbar\Omega_{14} & 0 & 0 & E_4 \end{pmatrix}, \tag{4.1}$$

where Ω_{14} is the coupling between the ground state and the excited state of the down-stream period. This Hamiltonian can be applied to the equation of the motion (equation 2.44), to obtain the population inversion and coherence of all energy states. By neglecting the electron excitation terms at low temperatures, the matrix $\mathcal{T}$ is constructed using the

relaxation and excitation rates shown in Figure 4.16 as

$$\mathcal{T} = \begin{pmatrix} -(\tau_{12}^{-1}+\tau_{13}^{-1}+\tau_{14}^{-1})\rho_{11} & 0 & \\ 0 & -(\tau_{23}^{-1}+\tau_{24}^{-1})\rho_{22}+\tau_{12}^{-1}\rho_{11} & \dots \\ 0 & 0 & \\ \tau_{\|14}^{-1}\rho_{14} & 0 & \end{pmatrix} \tag{4.2}$$

$$\dots \begin{pmatrix} 0 & \tau_{\|14}^{-1}\rho_{14} \\ 0 & 0 \\ \tau_{13}^{-1}\rho_{11}+\tau_{23}^{-1}\rho_{22}-\tau_{34}^{-1}\rho_{33} & 0 \\ 0 & \tau_{14}^{-1}\rho_{11}+\tau_{24}^{-1}\rho_{22}-\tau_{34}^{-1}\rho_{33} \end{pmatrix}, \tag{4.3}$$

where τ_{ij} for $i < j$ is the relaxation time of the carriers from $i \rightarrow j$. The electron excitation lifetimes (τ_{ij} for $i > j$) could be also included by adding the appropriate terms in the diagonal of the $\mathcal{T}$ matrix. The ρ_{ii} denotes the population of energy level i, ρ_{ij} denotes the coherence between the state i and j, and $\tau_{\|14}$ represents the dephasing time constant for the tunneling process.

By employing above matrices into the equation 2.44, the population of all levels and the coherence term is calculated. The population inversion ($\Delta\rho = \rho_{22} - \rho_{33}$) is hence analytically calculated as

$$\Delta\rho = \frac{\tau_{12}^{-1}(\tau_{34}^{-1}-\tau_{23}^{-1}) - \tau_{13}^{-1}(\tau_{24}^{-1}+\tau_{23}^{-1})}{\tau_{12}^{-1}(\tau_{34}^{-1}+\tau_{23}^{-1}) + (\tau_{23}^{-1}+\tau_{24}^{-1})(2\tau_{34}^{-1}+\tau_{13}^{-1}) + T_{41}\tau_{34}^{-1}(\tau_{12}^{-1}+\tau_{13}^{-1}+\tau_{14}^{-1})(\tau_{23}^{-1}+\tau_{24}^{-1})}, \tag{4.4}$$

where τ_{ij} is the various relaxation times, and T_{41} is the tunneling time between level 4 and level 1 of the downstream period, as defined from equation 2.47. By neglecting all the leakage channels and only considering $1 \rightarrow 2$, $2 \rightarrow 3$, and $3 \rightarrow 4$ relaxation channels, the population inversion is approximately estimated as

$$\Delta\rho = \frac{\tau_{23}-\tau_{34}}{\tau_{23}+\tau_{34}+2\tau_{12}+T_{41}}. \tag{4.5}$$

Equation 4.5 suggests that if very large upper lasing lifetime (τ_{23}) results in close to unity population inversion. This results agrees with the qualitative prediction earlier in this

section. The large lifetime of the population inversion is achieved using diagonal lasing transition, which results in lowering gain cross section.

The current density of the phonon-photon-phonon system, can be calculated starting from equation 2.49, and employing the Hamiltonian and the density matrix of the system under study (as in Figure 4.16). After some algebra and simplification the current density results in

$$\begin{aligned} J &= 2eN_{2D}\frac{L_{sp}-(Z_{11}-Z_{44})}{L_{sp}}\Omega_{14}\Im(\rho_{14}) \\ &= \frac{L_{sp}-(Z_{11}-Z_{44})}{L_{sp}}\frac{eN_{2D}}{t_{transit}}, \end{aligned} \tag{4.6}$$

where N_{2D} is the sheet doping density, $Z_{11}-Z_{44}$ is the static dipole moment between levels 1 and 4, L_{sp} is the length of a super-period, Ω_{14} is the coupling between levels 4 and downstream 1, $\Im(\rho_{14})$ is the imaginary part of coherence term between between levels 4 and downstream 1, and $t_{transit}$ is defined as

$$t_{transit}=\frac{\tau_{12}^{-1}(\tau_{23}^{-1}+\tau_{34}^{-1})+(\tau_{23}^{-1}+\tau_{24}^{-1})(2\tau_{34}^{-1}+\tau_{13}^{-1})}{\tau_{34}^{-1}(\tau_{12}^{-1}+\tau_{13}^{-1}+\tau_{14}^{-1})(\tau_{23}^{-1}+\tau_{24}^{-1})}+T_{41}. \tag{4.7}$$

As mentioned above, due to absence of the tunneling couplings, the gain is simply calculated using the product of gain cross section (equation 2.27), population inversion (equation 4.4) and a Lorentzian function. Assuming the lasing center energy of $E_{23}=E_2=E_3$, and FWHM of $2\tau_{\|23}^{-1}$, the gain as function of photon energy ($\hbar\omega$,) can be written as

$$G_{op}(\hbar\omega)=\frac{N_{3D}e^2n_g}{2m^*c\varepsilon_0\varepsilon_r}f_{23}\Delta\rho\Im\left(\frac{1}{(\hbar\omega-E_{23})-\jmath\tau_{\|23}^{-1}}\right). \tag{4.8}$$

4.3.2 Design process for phonon-photon-phonon active regions

One period of phonon-photon-phonon active region consists of two phonon and one photon energy spacings ($2\times 36\ meV+15\ meV\approx 87\ meV$). This means that the quantum wells

has to be deeper than three well RP based active regions, to accommodate all bound energy levels. The $AlGas/Al_{0.25}Ga_{0.75}As$ material system with conduction band offset of $\sim 230\ meV$ is therefore selected for realization of this design. After the first iteration, it was found that the thickness of one period is approximately 40 $\mathring{A}$. Therefore, the design electric field is calculated to be $E_{dsg} = 87\ mV/40\ \mathring{A} \approx 21\ kV/cm$.

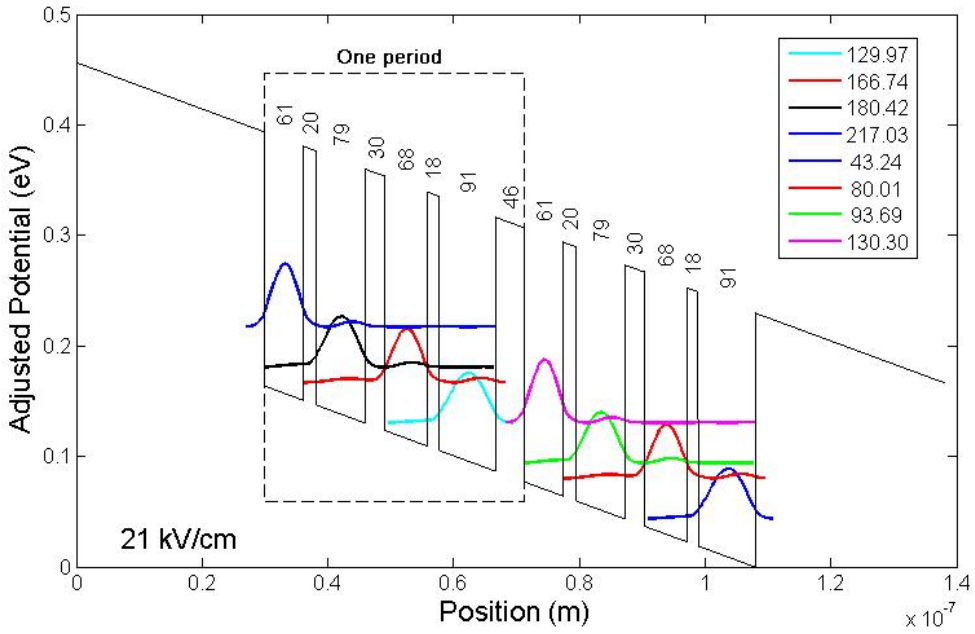

Figure 4.17: Conduction band diagram of the phonon-photon-phonon THz QCL structure under study at 21 kV/cm and the square modulus of the wavefunctions of inside the active region. The thickness in Angstrom of each layer is recalled in vertically oriented font. The material system is $AlGas/Al_{0.25}Ga_{0.75}As$.

Peak of the gain, as calculated in equation 4.8, is defined as a *figure of merit* for designing an efficient phonon-photon-phonon active region. For designing the active region, a double well for realizations of left two energy levels (levels 1 and 2) and another double well for realization of right two energy levels (levels 3 and 4) are designed. It is important

to find a structure with optimum overlap integral between all four energy states. Very small overlap integral causes tiny oscillator strength and small gain (equation 4.8). On the other hand, large overlap integral results in dominant leakage channels and hence reduces the population inversion (equation 4.4). The design process starts with finding all possible double well structures with the first two energy states spaced $\sim E_{LO} \pm 4\ meV$. These double well solutions are categorizes based on their overlap integrals. The next design step is to couple two double well solutions using a particular barrier width that gives desired E_{23} energy spacing between ground state of the left double well and excited state of the right double well. For this design exercise, the photon energy of $E_{23} \approx 15\ meV$ is targeted. The last step in the design is to calculate the tunneling barrier. Equation 4.4 suggests that the highest population inversion is achieved when the tunneling time is the smallest. In another word for a given structure, the gain is maximum when the tunneling detuning is zero. Therefore, the tunneling barrier width is calculated to provide zero detuning between levels 4 and 1".

After obtaining an active region design with desired E_{23} and arbitrary overlap integrals, the optimization process is performed to maximize the figure of merit (gain). For the optimization process, all the non-radiative relaxation and excitation times needs to be calculated for all the designs. A full optimization process requires very large computer power. Here a sample design, as a proof of concept, is presented by a simplistic optimization of the structure at 10 K; a comprehensive optimization process will result in the structures with higher gain. Figure 4.17 shows the conduction band diagram of the designed structure along with the square modulus of the wavefunctions. The photon energy of this design is $\sim 13.7\ meV$, which is equivalent to 3.4 THz. Assuming electron heating temperature of 50 K, the population inversion of $\sim 85\%$ at 10 K and 30% at 150 K is calculated. The oscillator strength for this design is 0.17, which is comparably small. The tunneling detuning is designed to be small ($\Delta_{14} = 0.33\ meV$), which results in fast 0.25 ps tunneling time.

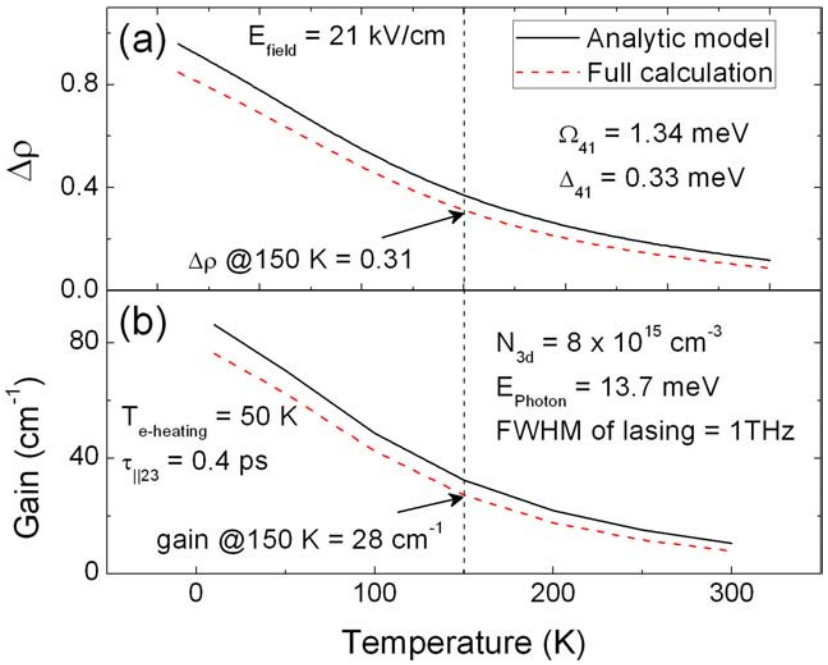

Figure 4.18: (a) The of population inversion of the phonon-photon-phonon design versus temperature. The approximated analytical model is compared with the full calculation including all emission and absorption channels. The active region shows more than 30% population inversion at 150 K. The panel (b) shows the gain for the calculated population inversion in panel (a). At 150 K, a gain of 28 cm^{-1} is predicted.

Figure 4.18-a and b compare the population inversion and gain of the structure presented in Figure 4.17 for analytical model (equation 4.5) and the full calculation including all emission and absorption channels. Figure 4.18-a shows that the leakage channels and phonon absorptions reduce the population by more than 5%. However the inversion scheme is so efficient in this structure that even at 150 K, 30% of carriers are efficiently inverted. Figure 4.18-b shows that the designed structure offers a gain of 28 cm^{-1} at 150 K, which is quite promising. The proposed structure in Figure 4.17 is just an starting point for further optimization and research on the phonon-photon-phonon lasing scheme.

4.4 Summary and conclusions

This chapter discussed design and measurement results of several RP based three-well THz QCLs. The recent work from Kumar et al. demonstrated that making the lasing transition more diagonal improves the maximum operating temperature [61]. It was analytically discussed in chapter 2 that the more diagonal design suppresses the wrong injection and extraction channels, leading to larger population inversion and consequently higher operating temperature. On the other hand it was shown in Equation 2.78 that very diagonal radiative transition reduces the gain cross section. Therefore there must be an optimum point that compromises the population inversion increase and gain coefficient reduction. This chapter targets to experimentally find an optimum level of diagonality for three well THz QCLs. For this purpose, seven different levels of oscillator strength (laser transition diagonality) between 0.25 and 0.67 were picked and the corresponding lasing double well and phonon well was designed.

For a given set of lasing double well and phonon well, Luo et al. showed experimentally that there exist an optimum injection and extraction barrier thicknesses [102] and [144]. This work was supported theoretically by Dupont et al.'s work, where the optimum barrier thicknesses could be calculated analytically [66]. This method is based on the carrier transport and gain calculated form density matrix model that was discussed in chapter 2. The first part of this chapter, discussed the optimization process for injection and extraction barrier thicknesses. Electron's heating temperature, lasing and non-lasing dephasing time constants are the three fundamental fitting parameters that are required to correctly calculate the gain of the THz QCLs. The values for these parameters were adopted from Dupont et al. work [66] as electron heating temperature of 80 K, lasing dephasing time constant of 0.85 ps and tunneling dephasing time constant of 0.4 ps, and then used to design new three-well RP based THz QCLs. The optimum values for injection and extraction barrier thicknesses were separately calculated, for all seven designs in the f-series study.

The numerical simulation showed that the T_{max} increases slowly as the oscillator strength decreases from 0.67 to around 0.4 (duo to enhance population inversion). When the oscillator strength went below 0.4, the maximum operating temperature started to drop quickly, due to small gain cross section. Three center values of oscillator strength (0.25, 0.35 and 0.47) were picked for growth and experimental verification. Each grown wafer was processed into MM waveguides using three studied metal combinations in chapter 3. The highest operating temperature of 170 K was observed from $f35$ sample fabricated using Ti/Au metal contacts. Comparing the measurement value with theoretically predicted 165 K value agreed well. Slightly improving the mirror loss for this device improved its T_{max} to 174.5 K. The experimental results revealed that as the level of diagonality increased, the THz QCLs become more sensitive to the waveguide loss. This means that slight improvement in the waveguide loos can drastically increase the maximum operating temperature. On the other hand it also means that any fabrication imperfection that translates into the waveguide loss can potentially impact the device performance.

Finally a new lasing scheme is proposed in this chapter that improves the weaknesses of the RP based THz QCL designs. The new structure consists of phonon-photon-phonon emission and can ideally provide near 100% population inversion. It emit an unmodified Lorentzian gain shape, with high peak values. The density matrix model is adopted for the proposed structure, and the analytical expression for the gain and current of such structure is calculated. Based on the model, a figure of merit is defined to design such structures. A sample design is proposed for proof of concept, which showed more than 30% population inversion at 150 K.

Chapter 5

Conclusions and future works

The THz region in the electromagnetic spectrum have remained largely underdeveloped mainly due to the lack of compact, convenient and efficient THz devices - sources, detectors, modulators, waveguides and switches. Considerable efforts are underway to fill this "THz gap" in view of the useful potential applications of THz radiation, such as chemical detection, astronomy, imaging and communication. Progress has been made in various THz technologies in recent years, the development of THz QCLs for wave generation, the development of THz quantum well photodetectors for wave detection, the development of active THz metamaterial devices for wave modulation, and other development of THz components for wave-guiding, interconnection and phase modulation, to name a few. Such rapid progress has exposed a new THz gap: the capacity to generate high bandwidth modulated sources and detectors having carrier frequencies in the 1-10 THz regime and the modulation bandwidths in the GHz range.

A great deal of research into THz QCLs has been focused on improvement of maximum operating temperature, through engineering band structures of MQW active region and optimizing the waveguide and device structures. This thesis presented the details of the design and implementation of THz QCLs, to generate THz field at higher temperatures.

Starting from the solutions of Schrödinger equation for multiple quantum well heterostructures and the Fermi's golden rule, the electron's interaction with photon and phonon were discussed. Through this discussion the intersubband gain cross section and non-radiative scattering times were calculated. On the other hand a density matrix based model were employed to analytically calculated the transport and gain for the three-well based THz QCLs. The analysis showed that the limiting factor for building high population inversion was the wring injection channels on the injection and on the extraction side. The numerical simulation showed that the extraction barrier side leakage is playing a major role in reduction of the upper lasing lifetime. The gain calculations also showed that the total gain consists of a modified Lorentzian term, which was proportional to the population inversion, and two stimulated Raman gain terms, which were proportional to the coherence between in the states at injection and extraction barriers. The modified Lorentzian term made the gain spectrum wider and reduced the peak of the gain, and the Raman term showed a inevrsionless dispersive like gain. An extensive discussion were followed on the behavior of the THz QCL gain.

Another important parameter that determines the temperature performance of the THz QCLs is the thermal and waveguide structural prosperities of the device. The experimental and analytical thermal modeling of the device were presented and the solutions have been discussed, to improve the heat removal from the active region. The heat removal engineering particularly becomes important for CW device operation. The waveguide design optimization of the Fabry-Perot laser ridges were also discussed for both major MM and SI-SP structures. The threshold gain of each waveguide structure were calculated and minimized for single mode operation of the device. Through this discussion the design and implementation of a THz QCL with electrically controllable transverse mode profile were presented. This device demonstrated the electrically controllable emission pattern direction, which can be handy for many THz applications.

The developed density matrix model made it possible to calculate the gain of the THz QCL at elevated temperatures. Calculation of the gain at various temperatures and electric fields, for a variety of injection and extraction barrier thicknesses, showed an optimum barrier thickness. This results agree well with the published experimental works, where optimum barrier thicknesses were found for a given set of double lasing wells and phonon well. The optimum value basically balances the higher population inversion for thin and higher modified Lorentzian peak gain for thicker barriers. Using this optimization technique, a second optimization procedure on the oscillator strength of the lasing transition was performed. It was found out that oscillator strength of around 0.4 provides the highest operating temperature of around 170 K, for a waveguide with 40 cm^{-1} threshold gain. Some of the designed structures were grown and fabricated using the optimized structure for verification purposes. A good agreement between the model and the experimental results were observed. It was also observed that the performance of the devices with lower oscillator strength (higher level of diagonality) are more sensitive to the cavity loss. The vision gained from the results of the density matrix based model were used to propose a new lasing scheme based on phonon-photon-phonon emission. The proposed structure is ideally capable of showing 100% population inversion and emitting an unmodified Lorentzian gain shape. A full density matrix model for the proposed structure was presented along with a proof of concept design. Further optimization of such lasing scheme opens the opportunity for future investigators to explore devices working at higher temperatures.

The structures reported in this thesis were demonstrating high temperature performance, as it was optimized from many discussed aspects. More optimization on the MQW active gain medium, waveguide structure and heat dissipation engineering is yet possible. The final goal is to push THz QCL operating temperature up to the ranges that are reachable by thermoelectric coolers ($\sim 220\ K$). From the active region point of view, the κT limit for the THz QCLs maximum operating temperature have been already surpassed. The new lasing schemes that eliminates the injection and extraction tunneling processes

for the populating and depopulating the lasing states improves the modified Lorentzian gain peak and is necessary to achieve sufficient gain at higher temperatures. The electron transition from lower to upper lasing states, due to phonon absorption, becomes also considerable at higher temperatures and reduces the population inversion. It is important to design a new structure that eliminated this backfilling process. Another limiting factor for high temperature operation of THz QCLs is the high electronic temperature, compared to the lattice temperature. Designing a structure with higher possibility phonon emission will possibly solve this issue. In the same time, the waveguide loss for MM structure at THz region must be further reduced. Using the Copper as the metal contact has demonstrated slight improvement on the maximum operating temperature. The heat dissipation, although it is not as detrimental in pulse mode, has to be also improved for higher temperature operation of the THz QCLs in the CW mode. The direct flip chip bonding of the lasing ridge on a very good thermal conductor (e.g. diamond) is, for instance, one approach to close the gap between maximum operating temperature of the device in CW and pulse modes.

The bi-modal operation of the SI-SP THz QCL showed that the electrical switching of the lateral mode results in electrical switching of the emission direction. The divergence of the beam switching can be further improved by increasing the spacing between two lobes of the TM_{01} mode. This can be achieved by introducing a gap in the middle of the top metal. Instead, it is possible to use techniques such as proximity effect of metallic or dielectric plungers, where the lateral mode becomes compressed or widened, respectively.

Appendix A

Equation for no laser coherences

Expansion of 16×16 system of linear equations in equation 2.52:

$$
\begin{pmatrix}
\jmath\Omega_{12} & 0 & 0 & 0 & -\jmath\Omega_{24} & 0 & 0 & 0 & 0 & 0 & 0 \\
-\Omega_{12} & 0 & -\Omega_{13} & 0 & \Omega_{24} & 0 & \Omega_{34} & 0 & 0 & 0 & 0 \\
0 & 0 & 0 & 0 & \jmath\Omega_{24} & 0 & \jmath\Omega_{34} & 0 & \jmath\Omega_{14} & 0 & 0 \\
0 & 0 & 0 & 0 & 0 & 0 & 0 & 0 & 0 & 0 & 0 \\
\jmath/\tau_{\parallel 12} & \Delta_{12} & 0 & 0 & 0 & \Omega_{14} & 0 & 0 & 0 & -\Omega_{24} & 0 \\
\Delta_{12} & \jmath/\tau_{\parallel 12} & 0 & 0 & -\Omega_{14} & 0 & 0 & 0 & -\Omega_{24} & 0 & -\Omega_{13} \\
0 & 0 & \jmath/\tau_{\parallel 13} & \Delta_{13} & 0 & 0 & 0 & \Omega_{14} & 0 & -\Omega_{34} & 0 \\
0 & 0 & \Delta_{13} & \jmath/\tau_{\parallel 13} & 0 & 0 & -\Omega_{14} & 0 & -\Omega_{34} & 0 & \Omega_{12} \\
0 & -\Omega_{14} & 0 & 0 & \jmath/\tau_{\parallel 24} & \Delta_{24} & 0 & 0 & 0 & \Omega_{12} & 0 \\
\Omega_{14} & 0 & 0 & 0 & \Delta_{24} & \jmath/\tau_{\parallel 24} & 0 & 0 & \Omega_{12} & 0 & -\Omega_{34} \\
0 & 0 & 0 & -\Omega_{14} & 0 & 0 & \jmath/\tau_{\parallel 34} & \Delta_{34} & 0 & \Omega_{13} & 0 \\
0 & 0 & \Omega_{14} & 0 & 0 & 0 & \Delta_{34} & \jmath/\tau_{\parallel 34} & \Omega_{13} & 0 & \Omega_{24} \\
0 & -\Omega_{24} & 0 & -\Omega_{34} & 0 & \Omega_{12} & 0 & \Omega_{13} & \jmath/\tau_{\parallel 14} & \Delta_{14} & 0 \\
-\Omega_{24} & 0 & -\Omega_{34} & 0 & \Omega_{12} & 0 & \Omega_{13} & 0 & \Delta_{14} & \jmath/\tau_{\parallel 14} & 0 \\
0 & -\Omega_{13} & 0 & \Omega_{12} & 0 & -\Omega_{34} & 0 & \Omega_{24} & 0 & 0 & \jmath/\tau_{\parallel 23} \\
\Omega_{13} & 0 & \Omega_{12} & 0 & -\Omega_{34} & 0 & -\Omega_{24} & 0 & 0 & 0 & \Delta_{23}
\end{pmatrix}
\cdots
$$

$$
\cdots
\begin{pmatrix}
0 & 0 & -(\tau_{\text{sti}}^{-1}+\tau_2^{-1}) & \tau_{\text{sti}}^{-1}+\tau_3^{-1} & 0 \\
0 & 0 & 0 & 0 & 0 \\
0 & \tau_1^{-1} & 0 & 0 & -\tau_4^{-1} \\
0 & 1 & 1 & 1 & 1 \\
\Omega_{13} & -2\Omega_{12} & 2\Omega_{12} & 0 & 0 \\
0 & 0 & 0 & 0 & 0 \\
\Omega_{12} & -2\Omega_{13} & 0 & 2\Omega_{13} & 0 \\
0 & 0 & 0 & 0 & 0 \\
-\Omega_{34} & 0 & -2\Omega_{24} & 0 & 2\Omega_{24} \\
0 & 0 & 0 & 0 & 0 \\
-\Omega_{24} & 0 & 0 & -2\Omega_{34} & 2\Omega_{34} \\
0 & 0 & 0 & 0 & 0 \\
0 & -2\Omega_{14} & 0 & 0 & 2\Omega_{14} \\
0 & 0 & 0 & 0 & 0 \\
\Delta_{23} & 0 & 0 & 0 & 0 \\
\jmath/\tau_{\|23} & 0 & 0 & 0 & 0
\end{pmatrix}
\times
\begin{pmatrix}
\rho_{21}-\rho_{12} \\
\rho_{21}+\rho_{12} \\
\rho_{31}-\rho_{13} \\
\rho_{31}+\rho_{13} \\
\rho_{42}-\rho_{24} \\
\rho_{42}+\rho_{24} \\
\rho_{43}-\rho_{34} \\
\rho_{43}+\rho_{34} \\
\rho_{41}-\rho_{14} \\
\rho_{41}+\rho_{14} \\
\rho_{32}-\rho_{23} \\
\rho_{32}+\rho_{23} \\
\rho_{11} \\
\rho_{22} \\
\rho_{33} \\
\rho_{44}
\end{pmatrix}
=
\begin{pmatrix}
0 \\ 0 \\ 0 \\ 1 \\ 0 \\ 0 \\ 0 \\ 0 \\ 0 \\ 0 \\ 0 \\ 0 \\ 0 \\ 0 \\ 0 \\ 0
\end{pmatrix}
\tag{A.1}
$$

Solution of this matrix provides the population inversion for all four energy states (ρ_{ii}), as well as the coherence terms between all twelve possible energy levels ($\rho_{ij} = \rho_{ji}^*$). By neglecting the cross terms, it becomes possible to find analytical solutions for above sixteen parameters. However for the numerical accuracy, the graphs in this thesis were calculated using numerical solution of the full matrix. MATLAB was used for the numerical calculations.

Appendix B

Measurement setup

B.1 LIV measurement

After mounting QCL bars on the package, the devices are placed in a closed cycle liquid Helium cooled cryostat for various measurements. The laser radiation passes through a polyethylene window, which is around 70% transparent in THz frequencies, and is detected by a far-infrared detector. It is worthy to mention that the detector is placed in the vicinity of the cryostat window to minimize possible attenuation of the THz beam due to strong absorption of moisture in the air, unless otherwise stated. To further reduce this loss, the space between the cryostat and the detector is purged with dry nitrogen. Either a liquid-He cooled Silicon bolometer (IR Lab Inc, Model HDL-5) or a Golay cell can be used for detecting THz signals. The Silicon bolometer has much higher sensitivity in THz frequency domain; it is used for most of the measurements. The THz signal, after passing through a polyethylene window of the bolometer, is collected by a Winston cone that is placed inside the bolometer dewar and the beam is guided onto the silicon detector part. The pyroelectric detector is sometimes used in measurements such as far-field beam patterns because it works at room temperature and it is much easier to operate.

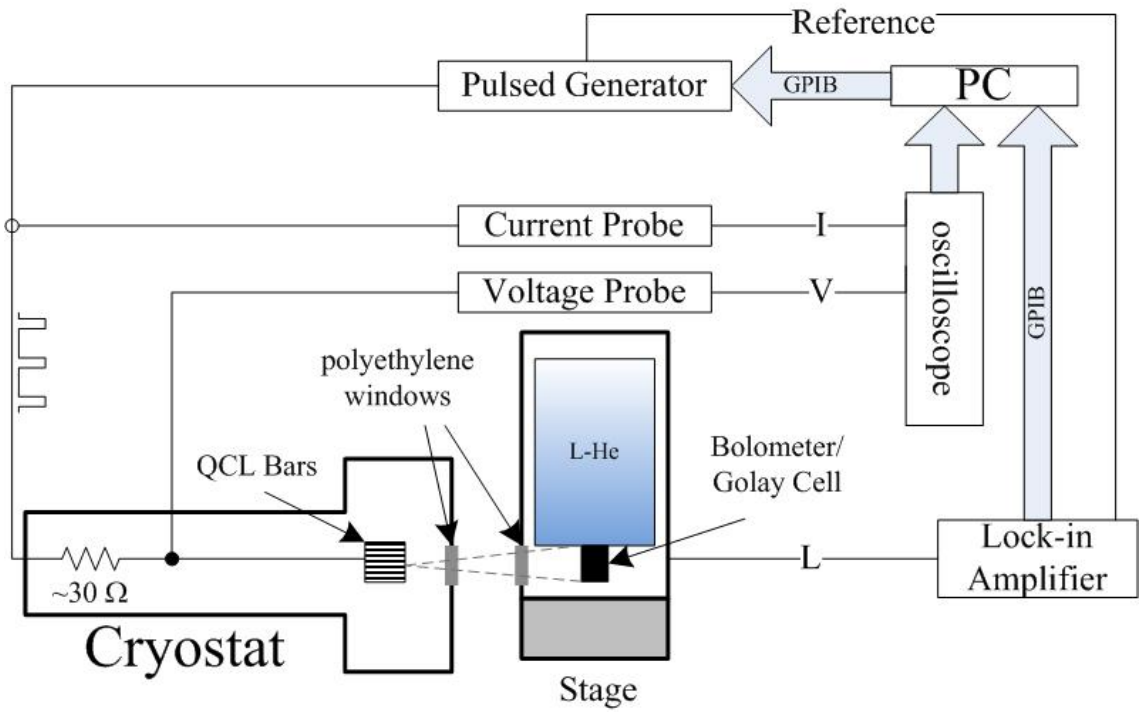

Figure B.1: Schematic diagram of characterization setup for QCL LIV measurements.

The required threshold input power (electric bias) of QCLs is provided from an AVTECH (AVO-6C-B) pulse generator. For pulsed mode operation, pulses with a 1 KHz frequency and a 200 ns pulse width are used, incase bolometer is being used. For Golay cell pulses with 25 Hz frequency and a 200 ns pulse width are used. Higher frequency operation is limited by the response time of the detectors, which is in range of milliseconds for bolometer and seconds for Golay cell. The duty cycle is basically set neither too low that falls below time response of the silicon bolometer nor too high that causes heating of laser active region. The cables inside the cryostat were replaced with 35 Ω lines and a T-matching circuit is designed to match it with pulse generator's 50 Ω. A series resistance is always put with in series with the laser to match its impedance to 35 Ω. Externally applied electric bias is simultaneously measured by a current probe and a voltage probe. The voltage reading

is across the laser in the cold region. Pulsed voltage and current signals are measured using a Tektronix oscilloscope (TDS2024A), averaged for > 100 periods in the flat pulse region. Measured light signal coming from the Si bolometer is collected through a lock-in amplifier. All data are acquired using a LabVIEW program. The responsivity of the Si bolometer is calibrated to be 9 kV/W multiplied by 200/1000 gain and the polyethylene window transparencies. A far-infrared filter with a cut-off wavelength of 40 μm is also used to suppress the noise. Light-current-voltage (LIV) curves of devices operating in pulsed mode at different temperatures are obtained by sweeping the voltage of pulse generator and reading the current and light intensity at each given temperature.

The Si bolometer is designed to operate in pulse mode, and hence for CW measurements the optical signal has to be chopped. However the blackbody radiation of a mechanical chopper at room temperature is calculated from Wiens's displacement law as

$$\lambda_{max} = \frac{2898\ \mu m \cdot K}{T(300\ K)} = 9.66\ \mu m. \tag{B.1}$$

This is in the detection range of the Si bolometer and would introduce background noise in measuring QCL signal. An upgraded setup is employed to measured DC optical signals. A DC power supply, HP E3622A, is used to replace the pulse generator to supply DC electric current to the device under test. The measured optical signal is directly collected from the preamplifier output of the Si bolometer, instead of from an AC coupled amplifier. Using a voltmeter with GPIB interface, the Si bolometer preamp output, which corresponds to light intensity, is acquired using a LabVIEW program. In order to have very stable bias on the detector, an external power supply is used. This eliminates any voltage drift resulted from the aging of a built-in 16 V battery.

B.2 Golay cell calibration

A black body system was used to calibrate the Golay cell. The user manual of the Golay cell claims that this detector has quite flat responsivity curve. Therefore, it is assumed that all the black body radiation is uniformly absorbed by the detector. By assuming the environment of much cooler than the black body, the power of a black body system with a given aperture size ($A_{aperture}$) and temperature (T) is give by StefanBoltzmann law as

$$P_{emit} \approx A_{aperture} \frac{2\pi^5 k_B^4}{15h^3c^2} T^4, \tag{B.2}$$

where K_B is the Boltzmann constant, h is the Planck's constant, and c is speed of light. By placing the Golay cell at a given distance d from the black body system, the collected power can be calculated by integrating the power over the small opening of the detector. For the calibration process the black body system was set to $T = 997.89\ K$ and the aperture size set to 0.025 inches.

The Golay cell is working based on heating and hence pressurizing a Xenon gas inside a metal cylinder with a diaphragm, by incoming infrared radiation. Therefore, it has very slow response time, in range of seconds. In order to get reasonable responsivity from this detector, the incoming radiation should be modulated below 100 Hz. It was found that $\sim 25\ Hz$ the responsivity is rather high. To avoid excessive heating of the THz QCLs under test, they are usually biased at very low duty cycles. Figure B.2 shows the calibrated responsivity of the Golay cell with 25 Hz modulation frequency versus various duty cycles. The responsivity defines as as the ratio of measured voltage at lock-in amplifier to the received power by the detector. Below 25% duty cycle, the responsivity drops linearly with the duty cycle. Therefore, the measured curve is extrapolated to zero to estimate the responsivity at the given duty cycle.

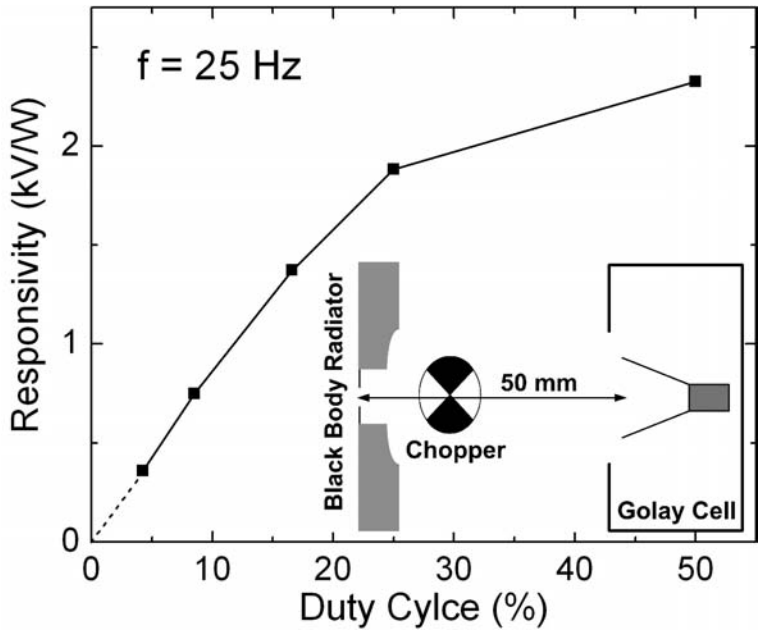

Figure B.2: Calibrated responsivity of Golay cell, collected from lock-in amplifier, with 25 Hz modulation frequency versus various duty cycles., the inset shows the schematic diagram of the calibration setup.

B.3 Spectrum measurement

Figure B.3 shows schematic diagram of a setup for measuring emission spectra of QCL devices. The emission beam is coupled into a DA8 BOMEM Fourier transform infrared spectrometer (FTIR) system using two parabolic reflectors. The operating principle of the FTIR system is based on a "Michelson interferometer". The spectrometer's computer reads the output of the Si bolometer at each position of the translating mirror and converts the data to spectrum through a Fourier transform. Time-constant of the low pass filter in the lock-in amplifier should be few times smaller than the period of the fringes, the frequency of which is

$$f_{fringe} = 2\alpha v, \tag{B.3}$$

where α is QCL beam frequency in $cm^{-1}$and v is translating mirror's speed in cm/s. For instance, for 3 THz QCL (100 cm^{-1}) and V of 0.1 cm/s, the frequency of output FTIR signal is calculated to be 20 Hz from equation B.3. This means that any time-constant smaller than 30 ms will pass the signal. However, a smaller time-constant also passes noise over a larger frequency band, which could sometimes exceed the real signal.

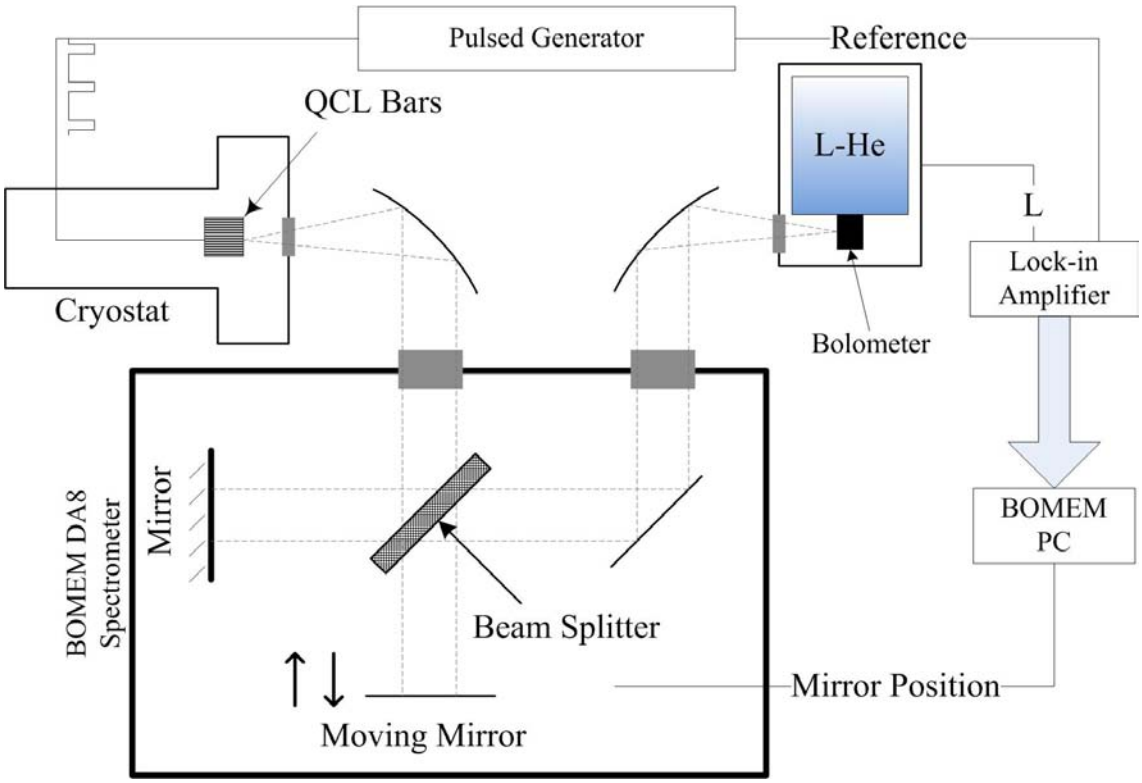

Figure B.3: Schematic diagram of characterization setup for QCL emission spectra measurements.

Appendix C

Trans-impedance amplifier circuit

Figure C.1 shows the schematic diagram of the designed trans-impedance amplifier, for the photo current amplification. The QWP bias is adjusted using the potentiometer (VR1) that changes the offset of the amplifier.

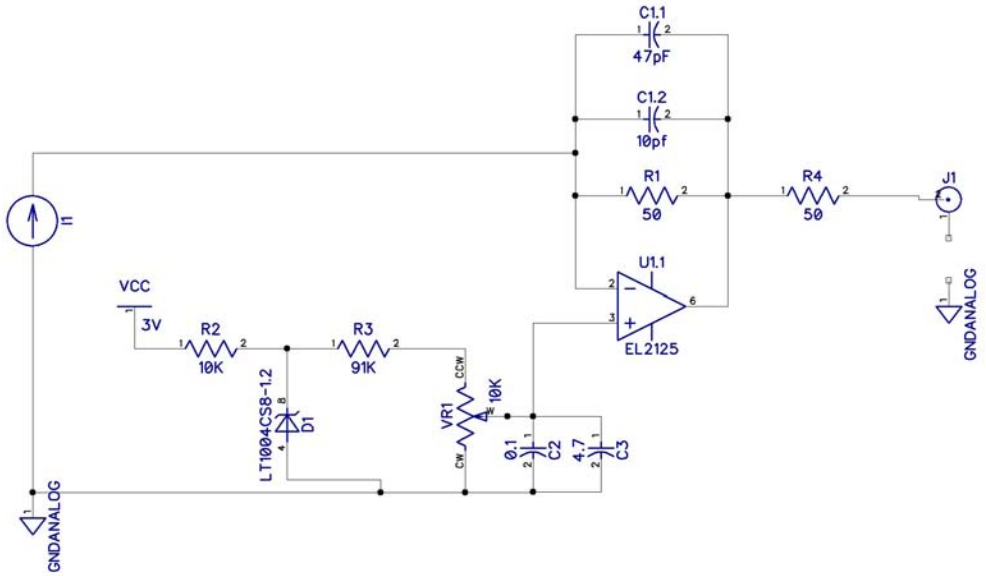

Figure C.1: Schematic of the designed trans-impedance amplifier

The output of the amplifier is opted for 50 Ω lines. The output pulses as small as 30 ns can be amplified and by this amplifier. Figure C.2shows the layout of the amplifier board.

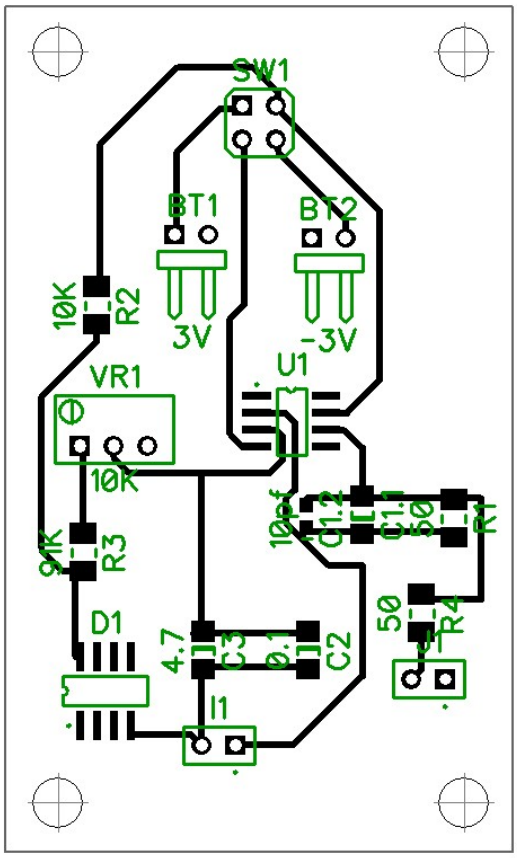

Figure C.2: Layout of the designed trans-impedance amplifier

References

[1] B. S. Williams. Terahertz quantum-cascade lasers. *Nat. Photon.*, 1:517–525, 2007. 1, 16, 17, 18, 23

[2] M. Tonouchi. Cutting-edge terahertz technology. *Nat. Photon.*, 1:97–105, 2007. 1, 4, 6, 7, 8, 139

[3] P. H. Seigel. Terahertz technology. *IEEE Trans. Microwave Theory Tech.*, 50:910–928, 2002. 1, 4, 9, 157

[4] S. Kumar. *Development of Terahertz Quantum-Cascade Lasers.* PhD thesis, Massachusetts Institute of Technology, 2007. 2, 44, 67, 162

[5] R. Kohler, A. Tredicucci, F. Beltram, H. E. Beere, E. H. Linfield, A. G. Davies, D. Ritchie, R. C. Iotti, and F. Rossi. Terahertz semiconductor-heterostructure laser. *Nature*, 417:156–159, 2002. 1, 11, 15, 83

[6] J. C. Wiltse. History of millimeter and submillimeter waves. *IEEE Trans. Microwave Theory Tech.*, 32:1118–1127, 1984. 2

[7] J. W. Fleming. High-resolution submillimete - wave fourier - transform spectrometry of gases. *IEEE Trans. Microwave Theory Tech.*, 22:1023–1025, 1974. 2

[8] A.M. Baryshev, P. Khosropanah, W. Zhang, W. Jellema, J.N. Hovenier, J.R. Gao, T.M. Klapwijk, D.G. Paveliev, B.S. William, S. Kumar, Q. Hu, J.L. Reno, B. Klein,

and J.L. Hesler. Phase-locking of a 2.7-thz quantum cascade laser to a microwave reference. In *20th International Symposium on Space Terahertz Technology,*, 2009. 3

[9] T. G. Phillips and J. Keene. Submillimeter astronomy [heterodyne spectroscopy]. *Proceedings of the IEEE*, 80:1662–1678, 1992. 3

[10] P. H. Seigel. Thz instruments for space. *IEEE Trans. Antenn. and Propag.*, 55:2957–2965, 2007. 4, 6

[11] J. Luhmann and W. A. Peebles. Instrumentation for magnetically confined fusion plasma diagnostics. *Rev. Sci. Instrum.*, 55:279–331, 1984. 4

[12] H. Liu, H. Zhong, N. Karpowicz, Y. Chen, and X. Zhang. Terahertz spectroscopy and imaging for defense and security applications. *Proceedings of the IEEE*, 95:1514–1527, 2007. 5, 6

[13] J. Deibel W. L. Chan and D. M. Mittleman. Imaging with terahertz radiation. *Rep. Prog. Phys.*, 70:1325–1379, 2007. 5, 6

[14] B. B. Hu and M. C. Nuss. Imaging with terahertz waves. *Opt. Lett.*, 20:1716–1718, 1995. 4

[15] K. J. Siebert, H. Quast, R. Leonhardt, T. Loffler, M. Thomson, T. Bauer, H. G. Roskos, and S. Czasch. Continuous-wave all-optoelectronic terahertz imaging. *Appl. Phys. Lett.*, 80:3003–3005, 2002. 6

[16] S. M. Kim, F. Hatami, J. S. Harris, A. W. Kurian, J. Ford, D. King, G. Scalari, M. Giovannini, N. Hoyler, J. Faist, and G. Harris. Biomedical terahertz imaging with a quantum cascade laser. *Appl. Phys. Lett.*, 88:153903, 2006. 6

[17] K. L. Nguyen, M. L. Johns, L. F. Gladden, C. H. Worrall, P. Alexander, H. E. Beere, M. Pepper, D. A. Ritchie, J. Alton, S. Barbieri, and E. H. Linfield. Three-dimensional

imaging with a terahertz quantum cascade laser. *Optics Express*, 14:2123–2129, 2006. 6

[18] V. P. Wallace, E. MacPherson, J. A. Zeitler, and C. Reid. Three-dimensional imaging of optically opaque materials using nonionizing terahertz radiation. *J. Opt. Soc. Am. A*, 25:3120–3133, 2008. 6

[19] A. W. M. Lee, B. S. Williams, S. Kumar, Q. Hu, and J. L. Reno. Real-time imaging using a 4.3-thz quantum cascade laser and a 320 × 240 microbolometer focal-plane array. *IEEE Phot. Technol. Lett.*, 18:1415–1417, 2006. 6

[20] A. W. M. Lee, Q. Qin, S. Kumar, B. S. Williams, Q. Hu, and J. Reno. Real-time terahertz imaging over a standoff distance (> 25 meters). *Appl. Phys. Lett.*, 89:141125, 2006. 6

[21] B. S. Williams, S. Kumar, Q. Hu, and J.L. Reno. High-power terahertz quantum-cascade lasers. *Electron. Lett.*, 42:89–90, 2006. 6, 18

[22] M. Helm. *Intersubband Transitions in Quantum Wells:Physics and DeviceApplications I*, volume 62, chapter Physics of optoelectronic devices. Academic Press, New York, 2000. 7, 12, 18, 31, 109

[23] S. Barbieri, W. Maineult, S. S. Dhillon, C. Sirtori, J. Alton, N. Breui, H. E. Beere, and D. A. Ritchie. 13 ghz direct modulation of terahertz quantum cascade lasers. *Appl. Phys. Lett.*, 91:143510, 2007. 7

[24] P. D. Grant, S. R. Laframboise, R. Dudek, M. Graf, A. Bezinger, and H. C. Liu. Terahertz free space communications demonstration with quantum cascade laser and quantum well photodetector. *Elect. Lett.*, 45:652–653, 2009. 7

[25] A. A. Danylov, T. M. Goyette, J. Waldman, M. J. Coulombe, A. J. Gatesman, R. H. Giles, W. D. Goodhue, X. Qian, and W. E. Nixon. Frequency stabilization of a

single mode terahertz quantum cascade laser to the kilohertz level. *Optics Express*, 17:7525–7532, 2009. 7

[26] J. Federici and L. Moelle. Review of terahertz and subterahertz wireless communications. *J. Appl. Phys.*, 107, 2010. 7

[27] H. Preier. Physics and applications of iv-vi compound semiconductor lasers. *Semi. Sci and Technol.*, 5:s12–s20, 1990. 8

[28] D. Saeedkia and S. Safavi-Naeini R. R. Mansour. Modeling and analysis of high temperature superconductor terahertz photomixers. *IEEE Trans. Appl. Superconduct.*, 15:1–9, 2005. 9

[29] E. K. Duerr. *Distributed photomixers*. PhD thesis, Massachusetts Institute of Technology, Department of Electrical Engineering and Computer Science. 9

[30] D. Saeedkia and S. Safavi-Naeini R. R. Mansour. Analysis and design of a continuous-wave terahertz photoconductive photomixer array source. *IEEE Trans. Anten. and Propag.*, 53:4044–4050, 2005. 9

[31] W. Shi, Y. J. Ding, N. Fernelius, and K. Vodopyanov. Efficient, tunable, and coherent 0.18-5.27-thz source based on gase crystal. *Opt. Lett.*, 27:1454–1456, 2002. 9

[32] E. Dupont, Z. R. Wasilewski, and H. C. Liu. Terahertz emission in asymmetric quantum wells by frequency mixing of midinfrared waves. *IEEE J. Quantum Electron.*, 42:1157–1174, 2006. 9

[33] M. A. Belkin, F. Capasso, A. Belyanin, D. L. Sivco, A. Y. Cho, D. C. Oakley, C. J. Vineis, and G. W. Turner. Terahertz quantum-cascade-laser source based on intracavity difference-frequency generation. *Nat. Photon.*, 1:288, 2007. 9

[34] K. Kawase, J. Shikata, and H. Ito. Terahertz wave parametric source. *J. Phys. D: Appl. Phys.*, 34:R1–R14, 2001. 9

[35] K. Kawase, Y. Ogawa, H. Minamide, and H. Ito. Terahertz parametric sources and imaging applications. *Semicond. Sci. Technol.*, 20:S258–S265, 2005. 9, 10

[36] D. J. M. Stothard, T. J. Edwards, D. Walsh, C. L. Thomson, C. F. Rae, M. H. Dunn, and P. G. Browne. Line-narrowed, compact, and coherent source of widely tunable terahertz radiation. *Appl. Phys. Lett.*, 92:141105, 2008. 9

[37] M. Inguscio, G. Moruzzi, K. M. Evenson, and D. A. Jennings. A review of frequency measurements of optically pumped lasers from 0.1 to 8 thz. *J. Appl. Phys.*, 60:R161–R192, 1986. 10

[38] A. Andronov. Hot electrons in semiconductors and submillimeter waves. *Sov. Phys. Semicond.*, 21:701–721, 1987. 10

[39] E. Brundermann, D.R. Chamberlin, and E.E. Haller. High duty cycle and continuous emission from germanium. *Appl. Phys. Lett.*, 76:2991–2993, 2000. 10

[40] I. V. Altukhov, E. G. Chirkova, M. S. Kagan, K. A. Korolev, V. P. Sinis, and F. A. Smirnov. Hot-hole far-ir emission from uniaxially compressed germanium. *Sov. Phys. JETP*, 74:404, 1992. 10

[41] M. S. Kagan, I. Altukhov, V. P. Sinis, S. G. Thomas, K. L. Wang, K. A. Chao, and I. N. Yassievich. Terahertz emission of sige/si quantum wells. *Thin Solid Films*, 380:237, 2000. 11

[42] J. Faist, M. Beck, T. Aellen, and E. Gini. Quantum-cascade lasers based on a bound-to-continuum transition. *Appl. Phys. Lett.*, 78:147–149, 2001. 11

[43] B. S. Williams, H. Callebaut, S. Kumar, Q. Hu, and J. L. Reno. 3.4-thz quantum cascade laser based on longitudinal-optical-phonon scattering for depopulation. *Appl. Phys. Lett.*, 82:1015–1017, 2003. 11, 16, 83

[44] S. L. Chuang. *Physics of optoelectronic devices*. John Wiley, New York, 1995. 11, 26, 31, 69, 83, 92, 146, 149

[45] R. F. Kazarinov and R. A. Suris. Possibility of the amplification of electromagnetic waves in a semiconductor with a superlattice. *Sov. Phys. Semicon.*, 5:707–709, 1971. 11, 13, 24, 50

[46] M. Helm, E. Colas, P. England, F. Derosa, and S. J. Allen. Observation of grating-induced intersubband emission from gaas/algaas superlattice. *Appl. Phys. Lett.*, 53:1714–1716, 1988. 12

[47] M. Helm, E. Colas, P. England, F. Derosa, and S. J. Allen. Intersubband emission from semiconductor superlattices excited by sequential resonant tunneling. *Appl. Phys. Lett.*, 63:74–77, 1989. 12

[48] B. S. Williams. *Terahertz Quantum Cascade Lasers*. PhD thesis, Massachusetts Institute of Technology, Department of Electrical Engineering and Computer Science. 13, 38, 104

[49] J. Faist, F. Capasso, D. L. Sivco, C. Sirtori, A. L. Hutchinson, and A. Y. Cho. Quantum cascade laser. *Science*, 264:553–556, 1994. 13, 14

[50] J. H. Smet. *Intrawell and interwell intersubband transitions in single and multiple quantum well heterostructures*. PhD thesis, Massachusetts Institute of Technology, Department of Electrical Engineering and Computer Science. 13

[51] O. Cathabard, R. Teissier, J. Devenson, J. C. Moreno, and A. N. Baranova. Quantum cascade lasers emitting near 2.6 μm. *Appl. Phys. Lett.*, 96:141110, 2010. 14

[52] J. Faist, F. Capasso, D. L. Sivco, A. L. Hutchinson, S. N. G. Chu, and A. Y. Cho. Short wavelength ($\lambda \sim 3.4\mu m$) quantum cascade laser based on strained compensated InGaAs / AlInAs. *Appl. Phys. Lett.*, 72:680–682, 1998. 14

[53] R. Colombelli, F. Capasso, C. Gmachl, A. L. Hutchinson, D. L. Sivco, A. Tredicucci, M. C. Wanke, A. M. Sergent, and A. Y. Cho. Far-infrared surface - plasmon quantum-cascade lasers at 21.5 μm and 24 μm wavelengths. *Appl. Phys. Lett.*, 78:2620–262, 2001. 14

[54] M. Beck, D. Hofstetter, T. Aellen, J. Faist, U. Oesterle, M. Ilegems, E. Gini, and H. Melchior. Continuous wave operation of a mid-infrared semiconductor laser at room termerature. *Science*, 295:301, 2002. 15

[55] C. Gmachl, A. Straub, R. Colombelli, F. Capasso, D. L. Sivco, A. M. Sergent, and A. Y. Cho. Single-mode, tunable distributed-feedback and multiple wavelength quantum cascade lasers. *IEEE J. Quantum Electron.*, 38:569–581, 2002. 15

[56] Y. Bai, S. Slivken, S. Kuboya, S. R. Darvish, and M. Razeghi. Quantum cascade lasers that emit more light than heat. *Nat. Phot.*, 4:99–102, 2010. 15

[57] C. Sirtori, H. Page, C. Becker, and V. Ortiz. GaAs-AlGaAs quantum cascade lasers: physics, technology and prospects. *IEEE J. Quantum Electron.*, 38:547, 2002. 15

[58] L. Diehl, S. Mentese, E. Muller, D. Grutzmacher, H. Sigg, U. Gennser, I. Sagnes, Y. Campidelli, O. Kermarrec, and D. Bensahel. Electroluminescence from strain compensated $Si_{0.2}Ge_{0.8}/Si$ quantum cascade structures based on a bound- to-continuum transition. *Appl. Phys. Lett.*, 81:4700, 2002. 15

[59] J. D. Heber, C. Gmachl, H. M. Ng, and A. Y. Cho. Comparative study of ultrafast intersubband electron scattering times at $\sim$ 1.55 μm wavelength in $GaN/AlGaN$ heterostructures. *Appl. Phys. Lett.*, 81:1237, 2002. 15

[60] C. Walther nad M. Fischer, G. Scalari, R. Terazzi, N. Hoyler, and J. Faist. Quantum cascade lasers operating from 1.2 to 1.6 thz. *Appl. Phys. Lett.*, 91:131122, 2007. 15, 16

[61] S. Kumar, Q. Hu, and J. L. Reno. 186 k operation of terahertz quantum cascade lasers based on a diagonal design. *Appl. Phys. Lett.*, 94:131105, 2009. 15, 18, 19, 23, 43, 56, 65, 66, 81, 139, 161, 166, 195

[62] B. S. Williams, S. Kumar, Q. Hu, and J. L. Reno. Operation of terahertz quantum-cascade lasers at 164 k in pulsed mode and at 117 k in continuous-wave mode. *Optics Express*, 13:3331–3339, 2005. 15, 18, 102, 104, 105, 112

[63] G. Scalari, L. Ajili, J. Faist, H. Beere, E. Linfield, D. Ritchie, and G. Davies. Far-infrared ($\lambda \simeq 87\mu m$) bound-to-continuum quantum-cascade lasers operating up to 90 k. *Appl. Phys. Lett.*, 82:3165–3167, 2003. 16

[64] B. S. Williams, S. Kumar, Q. Qin, Q. Hu, and J. L. Reno. Terahertz quantum cascade lasers with double-resonant-phonon depopulation. *Appl. Phys. Lett.*, 88, 2006. 19

[65] H. Luo, S. R. Laframboise, Z. R. Wasilewski, and H. C. Liu. Terahertz quantum cascade lasers based on a three-well active module. *Appl. Phys. Lett.*, 90:041112, 2007. 19, 24, 28, 29, 30, 42, 61, 82, 83, 91, 102, 166, 169

[66] E. Dupont, S. Fathololoumi, and H. C. Liu. Simplified density matrix model applied to three-well terahertz quantum cascade lsers. *Phys. Rev. B*, 81, 2010. 19, 22, 24, 29, 44, 47, 55, 58, 59, 61, 67, 68, 75, 96, 122, 125, 143, 151, 153, 161, 162, 163, 171, 176, 184, 195

[67] S. Kumar and Q. Hu. Coherence of resonant-tunneling transport in terahertz quantum-cascade lasers. *Phys. Rev. B*, 80:245316, 2009. 19, 44, 59, 62, 66, 77, 79

[68] M. A. Belkin, J. A. Fan, S. Hormoz, F. Capasso, S. P. Khanna, M. Lachab, A. G. Davies, , and E. H. Linfield. Terahertz quantum cascade lasers with copper metal-metal waveguides operating up to 178 K. *Opt. Exp.*, 16:3242–3248, 2008. 19, 56, 97, 99, 171, 180

[69] S. Kumar, C. Wang, I. Chan, Q. Hu, and J. L. Reno. Two-well terahertz quantum-cascade laser with direct intrawell-phonon depopulation. *Appl. Phys. Lett.*, 95:141110, 2009. 19, 44, 81

[70] G. Scalari, M. I. Amanti, C. Walther, R. Terazzi, and J. Faist M. Beck and. Broadband thz lasing from a photon-phonon quantum cascade structure. *Opt. Exp.*, 18:8043–8052, 2010. 19

[71] A. Wacker. Quantum kinetics of trasnport and gain in quantum cascade lasers: looking for the essential principles of design. In *CLEO / QELS 2010*, 2010. 20

[72] S. Kumar, C. W. I. Chan, Q. Hu, and J. L. Reno. Operation of a 1.8 thz quantum cascade laser above 160 k. In *CLEO / QELS 2010*, 2010. 20, 23, 187

[73] P. Harrison. *Quantum wells, wires and dots.* John Wiley, Chichester, 2005. 24, 38

[74] R. F. Kazarinov and R. A. Suris. Electric and electromagnetic properties of semiconductors with superlattice. *Sov. Phys. Semicon.*, 6:120–131, 1972. 24, 50, 51

[75] G. Bastard. *wave mechanics applied to semiconductor heterostructures.* Jouve, Paris, 1988. 25, 27, 29

[76] J. Shah. *Hot carriers in semiconductor nanostructures*, chapter Ultrafast luminescence studies of carrier relaxation and tunneling in semiconductor nanostructures. Academic Press, San Diego, 1992. 38

[77] M. S. Vitiello, V. Spagnolo G. Scamarcio, B. S. Williams, S. Kumar, Q. Hu, and J. L. Reno. Measurement of subband electronic temperatures and population inversion in THz quantum-cascade lasers. *Appl. Phys. Lett.*, 86:111115, 2005. 38, 45, 46, 163

[78] D. Indjin, P. Harrison, R. W. Kelsall, and Z. Ikonić. Mechanisms of temperature performance degradation in terahertz quantum-cascade lasers. *Appl. Phys. Lett.*, 82:1347–49, 2003. 43

[79] H. Callebaut, S. Kumar, B. S. Williams, Q. Hu, and J. L. Reno. Analysis of transport properties of tetrahertz quantum cascade lasers. *Appl. Phys. Lett*, 83:207–209, 2003. 43

[80] H. Callebaut, S. Kumar, B. S. Williams, Q. Hu, and J. L. Reno. Importance of electron-impurity scattering for electron transport in terahertz quantum-cascade lasers. *Appl. Phys. Lett*, 84:645–647, 2004. 43

[81] C. Jirauschek, G. Scarpa, P. Lugli, M. S. Vitiello, and G. Scamarcio. Comparative analysis of resonant phonon THz quantum cascade lasers. *J. Appl. Phys.*, 101:086109, 2007. 43

[82] C. Jirauschek and P. Lugli. Limiting factors for high temperature operation of THz quantum cascade lasers. *Phys. Stat. Sol. (c)*, 5:221–224, 2008. 43

[83] H. Callebaut and Q. Hu. Importance of coherence for electron transport in terahertz quantum cascade lasers. *J. Appl. Phys.*, 84:104505, 2004. 43, 48

[84] S. C. Lee and A. Wacker. Nonequilibrium greens function theory for transport and gain properties of quantum cascade structures. *Phys. Rev. B*, 66:245314, 2002. 43

[85] S. C. Lee, F. Banit, M. Woerner, and A. Wacker. Quantum mechanical wavepacket transport in quantum cascade laser structures. *Phys. Rev. B*, 73:245320, 2006. 43

[86] A. Wacker. Coherence and spatial resolution of transport in quantum cascade lasers. *Phys. Stat. Sol. (c)*, 5:215220, 2008. 43, 44

[87] T. Kubis, C. Yeh, P. Vogl, A. Benz, G. Fasching, and C. Deutsch. Theory of nonequilibrium quantum transport and energy dissipation in terahertz quantum cascade lasers. *Phys. Rev. B*, 79:195323, 2009. 43, 44

[88] T. Schmielau and M. F. Pereira. Nonequilibrium manu body theory for quantum transport in terahertz quantum cascade lasers. *Appl. Phys. Lett.*, 95:231111, 2009. 43, 44

[89] R. C. Iotti and F. Rossi. Nature of charge transport in quantum-cascade lasers. *Phys. Rev. Lett.*, 87:146603, 2001. 43, 47

[90] I. Waldmueller, W. W. Chow, E. W. Young, and M. C. Wanke. Nonequilibrium many-body theory of intersubband lasers. *IEEE J. Quant. Electr.*, 42:292–301, 2006. 43, 47

[91] I. Savić, N. Vukmirović, Z. Ikonić, D. Indjin, R. W. Kelsall, P. Harrison, and V. Milanović. Density matrix theory of transport and gain in quantum cascade lasers in a magnetic field. *Phys. Rev. B*, 76:165310, 2007. 43, 47

[92] R. Terazzi, T. Gresch, A. Wittmann, and J. Faist. Sequential resonant tunneling in quantum cascade laser. *Phys. Rev. B*, 78:155328, 2008. 43, 44, 47

[93] G. Scalari, R. Terazzi, M. Giovannini, N. Hoyler, and J. Faist. Population inversion by resonant tunneling in quantum wells. *Appl. Phys. Lett.*, 91:032103, 2007. 44, 51, 96, 154

[94] T. Unuma, M. Yoshita, T. Noda, H. Sakaki, and H. Akimaya. Intersubband absorption linewidth in GaAs quantum wells due to scattering by interface roughness, phonons, alloy disorder, and impurities. *J. Appl. Phys.*, 93:1586–1596, 2003. 45

[95] R. Nelander and A. Wacker. Temperature dependence of the gain profile for terahertz quantum cascade lasers. *Appl. Phys. Lett.*, 92:081102, 2008. 45

[96] F. Banit, S.-C. Lee, A. Knorr, and A. Wacker. Self-consistent theory of the gain linewidth for quantum-cascade lasers. *Appl. Phys. Lett.*, 86:041108, 2005. 45

[97] A. Wacker, R. Nelander, and C. Weber. Simulation of gain in quantum cascade lasers. In A. A. Belyanin and P. M. Smowton, editors, *Novel In-Plane Semiconductor Lasers VIII*, volume 7230, page 72301A, Bellingham, WA, 2009. SPIE. 45

[98] Rikard Nelander and Andreas Wacker. Temperature dependence and screening models in quantum cascade structures. *J. Appl. Phys.*, 106:063115, 2009. 45

[99] P. Harrison, D. Indjin, and R. W. Kelsall. Electron temperature and mechanisms of hot carrier generation in quantum cascade lasers. *J. Appl. Phys.*, 92:6921, 2002. 45

[100] M. S. Vitiello, G. Scamarcio, V. Spagnolo, T. Losco, R. P. Green, A. Tredicucci, H. E. Beere, and D. A. Ritchie. Electron-lattice coupling in bound-to-continuum THz quantum-cascade lasers. *Appl. Phys. Lett.*, 88:241109, 2006. 45

[101] T. Ando. Line width of inter-subband absorption in inversion layers: scattering from charged ions. *J. Phys. Soc. of Japan*, 54:2671–2675, 1985. 49

[102] H. Luo, S. R. Laframboise, Z. R. Wasilewski, and H. C. Liu. Effects of injector barrier on performance of terahertz quantum-cascade lasers. *IEEE Electr. Lett.*, 43:633–635, 2007. 56, 161, 162, 163, 195

[103] S. Fathololoumi, E. Dupont, D. Ban, M. Graf, S. R. Laframboise, Z. R. Wasilewski, and H. C. Liu. Time resolved thermal quenching of THz quantum cascade lasers. *IEEE J. Quantum Electr.*, 46:396–404, 2010. 62, 122

[104] J. B. Khurgin, Y. Dikmelik, P. Q. Liu, A. J. Hoffman, M. D. Escarra, K. J. Franz, and C. F. Gmachl. Role of interface roughness in the transport and lasing characteristics of quantum-cascade lasers. *Appl. Phys. Lett.*, 94:091101, 2009. 72, 73, 75

[105] O. Kocharovskaya, P. Mandel, and Y. V. Radeonychev. Inversionless amplification in the three-level system. *Phys. Rev. A*, 45:1997–2005, 1992. 73

[106] M. Troccoli, A. Belyanin, F. Capasso, E. Cubukcu, D. L. Sivco, and A. Y. Cho. Raman injection laser. *Nature*, 433:845–848, 2005. 73

[107] G. Scalari, M. I. Amanti, R. Terazzi, M. Beck, and J. Faist. Broadband thz lasing from a photon-phonon quantum cascade structure. *Opt. Exp.*, 18:8043–8052, 2010. 77, 81

[108] H. Yasuda, T. Kubis, P. Vogl, N. Sekine, I. Hosako, , and K. Hirakawa. Nonequilibrium greens function calculation for four-level scheme terahertz quantum cascade lasers. *Appl. Phys. Lett.*, 94:151109, 2009. 81

[109] Q. Hu, B. S. Williams, S. Kumar, H. Callebaut, S. Kohen, and J. L. Reno. Resonant-phonon-assisted thz quantum-cascade lasers with metalmetal waveguides. *Semicond. Sci. Technol.*, 20:S228–S236, 2005. 83, 84

[110] S. Kohen, B. S. Williams, and Q. Hu. Electromagnetic modeling of terahertz quantum cascade laser waveguides and resonators. *J. Appl. Phys.*, 97, 2005. 91, 92, 93, 118, 120, 148

[111] P. Gellie, W. Maineult, A. Andronico, G. Leo, C. Sirtori, S. Barbieri, Y. Chassagneux, J. R. Coudevylle, R. Colombelli, S. P. Khanna, E. H. Linfield, and A. G. Davies. Effect of transverse mode structure on the far field pattern of metal-metal terahertz quantum cascade lasers. *J. Appl. Phys.*, 104, 2008. 92, 143

[112] H. C. Liu, M. Wachter, D. Ban, Z. R. Wasilewski, M. Buchanan, G. C. Aers, J. C. Cao, S. L. Feng, B. S. Williams, and Q. Hu. Effect of doping concentration on the performance of terahertz quantum-cascade lasers. *Appl. Phys. Lett.*, 87, 2005. 97, 102, 170

[113] D. Ban, M. Wachter, H. C. Liu, Z. R. Wasilewski, M. Buchanan, and G. C. Aers. Terahertz quantum cascade lasers: Fabrication, characterization, and doping effect. *J. Vac. Sci. Technol. A*, 24:778–782, 2006. 97, 170

[114] J. S. Blakemore. Semiconducting and other major properties of gallium arsenide. *J. Appl. Phys.*, 55:R123–R181, 1982. 99, 109, 133

[115] V.W.L. Chin, T. Osotchan, M.R. Vaughan, T.L. Tansley, G.J. Griffiyhs, and Z. Kachwalla. Hall and drift mobilities in molecular beam epitaxial grown gaas. *J. Elect. Mat.*, 22:1317–1321, 1993. 99

[116] M.A. Ordal, R.J. Bell, R.W. Alexander, L.L. Long, and M.R. Querry. Optical properties of fourteen metals in the infrared and far infrared: Al, co, cu, au, pb, mo, ni, pd, pt, ag, ti, v, and w. *Appl. Opt.*, 24:4493–4499, 1985. 99

[117] D. C. Hall, L. Goldberg, and D. Mehuys. Technique for lateral temperature profiling in optoelectronic devices using a photoluminescence microprobe. *Appl. Phys. Lett.*, 61:384–386, 1992. 106

[118] V. Spagnolo, M. Troccoli, G. Scamarcio, C. Becker, G. Glastre, and C. Sirtori. Thermal resistance and temperature characteristics of $gaas/al_{0.33}ga_{0.67}as$ quantum-cascade lasers. *Appl. Phys. Lett.*, 78:1177–1179, 2001. 106

[119] S. M. Sze. *Physics of semiconductor devices.* John Wiley, New York, 1981. 112

[120] M. S. Vitiello, G. Scamarcio, and V. Spagnolo. Temperature dependance of thermal conductivity and boundary resistance in thz quantum cascade lasers. *IEEE J. Sel. Topics Quantum Electron.*, 14:431–435, 2008. 112, 133, 136

[121] S. Fathololoumi, D. Ban, H. Luo, E. Dupont, S. R. Laframboise, A. Boucherif, and H. C. Liu. Thermal behavior investigation of terahertz quantum-cascade lasers. *IEEE J. Quantum Electr.*, 44:1139–1144, 2008. 122, 131

[122] C. Pflugl, W. Schrenk, S. Anders, and G. Strasser. Spectral dynamics of distributed feedback quantum cascade lasers. *Semicond. Sci. Technol.*, 19:S336–S338, 2004. 122

[123] F. A. Hegmann, J. B. Williams, B. Cole, M. S. Sherwinb, J. W. Beeman, and E. E. Haller. Time-resolved photoresponse of a gallium-doped germanium photoconductor using a variable pulse-width terahertz source. *Appl. Phys. Lett.*, 76:262–264, 2000. 123

[124] P. D. Grant, R. Dudek, L. Wolfson, M. Buchanan, and H. C. Liu. Ultra-high frequency monolithically integrated quantum well infrared photodetector up to 75 ghz. *Electron. Lett*, 41:214–215, 2005. 123, 130

[125] H. Luo, H. C. Liu, C. Y. Song, and Z. R. Wasilewsk. Background-limited terahertz quantum-well photodetector. *Appl. Phys. Lett.*, 86, 2005. 123, 126

[126] H. C. Liu, H. Luo, C. Y. Song, Z. R. Wasilewski, A. J. SpringThorpe, and J. C. Cao. Terahertz quantum well photodetectors. *IEEE J. Sel. Topics Quantum Electron.*, 14:374–377, 2008. 127

[127] M. Hajenius, P. Khosropanah, J. N. Hovenier, J. R. Gao, T. M. Klapwijk, S. Barbieri, S. Dhillon, P. Filloux, C. Sirtori, D.A. Ritchie, and H. E. Beere. Surface plasmon quantum cascade lasers as terahertz local oscillators. *Opt. Lett.*, 33:312–314, 2008. 128, 140

[128] A. J. Borak, C. C. Phillips, and C. Sirtori. Temperature transients and thermal properties of $gaas/algaas$ quantum cascade lasers. *Appl. Phys. Lett.*, 82:4020–4022, 2003. 133

[129] M. S. Vitiello, G. Scamarcio, and V. Spagnolo. Time-resolved measurement of the local lattice temperature in terahertz quantum cascade lasers. *Appl. Phys. Lett.*, 92, 2008. 133

[130] E. E. Orlova, J. N. Hovenier, T. O. Klaassen, I. Kasalynas, A. J. L. Adam, J. R. Gao, T. M. Klapwijk, B. S. Williams, S. Kumar, Q. Hu, and J. L. Reno. Antenna model for wire lasers. *Phys. Rev. Lett.*, 96, 2006. 139, 149

[131] S. Kumar, B. S. Williams, Q. Qin, A. M. Lee, and Q. Hu. Surface-emitting distributed feedback terahertz quantum-cascade lasers in metal-metal waveguides. *Optics Express*, 15, 2006. 139

[132] E. Mujagic, C. Deutsch, H. Detz, P. Klang, M. Nobile, A. M. Andrews, W. Schrenk, K. Unterrainer, and G. Strasser. Vertically emitting terahertz quantum cascade ring lasers. *Appl. Phys. Lett.*, 95, 2009. 139

[133] Y. Chassagneux, R. Colombelli, W. Maineult, S. Barbieri, S. P. Khanna, E. H. Linfield, and A. G. Davies. Predictable surface emission patterns in terahertz photonic-crystal quantum cascade lasers. *Optics Express*, 17, 2009. 139

[134] M. I. Amanti, M. Fischer, C. Walther, G. Scalari, and J. Faist. Horn antennas for terahertz quantum cascade lasers. *Electr. LEtt.*, 43:450–451, 2007. 139

[135] J. Lloyd-Hughes, G. Scalari, A. van Kolck, M. Fischer, M. Beck, and J. Faist. Coupling terahertz radiation between sub-wavelength metal-metal waveguides and free space using monolithically integrated horn antenna. *Optics Express*, 17, 2009. 139

[136] A. W. M. Lee, Q. Qin, S. Kumar, B. S. Williams, Q. Hu, and J. L. Reno. High-power and high-temperature thz quantum-cascade lasers based on lens-coupled metal-metal waveguides. *Opt. Lett.*, 32, 2007. 139

[137] N. Yu, J. Fan, Q. J. Wang, C. Pflugl, L. Diehl, T. Edamura, M. Yamanishi, H. Kan, and F. Capasso. Small-divergence semiconductor lasers by plasmonic collimation. *Nat. Phot.*, 2, 2008. 139

[138] A. Danylov, J. Waldman, T. M. Goyette, R. H. Giles A. J. Gatesman and, K. J. Linden, W. R. Neal, W. E. Nixon, M. C. Wanke, and J. L. Reno. Transformation of the multimode terahertz quantum cascade laser beam into a gaussian, using a hollow dielectric waveguide. *Appl. Opt.*, 46, 2007. 139

[139] M. I. Amanti, M. Fischer, G. Scalari, M. Beck, and J. Faist. Low-divergence single-mode terahertz quantum cascade laser. *Nat. Phot.*, 3, 2009. 139

[140] S. Fathololoumi, E. Dupont, S. G. Razavipour, S. R. Laframboise, Z. R. Wasilewski, A. Delage, A. Bezinger, G. Z. Rafi, S. Safavi-Naeinia, D. Ban, and H.C. Liu. Electrically switching transverse modes in high power thz quantum cascade lasers. *Opt. Exp.*, 18:10036–10048, 2010. 140

[141] N. Yu, L. Diehl, E. Cubukcu, C. Pflugl, D. Bour, S. Corzine, J. Zhu, G. Hofler, K. B. Crozier, and F. Capasso. Near-field imaging of quantum cascade laser transverse modes. *Opt. Exp.*, 15:13227, 2007. 143, 145, 156

[142] J. T. Robinson, K. Preston, O. Painter, and M. Lipson. First-principle derivation of gain in high-index-contrast waveguides. *Opt. Exp.*, 16:16659, 2008. 149, 150

[143] A. Lyakha, P. Zory, D. Wasserman, G. Shu, C. Gmachl, M. DSouza, D. Botez, and D. Bour. Narrow stripe-width, low-ridge high power quantum cascade lasers. *Appl. Phys. Lett.*, 90, 2007. 150

[144] H. Luo, S. R. Laframboise, Z. R. Wasilewski, H. C. Liu, and J.C. Cao. Effects of extraction barrier width on performance of terahertz quantum-cascade lasers. *IEE Electr. Lett.*, 44:630–631, 2008. 161, 162, 163, 195

[145] A. Wacker. Semiconductor superlattices: a model system for nonlinear transport. *Physics Reports*, 357, 2002. 174